UNIVERSITEIT ANTWERPEN

Faculteit Wetenschappen

Departement Fysica

Quantum dots doped with few magnetic impurities

Kwantumstippen gedopeerd met enkele magnetische onzuiverheden

Proefschrift voorgelegd tot het behalen van de graad van
doctor in de wetenschappen
aan de Universiteit Antwerpen te verdedigen door

Nga Thi Thuy Nguyen

Promotor: Prof. dr. F. M. Peeters

Antwerpen 2010

Acknowledgments

The work present in this thesis would have taken far longer to complete without the support and encouragement from many people. It is my pleasure to thank the many people who contributed to my PhD thesis

First and foremost, I would like to express my deepest thanks to my thesis advisor, Prof. Dr. François Peeters, for his guidance and continuous encouragement throughout my PhD research period. I have been fortunate to be his student and have been shared many valuable aspects from his wise knowledge and thoughtful insight. The research project of *few-electron quantum dots doped with few magnetic impurities* that he pointed out has brought me opportunities to enrich my knowledge and filled out my life with prospectives and a lot of joy.

My sincere gratitude goes to Prof. Dr. Bart Partoens for his time, his kind help, and valuable advice. I thank him for sharing his deep knowledge in many parts of this thesis with me. I am also thankful to the rest of my PhD thesis committee: Prof. Dr. Jacques Tempère, Prof. Dr. Jozef Devreese, Prof. Dr. Etienne Goovaerts, Prof. Dr. Kristiaan Temst, and Prof. Dr. Reinhold Egger for their valuable time to read my thesis and share with me their critical comments, fruitful discussion, and hard questions.

I am indebted to Prof. Dr. Alexander Govorov for stimulating discussion.

Working in an international scientific environment like the CMT-group has been one of the most beautiful things that happened in my life. I wish to thank you all for providing such a rich source of education, multi-cultural experience, and joyful conversation. Your warm care and great enthusiasm will remain in my heart wherever I am.

I also wish to take this opportunity to thank the secretariat of the Department of Physics and the coordinator of DOCOP-UA for their kind help.

There are a lot of friends who constantly provided moral support and help during my stay in Antwerp. They deserve my special thanks for making my life so blessed by their friendship.

Last and most importantly, I thank my extended family: my parents, my parents-in-law, my two brothers, my sister, my brother-in-law, my sisters-in-law, my two lovely nieces and four adorable nephews for their special love, strong support, encouragement, and also sharing entertainments. Especially, I thank my parents, my two brothers, and my sister for loving me unconditionally and supporting me wholeheartedly. This thesis would have never been completed without the support from a very special person: my devoted husband. I thank him for his patience, his great enthusiasm, and his

love that keeps our little family filled with full of joy and happiness which encouraged me to achieve this goal. I dedicate this thesis to you all!

This work was financially supported by FWO-Vl (Flemish Science Foundation) and the Belgian Science Policy (IAP).

Contents

List of Abbreviations

0D	Zero dimensional
1D	One dimensional
2D	Two dimensional
3D	Three dimensional
2DEG	Two-dimensional electron gas
AFM	Anti-ferromagnetic
CI	Configuration Interaction
CR	Cyclotron resonance
DFT	Density functional theory
DMS(s)	Diluted magnetic semiconductor(s)
DRAM	Dynamic random access memory
ED	Exact Diagonalization
e-e	electron-electron
EEPROM	Electrically erasable programmable read-only memory
e-h	electron-hole
e-Mn	electron-Mn-ion
FIR	Far-infrared
FM	Ferromagnetic
FD	Fock-Darwin
GMR	Giant magnetoresistance
GS	Ground state
HF	Hartree-Fock
HR-TEM	High resolution transmission electron microscopy
LLL	Lowest Landau level
MBE	Molecule Beam epitaxy
MDD	Maximum density droplet
ML	Monolayer
MOCVD	Metal organic chemical vapor deposition
MRAM	Magnetic random access memory
OS	Oscillator strength
PL	Photoluminescence
QD(s)	Quantum dot(s)
QMC	Quantum Monte Carlo
QW	Quantum well
RAM	Random access memory
RKKY	Ruderman-Kittel-Kasuya-Yosida
SK	Stranski-Krastanov
SQD(s)	Self-assembled quantum dot(s)
STM	Scan tunneling microscopy
TEM	Transmission electron microscopy
UHF	Unrestricted Hartree-Fock

1 Introduction

1.1 Spintronics as an emerging field for future electronics

Conventional (silicon Si) electrically-based technology uses the binary flow of electron charges to facilitate communications between different microelectronic devices expressing data in the form of binary bits (ones and zeroes corresponding to the presence and absence of electron charges). The miniaturization obeying Moore's Law, which states that microprocessors would double in power every 18 months, has lead to an exponential increase in the quantity of information packed into a microprocessor. However, Moore's paradigm faces an early end when the size of a single bit approaches atomic scale dimensions. A vital question is whether or not it is possible to further keep increasing miniaturization. There are suggestions to enhance multifunctionalities by e.g. combining processing and date-storage in a single unit of an electronic device using the spin of the electron.

Spintronics [1, 2, 3] is an emerging interdisciplinary field where electronic properties are controlled by the spin degree of freedom. The electron spin which is a quantum phenomenon itself directly couples with its magnetic moment and the spin degree of freedom can be manipulated by applying an electric or magnetic field. The movement of spins, similar to the flow of charges, can carry information. The spin orientation of conduction electrons, i.e. their phase coherence, maintains within a timescale of nanoseconds, which is found considerably longer than the tens of femtoseconds for the momentum decay time of charges [4, 5, 6] which are easily destroyed by defects or impurities. This fact makes spintronic devices particularly attractive for memory storage and magnetic sensor applications and potential applications for quantum computing where electron spin represents a quantum bit of information. A typical spintronic device function is based on the

following steps: i) information is written in the form of spins, ii) the spins which are coupled to mobile electrons carry the information, and iii) the information is read at some terminal.

One of the main goals in achieving spintronic devices is to create magnetic random access memory (MRAM) which utilizes magnetic hysteresis to store data and magnetoresistance to read data [2]. Si-based semiconducting electronic devices retain memory based on an accumulated electric charge called dynamic random access memory (DRAM) that requires frequent refreshing. Because random electric fields are considerately stronger than random magnetic felds, DRAM-based devices consume more energy than a spintronic device (MRAM). Information stored in spintronic devices is nonvolatile, i.e. it retains when power is off. This makes spintronic devices very interesting due to the stand-by dissipation power (and time) savings. Thereby, spintronic devices are expected to be faster than conventional electronic devices. As compared to Si electrically erasable programmable read-only memory (EEPROM) and flash memory, MRAM is 1000 times faster, no wear-out with write cycling (EEPROM and flash wear out with about 1 million write cycles), and lower energy in writing. MRAM accesses data on a timescale $\sim$ 10,000 times smaller than the corresponding time for the present hard disk drive [2].

Activity in the spintronic field can be mainly classified into: i) applications that involve the presence of many spins, for example high density data storage and read-out, and ii) applications that involve a lower concentration of spins for future applications related to quantum information processing. The obstacle that needs to be overcome is to learn how to inject a sufficient number of spins into suitable materials which allow the process of manipulating different spin states and detecting information efficiently [2]. Materials that combine electronics with the magnetic properties governed by spin-related effects define new types of materials. Such materials are spin-polarized carrier sources which allow the integration with existing semiconductor devices, namely ferromagnetic semiconductors e.g. Mn-doped GaAs, CdTe, CdSe, compounds of EuS, GaN, etc and the group of materials with a significantly larger spin-polarization namely ferromagnetic oxides and other related alloys e.g. CrO_2, $La_{70}SrMnO_3$, Fe_3O_4, etc.

1.2 Diluted Magnetic Semiconductors

Electron spins, which are the key ingredients in spintronics, are used for their two possible spin orientations, either up or down with respect to the align-

ment of an applied magnetic field or the magnetization of a ferromagnetic (FM) film. The traditional method to generate a spin-polarized current in a metal is to pass the current through a FM sample. Regarding the field of magnetism (magnetic materials), the breakthrough discovery of giant magnetoresistance (GMR) effect on alternative Fe/Cr/Fe sandwich layers was extremely inportant. The experiment was conducted independently by the groups of P. Grünberg [7] and A. Fert [8] (2007 Nobel laureates). When the two magnetization vectors of the ferromagnetic (Fe) layers are anti-aligned, the electrical resistance through the layers will be significantly increased which can reach a value of $\Delta R/R \sim 40\%$ as compared to the aligned case. GMR effect is considered as the first experiment of spin manipulation which offers a means to produce an energy-conserving and fast switching device because the current can be controlled without changing the carrier concentration. Applications of the GMR effect can be found in e.g. the metallic spin-valve in high-density read heads or magnetic-field sensors in computer hard discs where data up to tens of gigabytes can be stored in a recording medium (disc).

A GMR-based metallic spin valve consists of two FM layers (often alloys of Fe, Ni, or Co) sandwiched by a thin non-magnetic layer (often Cu) subjected to a magnetic field with $\Delta R/R \sim 5 \div 20\%$ has been used widely in spin-based electronic devices e.g. MRAMs. However, metallic spin valves are not able to amplify signals. Materials which can be used to amplify signals are likely semiconductors that can be intergraded with existing semiconductor technology. Injecting spins in such materials is possible. One of the most direct ways to introduce spins in semiconductors is to inject magnetic atoms (with a net magnetic moment) into semiconductors. Such semiconductors are referred to diluted magnetic semiconductors (DMSs) [9, 10, 11, 12, 13]. By incorporating a diluted number of magnetic atoms into host semiconductors the system can result in ferromagnetism with a transition temperature defined as the Curie temperature T_c.

Semiconductors have low carrier density (as compared to metals) and high-quality materials merge with spin-based magnets forming semiconductor spintronics [14, 15]. This type of materials opens unique opportunities to tune the electronic properties by changing doping/ gate voltage. One of the ambitious goals is to create nanostructures that provide a strong ability for information processing and memory storage. When doped with magnetic impurities, Curie temperature T_c of the system increases. To date, the maximum $T_c = 188$ K was obtained in Ga(Mn)As films by Olejník *et al* [16] with a dopant density of Mn-atoms of about $x = 11\%$.

DMSs are formed by replacing a small fraction of the cations A of a

semiconductor compound AB by transition metal atoms (ions) or rare earth elements M. These transition substitutional atoms will affect many aspects of the DMSs and by changing the composition of the compound one can vary the energy gap, lattice parameters, etc, of the host material. Equivalently, DMS compounds can be called semimagnetic semiconuctors and described symbolically by $A_{1-x}M_xB$ or A(M)B, or AB(M). A is often a nonmagnetic cation and A and B can be group II-VI elements e.g. CdTe, ZnSe (which attracted primary attentions from beginning days), III-V e.g. GaAs, InAs, or IV-IV e.g. PbTe, SnTe elements.

The embedded magnetic element M is often the ion Mn^{2+} which is involved in DMSs because it can replace, theoretically, up to a large amount of cations ($\sim$ few tens %) in II-VI DMSs. Manganese is a transition metal with valence electrons corresponding to the $4s^2$ orbital. Mn^{2+} has the electron configuration $[Ar]4s^0 3d^5$. The presence of the Mn^{2+} is the origin for the formation of ferromagnetism [11] in DMSs where its 5 electrons in its outer $3d$-orbiral makes the Mn-ion bear a spin 5/2. This spin is relatively large and therefore becomes attractive for spin-related electronic properties.

Within the DMSs materials, II-VI and III-V groups are the most advanced groups (see review papers respectively by Furdyna [10] and Jungwirth [13]). II-VI DMSs were intensively studied in the early days however fabricating II-VI DMSs poses a severe problem because it was found very hard to inject the Mn-ions into the system. Earlier successful fabrications of group III-V DMS systems (e.g. In(Mn)As [17]) made this DMS group more promising for electronic technology such as: optics, micro-spectroscopies, etc. In this thesis I will focus on these first two groups of DMS materials

1.3 Ferromagnetism in III-V and II-VI DMSs

The origin of ferromagnetism in II-VI DMSs comes from the spin exchange interaction between the Mn-ions mediated by the carriers (conduction-band electrons or valence-band holes), in particular through the *sp-d* exchange interaction. The strength of this type of interaction is found to be considerable especially for II-VI compounds with a magnitude of eV for a system with a relatively large collection of Mn-ions. Whereas the origin of ferromagnetism in III-V DMSs is still under debate. Two widely-discussed models are the RKKY interaction and indirect exchange mechanism which can be double- or super-exchange (via a separate non-magnetic atom) between the Mn-ion spins. I will not go into detail about the origin of magnetism for III-V DMSs for which I recommend the reader to consult the recent review paper Ref.

[13].

The mechanism of spin transfer in magnetic (semiconducting) materials is based on the exchange interaction between the polarized carriers and static magnetic atoms, often the Mn^{2+}, which contributes to the understanding of spin electronic transport properties. Moreover, this type of interaction influences magneto-optical properties even for $B = 0$. On the other hand, the spin states of the magnetic atoms can be altered by changing the number of carriers (one-by-one) by e.g. the gate voltage [18]. Therefore, ferromagnetism at nanometer scale in such system can be controlled, i.e. its T_c is tunable. Knowledge about the lifetime of an isolated magnetic impurity plays a crucial role in spintronics.

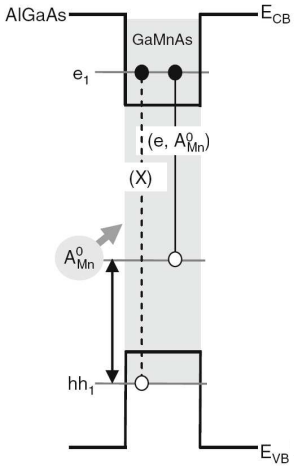

Figure 1.1: Possible optical transitions in III(Mn)V quantum wells. Band-edge along the growth direction showing optical transitions of excitons and Mn-acceptor emission. Reproduced after Ref. [1]

Information is read on the single spins which should have a relaxation time of about 10^{-3}s as has been measured in a dilute ensemble of Mn^{2+} in DMS CdSe [19]), and a coherence length much larger than that of the electronic-based devices.

1.3.1 Group III-V

In the III-V DMSs, divalent Mn-ions can substitute the trivalent cations due to the similarity in the $4s^2$-orbital and their $4p$-orbital is missing electrons that makes the Mn-ion acts as an acceptor and the *sp-d* bonding makes it as a source of a local moment with zero angular momentum. The acceptor state(s) stay within the band gap causing the Mn^{2+} to behave as optical spin center(s) (see Fig. 1.1). Besides, the acceptor can contribute holes to the system. In addition to the exciton (X) exchange splitting an apparent spectroscopic splitting of the Mn-acceptor occurs in e.g. GaAs as shown in Fig. 1.1. When the photo-excited electrons staying at the bottom of the conduction band recombine with the heavy holes at the valence band that are loosely bound to the Mn-ions [A^0_{Mn}=($hole$+Mn^{2+}) in Fig. 1.1] the system

($electron$, A^0_{Mn}) photoluminesces. The neutral acceptor complex A^0_{Mn} is in the AFM state where the hole and Mn-acceptor have anti-parallel spins.

Host-semiconductor III-V based crystals are found in zinc blende structure. To introduce Mn^{2+} into parent III-V semiconductors [11, 17] one needs to overcome the solubility obstacle because III-V DMSs exhibit a rather low solubility (maximum 10^{19} cm^{-3} $\sim 1\%$) to Mn^{2+}. With the advent of crystal growth technique the low solubility and aggregation can be improved and well-controlled by adjusting growth-conditions and co-doping [1] in low-temperature nonlinear MBE.

Most important physics in this group of materials are the ferromagnetism due to the coupling of the localized Mn^{2+} and the holes resulting in T_c. The formation of ferromagnetism due to the mediated-carrier interaction depends on the bound acceptor states (see e.g. Refs. [13, 21, 22, 23, 24, 25, 26]). III(Mn)V DMSs have a relatively large Curie temperature (about 170K for Ga(Mn)As - see e.g. Fig. 1.2) as compared to the II-V family (few K) because

$$T_c \propto (\Delta_{Mn-Mn})^2 \tag{1.1}$$

where Δ_{Mn-Mn} is the exchange coupling between the magnetic moments mediated by the host material carriers (electrons and holes) which is also the origin of ferromagnetism [5, 27] and can be estimated using second-order perturbation theory (see e.g. Ref. [28]).

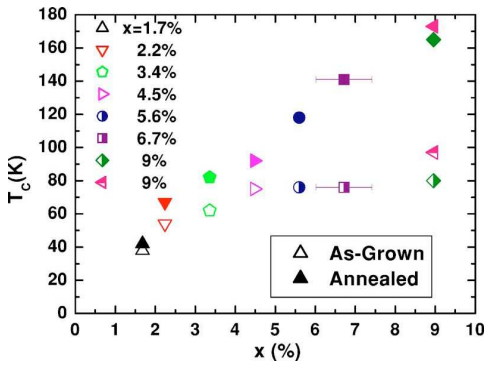

Figure 1.2: Experimental Curie temperature T_c vs total Mn doping. Open symbols refer to as-grown samples, half-open symbols to As-grown samples with large charge compensation, and filled symbols to annealed samples. Error bars are shown for the x=6.7% sample. After Ref. [20].

A milestone discovery in III-V group was the observation of carrier-

induced ferromagnetism in Ga(Mn)As [11, 29] and In(Mn)As [30] by Ohno *et al* which opened promising applications for quantum computing. Since the first report on the T_c = 7.5K by Ohno *et al* [30] in 1992 its value had increased further to 110K in 1998 by the same authors [11] and this Curie temperature at the time it was obtained was considered as the highest attainable T_c for Ga(Mn)As. The crucial quantity that determines T_c is the Mn-ion concentration and the free hole density. However, self-compensation by the interstitial sites in the sample, namely Mn-interstitials which act as donors and passivate substitutional Mn-acceptors, becomes the limiting factor for further increase of T_c for a doping beyond $x \sim 5\%$. Up to 2002, based on the advent of post-growth annealing where part of Mn-interstitials can be removed, T_c was further increased to 150K and 173K for Ga(Mn)As, respectively, by Ku *et al* [31] and Jungwirth *et al* [20] and its highest value to date is (188K) mentioned above by Olejnik *et al* [16] in 2008.

Experimental T_c shown in Fig. 1.2 is related to the work in Ref. [20]. T_c was measured from the anomalous Hall effect and concentration x_{Mn} was doped to GaAs sample by secondary ion mass spectroscopy. By increasing x_{Mn}, T_c was found increasing different for different As-grown samples. Black full-triangle refers to a slight increase of T_c for x-Mn$\sim$ 1.6% by using annealing post-growth.

Theoretically, T_c for such $Ga_{1-x}Mn_xAs$ systems with lattice constant a_0 and Bohr magneton μ_B can be estimated [20, 32] using a mean-field approximation:

$$k_B T_c = \frac{N_{Mn} S(S+1)}{3} \frac{J_{pd}^2 \chi_f}{(g\mu_B)^2}. \tag{1.2}$$

The above expression takes into account the Coulomb interaction between the valence holes which also plays a role in the increase of T_c. $N_{Mn} = 4x/a_0^3$ is the Mn-ion density, S is the total spin, J_{pd} is the exchange interaction strength between the Mn-ion and the electron, and χ_f is the electron-hole magnetic susceptibility. The Mn-ion-hole correlation is neglected. Using this approximation, the authors [20, 32] found that T_c was in good agreement with the experimental result T_c = 110K of Ref. [11]. However, the highest T_c so far is still far lower than room temperature which for the Ga(Mn)As samples would need a composition of at least 10% of Mn^{2+}.

1.3.2 Group II-VI

In spite of the fact that Mn differs from the group-II cations by the $3d^5$ shell which is only half-filled, Mn can contribute its $4s^2$ electrons to the s-p^3 bonding. Therefore, Mn can substitute the group-II elements in the

AB wurtzite or zinc blende structures. Following Hund's rule, these five d-electrons have parallel spins that adding another electron with opposite spin to the Mn-atom needs a considerably large energy. As a result, the $3d^5$ orbit is stable and the Mn-atom resembles a group-II element up to $x = 0.77$ [10].

In the II-VI DMSs, the Mn-ion is isoelectronic which means that no additional electric field is created and the number of carriers is conserved. Besides, the polarity of the elements in II-VI group is strong. This makes them attractive for interesting optical properties. For these DMSs both p- and n-type doped systems are possible therefore the II-VI DMSs provide good samples where both types of interactions such as Coulomb repulsion, and the electron-Mn or the Mn-Mn spin-spin exchange can be examined.

Most of the II-VI DMSs [10, 33], e.g. the Cd(Mn)Se or Cd(Mn)Te, have a direct energy gap which in the case of Cd(Mn)Te alloy is almost linearly dependent on the Mn-atom composition and hence most striking physics occur around the Γ point. Furthermore, Mn-ions interact strongly with the electrons in both the valence and conduction band via the spin exchange leading to giant Zeeman energy splitting [34, 35] between the band states for $B \neq 0$. Holes are introduced into II-VI either by the doping mechanism e.g. with Nitrogen (N)-doped in ZnTe [36, 37] or mostly by using photo-excitation with suitable intensities. In detail, the band-gap energy for Cd(Mn)Te [38] for different temperatures is expressed as

$$E_g(T = 300K) = (1.528 + 1.316x)\ \ (eV) \tag{1.3}$$

$$E_g(T = 4.2K) = (1.606 + 1.592x)\ \ (eV) \tag{1.4}$$

with $x \leq 0.77$ after Ref. [10]. This wide band gap property results in a small exchange interaction between the holes and the magnetic ions leading to a small value for T_c for the II-VI alloys. Furthermore, the spin-orbit interaction is found to be larger (0.7 eV) than that for the case of III-V DMSs.

The magnetic interaction in II-VI DMSs is dominated by antiferromagnetic exchange between the Mn spins, which results in paramagnetic, spin glass, and ultimately long-range antiferromagnetic behavior [10, 33]. Interplay between exchange interactions leads to the formation of robust (bound) magnetic polarons and significant magneto-optical properties [35, 37, 39, 40].

All of the above facts lead to relatively small T_c for the II-VI DMSs which has been found to be about few K. Most of the II-VI Mn-doped DMSs do not exhibit ferromagnetism at $B = 0$. However, the magnetic features of the system change dramatically in the presence of a magnetic field.

The magnetic impurities which generally have a zero total net magnetic moment will exhibit mediated ferromagnetism [41, 42] for $B \neq 0$. Their strength decreases rapidly when the Mn-atoms are positioned further from their nearest-neighbor separation, e.g. $\sim$5 times less if the atoms are located at the next-nearest-neighbors [43].

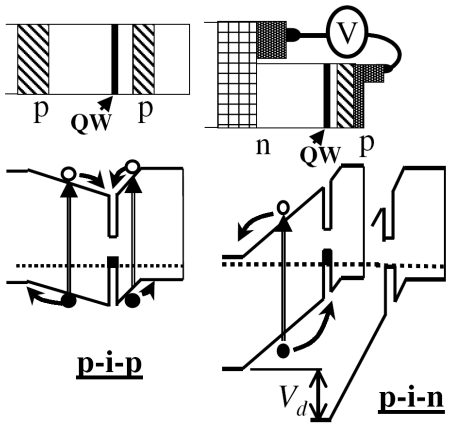

Figure 1.3: Schematic plot of p-i-p and p-i-n structure containing a Cd(Mn)Te QW and band alignments with and without a bias voltage V_d. After Ref. [41]

Even though Mn-ions can incorporate up to 77% in the host II-VI semiconductors, injecting Mn-ions into such materials was very hard due to the high sensitivity on the type of substrate which can lead to the creation of mixed crystals.

Very recently, several groups have succeeded in the realization of the II-VI DMS compounds such as colloidal wurtzite Mn^{2+}:CdSe QDs [44, 45] prepared using the direct chemical synthesis approach with a very low density of Mn-ions (from $0 \div 5\%$), zincblende Cd(Mn)Te quantum wells [46] with Mn-ions of about 2% at very low temperature (<2K), and CdTe QDs [47] doped with a single Mn^{2+} using epitaxial technique at $T \leq 7K$. Increasing attention is paid to the II-VI DMS systems with very small concentration of dopants.

Hole-mediated ferromagnetism in a modulation-doped Cd(Mn)Te QW can be tuned using PL which is presented in e.g. Ref. [41] (see Fig. 1.3). Here, the structures contain a single 8 nm QW of (Cd,Mn)Te, with typically 3% to 5% Mn-ion, and the (Cd,Mg,Zn)Te barriers. In the back barrier of the

p-i-p structure, a Nitrogen-doped layer is inserted at 100 nm from the QW. A hole gas in the QW is created by doping the top barrier with Nitrogen-acceptors with concentration $\sim 10^{17}\text{cm}^{-3}$. In the p-i-n structure, the back barrier doped with Aluminum resides 320 nm away from the QW, and the spacer between the QW and the p-doped layer is diminished to 10 nm. The density of holes of about 2×10^{11} cm^{-2} is found in the QW in both p-i-p and p-i-n structures which can be modulated by the bias voltage V_d (details see Ref. [41]). An experimental hole-density dependence of T_c for both p-i-p (circles) and p-i-n (squares) samples is shown in Fig. 1.4 which was in good agreement with theoretical mean-field approximation.

Recent progress in doping technology of II-VI materials has made it possible to use single Mn-ion spins for information storage in their magnetic moment e.g. single-doped Cd(Mn)Te DMS systems by Besombes *et al* [47, 48, 49] despite the low T_c. This is the main topic which will be discussed in the remaining parts of this thesis.

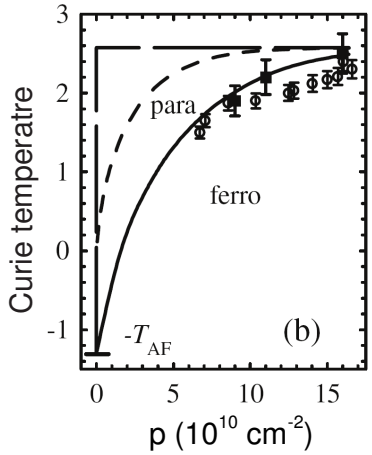

Figure 1.4: T_c versus hole density p for the p-i-p (circles) and p-i-n (squares) structure containing a Cd(Mn)Te QW. The lines show T_c values calculated by the mean-field approximation for different assumptions about the hole-spin susceptibility: the long-dashed line is for a 2D degenerate Fermi liquid, the short-dashed line for the effect of nonzero temperature on a clean Fermi liquid, and the solid line is obtained assuming a Gaussian broadening of the density of states. After Ref. [41]

1.3.3 Annealing

Annealing is a post-growth process to further improve the quality of a sample under heat treatment. In the case of Ga(Mn)As (see Fig. 1.2) annealing [31] at sufficiently low temperatures increases T_c. The increase depends on the annealing temperature T_A and annealing time t_A. From the relation (1.2), T_c is proportional to the free hole density via χ_f. Annealing at temperature T_A slightly larger than the growth temperature in Ga(Mn)As can weaken the sensitivity of active Mn-ions to a magnetic field or an electric field. Consequently, Mn-interstitials out diffuse during annealing toward the Ga(Mn)As surface increasing the density of holes unbound to the Mn-acceptors which leads to an increase of T_c.

For $x = 8.5\%$ (Mn-concentration), T_c was reported to increase from 110 K to 150 K [31] which is about a 30% increase at annealing temperature $T_A > 350°C$. Note that annealing at high T_A in large t_A can result in a suppression of T_c.

The highest up-to-date $T_c = 188$K [16] obtained for 11% Mn-doped in 35-nm Ga(Mn)As film grown by low-temperature MBE was annealed in air by placing the sample on a heat plate at $T_A = 200°C$. The annealing efficiency is enhanced by using surface oxide etching to control the passivation of the Mn-interstitials in a thin Ga(Mn)As layer. In addition to the standard continuous annealing [20, 31], a sequence of discrete etch-anneal steps was applied where after 30s an etching with 30% hydrochloric-acid (HCl), rinsed in water, and subsequently annealed for 5 min. The HCl etched-surface dried off immediately after the rinsing. The efficiency of etch-annealing as compared to standard annealing [31] was shown. In a continuous annealing process, the initial $T_c = 85$ K was increased to 137 K after t_A =15 min and the maximum $T_c = 176$K was reached after t_A =100 min. Now, by using the etch-anneal technique, $T_c = 170$ K was reached after only t_A =15 min and the saturated value of $T_c = 188$ K after $t_A = 40$ min. The surface-oxide etching is the reason for this relatively large reduction of t_A.

1.4 Magnetic quantum dots

1.4.1 DMS quantum dots as a promising candidate for quantum computing

A further step in spintronics development that have attracted great interest from both experimentalists and theoreticians is quantum computing. Individual qubits can be based on both spin and charge that are confined in a

system such as a QD doped with a very diluted density of Mn-ions.

Incorporated Cd(Mn)Se [44, 45] or Cd(Mn)Te [50] QDs are expected to be good candidates to achieve suitable nanoscaled ferromagnetism [41, 42]. Here, the $B \neq 0$ Mn-Mn ferromagnetic ordering strongly depends on their relative positions $\overrightarrow{R}_{Mn-Mn}$ [43] and can be controlled independently by controlling the number of electrons. In this context, magnetic dots embedded with a tunable number of carriers behave similarly as tunable nanomagnets [51]. This type of QDs is ideal for studies of spin-based quantum processing where detected spin states of the single magnetic impurities which are light-controlled can be envisaged and such QD can be used as a building block in a fully scalable quantum logic gate (see Refs. [52, 53]).

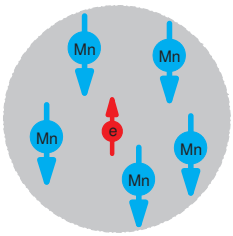

Figure 1.5: Schematic model of magnetic polaron state formed by a single valence-band electron and many Mn^{2+} located inside a QD.

1.4.2 Quantum dots with few Mn^{2+}

As mentioned above, despite the low T_c ($\sim$ few K) due to low concentration of holes because the magnetic dopants do not attract holes and due to large energy band gap E_g, the II-VI dots are considered as model systems to examine the electron-Mn-ion or Mn-Mn interaction due to the following facts.

When injecting charged particles into these DMS QDs, a long lifetime of excitons ($\sim$100 ns) [44, 45] was measured which was a result of the e-Mn exchange interactions and photoinduced magnetization can be measured.

The ultimate case of single-electron/-hole QD doped with few Mn^{2+} exhibits a robust magnetic polaron state which is strongly anisotropic and which can survive up to relatively large temperatures [37, 39, 40, 54, 55, 56, 57]. The magnetic polaron state was found to be different for different materials due to the functionalities of the Mn^{2+} in e.g. the III-V and II-VI DMSs. For the II-VI QD the formation of the Mn^{2+} can be described schematically in Fig. 1.5 where the single electron (w/o the presence of hole) couple AFM (or FM) with the localized Mn-ions forming the AFM (or FM) polaron state. This state is found to be strongly anisotropic due to the exchange interaction between the Mn-ions which will be explored thoroughly in chapter 7.

Alternatively, one has considered the situation where the Mn-ions outside a dot are bound to a single valence-band hole (due to opposite charges) - which is introduced in the dot by modulation doping of a substitutional atom e.g. N-doped in ZnTe [36, 37, 58] or Iodine(I)-doped in ZnSe [59]. In this case the magnetic polaron state is also formed with two possibilities for the AFM coupling between the hole and the Mn-ions (as a consequence of the penetration of the hole wave function in the barrier material) corresponding to two classical bit states of 0 and 1 as shown in Fig. 1.6. This magnetic polaron state is also anisotropic as a consequence of a large splitting between heavy- and light-hole levels in II-VI DMS dots.

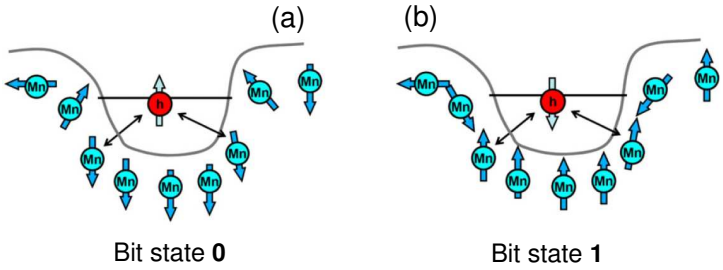

Figure 1.6: Schematic plots of spin structure of a single hole (red) orbiting in a Mn (cyan)-doped QD. Two stable states exist with the hole momentums $j_z = 3/2$ (a) and $-3/2$ (b) similar to classical bit 0 and 1. The arrows connecting the hole spin and Mn spins represent a carrier-mediated interaction; this interaction occurs between two stationary impurities via one orbiting hole. After Ref. [55].

A theoretical analysis which describes the magnetic polaron formed by confined holes and Mn-ions in a $N_{e(h)}$-electron (-hole) self-assembled (disk-like shape) QD with many Mn^{2+} using mean-field approach was realized by Govorov in Ref. [55] using the effective Hamiltonian:

$$\hat{H}_{eff} = \sum_{i=1}^{N_e(h)} \left(\hat{T}^{(i)} + U_h(\overrightarrow{r_i}) - J_{h-Mn} x_{Mn} N_0 \cdot \overrightarrow{l_z^i} \cdot \overrightarrow{S}(\overrightarrow{r_i}) \right) + H_{Coul} = H_0 + H_{Coul} \tag{1.5}$$

where

$$\bar{S}(\overrightarrow{r}) = SB_S\left(S\frac{J_{h-Mn} \cdot \bar{j}_z(\overrightarrow{r})}{k_B(T+T_0)} \right) = SB_S u, \tag{1.6}$$

with $u = S\frac{J_{h-Mn} \cdot \bar{j}_z(\overrightarrow{r})}{k_B(T+T_0)}$ and $S = 5/2$, is the local Mn-spin, B_S the Brillouin

function, and

$$\bar{j}_z(\overrightarrow{r}) = \langle\psi| \sum_{i=1}^{N_h} j_z^i \delta(\overrightarrow{r_i} - \overrightarrow{r_i}')|\psi\rangle \tag{1.7}$$

is the local hole-spin with $\psi(\{\overrightarrow{r_i}\})$ the many-body (hole) wave function. N_0 is the number of cations per unit volume, $\overrightarrow{l^i}$ the i^{th}-hole angular momentum, x_{Mn} the reduced spatial Mn-ion density, T_0 defines the AFM Mn-Mn coupling.

Due to modulation growth, the Mn^{2+}-spin axis is fixed along the z-direction, and the hole spin state will be

$$\hat{j}_z = \hat{l}_z + \hat{s}_z \tag{1.8}$$

where $s = 1/2$ and $l = 1$. This results in $j_z = \pm 3/2$ for the hole which corresponds to $|l_z = 1, s_z = 1/2\rangle$ and $|-1, -1/2\rangle$. The solution for the effective mean-field non-linear equation

$$\hat{H}_{eff}\psi(\{\overrightarrow{r_i}\}) = E\psi(\{\overrightarrow{r_i}\}) \tag{1.9}$$

is obtained as a minimum of the free-energy functional [57]:

$$F(\psi) = \langle|\hat{H}_0|\rangle - J_{h-Mn}x_{Mn}N_0\langle\psi|F_S\big(u\big)|\psi\rangle \tag{1.10}$$

where

$$F_S(u) = \frac{1}{u}Ln\left[\frac{sinh[(2S+1)u/2S]}{(2S+1)sinh(u/2S)}\right] \tag{1.11}$$

which relates to the Brillouin function by $B_S(u) = d[uF_S(u)]/du$. The stability of the hole-Mn magnetic polaron can be examined by the magnetic binding energy

$$E_{polaron} = -J_{h-Mn}x_{Mn}N_0\langle\psi|B_S Su|\psi\rangle \tag{1.12}$$

and the total Mn-ion spin

$$S_{Mn}^{tot} = x_{Mn}N_0 \int d\overrightarrow{r}\,\bar{S}_z(\overrightarrow{r}) \tag{1.13}$$

where the larger $E_{polaron}$ and S_{Mn}^{tot} the more stable the hole-Mn polaron will be to thermal fluctuations.

Practically, $J_{e-Mn} < 0$ and the h-Mn complex tends to form an AFM coupling. In order to lower the total energy, the holes and Mn-ions have spins antiparallel and form the AFM magnetic polaron state. For a sufficiently small N_h, the shell-filling due to Hund's first rule was found for the N_h holes. Particularly, for the cases $N_h = 4$ and 9 "robust" magnetic polaron states were obtained where the holes are half-filled the *p*- and the *d*- shell, respectively.

1.4.3 Quantum dots doped with a single Mn^{2+}

Increasing attention has been paid to recently realized DMS systems with a single Mn^{2+} doped to a CdTe QD grown on a ZnTe substrate [47] and later to a InAs QD grown on a GaAs substrate [21]. Recently, such a single magnetically doped QD made of the II-VI or III-V DMSs with well-interpreted spin states of the Mn-ion has been fully studied using optical means.

The former case of a CdTe dot [47, 48, 49, 60, 61] has attracted my attention because the single Mn-ion in this very diluted magnetic semiconductor system behaves similarly as a six-state quantum bit. This success [47] opens opportunities to store information in the magnetic moment of the Mn-ions. The spin memory of the magnetic ion was measured to be about few μs [62, 63] for $B = 0$. Furthermore, spins in DMS QD systems are expected to have a long lifetime [44, 64].

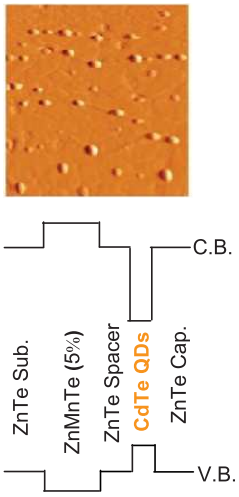

Figure 1.7: Top: 1 μm $\times$ 1 μm atomic force microscopy image under high vacuum illustrating the self-assembled QDs with density $\sim 5 \times 10^9$ cm^{-2}. Bottom: Band structure line up of conduction band (C.B.) and valence band (V.B.). After Ref. [49]

Experimental syntheses of CdTe/ZnTe quantum dots with a single Mn^{2+}

I will describe now the growth process of Mn-doped CdTe QDs on a ZnTe substrate, which was carried out by Besombes *et al* [47] and Maingault *el al* [65] at Laboratoire de Spectrométrie Physique, Centre National de la Recherche Scientique (CNRS), Grenoble (France).

The MBE method developed to grow such II-VI host QDs is described in Refs. [66, 67, 68] and in chapter 2 of this thesis with the creation of CdTe self-assembled dots on a ZnTe substrate (see Ref. [66]). A $Zn_{0.94}Mn_{0.06}Te$ barrier, which has a lattice mismatch $\sim 6.2\%$ as compared to the CdTe compound, followed by a ten monolayer ZnTe spacer is deposited on a ZnTe substrate. To introduce an extreme diluted density of magnetic impurities i.e. a single Mn^{2+} [69] in a CdTe QD the authors adjusted the density of Mn atoms in the QD layer to be equal to

the density of CdTe QDs ($\approx 5 \times 10^{-9}$ cm^{-2}). The CdTe QD layer is then deposited and capped with a ZnTe barrier (the method how to conduct this step can be found in Ref. [68]). The grown dots and a schematic picture of the conduction and valence band line up is shown in Fig. 1.7. The Mn-ion intermixing during the growth of the ZnTe spacer creates a sparse distribution of Mn^{2+} in the QD layer. Cd(Mn)Te QD was fabricated on the substrate of ZnTe is p-type.

To realize the ultimate structure of a dot containing a single Mn^{2+} [65], Maingault *et al* examined different dots. A 488 nm line of an Argon-laser was used to excite an individual QD which afterwards is collected through a large numerical aperture microscope objective and aluminum shadow masks with $0.2 \div 1.0$ μm apertures. The PL is then dispersed by a 2 m additive double monochromator and detected by a nitrogen cooled Si charge coupled device (CCD). Results showed that when more than one Mn-ion interacts with the confined QD exciton, only broad lines appear due to statistical magnetic fluctuations of all the spins of the Mn ions present in the QD. A simple geometric model shows that if one optimizes the Mn density n_{Mn} as compared to the density of QDs n, one finds that about half ($\sim$ 40%) of the total QD ensemble is doped with only one Mn^{2+}. In the latter case, the six-line emission in the PL spectroscopy of single electron (and hole) is well-detected as shown in Fig. 1.8 in case the Mn-ion is found close to the center of the QD. I will clarify this point in the theoretical examination in chapter 4.

1.4.4 Cd(Mn)Te quantum dots doped with a single Mn-ion

CdTe/ZnTe self-assembled QDs [68] (growth method is discussed in detail in chapter 2) permits to introduce the Mn-ion directly into the QD with conserved good-optical-properties. Before 2004, however, all the experimental studies on these diluted magnetic QDs were focused on the interaction of a single carrier spin with its paramagnetic environment consisting of a collection of Mn-ions [40] (and references therein).

Holes were introduced to such a CdTe dot [47, 48] using e.g. micro-PL excitation spectroscopy. The excited electron is bound to the hole left in the valence band forming a confined exciton where the self-confining potential is defined by the e-hole interaction. The system exhibits a series of emission peaks as shown in Fig. 1.8 where the B-field dependence of the emission results in anti-crossing of bright ($J_z = s_z + j_z = -2$) and dark ($J_z = -1$) states around $B = 6$ T is shown in Fig. 1.8(a). Optical transitions in circularly-right-polarized (σ^-) light polarization ($\Delta l = 1$)

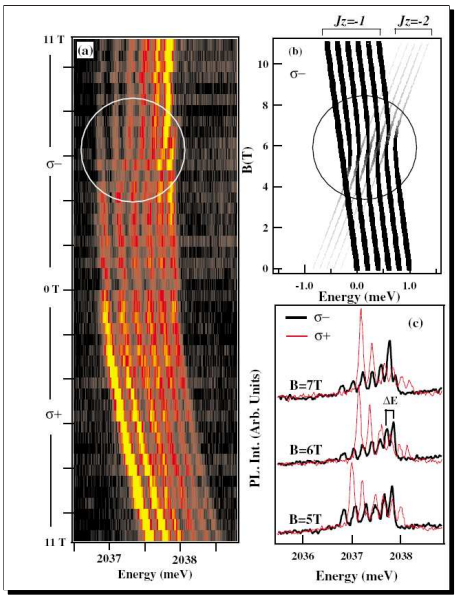

Figure 1.8: (a) The B-field dependence of the emission of a Mn-doped QD and (b) Optical transitions in σ^- polarization. (c) Detail of the circularly polarized emission spectrum around the anti-crossing for three different B-field. After Ref. [47].

[Fig. 1.8(b)] are obtained from the diagonalization of the spin Hamiltonian and Zeeman-splitting Hamiltonian (the diamagnetic component is excluded) in the subspace of the heavy-hole exciton and spin projections. The thickness of the lines is proportional to the oscillator strength of the transition. Details of the circularly-polarized emission spectra around the anti-crossing where a series of emission-lines is resolved at three different B-fields in σ^- polarization are shown in Fig. 1.8(c).

Experimental results of the spin states of the Mn-ion in such a dot were analyzed in Refs. [47, 48, 60, 61]. These states are determined by the FM (AFM) coupling of the single Mn^{2+} with the confined exciton as is illustrated in Fig. 1.9. In nonmagnetic QDs as shown in Fig. 1.9(a), narrow PL peaks (limited by the spectrometer resolution of 50 μeV) can be resolved, each one is attributed to the recombination of a single electron-hole pair in a single QD. Possible spin states of the Mn-ion (S_z) and the confined exciton $J_z = s_z + j_z$ present in Fig. 1.9(b) result in various total spin states of the dot which exhibit e.g. the six ($\overrightarrow{J} + \overrightarrow{S} = \overrightarrow{5/2}$) or seven ($\overrightarrow{J} + \overrightarrow{S} = \overrightarrow{3}$) different

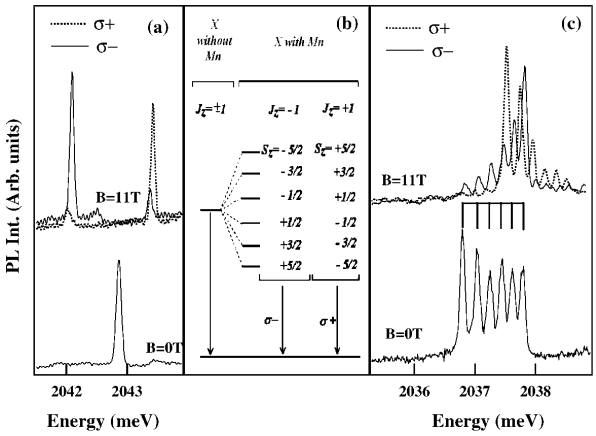

Figure 1.9: PL spectroscopy obtained at two different fields $B = 0$ and $B = 11$ T at $T = 5$ K for an individual isotropic CdTe/ZnTe QD (a) and a Mn-doped QD (c). (b) Schematic diagram of the bright state energy levels of the Mn-exciton coupling system at $B = 0$. The exciton-Mn-ion exchange interaction shifts the exciton energy depending on the Mn-ion z-spin which is labeled by S_z. After Ref. [47].

PL-peaks for, respectively, $B = 0$ and 11 T as seen in Fig. 1.8(a) and (c). Practically, most of the individual emission peaks of magnetic single QDs are characterized by a rather large line width of about $\Delta E \sim 0.5$ meV. This broadening is related to the influence of the Mn-ion position which is located within the spacial extent of the exciton wave function. The single-Mn-doped QD studied in Fig. 1.8 has the fine structure that can be resolved and the multi-peak PL-lines are clearly observed.

Theoretical model that describes the spin exchange between different particles in the above Cd(Mn)Te QD [47, 48, 49, 54, 94] reads:

$$H_{exc} = -J_{e-Mn}(\overrightarrow{s_e} \cdot \overrightarrow{S})\delta(\overrightarrow{r_e} - \overrightarrow{R}_{Mn}) - J_{h-Mn}(\overrightarrow{j_h} \cdot \overrightarrow{M})\delta(\overrightarrow{r_h} - \overrightarrow{R}_{Mn}) + H_{exc}^{e-h} \tag{1.14}$$

where spins and coordinates of the valence-band electron, conduction-band hole, and the Mn-ion is, respectively, $\overrightarrow{s}$, $\overrightarrow{j}$, and $\overrightarrow{S}$, and $\overrightarrow{r_e}$, $\overrightarrow{r_h}$, and $\overrightarrow{R}_{Mn}$ with their spin size, respectively, 1/2, 3/2, and 5/2. Each state in the exciton+Mn^{2+} is described by

$$|\Psi\rangle_{(Mn)}^{exciton} = |M_z\rangle \cdot |j_z\rangle \cdot |s_z\rangle \tag{1.15}$$

with $M_z = \pm 5/2$, $j_z = \pm 3/2$ and $s_z = \pm 1/2$. The spin-part Hamiltonian

related to the exciton is built up based on this basis and its eigenvalues can be obtained by diagonalization (technique in detail is presented in chapter 3). The strength of the exchange interaction between the electron (hole) and the Mn-ion is evaluated via $J_{e(h)-Mn}$:

$$J_{e(h)-Mn}\big(\overrightarrow{R}_{Mn}\big) = \int_0^{+\infty} d\overrightarrow{r}_{e(h)} K\big(\overrightarrow{r}_{e(h)}, \overrightarrow{R}_{Mn}\big), \tag{1.16}$$

which is about $J_{e-Mn} \propto 15$ meV nm^{-3} [54] and $J_{h-Mn} \propto -57$ meV nm^{-3} [70] in II(Mn)VI samples with fraction of $x \simeq$ few %. J_{e-Mn} and J_{h-Mn} can be measured directly through the examination of the giant Zeeman spin splittings using Raman scattering [70]. The kernel $K(\overrightarrow{r}_{e(h)}, \overrightarrow{R})$ in Eq. (1.16) is defined through the δ-function exchange interaction and the wave functions of the host electrons (holes)

$$K\big(\overrightarrow{r}_{e(h)}, \overrightarrow{R}_{Mn}\big) = \varphi^*\big(\overrightarrow{r}_{e(h)}\big)\delta\big(\overrightarrow{r}_{e(h)} - \overrightarrow{R}_{Mn}\big)\phi\big(\overrightarrow{r}_{e(h)}\big). \tag{1.17}$$

H_{exc}^{e-h} is the confining $e-h$ potential which defines the bound exciton state.

The intensities of the lines e.g. the series observed in Fig. 1.8 reflect the probability for the Mn^{2+} to be in one of its six-spin-state components and an efficient Mn-ion spin readout can be obtained [62, 71].

1.4.5 In(Mn)As quantum dots doped with a single Mn-ion

Mn^{2+} donates both charge (acceptor) and a spin in III-V based QDs. Even though the physics of the growth of III-V host semiconductors has been well developed in the past the systems of III-V semiconductor QDs containing a single Mn^{2+} have been realized recently by the MBE method on InAs self-assembled QDs deposited on a GaAs semi-insulating substrate [21]. Here the Mn-ion presents a two-level system separated from the excited states. In such a system, because the Mn-ion can create an electric field for the carriers, their appearance can influence the motion of the host electrons leading to the existence of bound acceptor states and change the physics of the excitonic complex [21].

1.4.6 Future accomplishment

Future progress on such QDs will focus on detecting a larger lifetime [62, 63] of the spins of an isolated magnetic moment (milliseconds) to fully control the optical properties of the system in the dynamics and its optical spin orientation in case $B = 0$. In Refs. [62, 63] a non-equilibrium situation was

prepared using fully-resonant optical excitation, which strongly depends on the magnetic anisotropy induced by the built-in strain of the dot. Thereby, the distribution of the Mn-ion is conserved and the spin lifetime was measured in order of microseconds [62].

1.4.7 Review of the work on magnetic quantum dots

Motivated by the very recent success in the realization of very diluted magnetic II(Mn)VI e.g. Cd(Mn)Te [47, 48, 60, 61, 62, 65, 71] and Cd(Mn)Se [44, 45] based QDs as discussed earlier in this chapter, the work presented in this thesis aims to contribute to a theoretical understanding of magnetic properties in strongly-correlated few-electron II-VI based QDs containing few localized magnetic impurities.

Few-electron QD system doped with a single (few) Mn-ions is attractive for quantum information applications because it has the advantage of i) being small (few tens of nm), ii) having a small number of N_e (N_h) which is controllable, and iii) exhibiting anisotropic exchange energy ($\sim$ few meV). Theoretical work involved in Refs. [28, 50, 54, 55, 56, 57, 64, 66] and Refs. from [72] to [99] explore the magnetic properties of such systems. Mn^{2+} with spin 5/2 has a giant Zeeman splitting energy due to the spin exchange with the host electrons resulting in the appearance of many prominent phenomena. This type of exchange interaction competes with the Mn-Mn direct exchange interaction, the electron-electron interaction, and the kinetic energy leading to the formation of e.g. (bound) magnetic polarons [37, 39, 55, 56, 67, 98], anisotropic magnetization [44, 45, 55, 76, 98], RKKY effect [28, 76], different magnetic phases (ferromagnetic/antiferromagnetic) [47, 60, 62, 85], and substantial changes in magneto-optical resonances [35, 85, 86, 89] in the presence of a magnetic field.

The Mn-ion with spin size 5/2 in this type of DMSs has a g-factor $g_{Mn} \sim 2$ leading to dominant behaviors of the Zeeman splitting energies in a specific range of magnetic field [34, 75, 83, 85]. The dynamics [62, 63, 71, 73] of the Mn^{2+} ensemble has been studied which indicates that the presence of magnetic field significantly increases the spin relaxation time by ~ 3 orders of magnitude as compared to the case $B = 0$ [73]. Once the spin dynamics is considered, the Mn^{2+} acts as an effective magnetic field on the exciton [71]. During the lifetime of the exciton ($\sim$ 10 ps [74]) the Mn-ion spin was flipped due to the exciton-Mn-ion spin interaction. This increases the probability of single-phonon induced spin-flips. Knowing this timescale is very important for experiments to control the dynamical behavior of the spin states of an isolated Mn-ion.

1.5 Structure of the thesis

In this thesis, I investigate the electronic and magnetic properties of a few-electron QD system doped with up to two magnetic ions subjected to an external perpendicular magnetic field. The (Coulomb) interacting electrons are strongly confined in a quasi-2D parabolic potential. By adopting the configuration interaction (CI) method and employing the exact diagonalization (ED) approach I obtain the "exact" solutions numerically.

The thesis is organized as follows. The two following chapters (**2** and **3**) present the theory and the methodology applied to a few-electron QD system, respectively, without and with a single-doped Mn-ion. I discuss in detail the CI method used to solve the many-body Schrödinger equation. This leads to a huge set of coupled algebraic equations. The Hamiltonian is turned into a matrix whose eigenvalues are obtained numerically by the ED technique. Electronic and magnetic properties of magnetically-single-doped (Mn^{2+}) QDs are obtained in **chapter 4**. Shell-filling characteristic, magnetic phase-diagram, magnetic phase transition, magnetic anisotropy, electron-electron correlations, MDD breaking, and composite fermions are the major subjects which will be elucidated in **chapter 5**. All of the above physics are found to depend significantly on the position of the Mn-ion inside the dot and the effective electron-electron interaction strength.

Magneto-optical properties of II(Mn)VI systems with a single Mn-ion are studied in **chapter 6**. My work on this subject aims to study different excitations which occur due to the spin exchange interaction and explore how the FIR absorption spectrum will change due to the presence of spin-spin electron-Mn-ion exchange interaction. More specifically, the important question "Would the magneto-optical absorption energy spectrum be independent of the electron-electron interaction and hence independent of N_e?" will be investigated, i.e. "is Kohn's theorem still valid?"

In the system with a single electron and a collection of Mn-ion spins, a stable magnetic polaron state was obtained earlier. In **chapter 7**, I examine such behavior for the system which consists of only two Mn-ions where their nearest AFM exchange interaction at $B = 0$ gives rise to very rich physics such as the appearance of FM and AFM polarons governed by magnetic field. I investigate the effect of symmetric and anti-symmetric position of the Mn-ions on the magnetic polaron states. The full local magnetic phase diagram for the Mn-ion subsystem is computed exhibiting frustrated magnetic regions. I investigate the interplay between different spin-related terms in the total energy that accounts for the occurrence of frustration. This effect depends strongly on the number of electrons present N_e. In the

highly polarized situation, I obtain molecule states which are similar to the molecule states obtained earlier in noncircular QDs due to the anisotropy of the confining potential in the absence of the Mn-ions, i.e. the breakdown of the maximum density droplet (MDD) state. Magnetic anisotropy is illustrated in detail.

The last chapter is devoted to concluding remarks and future research agenda.

2

Non-magnetic quantum dots

In this chapter, I briefly review non-magnetic quantum dots containing few electrons in the presence of a magnetic field. Different fabrication techniques including gate-control, MBE, organic chemical synthesis and theoretical approaches for few-electron dots are reviewed in short. Details of the configuration interaction method is introduced which is the method I used to investigate quantum dots with magnetic impurities.

2.1 Quantum dots as manufactured atoms

Quantum dots (QDs) [100, 101, 102], often called "artificial atoms" [103, 104], are zero-dimensional objects where all the three spatial dimensions are quantized with sizes smaller than some specific characteristic lengths, e.g. the exciton Bohr radius. Note that QD is also referred to "artificial atom" because the strong confinement in all spatial dimensions makes the single-particle energy spectrum of a QD discrete and similar to the atom energy levels. However, it is not a real atom because its size can vary from a few to hundreds of nanometers and can trap from a very small number of electrons ($N_e < 10$) to $50-100$ electrons or more. Their shape, size, energy structure, etc, can be precisely manufactured at wish. Therefore QDs are unique for quantum studies in atom-like set-ups.

2.2 Quantum-dot fabrication

QDs can be fabricated in different ways, and can be classified in different types such as metal or super-conducting dots; self-assembled dots, lateral or vertical dots, colloidal dots, etc. Techniques to fabricate those dots can be very different such as etching, regrowth from quantum well structures, epitaxy, lithography, holograph patterning, chemical synthesis, etc. A com-

plete review on fabrication of QDs can be found in Refs. [100, 105, 106, 107]. Utilizing molecular beam epitaxy makes it possible to grow 2D gated QDs and self-assembled dots which have been widely studied in the literature. In addition, I discuss 3D-colloidal dots.

2.2.1 Gated quantum dots

I describe how GaAs QDs are grown, in two different geometries: vertical (see Fig. 2.1) and lateral (see Fig. 2.3), in the GaAs/AlGaAs semiconductor heterostructures using gated-control fabrication. Methods to grow such dots were investigated and are by now well-advanced in the literature (see Refs. [103, 104, 108, 109] and references therein).

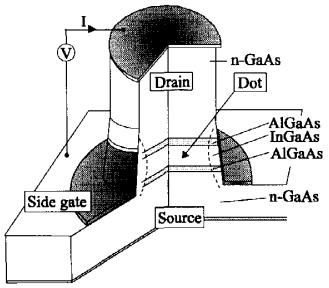

Figure 2.1: Vertical gated-QD grown from GaAs/AlGaAs heterostructure. After Ref. [108]

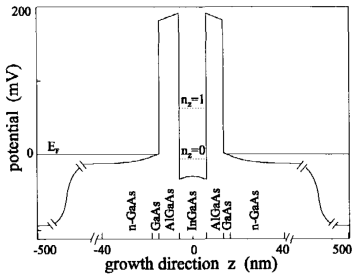

Figure 2.2: Self-consistent energy diagram of the unpatterned double-barier heterostructures as shown in Fig. 2.1. After Ref. [111]

An example of the configuration for such a vertical dot is schematically outlined in Fig. 2.1 [108, 111] consisting of, from bottom to top, an n-doped GaAs substrate, 7.5 nm un-doped $Al_{0.22}Ga_{0.78}As$ layers, 12 nm $In_{0.05}Ga_{0.95}As$, 9.0 nm $Al_{0.22}Ga_{0.78}As$, and a $\sim$500 nm n-doped GaAs top-layer. The pillar (with diameter 50 μm) is fabricated using electron-beam lithography and etching techniques from a double-barrier heterostrucutres which confines the electron along the xy-plane by the applied gate-voltage V_g. Source and drain electrical wires are connected to the top and substrate contacts. A third wire is attached to the metal that is "wrapped" around the pillar indicated as the side gate electrode in Fig. 2.1. The doping of Al (up to 22%) or In 5% to GaAs to create AlGaAs or InGaAs, respectively,

results in different energy band gaps where the bottom level of the conduction band of the disk-like-shape InGaAs is $\sim$ 32meV lower than the Fermi energy level of the AlGaAs contacts (see Fig. 2.2). This change in band-gap energy is not influenced by the applied gate-voltage. When these AlGaAs or InGaAs layers are contacted, a current of electrons can flow from AlGaAs to InGaAs. Note that the AlGaAs layer is made sufficiently thin to permit the electrons to tunnel vertically from the source to the drain through the InGaAs sample.

The number of electrons N_e, which move along the xy-plane with confining potential V_c defined by the 50-μm-pillar, is tuned by adjusting the gate-voltage V_g. By making the gate voltage V_g more negative one can electrically squeeze the effective diameter of the InGaAs disk from a few hundreds of nm down to zero. Equivalently, the number of electrons N_e decreases one-by-one.

A QD with lateral geometry [103, 104, 112] (Fig. 2.3) is obtained by patterning a 2DEG that is created from a AlGaAs/GaAs heterostructure. When an AlGaAs crystal is grown on top of a GaAs crystal a 2DEG is found at the interface between the two crystals, $\approx$ 100nm below the surface of the heterostructure (as the small dark pool in Fig. 2.3). The metallic gates patterned at the surface will control the motion of the electrons along the z-direction and the other directions under suitable applied electric field. The lateral QD is coupled to the reservoirs via tunneling barriers by which the number of electrons N_e can be altered (see Fig. 2.3). When voltage probes are attached to the reservoirs the electronic properties of the system can be measured. An advantage of this dot configuration is that the tunneling rate of the electrons through the barriers can be tuned by changing the gate-voltage.

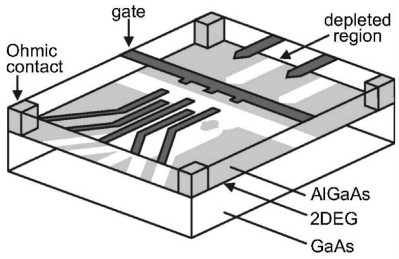

Figure 2.3: Lateral gated-QD as indicated by the small dark region from a 2DEG. After Ref. [111]

2.2.2 Self-assembled quantum dots

Self-assembled QDs [113], also referred to as self-organized QDs with size down to a few (typically 50 nm) can confine both electrons and holes. They

are formed spontaneously under certain growth conditions during molecular beam epitaxy (MBE) or metal organic chemical vapor deposition (MOCVP). The QD formation is a consequence of significant lattice mismatch $\Delta a/a$ between the deposited material (often semiconductors) and the underlying substrate using Stranski-Krastanov (SK) mode in layer-by-layer strained epitaxy. The SK mode is widely used to fabricate self-assembled QDs where the dots are created as islands. For a complete overview of the growth of self-assembled QDs, see Refs. [113, 114, 115]. In what follows I briefly describe the formation of InAs/GaAs dots using the SK mode which are well advanced [113, 115, 116].

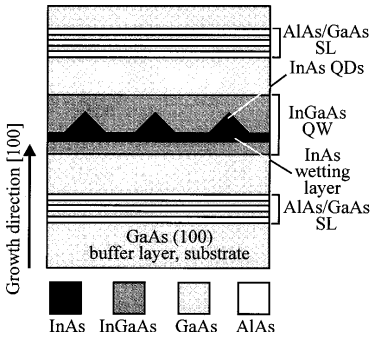

Figure 2.4: Schematic plot of InAs/GaAs QDs that are grown by SK mode where the layer sequence of the structure are shown. After Ref. [116]

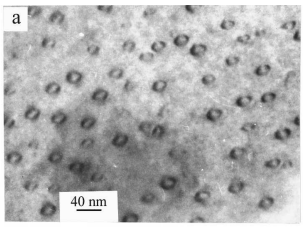

Figure 2.5: Bright-field TEM image along [100] zone for an InAs QD array in a 10 nm $In_{0.12}Ga_{0.88}As$ QW. After Ref. [116]

In SK epitaxy growth [113, 115, 116, 117], the formed heterostructures are initiated from a 2D layer (thin film) where the lattice constant of the deposited material is considerably larger, $\Delta a/a \gtrsim 6\%$, than that of the substrate which results in a large strain. By adding layers, the elastic strain energy of the structure gradually increases. The wetting layer becomes thicker reaching a critical value, often about a few mono-layers (MLs) e.g. 1.5 ML for InAs/GaAs QDs [118] after which island formation starts to occur instead of homogenous growth. Thus, in order to lower the total energy randomly distributed islands, of regular shape and similar sizes, are created on top of the wetting layer. These islands are then embedded in a larger band gap material. QDs grown under this condition are called self-assembled [113, 114, 119].

A schematic view of a typical QD structure that is grown according to the SK mode for InAs QDs on GaAs substrate with significant lattice mismatch $\Delta a/a \sim 6.7\%$ is schematically depicted in Fig. 2.4. The GaAs substrate layer is 0.12 μm thick. An AlAs/GaAs superlattice is added on the substrate which acts as a barrier to separate the dots with the back contact. The structure was grown under As-stabilized conditions at the substrate temperature $T_s = 485°C$. Another AlAs/GaAs superlattice is added between the dots and the sample surface which plays the role as a second barrier to prevent the electrons of the dots from tunneling to the surface. In addition, the number of electrons can be controlled by adding a suitable gate voltage V_g between the gate electrode and the back contact GaAs (see e.g. Refs. [18, 120]).

QDs formation can be monitored *in situ* by reflection high energy electron diffraction (RHEED). The QD shape is often measured by TEM (plan-view of InAs dots as seen in Fig. 2.5) and scanning tunneling microscopy (STM). For the above InAs dots, the surface density of the islands is about $(3 \div 4) \times 10^{10}$ cm^{-2}. The dots are about 20 nm large and $5 \div 6$ nm high. The density of dots can be increased independently with only small changes in the dot size.

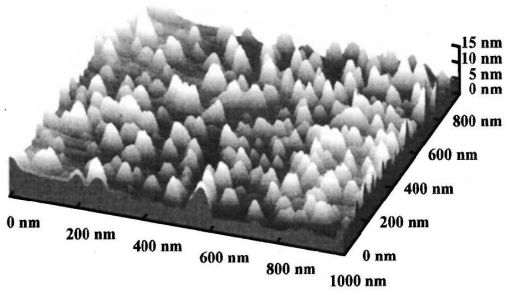

Figure 2.6: Ultrahigh vacuum atomic force microscopy image of 4.5 ML CdTe grown on ZnTe by SK mode. After Ref. [68]

Similar self-assembled CdTe/ZnTe dots (ultrahigh vacuum atomic force microscopy image as shown in Fig. 2.6) were grown by this method [65, 68]. CdTe/ZnTe has mismatch $\Delta a/a = 5.8\%$.

2.2.3 3D-colloidal quantum dots

Colloidal QDs are synthesized by techniques from organic chemistry using precursor compounds dissolved in solution which rely on fast nucleation followed by a slow heating growth. A particular crystal size can be obtained by stopping the growth after a certain time. Dots grown by this method are typically CdSe (see e.g. [44]), CdTe (see e.g. [121, 122]), CdS, InAs, and InP which can contain 100 to 100,000 atoms in the dot volume of diameter

about $10 \div 50$ atoms (homogeneity of about 5%) corresponding to $2 \div 10$ nm. The II-VI CdSe DMS nanocrystal dots [44] mentioned in chapter 1 which offer a tool to probe carrier-mediated ferromagnetism by PL spectroscopy are grown by colloidal-dot synthesis.

2.3 Theoretical approaches

Boundaries formed while QDs are grown play the role in determining the form of the confining potential and may also determine the selection rules for different optical excitations. Many man-made gated QDs are realized where the electron confinement can be modeled by a parabolic potential [108, 110, 123, 124]. Most of the QDs are the disk-like-shaped, they posses circular symmetry and the confinement perpendicular to the disk is much larger than in the plane resulting in a quasi-2D system. Such systems are expected to exhbit many similar physics as real atoms [18, 108, 110]. Such a QD system can be described theoretically by the Hamiltonian:

$$\hat{H} = \sum_{i=1}^{N_e} \Big[\frac{(-i\hbar\overrightarrow{\nabla_i} + e\overrightarrow{A_i})^2}{2m_e^*} + V_{ic} \Big] + \frac{1}{2} \sum_{i \neq j}^{N_e} \frac{e^2}{4\pi\epsilon\epsilon_0 |\overrightarrow{r_{ij}}|}. \tag{2.1}$$

The first term in Eq. (2.1) is the sum of the single-particle Hamiltonian for the i^{th} electron (effective mass m_e^*) that includes the kinetic and confining energy. The last sum is the Coulomb potential. We note that the electrostatic image force, which arises due to the difference in dielectric constants between different materials, can be neglected in our studied CdTe($\epsilon = 10.6$)/ZnTe($\epsilon = 9.7$) QDs because $\Delta\epsilon/\epsilon << 1$.

The problem of few-electron QD, except for some very specific problems e.g. in 1D, 2D [125, 126, 127], in most of the cases cannot be solved exactly due to the presence of the Coulomb pair interaction. To treat this many-body effect, a few theoretical approximations were proposed and many numerically computational approaches have been developed [106, 109, 128].

Theoretical models which are adapted widely in QD science include DFT, many-body path-integral, Hartree-Fock approximation both restricted and unrestricted (or sometimes called open-shell) HF treatments [129, 130, 131, 132, 133, 134] which have been used to study e.g. Wigner molecule, maximum density droplet (MDD), etc. Unrestricted HF is also used for some problems where the basis is not orthonormal and which is referred to Hartree-Fock-Roothaan (HFR) equations [135, 136, 137].

A direct approach that most precisely describes such few-electron QDs is the Configuration Interaction (CI) method. This method is limited to

small systems ($N_e \leq 10$) and is successful in explaining shell-structure (also Hund's rule) and the formulation of magic quantum numbers. There are two major properties that make QDs analogous to natural atoms and where electron-electron correlation plays an essential role. Because it is possible to obtain a relatively large range of excited energy levels, optical and FIR spectroscopy can be well interpreted.

Besides the HF mean-field-approximation, the (Spin) Density Functional Theory (SDFT) has been used which offers e.g. studies on the limit of Hund's first rule for circular and noncircular dots (it turned out to be valid up to about $N_e = 22$ electrons) [106, 138, 139, 140, 141, 142]. The advantage of DFT is that it can handle systems with relatively large N_e where e-e correlation is examined on the mean field description level. The many-body path-integral (see e.g. Refs. [143, 144, 145]) approach is a numerical technique that allows to investigate many-electron states in confined systems. A variational principle for a finite number of identical particles was formulated in Refs. [143, 144] and has been used for the calculation of the many-body partition function accounting for the permutations of identical particles, etc. Monte-Carlo, Quantum Monte Carlo [106] are alternative approaches which are in principle exact and can deal with relatively larger systems but are limited to ground-state (GS) properties.

There is a huge number of scholars who have contributed their work to define the science of QDs. A detailed review to major achievements can be found in e.g. Refs. [100, 101, 106, 109, 128, 142] (and references therein). In the context of the thesis, I introduce the CI method as applied to few-electron nonmagnetic (in this chapter) and magnetic (in chapter 3) parabolic QDs.

2.3.1 Single-particle spectrum

Fock-Darwin wave functions

For the simplest case of a 2D electron confined in a parabolic potential $V_{ic} = \frac{1}{2} m_e^* \omega_0^2 \overrightarrow{r_i}^2$, a fully analytical solution was obtained independently by Fock [146] and Darwin [147]. Detailed solution of how to obtain the Fock-Darwin (FD) states can be found explicitly in e.g. Ref. [101]. The FD state (n_r, l) has energy

$$E(n_r, l) = \hbar\omega_0(2n_r + |l| + 1) \tag{2.2}$$

and wave function

$$\varphi_{n_r,l}(r,\theta) = \frac{1}{l_0}\sqrt{\frac{n_r!}{\pi(n_r+|l|)!}}\left(\frac{r}{l_0}\right)^{|l|} e^{-r^2/2l_0^2} e^{-il\theta} L_{n_r}^{|l|}\left(\frac{r^2}{2l_0^2}\right) \tag{2.3}$$

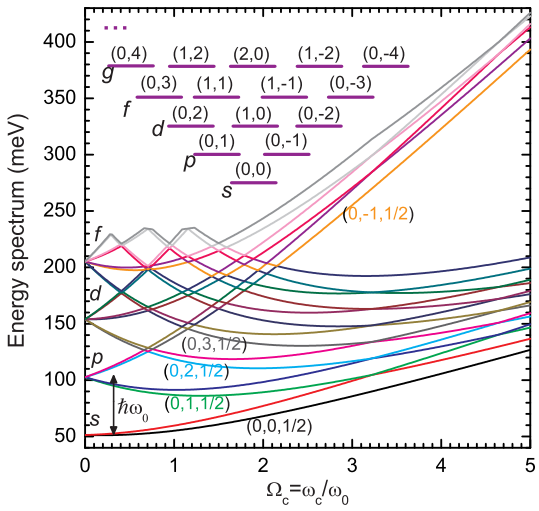

Figure 2.7: Theoretical Fock-Darwin levels labeled by (n_r, l, s_z) extended to the case with Zeeman spin splitting included for $\hbar\omega_0 = 51.32$ meV (solid-line curves) as a function of magnetic field. Inset is schematic plot of the $B = 0$ single-particle energy levels (up to the g-shell) labeled by (n_r, l).

where each couple of two quantum numbers (n_r, l) with $(n_r = 0, 1, 2, 3, ...)$ and $(l = 0, \pm1, \pm2, \pm3, ...)$ are, respectively, the radial and azimuthal quantum numbers. $L_{n_r}^{|l|}$ is the Laguerre polynomial [148]. $\hbar\omega_0$ is the confinement energy. The quantum states (orbitals) that fulfill $2n_r + |l| = const$ define a 2D shell. Those states that belong to the same shell share the same mathematic parity (odd or even) of the azimuthal quantum numbers. The lowest shell in energy has $(n_r, l) = (0, 0)$ corresponding to the s-orbital. Subsequently, we have the p-shell $(0, \pm1)$, d-shell $(0, \pm2)$ and $(1, 0)$, etc (see e.g. the inset of Fig. 2.7).

In the presence of a magnetic field, the wave function is squeezed to the center of the QD by an effective scaling

$$\lambda^2 = (1 + \Omega_c^2/4)^{-1/2} \tag{2.4}$$

where $\omega_c = eB/m_e^*$ is the cyclotron frequency and $\Omega_c = \omega_c/\omega_0$ is a dimensionless parameter. Technically, the effective length l_0 as for the $B = 0$ is replaced by a new effective length l_H

$$l_H^2 = \hbar/(m_e^*\omega_H) \tag{2.5}$$

which is determined via the hybrid frequency

$$\omega_H = \omega_0\sqrt{1+\Omega_c^2/4}. \qquad (2.6)$$

The single-electron energy spectrum as a function of magnetic field is:

$$E(n_r, l) = \hbar\omega_H(2n_r + |l| + 1), \quad (2.7)$$

as plotted in Fig. 2.7. There appear crossings in the energy levels which correspond to changes in the FD states as indicated for a very specific value of the B-field in Fig. 2.8. The FD states with positive l such as $(0,1)$, (0,2), etc, have smaller energy than the other states in the same shell when B is increased.

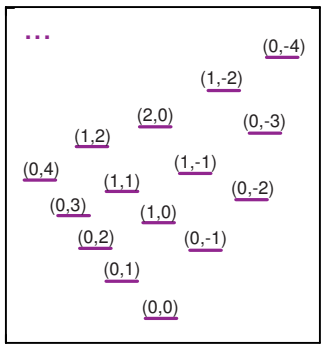

Figure 2.8: FD states at a magnetic field $\Omega_c \neq 0$.

It is worth noting that in case the confining potential term approaches zero, the FD levels are

$$E_{n_L} = \hbar\omega_c(n_L + 1/2), \qquad (2.8)$$

with $n_L = 0, 1, 2, 3, ...$, recognized as the Landau-levels with energy spacing $\hbar\omega_c$. In the high-field-limit, the single-particle energy levels are arranged such that the lowest energy levels have $n_r = 0$. These quantum states define a series of the so-called lowest Landau levels (LLL).

2.3.2 Many-body effects

The interplay between the different interactions in Hamiltonian (2.1) are examined in Fig. 2.9 as a function of magnetic field. The pair Coulomb interaction exhibits a series of downward cusps which are identical to the cusps found in the total energy except for one cusp (in the total energy) which is the intercept between the Coulomb energy and the single-particle energy. These cusps appear each time the dot system transits to a new many-body quantum state (L_z, S_z).

Electron-electron correlation was studied "exactly" for systems with different number of electrons: $N_e = 2$ in Refs. [125, 127] where the solution of two-electron QDs were solved analytically and for 3÷6 electrons in Refs. [149, 150, 151, 152, 153, 154] using the CI method.

An important property that makes few-electron QDs attractive subjects is shell-filling [108, 141, 155, 156, 157]. Due to the Pauli exclusion principle, electrons fill different quantum orbitals. For example, in a three-electron QD, the electrons can occupy various FD levels with different spin states such that the total angular momentum number L_z and z-spin S_z can have $(L_z, S_z) = (\pm 1, \pm 1/2)$ which is the case when the s-shell is fully-filled and the p-shell is partially-filled with the remaining spin-up (-down) electron, or $(3, 3/2)$ which is the case when all three electrons have spins up and partially filling the s-, $p-$, and the d-shell.

It is convenient to define a filling factor

$$\nu = N_e(N_e - 1)/2L, \tag{2.9}$$

which defines the so-called shell-strucutre in QDs (see e.g. Fig. 2.10). The formation of closed shells for $N_e = 2, 6, 12, ...$ electrons are found for a 2D QD system which are similar to the noble gases of natural atoms. Hund's rule is a heuristic rule to predict the filling of subsequent orbitals. Due to the competition of Coulomb repulsion and Pauli principle, the electrons populate different quantum orbitals such that its total spin is maximal which corresponds to the half-filling case. It works very well for almost all cases with few exceptions at the d-sub-level of the most outer shell and the subsequent s-level [140]. For parabolic QDs, Hund's first rule is valid for up to tens of electrons [106, 108, 109]. Both the shell-filling effect and Hund's first rule could be examined using addition energy measurements, i.e. it measures the energy difference when we add another electron to a N_e-electron QD system.

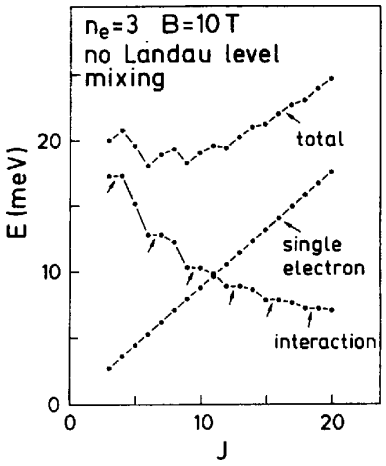

Figure 2.9: Angular momentum dependence of three different energies in a three-electron GaAs QD calculated for $B = 10$ T. After Ref. [149]

For example, in Fig. 2.10, Hund's rule is confirmed through an experimental study on vertical gated-QD with $N_e = 3 \div 6$ electrons where the number of electrons in the dot is loaded one by one. By calculating the position of the peaks in the electron current as a function of gate voltage V_g

[Fig. 2.10(a)], a dot with a different N_e is found where the larger the dot the more-negative-V_g shifted is the peak. Hund's rule is examined by studying the electro-chemical potential $\mu(N_e) = E_{N_e+1} - 2E_{N_e} + E_{N_e-1}$ as the energy difference when one electron is added to the dot [Fig. 2.10(b)]. Followed Hund's first rule when B-field is sufficiently small to keep the dot electrons away from strong spin-polarization (arrows in the boxes correspond to different orbitals in 2D-shells), the electrons occupy gradually from the s-level and fully fill the p-shell for $N_e = 6$. Both of these observations depend on the magnetic field.

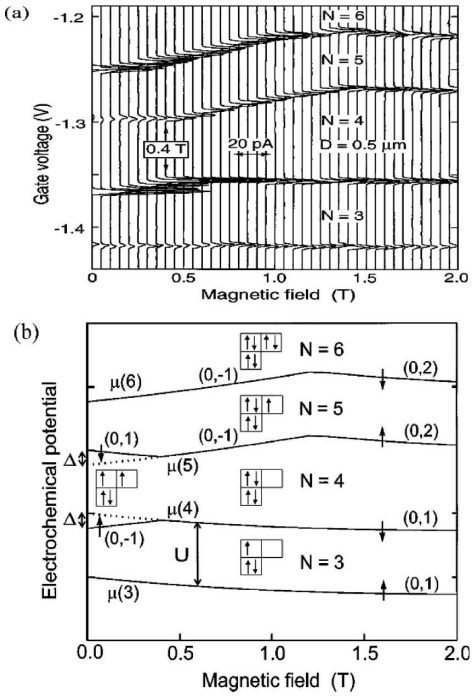

Figure 2.10: Hund's rule in QDs. (a) Current peaks for $N_e = 3, 4, 5$, and 6; (b) constant-interaction model, taking into account exchange effects. The energy splitting accounts for the energy gain by spin alignment, following Hund's rule for orbital degeneracy at $B = 0$. Insets are schematic representations of the filling of the different electron states. After Ref. [108].

The presence of a magnetic field breaks the $l \rightarrow -l$ symmetry and the $s_z \rightarrow -s_z$ symmetry and thus lifts the degeneracy of the single-particle energy levels. When B-field is further increased, electron spins tend to

stay parallel with respect to each other. Consequently, higher FD-levels are populated (see Fig. 2.7) leading to a total spin $S_z \sim N_e/2$ called strongly-polarized state.

In the strongly-polarized state, there exists a series of angular momentum quantum number L_z transitions in the GS when increasing the magnetic field. When we further increase the magnetic field a parabolic QD containing $\mathrm{N}_e \geq 3$ electrons can arrange themselves in the form of a polygon pattern with N_e and $M(< N_e)$ apexes. As an example see Fig. 2.11 where electron radial density is shown by calculating the spin-spin pair correlation between the electrons. Such pair correlation is obtained by pinning one electron at a certain position $\overrightarrow{r_0}$. The radial density of the remaining electrons is evaluated with respect to the fixed electron. In Fig. 2.11, the cases for $\mathrm{N}_e = 3 \div 5$ electrons exhibit N_e-apex polygons whose apexes refer to the maximum probability to find the electrons. The cases $\mathrm{N}_e = 6$ and 7 electrons form (N_e-1)-apex polygons where one electron is located in the canter of the polygon. These correspond to two types of magic number sets: for $N_e \leq 6$ [158, 159]

$$L_z = \frac{N_e(N_e-1)}{2} + iN_e, \quad (i = 0, 1, 2, 3, ...), \tag{2.10}$$

and $N_e > 6$ [159] electrons

- N_e-apex polygon pattern

$$L_z = \begin{cases} N_e(i+\frac{1}{2}) & \text{if } N_e = 0, 2, 4, ...; \\ iN_e & \text{if } N_e = 1, 3, 5, ... \end{cases} \tag{2.11}$$

- (N_e-1)-apex polygon

$$L_z = \begin{cases} (N_e-1)i & \text{if } N_e = 0, 2, 4, ...; \\ (N_e-1)(i+\frac{1}{2}) & \text{if } N_e = 1, 3, 5, ... \end{cases} \tag{2.12}$$

which fulfill the Pauli exclusion principle $L \geq N_e(N_e-1)/2$. Magic quantum numbers are the physics occurring when the system of strongly-polarized-electron QDs transit to different quantum states with larger L_z when increasing the applied magnetic field. This results in a series of corresponding filling-factors in Eq. (2.9). For example, for $\mathrm{N}_e = 3$ electrons, such quantum states are $L_z = 3, 6, 9, 12, ...$ ($\nu = 1, 1/2, 1/3, 1/4, ...$) and for $\mathrm{N}_e = 4$ electrons $L_z = 6, 10, 14, 18, ...$ ($\nu = 1, 3/5, 3/7, 3/9, ...$), etc. Magic quantum numbers in terms of filling-factor can be used to elucidate e.g. composite-fermion state (see e.g. Refs [152, 153, 154, 160]) in few-electron parabolic

dots. A composite fermion is a combo of an electron bound to an even number of flux quanta which are often called vortices. Vortices are the points where the many-body wave function is zero. Detailed discussion can be found in chapter 5. For a relatively larger system with $N_e \geq 20$ electrons, the magic number sets could be formulated using e.g. HF theory [162].

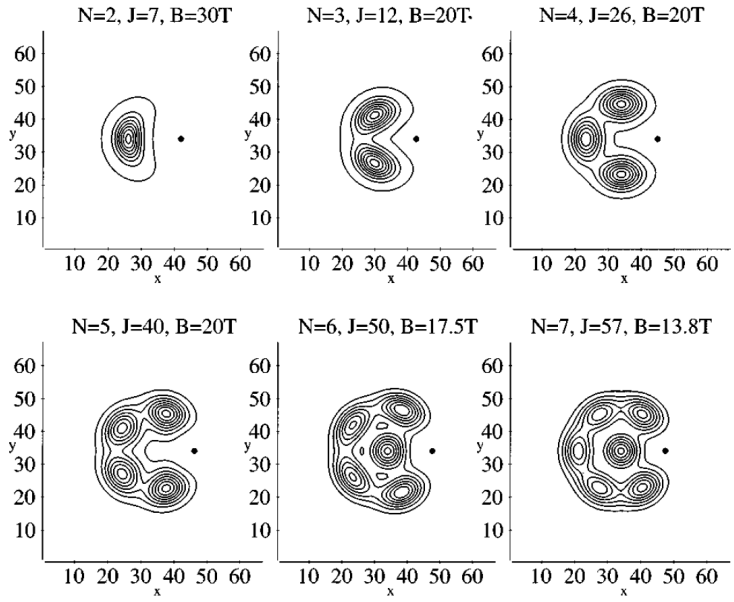

Figure 2.11: Contour plot of the spin pair-correlation function for magic GS for QDs containing $N_e = 2 \div 4$ (top) $5 \div 7$ (bottom) electrons. Black dots denote the fixed electron. The x and y unit is 1.89 nm. J in this plot labels total angular momentum L_z in the text. After Ref. [163].

Besides magic angular momentum series, increasing the field in few-electron QDs leads to the appearance of different phenomena. One of which is the Maximum Density Droplet (MDD) state that is found when the electrons are fully polarized and occupy adjacent Landau levels from $(n_r = 0, l = 0)$. Hence, the total angular momentum is

$$L_z = 0 + 1 + 2 + ... + N_e - 1 = N_e(N_e - 1)/2. \tag{2.13}$$

This is also the smallest value of the GS total angular momentum which results in unit filling factor

$$\nu = N_e(N_e - 1)/2L_z = 1. \tag{2.14}$$

The spin state of such a state for a three-electron dot can be schematically depicted in Fig. 2.12.

The system is described as a droplet whose radius decreases by increasing B-field. Electron density at the MDD state is maximal ($n_e \approx (\pi l_c^2)^{-1}$ with $l_c^2 = \hbar/m_e^*\omega_c$ the magnetic length) due to the compact arrangement of the electrons. This state was first studied by MacDonald *et al* in 1993 [164] and then fully discussed in e.g. Refs. [123, 140, 153, 154, 165] using e.g. CI, HF, or multi-centered HF wave function with the restricted Hatree-Fock mechanism.

Using SDFT, Reimann *et al* [140, 166] found a breaking of symmetry for $N_e = 20$ MDD-electrons in a GaAs QD $\hbar\omega_0 = 1.98$meV by the appearence of the Chamon-Wen edge like state [167]. Such state was investigated earlier [167] for the quantum Hall liquid with bulk filling factor $\nu = 1$ where a stripe or ring of electron density breaks off from the homogeneous bulk. In few-electron QDs where Coulomb repulsion becomes dominant a re-arrangement of the MDD electrons occurs in order to balance the compression of the electron-spins due to an increasing B and the inhibition by electron-electron correlation. This is illustrated in Fig. 2.13. The angular momentum occupation number P_l (which is P_m as shown in Fig. 2.13) is defined as the projection of the Kohn-Sam single-particle wave function Ψ_i [140] on the FD state

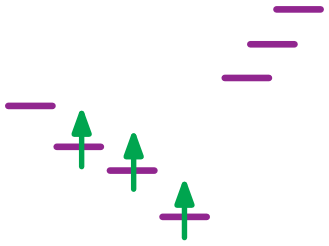

Figure 2.12: Electrons occupying the lowest Landau levels in a three-electron QD at a sufficiently large B-field.

$$P_l = \sum_{n_r} \sum_i |\langle n_r, l|\Psi_{i,\downarrow}\rangle|^2. \tag{2.15}$$

For the MDD state (top panel in Fig. 2.13), the angular momentum occupation number is one everywhere inside the droplet radius. Therefore, a filled ring shape is found for the radial electron density. The Chamon-Wen edge state is formed at $B \geq 3$T with $L_z \geq N_e(N_e-1)/2$. The orbitals with angular momentum smaller than $N_e - 1$ are no longer fully occupied (see the l-occupation in the right-column in Fig. 2.13). Instead, part of the electron number will occupy orbitals with $l \geq N_e - 1$. Consequently, the radial electron density exhibits a series of lumps at the ring (diameter $\sim 2l_c$) edge, which is similar to the sharp boundaries found in quantum Hall liquids [167], to maintain the MDD state.

For the system with a smaller N_e, say $N_e \leq 6$ [106, 152], the Chamon-Wen edge like state does not exist. Instead, there are peaks corresponding to the most probable position of the electrons as shown in Fig. 2.14. This is the starting of the Wigner molecule formation [168] which is found in the large-field limit. Recall that in semiconductor QDs with a rather low electron density (lower than the critical Wigner-Seitz density, namely $n_0 = 1/\pi r_s^2$ [106, 166]) there exists a state where the electrons at the GS are strongly localized with respect to each other, forming a classical lattice state which is referred as Wigner-like.

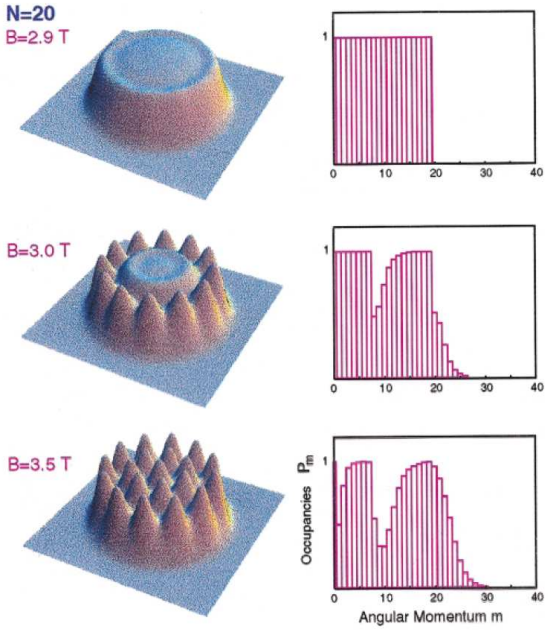

Figure 2.13: Self-consistent densities for a 20-electron GaAs QD shortly before edge reconstruction at $B = 2.9$ T (top), forming the broken-symmetry Chamon-Wen edge like state at 3 T (middle) and being fully reconstructed at 3.5 T (bottom). Right: Angular momentum occupancies P_m. In this plot, m labels the angular momentum number. After Ref. [140]

Such Wigner crystallization (liquid-crystal transition) is found when the Coulomb interaction (proportional to $D^{-1} \sim \sqrt{n_e}$ with D the relative size of the dot and $n_e \sim \mid \Psi(\overrightarrow{r}) \mid^2$ the electron density) becomes dominant over the kinetic energy (proportional to $D^{-2} \sim n_e$). This state is observed for strong

Coulomb interaction and weak confinement strength even in a relatively small QD [166]. The relative distance between the electrons becomes larger than the magnetic length l_c. It means that there appears transition from the MDD state to Wigner crystallization formation of electrons [152, 154, 165, 166]. For $N_e = 5$ electrons, the authors [154] obtained such a MDD-Wigner transition through the breaking of the MDD state as shown in Fig. 2.14. Different L_z states initiating from $L_z = 15$ are obtained by increasing the B-field. The Wigner molecule is formed at $L_z = 35$. Shortly before this crystallization, the system experiences several MDD-breaking states where the "droplet" becomes more separated and the maximum probability to find electrons is at some particular positions which stay rigidly with respect to each other.

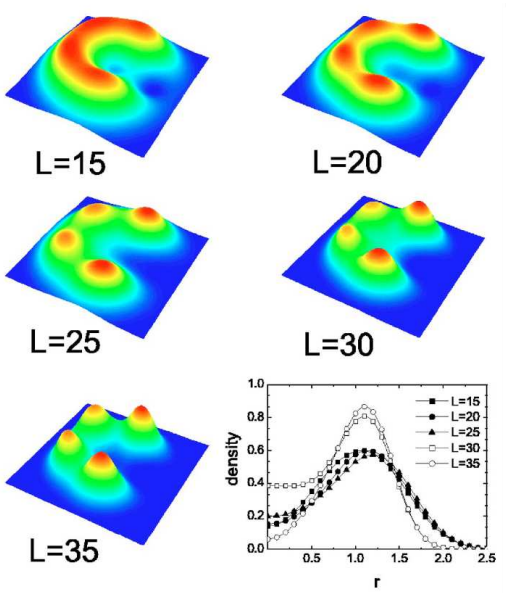

Figure 2.14: Pair-correlation functions for several ground states at λ_C=1 and Ω_c for which this state is the GS for $N_e = 5$ electrons. The angular momentum is indicated next to the plots. Notice how a Wigner crystal forms. The plot in the bottom right corner shows the electron density as a function of r, the distance from the center of the dot, for several GS. After Ref. [154]

As investigated in the above MDD-related references, the stability of the MDD phase eases when N_e increases or when $|\overrightarrow{B}|$ is sufficiently large leading to the breakdown state after the MDD formation. Fig. 2.15 summarizes the

different ground states as a function of magnetic field and the number of electrons for the above GaAs QD [140].

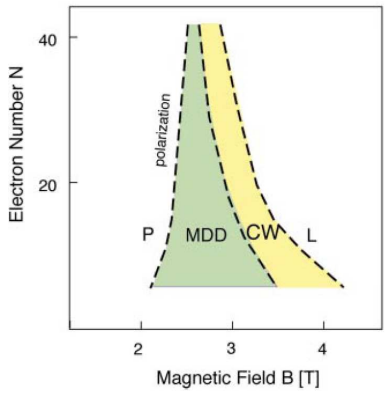

Figure 2.15: Phase diagram as a function of applied B-field and the number of electrons (N in this plot). P, MDD, CW, and L stands for, respectively, polarization, maximum density droplet, Chamon-wen edge like, and localization state. After Ref. [106]

2.4 Configuration Interaction

The CI method is in principle an "exact" method to study many-body effects in QDs containing few electrons. The wave function of the N_e-electron system is written as a linear combination of all possible quantum configuration states for the N_e non-interacting electrons:

$$\Psi(\overrightarrow{x_1^*}, \overrightarrow{x_2^*}, ..., \overrightarrow{x_{N_e}^*}) = \sum_k C_k \Psi_k(\overrightarrow{x_1^*}, \overrightarrow{x_2^*}, ..., \overrightarrow{x_{N_e}^*}) \tag{2.16}$$

where each quantum configuration state Ψ_i is the Slater determinant of N_e electrons with configuration $\{k\} = \{\alpha, \beta, ..., \xi\}$:

$$\begin{aligned} \Psi_k &= \frac{1}{\sqrt{N_e!}} \begin{vmatrix} \psi_\alpha(\overrightarrow{x_1^*}) & \psi_\alpha(\overrightarrow{x_2^*}) & ... & \psi_\alpha(\overrightarrow{x_{N_e}^*}) \\ \psi_\beta(\overrightarrow{x_1^*}) & \psi_\beta(\overrightarrow{x_2^*}) & ... & \psi_\beta(\overrightarrow{x_{N_e}^*}) \\ ... & & & \\ \psi_\xi(\overrightarrow{x_1^*}) & \psi_\xi(\overrightarrow{x_2^*}) & ... & \psi_\xi(\overrightarrow{x_{N_e}^*}) \end{vmatrix} \\ &= \frac{1}{\sqrt{N_e!}} \sum_{P_{\alpha^*}} sgn(P_{\alpha^*}) \prod_{i=1}^{N_e} \psi_{P_{\alpha^*(i_k)}} \end{aligned} \tag{2.17}$$

where P_{α^*} stands for a permutation α^* of the N_e numbers $(\alpha, \beta, ..., \xi)$ and $\overrightarrow{x_i^*}=(\overrightarrow{r_i}, \overrightarrow{s_i})$ stands for the coordinates and spin of a single electron. The single-particle states are characterized by the quantum numbers α, β, ..., ξ. Explicitly, for the case of quadratic confining QD with the basis chosen as the FD solutions [Eq. (2.3)], the single-particle wave function ϕ_α is the product of the FD function and the electron spin part:

$$\psi_\alpha(\overrightarrow{x_i^*}) = \varphi_\alpha(\overrightarrow{r_i})\chi_\alpha(\overrightarrow{s_i}). \tag{2.18}$$

The CI wave function takes into account the electron-electron exchange and correlation. For this reason, CI method is also considered as one of the theoretical approaches of the post-Hartree-Fock formalism in which the electron-electron correlation plays an essential role. It is also an useful method to examine electron excitations in QDs.

In quantum chemistry, the CI method is very popular because of its efficiency in describing bonds even in strongly-correlated regime. Even though CI is limited to a small number of electrons to date, say, $N_e \leq 10$, due to numerical time-consuming and data-storage difficulty, however, because the solutions are obtained by diagonalizing the Hamiltonian matrix (details how to obtain this matrix from the Hamiltonian will be shown in chapter 3) which is an exact process. Therefore, the CI is a powerful method and often used as a "standard" reference to measure the accuracy of different methods such as the (restricted/unrestriced) HF, Monte Carlo [168], etc in the limit of small N_e.

Due to the fact that in few-electron parabolic QD system, the z-projection of the total electron spin operators of S_z and their total angular momentum commute with the total Hamiltonian $[S_z, H] = 0$ and $[L, H] = 0$, eigenfunctions of the (S_z, L) operators will also be the eigenfunctions of the total Hamiltonian [152]. This brings the advantage of Hamiltonian matrix rank reduction and leads to a strong reduction in the size of the considered matrix that has to be diagonalized.

3

The model and methodologies

Theoretical and numerical methodologies are presented to solve the few-electron QD problem in the presence of a single Mn-ion in a magnetic field. The presence of the Mn-ion leads to an enhanced complexity. I describe how the CI theory is adopted to build up the Hamiltonian matrix and employ the exact diagonalization approach in order to obtain "exact" numerical results.

3.1 The Hamiltonian

A quasi-2D parabolic QD containing N_e electrons (effective mass m_e^*, radial coordinate $\overrightarrow{r_i}$, spin $\overrightarrow{s_i}$) doped with a single magnetic ion Mn^{2+} (located at position $\overrightarrow{R}_{Mn}$, spin $\overrightarrow{M}$) ($N_{Mn} = 1$) subjected to an external magnetic field $\overrightarrow{B}$ is described by the following Hamiltonian:

$$\hat{H} = \sum_{i=1}^{N_e} \left[\frac{\left(-i\hbar\overrightarrow{\nabla}_i + e\overrightarrow{A_i}\right)^2}{2m_e^*} + V_c\left(\overrightarrow{r_i}\right) \right] + \frac{1}{2}\hbar\omega_c m^* g_e S_z + \frac{1}{2}\sum_{i\neq j}^{N_e} V\left(\overrightarrow{r_i} - \overrightarrow{r_j}\right) + \frac{1}{2}\hbar\omega_c m^* g_{Mn} M_z - J_c \sum_{i=1}^{N_e} \overrightarrow{M}.\overrightarrow{s_i}\,\delta\left(\overrightarrow{r_i} - \overrightarrow{R}_{Mn}\right) \quad (3.1)$$

The first four terms describe the usual few-electron parabolic QD without a Mn-ion. The first sum corresponds to N_e-times the single-particle energy which includes the kinetic energy and the confining potential which we take of the form

$$V_{ic} = \frac{1}{2} m_e^* \omega_0^2 \overrightarrow{r_i}^2 \quad (3.2)$$

The results presented in this chapter were published as:

- N. T. T. Nguyen and F. M. Peeters, Phys. Rev. B **76**, 045315 (2007).

where ω_0 is the confinement frequency. ω_0 is related to the confinement length l_0 by: $l_0 = \sqrt{\hbar/m_e^*\omega_0}$. The vector potential $\overrightarrow{A}$ is taken in the symmetric gauge:

$$\overrightarrow{A} = B/2(-y, x, 0) \tag{3.3}$$

where the magnetic field $\overrightarrow{B}$ points perpendicular to the plane of the interface. The third term describes the Zeeman spin splitting of the electrons in a magnetic field and the fourth term is the Coulomb interaction between the electrons. g_e and g_{Mn} are the Landé g-factor of the host semiconductor and the magnetic ion, respectively. The last two terms correspond to, respectively, the Zeeman spin splitting of the Mn-ion and the electron-Mn-ion spin-spin exchange interaction which is given by a contact interaction. This spin exchange is similar to the term in Kondo and Anderson models, see e.g. Ref. [169]. Note that the number of electrons in the studied Cd(Mn)Te/Zn(Mn)Te QDs [47] can be tuned one-by-one from $N_e = 0$ by applying a gate voltage at the back contact of the QW heterostructure (see the band structure line up in Fig. 1.7) connecting to the top gate, which is analogous to the voltage-tunable InGaAs/GaAs dots studied in e.g. Refs. [18, 120].

I introduce a dimensionless parameter which is the Coulomb interaction strength λ_C that is defined as:

$$\lambda_C = \frac{e^2/(4\pi\epsilon_0\epsilon r)}{\hbar\omega_0} = \frac{l_0}{a_B^*} \tag{3.4}$$

with $a_B^* = 4\pi\epsilon_0\epsilon\hbar^2/m_e^*e^2$ the effective Bohr radius. The effective Coulomb interaction strength λ_C is a measurement of the electron-electron energy versus the confinement energy.

Next, I transform the Hamiltonian (3.1) into the second-quantization form by introducing the quantum field operator

$$\varphi^f(\overrightarrow{x^*}) = \sum_{i,\sigma} \varphi_i(\overrightarrow{r})\chi_\sigma(\overrightarrow{s})c_{i\sigma} \tag{3.5}$$

where $\overrightarrow{x^*} = (\overrightarrow{r}, \overrightarrow{s})$, $\varphi_i(\overrightarrow{r})$ is the single-particle function whose possible choice would be discussed afterwards and $c_{i\sigma}$ ($c_{i\sigma}^\dagger$) is the annihilation (cre-

ation) operator of the single-particle quantum state $\mid i,\sigma >$:

$$\begin{aligned}\hat{H} =& \sum_{i,\sigma} E_{i,\sigma} c^{+}_{i,\sigma} c_{i,\sigma} + \frac{1}{2} \sum_{ijkl\sigma\sigma'} \langle i,j|V_0|k,l\rangle c^{+}_{i,\sigma} c^{+}_{j,\sigma'} c_{k,\sigma'} c_{l,\sigma} \\ &+ \frac{1}{2}\hbar\omega_c \left(g_e m^* S_z + g_{Mn} m^* M_z\right) \\ &- \sum_{ij} \frac{1}{2} J_{ij}\left(\overrightarrow{R}_{Mn}\right) \Big[\left(c^{+}_{i\uparrow} c_{j\uparrow} - c^{+}_{i\downarrow} c_{j\downarrow}\right) M_z \\ &\qquad + c^{+}_{i\uparrow} c_{j\downarrow} M^{-} + c^{+}_{i\downarrow} c_{j\uparrow} M^{+} \Big]. \end{aligned} \tag{3.6}$$

$(J(\overrightarrow{R}_{Mn}))$ stands for the exchange interaction matrix whose element

$$J_{ij}(\overrightarrow{R}_{Mn}) = J_c \varphi^*_i(\overrightarrow{R}_{Mn}) \varphi_j(\overrightarrow{R}_{Mn}) \tag{3.7}$$

determines the overlap between two single-electron quantum states i and j, due to the electron-Mn-ion interaction, calculated at the position of the Mn-ion. Within the second-quantized form, the e-Mn-ion interaction [the last sum in Eq. (3.6)] consists of the "direct" and "indirect" interaction terms between the electrons and the Mn-ion. The direct term measures the differences in the number of spin-up (-down) electrons between states i and j and acts as the local Zeeman energy whereas the indirect term accounts for the exchange with a flip of the spins of the electrons and the Mn-ion. M_z, M^+, and M^- are the z-projection, raising, and lowering operators, respectively, of the Mn-ion spin.

The exchange interaction strength given by the pre-factor J_c which, as in Ref. [54], is taken to be 1.5 eVÅ^2 for a 2D CdTe based system, and is assumed to be independent of the lateral dimension of the QD. This type of spin interaction can be described as a scattering process where there is an exchange between the spin of the electron and the Mn-ion in such a way that $S_z + M_z = \text{const}$. It is worth noting that the Zeeman spin splitting term is not negligible in this system. I will demonstrate that, in fact, this Zeeman contribution becomes comparable with the exchange energy in the small-magnetic-field range. Another fact to note is that the Zeeman energy has the opposite sign for the electron and the Mn-ion because of their opposite sign of g-factors. This will be the reason for the existence of different magnetic phases with increasing magnetic field.

Based on the fact that most of the self-assembled QDs have the thickness much smaller than the in-plane circular diameter and that it is smaller than the characteristic length, i.e. the Bohr radius, the motion of the electrons

are strongly confined along the z-direction and the system can be described as a quasi-2D system.

Practically, there exist two possible spin coupling states for the electrons with the Mn-ion: ferromagnetic (FM) and antiferromagnetic (AFM), which, respectively, corresponds to parallel and antiparallel spin orientation of the electrons and the Mn-ion. These magnetic states are formed depending on the position of the Mn-ion, and the strength of the magnetic field. Therefore, the system exhibits two different phases the FM and AFM. Accordingly, the exchange energy $-J_c \sum_{i=1}^{N_e} \overrightarrow{M}.\overrightarrow{s_i}\delta\left(\overrightarrow{r_i} - \overrightarrow{R}_{Mn}\right)$ will have a minus (plus) sign when the electron and the Mn-ion spin are oriented parallel and anti-parallel.

The set of parameters mostly used in this thesis is applicable to Cd(Mn)Te [28, 47, 50] which is a II(Mn)VI QD with typical lateral size of about tens of nanometers and the thickness of $d = 2$ nm. This size parameter is taken from the experimental dots realized in Ref. [47] (see also Fig. 2.6). The dielectric constant $\epsilon = 10.6$, effective mass $m_e^*/m_0 = m^* = 0.106$, $a_B^* = 52.9$Å, $g_e = -1.67$, $g_{Mn} = 2.02$, $J_c = 1.5\times10^3$meVÅ^2, and l_0 about tens of nanometers ($\hbar\omega_0$ is typically few tens of meV). For example, $\hbar\omega_0 = 51.32$ meV gives $l_0 = 26.45$Å.

The following part of this chapter discusses the method to translate the Hamiltonian (3.6) into a Hamiltonian matrix whose eigenfunctions (eigenvalues) determine the major physical properties of the problem.

3.2 CI for the few-electron quantum dot doped with a single Mn-ion

The FD states, which are defined in Eq. (2.3) in chapter 2, are taken as our basis for the single-particle states. The exchange interaction matrix (J) can be evaluated thereafter. The e-Mn-ion interaction strength in case the electrons occupy in either s- or p- or d-shell [(n_r, l)=(0,0), $(0, \pm1)$, or $(0, \pm2)$ and (1,0), respectively] is shown in Fig. 3.1 as a function of the x- and y-coordinate of the Mn-ion position. When the Mn-ion is located at the center of the QD its exchange interaction with the s- or d- [for the (1,0)-state] electron is found to be maximal and zero with the p- and the d- [for the (0,±2)-state] electron. Note that these contour plots are in fact a map of the electron wave function because of the contact interaction. Displacing the Mn-ion to different positions inside the dot will change the strength of its coupling with the electrons.

The two quantum numbers: total angular momentum L_z and z-component of the total spin S_z of the electrons are not conserved due to the presence of

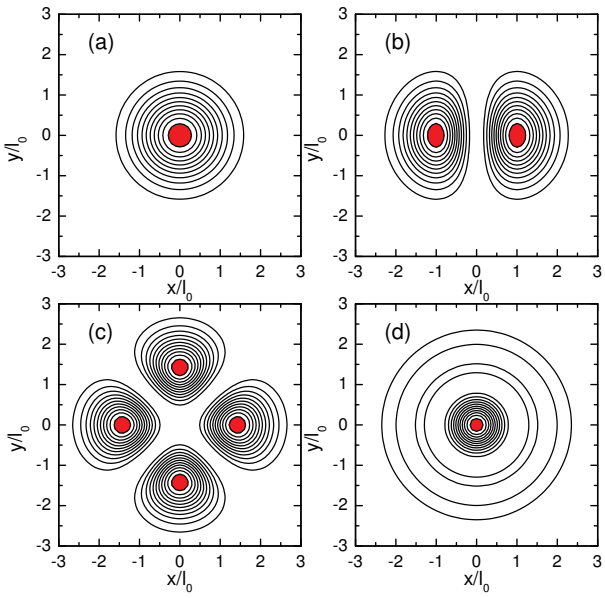

Figure 3.1: Contour plot of the diagonal elements of the exchange interaction matrix as a function of radial coordinate calculated for s- (a), p- (b), and d- [for the $(0, \pm 2)$-state] (c) and d- [for the $(1, 0)$-state] (d) shell at $B = 0$. Red region indicates the maximal values.

the Mn-ion whose spin $\overrightarrow{M}$ interacts with the spins of the electrons. Recall that without the magnetic impurity those numbers would be conserved and the eigenvalue of L_z and S_z are good quantum numbers reducing considerably the Hamiltonian matrix size. Ground-state properties of the latter problem can be described in the subspace (L_z, S_z). Therefore, adopted CI theory is applied to each choice of eigenvalue-subspace of (L_z, S_z) and there is no interference between two different subspaces. The full Hamiltonian matrix therefore consists of independent blocks such as

$$\left(\begin{array}{c|c|c|c} (L_z,S_z)_1 & 0 & 0 & \dots \\ \hline 0 & (L_z,S_z)_2 & 0 & \dots \\ \hline 0 & 0 & (L_z,S_z)_3 & \dots \\ \hline \dots & \dots & \dots & \dots \end{array}\right).$$

When the system contains a single Mn-ion which interacts with the electrons by the spin exchange interaction, which depends on both the radial

coordinates of the electrons and their spins, the operators (L_z, S_z) no longer commute with the total Hamiltonian resulting in non-zero matrix terms between different (L_z, S_z) subspaces. Therefore, we will need the entire Hilbert space to build up the Hamiltonian matrix.

According to the CI method introduced in chapter 2 for non-magnetic QDs, we construct the many-particle wave function as follows

$$\Psi\left(\overrightarrow{x_1^*}, \overrightarrow{x_2^*}, ..., \overrightarrow{x_{N_e}^*}, \overrightarrow{M}\right) = \sum_{k=1}^{N_c} C_k \Psi_k \left(\overrightarrow{x_1^*}, \overrightarrow{x_2^*}, ..., \overrightarrow{x_{N_e}^*}, \overrightarrow{M}\right) \tag{3.8}$$

which is a linear combination of N_c configuration state wave functions Ψ_k with

$$\begin{aligned} \Psi_k &= \frac{1}{\sqrt{N_e!}} \begin{vmatrix} \psi_{\alpha_{1k}}(\overrightarrow{x_1^*}) & \psi_{\alpha_{1k}}(\overrightarrow{x_2^*}) & ... & \psi_{\alpha_{1k}}(\overrightarrow{x_{N_e}^*}) \\ \psi_{\alpha_{2k}}(\overrightarrow{x_1^*}) & \psi_{\alpha_{2k}}(\overrightarrow{x_2^*}) & ... & \psi_{\alpha_{2k}}(\overrightarrow{x_{N_e}^*}) \\ ... & & & \\ \psi_{\alpha_{N_e k}}(\overrightarrow{x_1^*}) & \psi_{\alpha_{N_e k}}(\overrightarrow{x_2^*}) & ... & \psi_{\alpha_{N_e k}}(\overrightarrow{x_{N_e}^*}) \end{vmatrix} \chi_{\sigma_{M_z k}}(\overrightarrow{M}) \\ &= \frac{1}{\sqrt{N_e!}} \sum_{P_\alpha} sgn(P_\alpha) \prod_{i=1}^{N_e} \psi_{P_{\alpha(i_k)}} \chi_{\sigma M_{zk}}(\overrightarrow{M}) \end{aligned} \tag{3.9}$$

is the k-th state ($k = \{\alpha_{1k}, \alpha_{2k}, ..., \alpha_{N_e k}, \sigma_{Mzk}\}$) of the non-interacting many-electron wave function of N_e electrons and the spin state of the Mn-ion spin. The single-electron states are $\psi_{\alpha_{ik}} = \varphi_{ik}(\overrightarrow{r_i})\chi_{\sigma_{ik}}(\overrightarrow{s_i})$ where $\{\varphi_{ik}\}$ is taken to be the FD basis and $\chi_{\sigma_{ik}}$ is the electron spin state. The configuration state wave function (3.9) differs from the one without a Mn-ion (2.17) by the Mn-ion-spin state wave function.

The number of possible configurations N_c depends on the number of electrons, N_e, the number of single orbitals N_s that determines the size of the exchange interaction matrix (J), and the size of the spin, $\mathbf{M}$, of the magnetic impurity Mn^{2+}. The numerical results are obtained with N_c sufficiently large to guarantee convergence. That N_e electrons interact with the single magnetic impurity via the contact interaction implies that different single orbitals will couple with one another. As a consequence states with different total angular momentum and/or different total spin of electrons can scatter to other states. Therefore, all states generated from the three specific numbers: N_e, N_s and M (M= 5/2) need to be taken into account. The solution is exact when $N_c \to \infty$.

In the second-quantization representation, the state Ψ_k (3.9) can be translated into a ket vector $|k\rangle$ grouping a total of N_e electrons into $N_\uparrow$

electrons with z-component of spin up and $N_\uparrow = N_e - N_\uparrow$ electrons with z-component of spin down and the Mn-ion spin part:

$$\Psi_k \Longrightarrow |k\rangle = |c^+_{i_1\uparrow}, c^+_{i_2\uparrow}, ..., c^+_{i_{N\uparrow}}\rangle |c^+_{j_1\downarrow}, c^+_{j_2\downarrow}, ..., c^+_{j_{N\downarrow}}\rangle |M_z\rangle. \tag{3.10}$$

Here $i_{1\uparrow} \div i_{N\uparrow}$ and $j_{1\downarrow} \div j_{N\downarrow}$ are the indices of the single-electron states for which each index is a set of two quantum numbers (radial and azimuthal quantum numbers), as mentioned above. For the Mn-ion spin we have the quantum number $M_z = \mp 5/2, \mp 3/2, \mp 1/2$.

Now I will show how the Hamiltonian matrix can be derived from the Hamiltonian (3.6). By inserting the wave function (3.8) into the Schödinger equation

$$\hat{H}\Psi(\{\overrightarrow{x_i^*}\}) = E\Psi(\{\overrightarrow{x_i^*}\}) \tag{3.11}$$

and multiplying the left-hand-side with the hermitian adjoint Ψ_i^*, we come up with the following set of equations:

$$\sum_{k=1}^{N_c}(H_{ik} - E\delta_{ik})C_k = 0; \quad i = 1 \div N_c \tag{3.12}$$

where

$$H_{ik} \;=\; \int\int d\{\overrightarrow{x_i^*}\}d\{\overrightarrow{x_k^*}\}\Psi_i^*\hat{H}\Psi_k, \tag{3.13}$$

with $d\{\overrightarrow{x_i^*}\} = (d\overrightarrow{x_1^*}d\overrightarrow{x_2^*}...d\overrightarrow{x_{N_e}^*})_i$, is an element of the Hamiltonian matrix (H). Solving the set of equations (3.12) to find its roots E is equivalent to diagonalizing the matrix (H).

Because the configuration state wave function $\{\Psi_i\}$, see Eq. (3.9), is a sum of $N_e!$ (N_e+1)-factor products, Eq. (3.13) becomes

$$H_{ik} = \frac{1}{N_e!}\sum_{P_\alpha}\sum_{P_\beta} sgn(P_\alpha)sgn(P_\beta)B_{ik}^{\alpha\beta} \tag{3.14}$$

where

$$B_{ik}^{\alpha\beta} = \prod_{j=1}^{N_e}\prod_{l=1}^{N_e}\int\int d\{\overrightarrow{x_i^*}\}d\{\overrightarrow{x_k^*}\}\psi^*_{P_\alpha(j_i)}\chi^*_{\sigma_{M_{zi}}}(\overrightarrow{M})\hat{H}\psi_{P_\beta(l_k)}\chi_{\sigma_{M_{zk}}}(\overrightarrow{M}) \tag{3.15}$$

is the matrix element constructed from the single-electron FD states.

Note that $\hat{H}$ (3.6) can be expressed as a sum of different operators: the kinetic, the Coulomb interaction, Zeeman energy, and the exchange

interaction operators. The kinetic and Zeeman energy are diagonal which are obtained directly.

In what follows I will discuss how the algebraic expressions of the electron pair Coulomb interaction V_{ijkl} and spin exchange interaction matrix J_{ij} elements are obtained which are the basic ingredients needed in order to obtain the eigenvalues of the Hamiltonian matrix (H) numerically.

First, I show the results for the case of the Coulomb interaction. I calculate the pair interaction element for two electrons $(\overrightarrow{r_1}, \sigma_1)$ and $(\overrightarrow{r_2}, \sigma_2)$ with single-particle states, respectively, ψ_i and ψ_j corresponding to the FD state $i = (n_r, l)_i$ and $j = (n_r, l)_j$. Without loss of generality I denote the initial states $|ij\rangle$ as $|12\rangle$ with their quantum numbers $(n_{r_1}, l_1, \sigma_1, \sigma_{M_{z1}})$ and $(n_{r_2}, l_2, \sigma_2, \sigma_{M_{z2}})$. Idem remark for the final states $|kl\rangle$ as $|34\rangle$. Now the Coulomb matric element can be written as:

$$V_{12;34} = \delta_{\sigma_{M_{z1}},\sigma_{M_{z2}}} V_{n_{r_1},l_1,\sigma_1,n_{r_2},l_2,\sigma_2\,;\,n_{r_3},l_3,\sigma_3,n_{r_4},l_4,\sigma_4} = \delta_{\sigma_{M_{z1}},\sigma_{M_{z2}}}\, V_0 \langle 12|\frac{1}{r_{12}}|34\rangle \tag{3.16}$$

with $V_0 = e^2/(4\pi\epsilon_0\epsilon l_H)$ and the matrix element

$$\langle 12|\frac{1}{r_{12}}|34\rangle = \delta_{\sigma_1,\sigma_3}\delta_{\sigma_2,\sigma_4} \int d^2\overrightarrow{r_1} \int d^2\overrightarrow{r_2} \varphi^*_{(n_{r_1},l_1)}(\overrightarrow{r_1})\varphi^*_{(n_{r_2},l_2)}(\overrightarrow{r_2})\frac{1}{|\overrightarrow{r_{12}}|} \varphi_{(n_{r_3},l_3)}(\overrightarrow{r_1})\varphi_{(n_{r_4},l_4)}(\overrightarrow{r_2}). \tag{3.17}$$

In the case of the FD basis this matrix element can be calculated analytically using the technique of center-of-mass and the relative-motion complex-coordinate. This was first shown by Girvin and Jach [170] for the case of lowest-Landau-level (LLL) states. Tsiper [171] obtained similar results for general Landau levels using Darling's theorem for the products of generalized hypergeometric series (details see Ref. [171]). In this thesis, I introduce the technique used by Girvin and Jach [170] to calculate the Coulomb matrix element for a FD basis. Note that r_{12} in the above expression is in units of l_H. Substituting the FD states as mentioned in chapter 2 as:

$$\varphi_{n_r,l}(r,\theta) = \frac{1}{l_H}\sqrt{\frac{n_r!}{\pi(n_r+|l|)!}}\left(\frac{r}{l_H}\right)^{|l|} e^{-r^2/2l_H^2} e^{-il\theta} L_{n_r}^{|l|}\left(\frac{r^2}{2l_H^2}\right)$$

with the explicit form of the associated Laguerre polynomials

$$L_{n_r}^{|l|}(r) = \sum_{j=0}^{n_r}(-1)^j \binom{n_r+|l|}{n_r-j}\frac{r^j}{j!}. \tag{3.18}$$

In the matrix element appears now the four products

$$(r_1 \exp^{i\theta_1})^{\gamma_1}(r_2 \exp^{i\theta_2})^{\gamma_2}(r_2 \exp^{-i\theta_3})^{\gamma_3}(r_1 \exp^{-i\theta_4})^{\gamma_4}.$$

where $\gamma_i; i = 1 \div 4$ are defined by the angular momenta $l_i; i = 1 \div 4$ as:

$$\begin{aligned}
\gamma_1 &= j_1 + j_4 + (|l_1| + l_1)/2 + (|l_4| - l_4)/2\,, \\
\gamma_4 &= j_1 + j_4 + (|l_1| - l_1)/2 + (|l_4| + l_4)/2\,, \\
\gamma_2 &= j_2 + j_3 + (|l_2| + l_2)/2 + (|l_3| - l_3)/2\,, \\
\gamma_3 &= j_2 + j_3 + (|l_2| - l_2)/2 + (|l_3| + l_3)/2
\end{aligned} \tag{3.19}$$

where $\gamma_1 + \gamma_2 = \gamma_3 + \gamma_4$ expresses the conservation of total angular momentum $l_1 + l_2 = l_3 + l_4$. To eliminate the denominator of the Coulomb interaction term, the following trick was used based on complex numbers for the center-of-mass and relative coordinates of the two electrons:

$$\begin{aligned}
Z + z/2 = z_1 = (x_1, y_1) &= r_1 \exp^{i\theta_1} \\
Z - z/2 = z_2 = (x_2, y_2) &= r_2 \exp^{i\theta_2} \\
z &= z_1 - z_2
\end{aligned} \tag{3.20}$$

which transforms the integral (3.17) into two separable Gaussian integrations regarding the Z and z complex variables. Such a calculation of the Coulomb matrix element for the Fock-Darwin basis can be found in e.g. Refs. [172, 173] and results into:

$$\begin{aligned}
\langle 12|\frac{1}{r_{12}}|34\rangle = \; & \delta_{\sigma_1,\sigma_3}\delta_{\sigma_2,\sigma_4}\,\delta_{l_1+l_2,l_3+l_4}\sqrt{\prod_{i=1}^{4}\frac{n_{r_i}!}{(|l_i|+n_{r_i})!}}\sum_{(4)j=0}^{n}\frac{(-1)^{j_1+j_2+j_3+j_4}}{j_1!j_2!j_3!j_4!} \\
& \times\left[\prod_{i=1}^{4}\binom{n_{r_i}+|l_i|}{n_{r_i}-j_i}\right]\frac{1}{2^{(G+1)/2}}\sum_{(4)m=0}^{\gamma}(-1)^{\gamma_2+\gamma_3-l_2-l_3} \\
& \times\delta_{m_1+m_2,m_3+m_4}\left[\prod_{i=1}^{4}\binom{\gamma_i}{l_i}\right]\Gamma(1+\frac{\Lambda}{2})\Gamma(\frac{G-\Lambda+1}{2})
\end{aligned} \tag{3.21}$$

where

$$G = \sum_{i=1}^{4}\gamma_i\;, \qquad \sum_{(4)j=0}^{n} \equiv \sum_{j_1=0}^{n_{r_1}}\sum_{j_2=0}^{n_{r_2}}\sum_{j_3=0}^{n_{r_3}}\sum_{j_4=0}^{n_{r_4}}\;, \qquad \Lambda = \sum_{i=1}^{4}m_i, \tag{3.22}$$

$\binom{n}{m} = \frac{n!}{m!(n-m)!}$ is the binomial coefficient, and $\Gamma(x)$ is the gamma function.

Secondly, I discuss how to obtain the exchange interaction sub-matrix elements J_{ij}. Note that the sub-matrix (J) is obtained directly from the FD basis as in Eq. (3.7)

$$J_{ij}(\overrightarrow{R}) = J_c \varphi_i^*(\overrightarrow{R})\varphi_j(\overrightarrow{R})$$

where i and j are shorthand notation for the two quantum numbers (n_r, l). I will give a few examples how to evaluate J_{ij}. First, I calculate the diagonal elements of the (J) matrix. I denote the lowest-energy state, the s-shell (0,0) [see Fig. 3.1(a)] as J_{11}, the $p^{\pm} = (0, \pm 1)$ as $J_{22(33)}$ [Fig. 3.1(b)], the $d^{\pm} = (0, \pm 2)$ as $J_{44(66)}$ [Fig. 3.1(c)], and the $d^0 = (1, 0)$ as J_{55} [Fig. 3.1(d)], etc. Overlap between those $s-p$, $s-d$, $p-d$, etc, states thereby can be obtained through the terms, respectively, $J_{12(2)}$, $J_{14(6)}$, J_{15}, ..., J_{56}, etc. These elements are derived as follows:

$$\begin{aligned}
\langle 0,0|J|0,0\rangle \quad &= J_{11} \quad &&= J_c \varphi^*_{(0,0)}(\overrightarrow{R})\varphi_{(0,0)}(\overrightarrow{R}) \\
&&&= \frac{J_c}{\pi l_H^2} \exp(-\tilde{R}^2) \\
\langle 0,\pm 1|J|0,\pm 1\rangle \quad &= J_{22(33)} \quad &&= J_c \varphi^*_{(0,\pm 1)}(\overrightarrow{R})\varphi_{(0,\pm 1)}(\overrightarrow{R}) \\
&&&= \frac{J_c}{\pi l_H^2} \tilde{R} \exp(-\tilde{R}^2) \\
\langle 0,\pm 2|J|0,\pm 2\rangle \quad &= J_{44(66)} \quad &&= J_c \varphi^*_{(0,\pm 2)}(\overrightarrow{R})\varphi_{(0,\pm 2)}(\overrightarrow{R}) \\
&&&= \frac{J_c}{2\pi l_H^2} \tilde{R}^4 \exp(-\tilde{R}^2) \\
\langle 1,0|J|1,0\rangle \quad &= J_{55} \quad &&= J_c \varphi^*_{(1,0)}(\overrightarrow{R})\varphi_{(1,0)}(\overrightarrow{R}) \\
&&&= \frac{J_c}{\pi l_H^2} (1-\tilde{R}^2)^2 \exp(-\tilde{R}^2) \\
\langle 0,0|J|0,\pm 1\rangle \quad &= J_{12(3)} \quad &&= J_c \varphi^*_{(0,0)}(\overrightarrow{R})\varphi_{(0,\pm 1)}(\overrightarrow{R}) \\
&&&= \frac{J_c}{\pi l_H^2} \tilde{R} \exp(\mp i\theta) \exp(-\tilde{R}^2) \\
\langle 0,0|J|0,\pm 2\rangle \quad &= J_{14(6)} \quad &&= J_c \varphi^*_{(0,0)}(\overrightarrow{R})\varphi_{(0,\pm 2)}(\overrightarrow{R}) \\
&&&= \frac{J_c}{\sqrt{2}\pi l_H^2} \tilde{R}^2 \exp(\mp 2i\theta) \exp(-\tilde{R}^2) \\
\langle 0,0|J|1,0\rangle \quad &= J_{15} \quad &&= J_c \varphi^*_{(0,0)}(\overrightarrow{R})\varphi_{(1,0)}(\overrightarrow{R}) \\
&&&= \frac{J_c}{\pi l_H^2} (1-\tilde{R}^2) \exp(-\tilde{R}^2)
\end{aligned}$$

$$
\begin{aligned}
\langle 0,1|J|0,-1\rangle \quad &= J_{23} \quad && = J_c \varphi^*_{(0,1)}(\overrightarrow{R})\varphi_{(0,-1)}(\overrightarrow{R}) \\
& && = \frac{J_c}{2\pi l_H^2}\tilde{R}^2 \exp(2i\theta)\exp(-\tilde{R}^2) \\
\langle 0,1|J|0,\pm 2\rangle \quad &= J_{24(6)} && = J_c \varphi^*_{(0,1)}(\overrightarrow{R})\varphi_{(0,\pm 2)}(\overrightarrow{R}) \\
& && = \frac{J_c}{\sqrt{2}\pi l_H^2}\tilde{R}^3 \exp(i(1\mp 2)\theta)\exp(-\tilde{R}^2) \\
\langle 0,1|J|1,0\rangle \quad &= J_{25} && = J_c \varphi^*_{(0,1)}(\overrightarrow{R})\varphi_{(1,0)}(\overrightarrow{R}) \\
& && = \frac{J_c}{\pi l_H^2}\tilde{R}(1-\tilde{R}^2)\exp(i\theta)\exp(-\tilde{R}^2) \\
\langle 0,-1|J|0,\pm 2\rangle \quad &= J_{34(6)} && = J_c \varphi^*_{(0,-1)}(\overrightarrow{R})\varphi_{(0,\pm 2)}(\overrightarrow{R}) \\
& && = \frac{J_c}{\sqrt{2}\pi l_H^2}\tilde{R}^3 \exp(-i(1\pm 2)\theta)\exp(-\tilde{R}^2) \\
\langle 0,-1|J|1,0\rangle \quad &= J_{35} && = J_c \varphi^*_{(0,-1)}(\overrightarrow{R})\varphi_{(1,0)}(\overrightarrow{R}) \\
& && = \frac{J_c}{\pi l_H^2}\tilde{R}(1-\tilde{R}^2)\exp(-i\theta)\exp(-\tilde{R}^2) \\
\langle 0,2|J|1,0\rangle \quad &= J_{45} && = J_c \varphi^*_{(0,2)}(\overrightarrow{R})\varphi_{(1,0)}(\overrightarrow{R}) \\
& && = \frac{J_c}{\sqrt{2}\pi l_H^2}\tilde{R}^2(1-\tilde{R}^2)\exp(2i\theta)\exp(-\tilde{R}^2) \\
\langle 0,2|J|0,-2\rangle \quad &= J_{46} && = J_c \varphi^*_{(0,2)}(\overrightarrow{R})\varphi_{(0,-2)}(\overrightarrow{R}) \\
& && = \frac{J_c}{2\pi l_H^2}\tilde{R}^4 \exp(4i\theta)\exp(-\tilde{R}^2) \\
\langle 1,0|J|0,-2\rangle \quad &= J_{56} && = J_c \varphi^*_{(1,0)}(\overrightarrow{R})\varphi_{(0,-2)}(\overrightarrow{R}) \\
& && = \frac{J_c}{\sqrt{2}\pi l_H^2}\tilde{R}^2(1-\tilde{R}^2)\exp(2i\theta)\exp(-\tilde{R}^2)
\end{aligned}
\tag{3.23}
$$

where $\tilde{R} = R/l_H$.

Now, I estimate the above elements. For example, for $R = 0$ and zero B-field, these above low-energy levels have J-elements as $J_{11} = 2J_{55} \approx 6.8$ meV, $J_{22} = J_{33} = J_{44} = J_{66} = 0$, etc. If the Mn-ion is moved to a different position, the J-elements will change accordingly because of the overlap of the electron wave functions i and j.

Because the Mn-ions bear a spin 5/2 this causes the total Hamiltonian matrix to be six times larger in size (i.e. six times more rows and six times

more columns, and the number of matrix elements increased by a factor of 36) than that in case without a Mn-ion. Consequently, the virtual memory increases rapidly and the convergency process slows down significantly. Therefore, the price for energy spectrum becomes rather expensive with increasing number of electrons N_e.

3.3 Exact Diagonalization

The eigenvalues of the entire Hamiltonian matrix (H) can be solved numerically using the so-called exact diagonalization. ED technique allows to precisely obtain a relatively wide range of the energy spectrum for few-particle quantum system. For a small number of particles, one can use the Lanczos algorithm [174] to diagonalize the large matrix. The Lanczos algorithm is an iterative method that works effectively for sparse matrices with relatively large eigenvalues where the fraction of the number of nonzero elements over the total number of matrix element is very small. In principle, Lanczos is applicable for hermitian matrices. Thank to the symmetries in the Hamiltonian matrix which reduce significantly the complexity, the original matrix can be transformed to an identical one with much less off-diagonal elements, e.g a tridiagonal matrix. The eigenvalue problem for tridiagonal matrices can be solved using the libraries e.g. LAPACK [175] or ARPACK [176].

The Lanczos method starts with a randomly-chosen initial vector state, say ψ_0 (norm $||\psi_0||$=1). Subsequent states $\psi_i; i = 1, 2, 3, ...$ are obtained as

$$\psi_{n+1} = \frac{H\psi_n}{||H\psi_n||}. \tag{3.24}$$

wih (H) the matric I want to diagonalize. The sequence of $\{\psi_i\}$ is now used to build an orthogonal basis $\{\phi_i\}$ which is constructed as a span of $\{\psi_i\}$ and will be used to create a matrix, say $(\tilde{R})$, whose eigenvalues converge to the eigenvalues of the matrix (H). Such transformation is defined as

$$\beta_{i+1}\phi_{i+1} = H\phi_i - \alpha_i\phi_i - \beta_i\phi_{i-1}\,; \quad i \leq N_c - 1 \tag{3.25}$$

$$\alpha_i = \phi_i^\dagger H\phi_i \tag{3.26}$$

$$\beta_i = \phi_i^\dagger H\phi_{i+1} \tag{3.27}$$

with

$$\phi_i\phi_j = \delta_{ij} \tag{3.28}$$

called the Lanczos recursion where the series of $\{\alpha_i\}$ and $\{\beta_j\}$ form the tridiagonal symmetric matrix $(\tilde{R})$:

$$\tilde{R}_{ij} = \begin{cases} \alpha_i & \text{if i=j,} \\ \beta_i & \text{if j=i+1.} \end{cases} \tag{3.29}$$

Once the eigenvalue problem for $(\tilde{R})$ is solved, the eigenvectors are also calculated. The eigenvectors for the original Hamiltonian (H) can then be obtained using the Lanczos transformation

$$\Psi = \sum_{i=1}^{N_c-1} C_i \phi_j \tag{3.30}$$

with $\{C_i\}$ corresponding to an eigenvector of the matrix $(\tilde{R})$.

According to the Lanczos algorithm when the iteration number exceeds (N_c-1), the diagonalization problem is converged. The first few lowest energy levels are obtained rather fast while it is much more time-consuming to obtain a large number of eigenvalues due to the increase in memory.

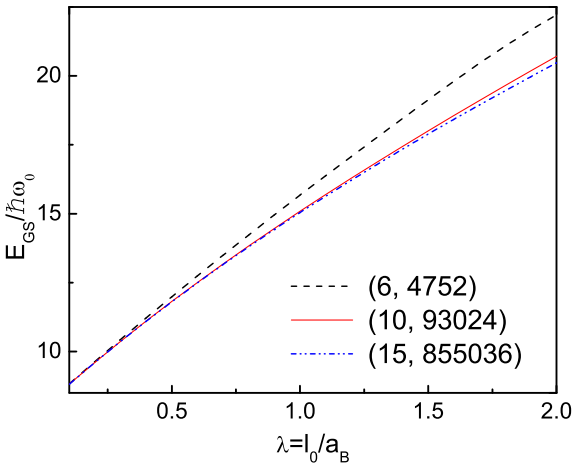

Figure 3.2: Illustration of the convergency of the GS energy for a five-electron QD in case the Mn-ion is located at the center of the dot. λ measures the effective Coulomb interaction strength. Numbers in brackets are the included single-particle orbital number N_s and the corresponding configuration number N_c.

With increasing N_e, the size of the matrix increases very fast and the problem becomes more complex. First, the Coulomb interaction becomes

active which results in many nonzero off-diagonal elements. Second, the spin exchange interaction and Pauli exclusion principle are taken into account resulting in the occurrence of another number of nonzero off-diagonal elements and additional energy contributions to many diagonal elements. The latter fact was discussed in the beginning of this chapter when I described the last sum in Eq. (3.6).

3.4 Convergency

We investigate the convergency of the above numerical implementation as a function of the number of 2D orbitals N_s that are included in the numerical calculation. As an example, let us consider the three-electron QD. If one includes only the *s*- and *p*-shell, i.e. only three orbitals along with the two possibilities for the electron spin 1/2 one will have $N_c = 120$ $(= 6 \times \binom{6}{3})$ configurations and the matrix is $N_c \times N_c$ and contains 14,400 elements. If one includes the *s*-, *p*- and *d*-shell one would have $N_c = 1320$ $(= 6 \times \binom{12}{3})$ configurations. The number of configurations would be $N_c = 166,572$ if one includes 28 orbitals which results into a matrix consisting of 2.8×10^{10} elements.

For $\mathrm{N}_e = 5$ (see Fig. 3.2), the convergency as a function of Coulomb interaction strength in case the Mn-ion is located at the center of the dot is obtained by gradually increasing the number of included configurations N_c as illustrated in Fig. 3.2. For example, the case for $\lambda_C = 0.5$ has the energy 11.81758 $\hbar\omega_0$ when $\mathrm{N}_c = 93,024$ and 11.80572 $\hbar\omega_0$ when $\mathrm{N}_c = 855,036$. The relative difference is 0.1%. Note that with increasing Coulomb interaction strength more configurations have to be included in order to obtain convergency.

4

Correlated many-electron states in a quantum dot containing a single magnetic impurity

The few-electron states of a parabolic confined quantum dot is studied in the presence of a Mn-ion. The electrons interact with a single Mn-ion (Mn^{2+}) which is located in the quantum dot at arbitrary position. The local Zeeman spin splitting is calculated for different number of electrons ($N_e = 1, 2, 3, ..., 10$). The effect of the position of the Mn-ion on the energy levels (both ground state and excited states) is investigated. We calculate the heat capacity as function of temperature, the position of the impurity and the Coulomb strength.

4.1 Introduction

This chapter explores the electronic properties of the ground state of N_e interacting electrons confined by a parabolic potential containing a single Mn^{2+} at zero magnetic field. This is the situation recently studied in Ref. [77], where the authors found a local Zeeman spin splitting independent of the position of the impurity for $N_e = 1, 2, ..., 6$ including only *s*-, *p*- and *d*-shell. In the preceding calculations, the Mn-ion was fixed at the position $(l_0, 0)$ and the Coulomb strength was kept at a specific value $\lambda_C = 0.5$. In this chapter, we extend those calculations to a QD containing up to ten electrons where the Coulomb interaction strength will be varied and the single Mn-ion may be located at an arbitrary position inside the dot. We enlarge the size of the Hilbert space, as compared to Ref. [77], by including higher levels, beyond the *s*, *p*, *d* shells. Besides the ground state energy, we

The results presented in this chapter were published as:

- N. T. T. Nguyen and F. M. Peeters, Phys. Rev. B **76**, 045315 (2007).

will also investigate thermodynamic properties as the specific heat.

In the previous calculations [77] the Mn-ion was fixed at the location $(l_0, 0)$ inside the quantum dot. Here we will release this restriction and investigate the dependence of the quantum properties on the position of the *Mn*-ion.

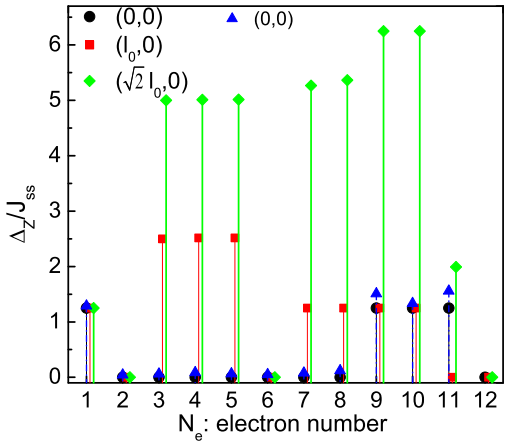

Figure 4.1: Zeeman spin splitting vs number of electrons calculated for the partially filled and for the case that all possible configurations of the *s*, *p* and *d* shells are included (blue triangles). The Coulomb strength was 0.2.

4.2 Local Zeeman energy

The Zeeman term contribution is calculated as being the energy difference between the QD with and without the magnetic impurity:

$$\Delta_Z = E_{UC} - E_C. \tag{4.1}$$

We reproduced the results for the local Zeeman splitting as obtained recently by Qu and Hawrylak [77] for partly-filled shells for $N_e = 1, 2, ..., 6$ of the *s*, *p* and *d* shells in Fig. 4.1 by the red squares. Besides, we also show the results for some typical positions of the Mn-ion. The black circles are results for the case the Mn-ion located at the center of the dot, the green lozenges for the Mn-ion located at $(\sqrt{2}l_0, 0)$. The blue triangular is representative for the case that all possible configurations of the *s*, *p*, and *d* shells are included and the Mn-ion is located at the center of the QD. These results were not presented in Ref. [77]. Furthermore, we found clearly that the quantitative

results depend on the exact location of the Mn-ion. The Coulomb interaction strength is chosen to be 0.2 to ensure the accuracy of the result when N_e is increased above 6 electrons.

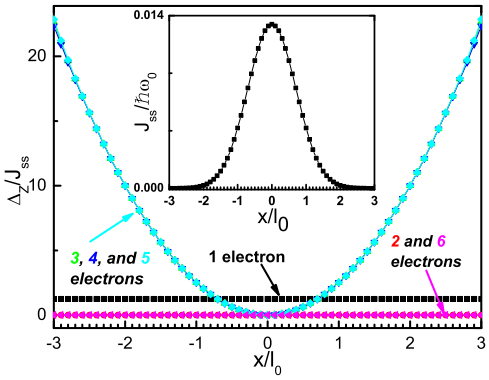

Figure 4.2: Mn-ion position dependence of the Zeeman spin splitting for the cases of one to six electrons. J_{ss} is a function of the position of the impurity as shown in the inset. The Coulomb strength is 0.2.

The partly filled shell calculations are done for those configurations of electrons at which there is no excitation from lower to higher electronic single particle levels. For instance, three electrons in partly filled shells first fill up the s-shell by two electrons then fill up one of the four possibilities of the p-shell by the remaining electron. To follow this definition, we realize that two-, six-, and twelve-electron quantum dots are special in a sense that two electrons fully fill the s-shell and six electrons fully fill the three orbitals (six possibilities) of the s and p shells and twelve electrons fully fill the s, p, and d shells resulting in zero Zeeman spin splitting.

4.3 Dependence on the position of the Mn-ion

The authors of Ref. [77] found the unexpected result that the exchange term Δ_Z was independent of the filling of the shell in a limited Hilbert space (involving only the partially filled s, p, d shells). If all configurations are included the Δ_Z slightly changed due to the presence of excitations. Additionally, they claimed that the result was independent on the position of the Mn-ion.

Our numerical calculations on the other hand show that in general, the local Zeeman term itself depends on the position of the impurity. More

specific, when we consider the partially filled s, p shells, the Δ_Z of $N_e = 1, 2, ..., 6$ changes consistently with changes in the J_{ss}, J_{pp}. When all possible configurations of those shells are included, the situation changes due to the mutual interactions of the overall orbitals.

We plot in Fig. 4.2 the dependence of the local Zeeman energy on the position of the impurity for 1, 2, ..., and 6 electrons as obtained by including only the *partly filled* s, p, d shells when no excitation is taken into account. We found $\Delta_Z = 0$ and no dependence of the local Zeeman energy of the two- and six-electron QD on the position of the impurity. The one-electron QD Δ_Z has only a very weak dependence. This can be explained in the following way. In the case of two- and six-electron QDs the s and then p shells were fully filled (closed shells). Therefore, there is zero-contribution from the local Zeeman part to the energies of those QDs. For the one-electron problem, Δ_Z changes consistently with the change in J_{ss}. This results in the ratio of the local Zeeman term to the J_{ss} that is almost independent on the position of the magnetic ion.

For the three-, four- and five-electron QDs we obtained the same dependence for the local Zeeman energy on the position of the impurity in case of partially-filled s and p shells. We found zero-contribution of the local Zeeman energy at position $(0, 0)$. The reason is when we take into account the partially-filled s and p shells, the exchange matrix elements describing the mutual couplings of orbitals from s and p shells and the exchange matrix elements between the p-shell themselves are zero when the Mn is at the center of the dot. We also found that the curve has a parabolic form that is also the form of the ratio of J_{pp}/J_{ss} vs the position of the Mn-ion different by a constant factor. The form of the curve changes when we include the d shell orbitals.

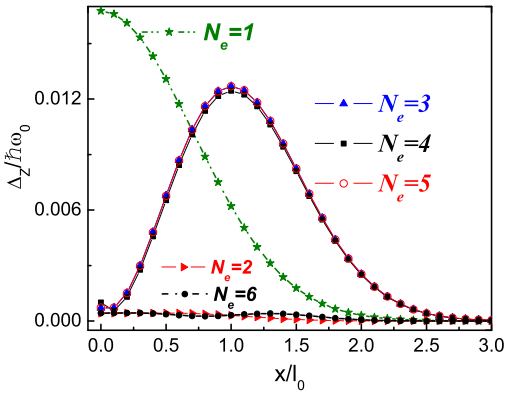

Figure 4.3: Mn-position dependence of the Zeeman spin splitting when all the possible configurations of s, p, and d shells are included. The Coulomb strength is 0.2

Fig. 4.3 shows the impurity-position dependence of the local Zeeman energy but now scaled to the confinement energy. All possible configurations

were included. For $N_e = 1$ electron, we see a peak of Δ_Z at $x = 0$. This is because J_{ss} contributes mainly to Δ_Z which has also a peak at $x = 0$. When the number of electrons in the QD increases the contributions of the exchange matrix elements from higher levels, e.g. the p, d, f, ... shells increases. It leads to a displacement of the peak to $x = l_0$, as we see for $N_e = 3, 4$, and 5 electrons.

When we move the Mn-ion far away from the center, the exchange matrix elements tend to zero. The problem is converted to an uncoupled problem because the overlap with the electron wave function decreases exponentially to zero.

When the Coulomb interaction strength, λ_C, approaches zero it means that the ratio l_0/a_B also approaches zero. Consequently, the exchange energy, Δ_Z, is now zero at any position of the Mn-ion, except for the center of the dot. The effect of the Coulomb interaction is to extend the region where the Mn-ion can be located where it gives a nonzero contribution of Δ_Z to the total energy of the system. Increasing the Coulomb interaction strength moves the maximum contribution of the local Zeeman splitting term to a position further from the origin of the dot.

4.4 Excited states

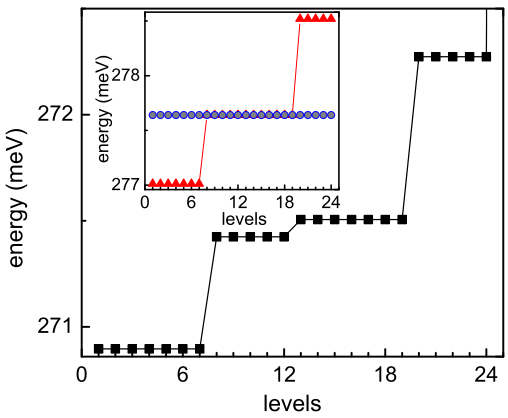

Figure 4.4: Energy spectrum of a three-electron QD calculated for the case the Mn-ion is located at the position $(l_0, 0)$ and the Coulomb interaction strength is 0.5. The inset is the low energy spectrum with (the red triangles) and without (the blue dots) the Mn-ion when the partially filled p-shell is considered.

In the previous sections, we mentioned the "partially filled" concept where excitation was not taken into account in order to see the contribution of the local Zeeman term to the energy spectrum. In this section, we consider excited states where we will include higher single particle levels. We present in Fig. 4.4 the energy of the first 24 energy levels for the case of $N_e = 3$ electrons where we include 21 single particle orbitals. The inset is the spectrum when only the orbitals up to the partially filled p-shell are included. In this inset, we show also the spectrum as obtained without interaction with the Mn-ion as the constant energy level (blue circles) with degeneracy 24 (4 degenerate possibilities of the p-electron and 6 possibilities of the spin of the Mn-ion). In the presence of the Mn-ion, the spectrum splits into three levels. The GS energy is shifted to lower energy with degeneracy 7 (spin degeneracy of the Mn-ion 5/2 plus 1/2 for the third electron) as indicated by the triangles, and the first excited state with degeneracy 12 equals to the ground state energy of the case without interaction with the Mn-ion. This is a result of the intra-level interactions. When we include even more single particle levels we obtain the results as given in the main plot of Fig. 4.4 where we took into account inter-level interactions, in this case $N_s = 21$. Note that the ground state energy is even further reduced in energy and the degeneracy of the excited state is further reduced. However, the ground state energy in both cases has a degeneracy of 7, which is related to the fact that the Mn spin is FM coupled to the electron that couples to the p shell. We see that the excited states split into more levels as compared to the case in the inset. The precious first excited states is split into a level with degeneracy 5 (= spin degeneracy due to total spin of $5/2 - 1/2 = 2$) and a level with degeneracy 7. In the main figure we see several different energy gaps between the excited states. These gaps will have an effect on the contribution to the possible energy storage of the system that will be manifested in the heat capacity.

4.5 Heat capacity

Since we have the complete spectrum we can calculate all thermodynamic properties. One important quantity that is concerned with storage of energy is the heat capacity:

$$C_V\left(\lambda_C, T, R_{Mn}\right) = \frac{\partial \langle E\left(\lambda_C, T, R_{Mn}\right)\rangle}{\partial T} \tag{4.2}$$

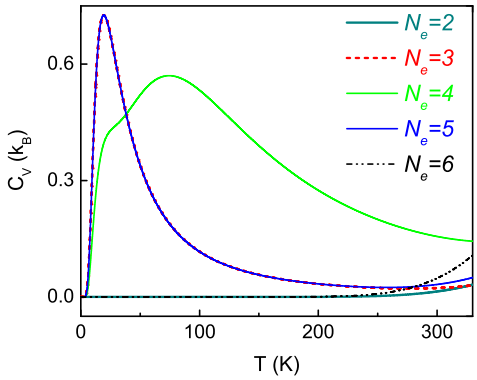

Figure 4.5: Heat capacities vs Temperature plot for 2 to 6 electrons obtained for all possible configurations of s, p and d shells. The impurity was located at $(l_0, 0)$ and the Coulomb strength was 0.2.

where:

$$\langle E\left(\lambda_C, T, R_{Mn}\right)\rangle = \frac{\sum_{\alpha=1}^{N_\alpha} E_\alpha e^{-E_\alpha/k_B T}}{\sum_{\alpha=1}^{N_\alpha} e^{-E_\alpha/k_B T}}, \tag{4.3}$$

is the average energy that is a function of the Coulomb strength λ_C, temperature T and the position of the impurity R_{Mn}. E_α is the α-th energy level of the many-body energy spectrum.

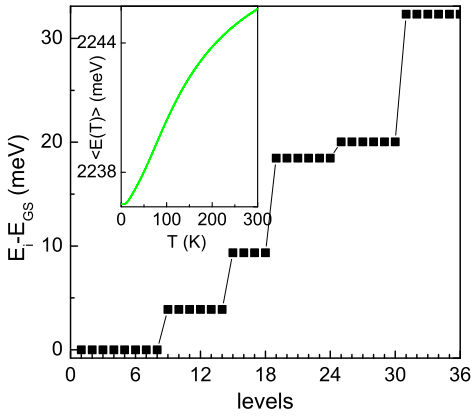

Figure 4.6: Spectrum of a four-electron QD with the Mn-ion located at the position $(l_0, 0)$ when the three shells of s, p and d are included. The inset is the statistical average of the energy over temperature.

We present in Fig. 4.5 the heat capacities of quantum dots containing

from 2 to 6 electrons. The impurity was located at the position $(l_0, 0)$. The heights and widths of the pronounced peaks of those curves are determined by the energy gaps between the respective ground state and the excited state energies.

We plot in Fig. 4.6 the energy spectrum of the first 36 levels of the four electron QD in order to understand the heat capacity. The number of energy levels is relevant for the considered temperature range. From this figure we realize that the first peak in the heat capacity (see Fig. 4.5) is related to the turn of the averaged energy quantity (see the inset) at $T = 74.4K$. The flat-like region in the average energy results in a zero heat capacity for temperatures close to zero. Besides, we see that the ground state energy has degeneracy 8 resulting from the total spin of $5/2 + 1 = 7/2$ while the first excited state has degeneracy 6 that is from the total spin of $5/2 + 0 = 5/2$, and so on for the higher energy levels.

In Fig. 4.7 we extend the result of Fig. 4.5 to $N_e = 7$ up to 10. Notice that for $N_e > 4$ the heat capacity exhibits a clear peak structure for temperatures $T < 100K$. The position of the peak depends sensitively on the number of electrons in the dot.

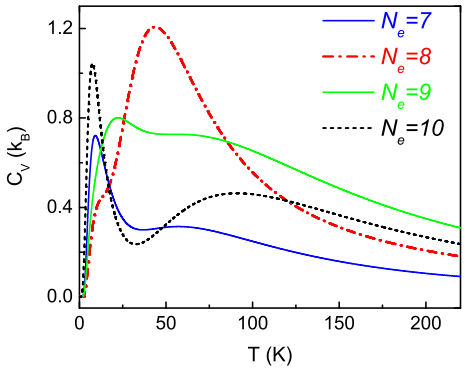

Figure 4.7: The same as Fig. 4.5 but obtained for 7 to 10 electrons.

Fig. 4.8 shows a 3D-plot of the heat capacity obtained as a function of temperature, T, and Coulomb strength, λ_C, of a three-electron QD at a specific position of the Mn-ion, $(l_0, 0)$ and shows clearly the effect of the Coulomb interactions. The result was obtained when all the possible electronic configurations of the s, p, d, f, and g shells were included. We see a shift in the peak of the heat capacity to smaller temperatures when increasing the Coulomb interaction strength λ_C. Fig. 4.9, plotted for two extremes (i.e. 0.1 and 1.0) of the Coulomb interaction strength used in Fig. 4.8, and it illustrates the respective energy spectra of these cases and their statistical average energies over temperature (the two insets). We see that at these two parameters of $\lambda_C = 0.1$ and $\lambda_C = 1.0$, the respective energy spectra are significantly different explaining the shift in the peak structure of the specific heat. Because the peak of the specific heat is relevant to the gap

between the energy levels and consequently to the temperature. If one plots the specific heat versus different Coulomb interaction strengths λ_C, which is proportional to $1/\sqrt{\omega_0}$, and different temperatures one could see that the peak in the specific heat moves to lower temperature with increasing λ_C.

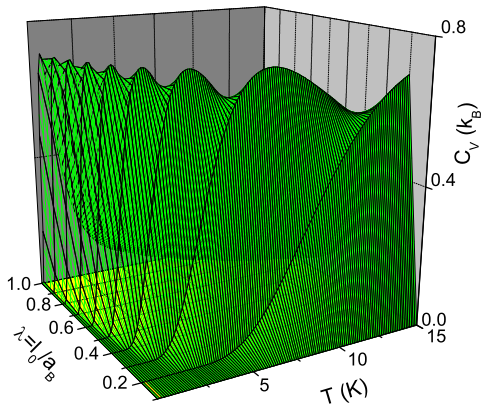

Figure 4.8: 3D plot of the heat capacity of the three-electron QD containing a single impurity located at $(l_0, 0)$ vs temperature and Coulomb strength λ_C.

To complete the discussion on the heat capacity, let us discuss the dependence of the heat capacity on the spin size $\mathbf{M}$ of the Mn-ion. Fig. 4.10 shows that when the spin size of the impurity is changed from 1/2 to 7/2 the position of the peak in the heat capacity, along with it's height and width, is shifted to higher temperatures. Notice that with increasing $\mathbf{M}$ the peak structure shifts to higher temperatures due to the increased interaction energy that leads to a larger gap in the energy spectrum.

4.6 Conclusions

In conclusion, we examined the behavior of few-electron QDs confined to a lateral parabolic potential in interaction with a single Mn-ion in the absence of an external magnetic field. The Mn impurity is engineered at different positions. We produced results obtained for a few discrete positions and focused on three locations where the diagonal exchange matrix elements have a maximum: the center of the dot, the position $(l_0, 0)$, and the position $(\sqrt{2}l_0, 0)$. Results are intended to exhibit the electronic ground state

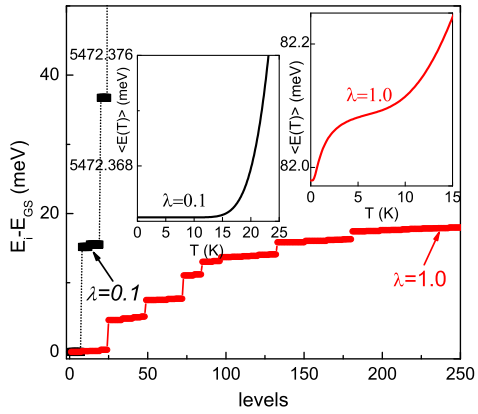

Figure 4.9: Spectrum of a three-electron QD with the Mn-ion located at $(l_0, 0)$ for two values of the Coulomb interaction strength.

properties when the number of carriers is changed and many single-electron levels are included due to a desire to sample as many electronic configurations as possible. We obtained different behaviors for different positions of the Mn-ion.

In fact, the exchange matrix elements (the electron-Mn interaction terms) are much smaller than $\hbar\omega_0$ (at most $1-2\%$), particularly when we move the Mn-ion away from the center of the dot. The diagonal elements become dominant in comparison to contributions from the exchange interaction terms. Therefore, Δ_Z is of the same order as those small parameters.

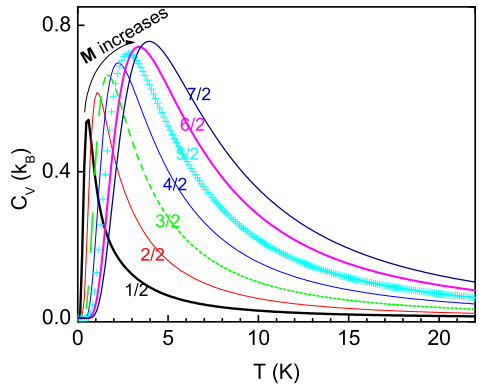

Figure 4.10: Heat capacity for $N_e = 3$ and different values of the spin of the Mn-ion from 1/2 to 7/2. The Mn-ion was located at $(l_0, 0)$ and $\lambda_C = 0.5$.

Extending the Hilbert space allows us to understand physics beyond the *s*-, *p*-, and *d*-shell interactions and we can study the properties in the case of larger Coulomb interaction strength. We found that Δ_Z is related to the Coulomb strength λ_C and the position of the Mn-ion. λ_C can for example be changed by changing the size of the QD.

When λ_C is small, meaning that the electrons in the quantum dot are more strongly localized, Δ_Z changes consistently with changes in the diagonal $electron - Mn$ exchange matrix elements. In contrast, when λ_C is large the electrons in the quantum dot become more strongly correlated. The contribution to the energy of the system spreads over more matrix elements, and Δ_Z becomes maximum at different positions of the Mn impurity.

With changing number of electrons in the QD system and changing position of the Mn-ion results in changes in the heat capacity both in its shape and the position of the peaks. Larger Coulomb interaction strength moves the peak of the heat capacity to lower temperature.

5

Magnetic field dependence of the many-electron states in a magnetic quantum dot: The FM-AFM transition

The e-e correlations in a many-electron ($N_e = 1, 2, ..., 5$) QD confined by a parabolic potential is investigated in the presence of a single Mn-ion and a perpendicular magnetic field. We obtained the energy spectrum and calculated the addition energy which exhibits cusps as function of the magnetic field. The vortex properties of the many-particle wave function of the ground state are studied and for large magnetic fields are related to composite fermions. The position of the Mn-ion influences strongly the spin-pair correlation function when the external field is large. In small applied magnetic field, the spin exchange energy together with the Zeeman terms leads to a ferromagnetic-antiferromagnetic (FM-AFM) transition. When the Mn-ion is shifted away from the center of the QD a remarkable re-entrant AFM-FM-AFM transition is found as function of the strength of the Coulomb interaction. Thermodynamic quantities as the heat capacity, the magnetization, and the susceptibility are also studied. The cusps in the energy levels show up as peaks in the heat capacity and the susceptibility.

5.1 Introduction

In the present study, we investigate theoretically the few-electron 2D confined QD system that contains a single Mn-ion in the presence of an external

The results presented in this chapter were published as:

- N. T. T. Nguyen and F. M. Peeters, Phys. Rev. B **78**, 045321 (2008).
- N. T. T. Nguyen and F. M. Peeters, Physicalia Magazine **30**, 169 (2008).

magnetic field taking into account a sufficient large number of single-particle orbitals such that numerical "exact" results are obtained.

We explore how sensitive the whole system is to the position of the Mn-ion in the QD and to the presence of a magnetic field and investigate the competition between the following three energies: i) the interaction of the Mn-ion with the electrons, ii) the interaction of the Mn-ion with the magnetic field, and iii) the interaction of the external field with the electrons. These terms affect the spin polarization of the N_e electrons in the QD.

Here, we will examine thoroughly the exact properties of the system containing several correlated electrons and a single magnetic impurity in the presence of a magnetic field. In our numerical "exact" diagonalization approach we include an arbitrary number of single-particle states to guarantee the accuracy of our results. We investigate the influence of the strength of the inter-particle interaction and the position of the Mn-ion on the ground state of the system. We predict the interesting phenomenon that the Mn-ion FM couples with the electrons in a region below a critical magnetic field and AFM with the electrons above this critical field. Thermodynamic properties as magnetization, susceptibility, and the heat capacity are investigated as function of magnetic field and temperature.

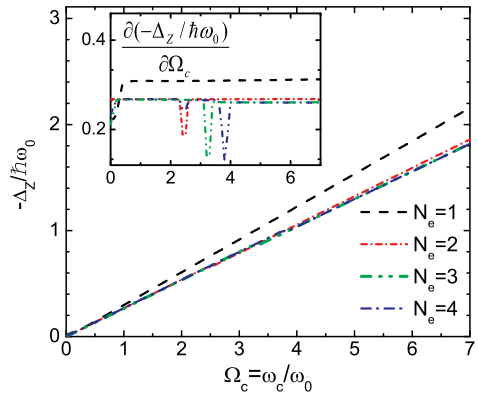

Figure 5.1: Total Zeeman energy for a QD with different number of electrons. The Mn-ion is located at $(0.41l_0, 0)$, and the Coulomb interaction strength $\lambda_C = 0.2$. The inset is the first derivative of Δ_Z with respect to Ω_c that highlights the non-linearity of Δ_Z in certain regions of the magnetic field.

5.2 Ground-state properties

5.2.1 Zeeman energy

We first explore the magnetic field dependence of the total Zeeman energy:

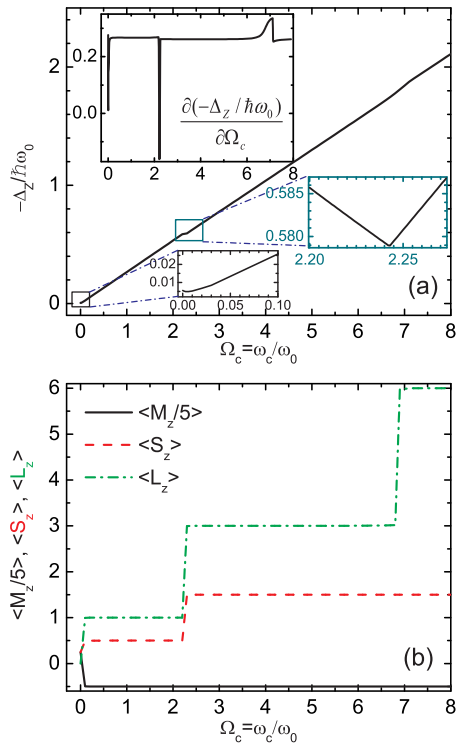

Figure 5.2: Total Zeeman energy (a) calculated for a three-electron QD with the Mn-ion at $(0.5l_0, 0)$ and $\lambda_C = 0.5$. The upper inset is the first derivative of the main plot with respect to Ω_c to visualize more clearly the cusps. The lower inset is a zoom of the rectangular regions of the main plot. (b) The z-projection of the total spin of the Mn-ion (solid black curve), of the electrons (dashed red curve), and the total angular momentum (dash-dotted green curve).

$$\Delta_Z = \Delta_Z^{electron} + \Delta_Z^{Mn} + (-\Delta_Z^{exc}) \tag{5.1}$$

which is the difference in energy in the presence and without a Mn-ion. It consists of three terms: the difference of the Zeeman energy of the electrons

$\Delta_Z^{electron}$, the Zeeman energy describing the interaction of the Mn-ion having spin $\mathbf{M} = 5/2$ with the magnetic field, Δ_Z^{Mn}, and the exchange interaction of the ion with the electrons, $-\Delta_Z^{exc}$. Δ_Z^{exc} is just the so called "local Zeeman splitting term" as discussed in Ref. [82]. This sum is basically the difference in the Zeeman energy of the electrons between the cases with and without a Mn-ion plus the energy contribution of the Mn-ion.

For $N_e = 1$, we find a total Zeeman energy that appears linear in magnetic field. A similar linear behavior is also found in the cases with $N_e > 1$ but with different slopes (see Fig. 5.1). Let us suppose, in Hamiltonian (3.1), that the contribution from the last term (the local Zeeman energy or the exchange interaction term) is zero. For instance this is the case when a Mn-ion is located at the center of the QD having three-electrons in the partially filled p-shell, in which the first two-electrons fully fill the s-shell and the remaining one is in either of the orbitals of the p-shell. Then a perfect linear behavior of the total Zeeman energy is found.

A closer look to Δ_Z gives us a slightly different picture, as is provided by taking the derivative (see the inset of Fig. 5.1). Notice that the total Zeeman term Δ_Z has pronounced cusps and the number and positions of these cusps are different for different number of electrons N_e. There exists one at $\Omega_c = 2.6$ for a two-electron QD, one at $\Omega_c = 3.4$ for a three-electron QD, and two at $\Omega_c = 2.5$ and 3.8 for the four electron QD, with the Mn-ion located at $(0.41l_0, 0)$. The three-electron system exhibits a much richer behavior when we increase the Coulomb interaction strength to $\lambda_C = 0.5$ as seen in Fig. 5.2(a) where we placed the magnetic ion at $(0.5l_0, 0)$. Cusps, which are highlighted in the two insets in Fig. 5.2(a), appear when the total angular momentum and/or the total z-projection of the spin of the electrons change abruptly with magnetic field. Notice that the total Zeeman energy of a two-electron QD in the presence of the Mn-ion does not produce a similar behavior due to the fact that the z-projection of the total spin is zero making the main contribution (from the Zeeman spin term of the Mn-impurity) negligible.

The Coulomb strength and the position of the Mn-ion affects the total Zeeman energy and influences the number and the position of the cusps. The first pronounced cusp appears at lower magnetic field for larger λ_C. This is a consequence of the competition between the Coulomb energy and the energy gap of the single-particle problem. Larger λ_C (smaller energy gap) leads to stronger e-e correlation and consequently the electrons are more clearly separated from each other. It results into a high probability for finding the electrons to occupy higher energy states. That also means that the system transfers to a configuration with larger S_z and L_z at smaller

applied field.

We also found that the ground-state energy is sensitive to the presence of the magnetic field. In zero magnetic field, the ground state receives contributions from many different configurations having z-projection of the Mn-ion, M_z, from $-5/2$ to $5/2$. When a magnetic field is applied, the ground state favors states with projection of the spin of the Mn-ion down and the states with $M_z = -5/2$ give the main contribution to the ground state.

Fig. 5.2(b) shows the average of the three quantities M_z, S_z, and L_z of the three-electron QD as a function of the magnetic field for $\lambda_C = 0.5$. We realize that with increasing λ_C the $< L_z >$ ($< S_z >$) exhibits jumps at smaller critical Ω_c (compare green dash-dot-dot curve in Fig. 5.1).

5.2.2 AFM coupling

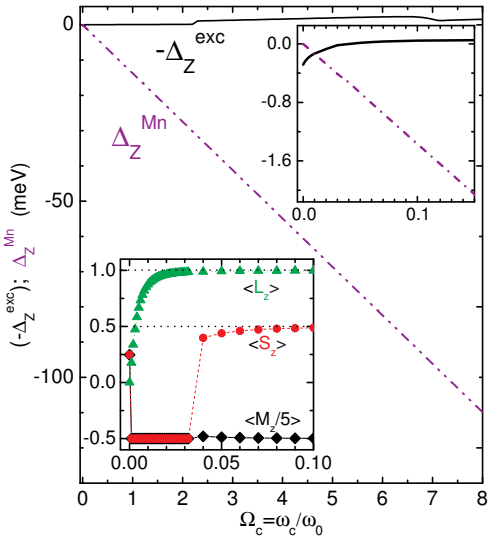

Figure 5.3: Zeeman energy of the Mn-ion and exchange interaction of a three-electron QD with the Mn-ion located at $(0.5l_0, 0)$ and $\lambda_C = 0.5$. The upper inset is a zoom of the small magnetic field region and the lower one presents the average of M_z, S_z, and L_z for the ground state at very small magnetic fields.

Now we direct our attention to the very small magnetic field behavior. There exists a very small region of the magnetic field where the total spin of electrons and the total spin of the magnetic ion are oriented parallel, we

found this earlier in Ref.[82] for the zero magnetic field case. These results are now extended to nonzero magnetic field. This is made more clear in the upper inset of Fig. 5.3 where the crossing point of the two terms: the Zeeman energy of the Mn-ion (Δ_z^{Mn}) and the exchange interaction (Δ_z^{exc}), occurs at $\Omega_c = 0.01$ (converted to $B \approx 0.1T$ for the considered system). This FM coupling extends further, up to $\Omega_c = 0.04$ (see the lower inset of Fig. 5.3).

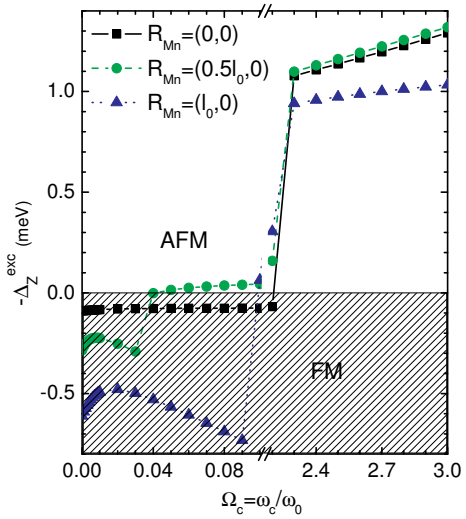

Figure 5.4: Exchange interaction of a three-electron QD with the Mn-ion located at three different positions: $(0,0)$, $(0.5l_0,0)$, and $(l_0,0)$ for $\lambda_C = 0.5$. The horizontal line at $\Delta_Z^{exc} = 0$ separates the Δ_Z^{exc} plane into FM and AFM regions.

It is worth noticing that this FM coupling is extended to a much larger magnetic field range (up to $\Omega_c = 2.3$) if we move the Mn-ion to the center of the QD (see Fig. 5.4). This can be understood as follows. When the Mn-ion is located at the center of the dot and the magnetic field is very small the absolute value of Δ_z^{Mn} always dominates over Δ_z^{exc}. This is opposite to the case when the Mn-ion is located at $(0.5l_0,0)$. Recall that in Ref.[82] we found for zero field that the exchange Zeeman energy is minimum when the Mn-ion is at the center of the QD and approximately zero at positions very far from the center of the QD.

Fig. 5.4 tells us that the magnetic field where the AFM coupling between electron and the Mn-ion starts depends on the position of the Mn-ion in the QD. The system with the Mn-ion located at $(l_0,0)$ exhibits an AFM coupling

for $\Omega_c \geq 0.1$, that is larger than $\Omega_c = 0.05$ in case of $(0.5l_0, 0)$.

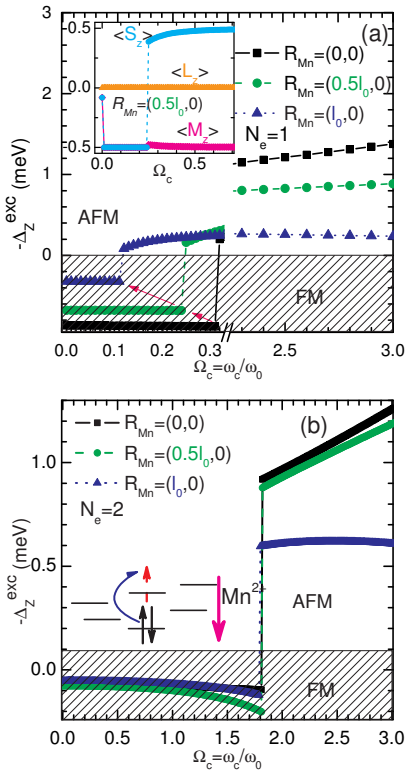

Figure 5.5: Exchange interaction of a one-electron (a) and two-electron (b) QD with the magnetic ion located at three different positions and $\lambda_C = 0.5$. The inset in the upper plot are the averages of the three quantities: M_z, S_z, and L_z with the ion located at $(0.5l_0, 0)$ at small magnetic fields. The horizontal line separates the plane into FM and AFM regions in both two plots. The schematic diagram in (b) explains why the exchange energy is almost zero in the case $N_e = 2$.

We have discussed the appearance of antiferromagnetism in a three-electron QD. Now we go back to the two simpler cases with the number of electrons $N_e = 1, 2$ (see Fig. 5.5). Let us first discuss the results for $N_e = 1$ as given in Fig. 5.5(a). The AFM coupling between the electron and the Mn-ion starts at smaller magnetic field as the Mn-ion is moved. This is different from the previous results for $N_e = 3$. The reason is as follows: for the QD with a single electron, the electron tends to accommodate

permanently the s-shell with $< L_z >= 0$ (see the inset of Fig. 5.5(a)) in the ground state while the exchange parameter in the s-shell (J_{ss}) is found to be maximum right at the center of the QD. Moving the Mn-ion away from the center of the dot, this J_{ss} is found to be smaller and as a consequence the exchange electron-Mn interaction becomes smaller than the electron Zeeman energy, leading to an AFM coupling at smaller magnetic field. The

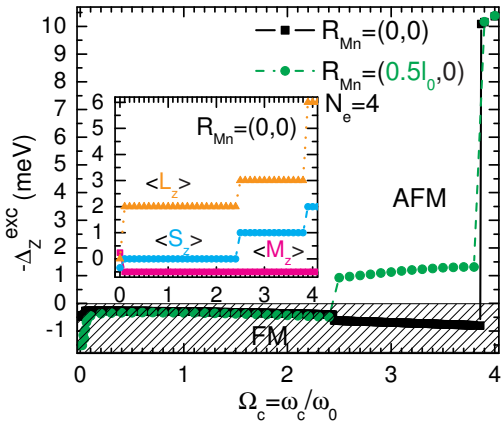

Figure 5.6: Exchange interaction of a four-electron QD with the Mn-ion located at three different positions and $\lambda_C = 0.2$. The horizontal line separates the plane into FM and AFM regions. The inset shows the total z-projection of the M_z, S_z, and L_z of the electron system with the Mn-ion located at the center of the dot.

story for $N_e = 2$ electrons [see Fig. 5.5(b)] is now interesting since the two electrons accommodate the s-shell with spins antiparallel making the total spin of the electron zero in the ground state with almost unit probability. This leads to zero contribution to the first term written in the last line in (3.6) for diagonal elements. Therefore, the main contribution (even very small) to the exchange energy is now expected to come from coupling with configurations where one of the electrons (spin down) stays in the s level and the other occupies higher level [see the schematic diagram in Fig. 5.5(b)]. In this diagram, the Mn-ion is assumed to be located at the center of the dot with spin down ($-5/2$). The coupling of the electron (spin up) in the s orbital with an electron from either of the p-shell is zero. The only non-zero coupling is with an electron with the quantum numbers (1,0) of the d-shell (as shown in the diagram and this quantum state would change if the ion is located away from the center of the dot) with the amount of about -10^{-2}.

This picture remains valid until the magnetic field is high enough to excite one electron from the s-shell to a higher quantum state forming the ground state with two up spins AFM coupling with the Mn-ion. For smaller λ_C, the AFM behavior occurs at larger magnetic field since the two electrons repel each other less and consequently they stay longer antiparallel in the s-shell.

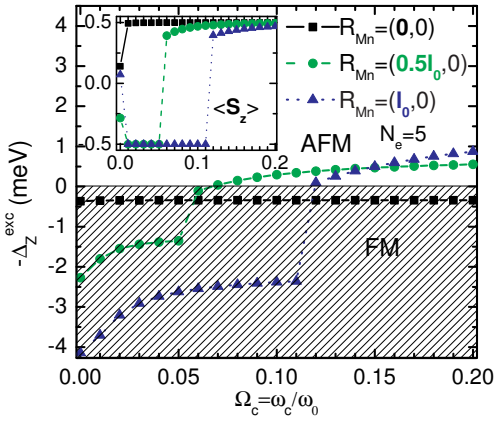

Figure 5.7: Exchange interaction of a five-electron QD with the Mn-ion located at several positions and $\lambda_C = 0.2$. The horizontal line separates the plane into FM and AFM regions. The inset shows S_z alone vs. magnetic field.

From the $N_e = 2$ result we may ask a question: whether a four-electron QD has similar properties since the number of electrons in both cases are even and one may have a situation where the total spin of the electrons is zero. Indeed, if the Mn-ion is located at the center of the QD even though for $N_e = 4$ the outer shell is half-filled, this is possible as illustrated in Fig. 5.6 where the AFM coupling occurs at $\Omega_c = 3.87$ at which the total spin of the electrons reaches the maximum value $< S_z >= 2$. In this case, the first two electrons will occupy the s-shell and the remaining two will occupy two of the five orbitals of the p and d-shells. This picture holds at small magnetic field. However, there is a big difference in the exchange energy as compared to the previous case of $N_e = 2$ when the ion is shifted away from the center of the dot, e.g. in this plot at $(0.5l_0, 0)$. The exchange energy is much larger than the result obtained for $R_{Mn} = (0, 0)$ because when the ion is out of the center of the QD, the two remaining electrons at higher orbitals have a non-zero contribution in the diagonal exchange

elements dominating the exchange energy of the ground state. This is the reason why the AFM transition occurs at smaller magnetic field ($\Omega_c = 2.5$) as compared to the case when the ion is at the center of the dot ($\Omega_c = 3.87$) although the pictures of the M_z and L_z transition in these cases are similar.

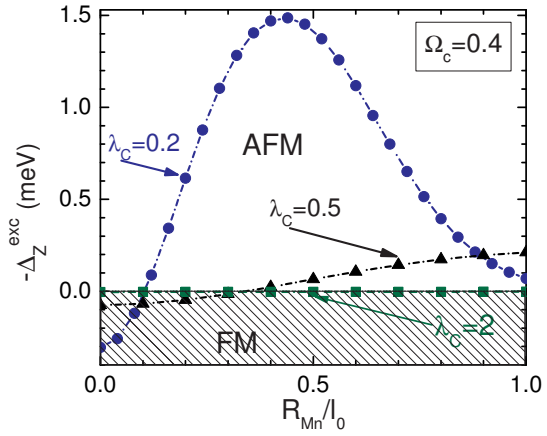

Figure 5.8: The Mn-ion position dependence of the exchange interaction of a three-electron QD for $\lambda_C = 0.2$, 0.5, and 2 at $\Omega_c = 0.4$. The horizontal dotted line at $\Delta_Z^{exc} = 0$ separates the plane into FM and AFM regions.

To complete the picture for few-electron QD system, we will discuss the AFM behavior for the system with the highest number of electrons, $N_e = 5$, where we were able to obtain accurate numerical results. We focus on the small magnetic field region (see Fig. 5.7). For the Mn-ion in the center of the dot, the FM coupling is dominant in the shown magnetic field region because the diagonal exchange matrix elements dominate over the Zeeman energies of the electrons and of the Mn-ion. This is different for the cases with the Mn-ion displaced a bit from the center of the QD. The FM-AFM occurs at $\Omega_c = 0.07$ and $\Omega_c = 0.12$ for $R_{Mn} = (0.5l_0, 0)$ and $R_{Mn} = (l_0, 0)$, respectively. It is similar to the cases for the system with $N_e = 1, 3$ due to the zero coupling between the orbitals from the p-, d-shell with the s-orbital. To observe the AFM behavior for the system with the Mn-ion located at the center of the dot where the diagonal exchange elements are almost zero, it is crucial to include enough quantum orbitals (that rapidly increases the size of the Hamiltonian matrix resulting in very time consuming calculations) so that one allows the electrons to jump to higher energy levels and having parallel spins as previously shown for the case $N_e = 4$ (see Fig. 5.6). In that

case, the four-electron system exhibits an AFM coupling with the Mn-ion at the magnetic field where the total z-projection of the spin is maximum $S_z = 2$. The system is strongly polarized. For the case $N_e = 5$, up to $\Omega_c = 0.2$, the total $S_z = 0.5$ and the total $L_z = 1$. The inset in Fig. 5.7 supports the AFM behavior for the out of center Mn as obtained in the main plot.

5.2.3 Phase diagram for the FM-AFM transition

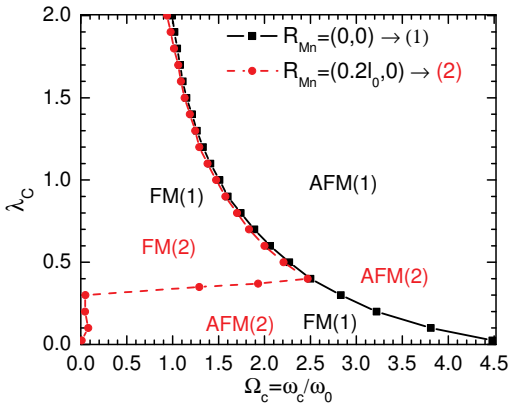

Figure 5.9: Phase diagram for the FM-AFM transition of a three-electron QD with the Mn-ion located at $(0,0)$ [black squares referred to (1)] and $(2l_0 = 5.29\mathring{A}, 0)$ [red circles referred to (2)].

Now we change λ_C and explore the magnetic behavior as function of the position of the Mn-ion. From Fig. 5.8, it is clear that when reducing the Coulomb interaction the system undergoes a FM to AFM transition at gradually larger magnetic fields for Mn^{2+} positions that are closer to the center of the dot. We see that $-\Delta_Z^{exc}$ has a peak structure with a maximum at some specific position of the magnetic ion, e.g. see the peak for the case $\lambda_C = 0.2$ (the blue full circles). However, it is certain that at high magnetic field, the system is always AFM.

The FM-AFM phase diagram for a three-electron QD in (λ_C, Ω_c) space is shown in Fig. 5.9 for two different positions of the Mn-ion. When the magnetic ion is in the center of the QD (black curve with squares in Fig. 5.9) the critical magnetic field increases as λ_C decreases. The reason is that increasing the Coulomb interaction helps the electrons to approach closer

the Mn-ion and therefore the critical magnetic field for the system to transit to the AFM phase decreases.

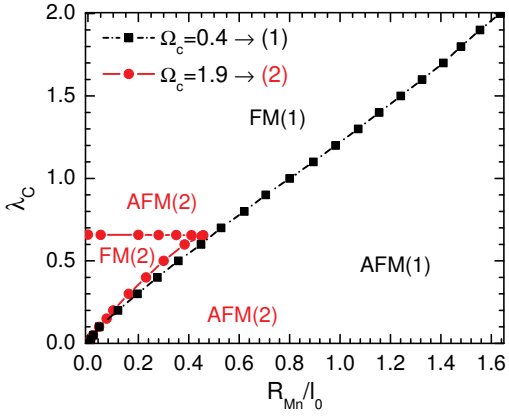

Figure 5.10: Phase diagram for FM-AFM transition of a three-electron QD in an applied field of $\Omega_c = 0.4$ [black squares referred to (1)] and $\Omega_c = 1.9$ [red circles referred to (2)].

Now we move the Mn-ion away from the center of the QD and we obtain the phase diagram as shown by the red curve (with solid circles) in Fig. 5.9. For $\lambda_C < 0.4$, the stability of the FM phase with respect to an applied magnetic field is strongly reduced and a small magnetic field turns the three-electron system into the AFM phase. Notice that for sufficient strong e-e interaction (i.e. $\lambda_C \geq 0.4$) we obtain practically the same FM-AFM phase diagram as for the case the Mn-ion is located in the center of the QD.

A remarkable re-entrant behavior is found in the region $0.3 < \lambda_C < 2$ and $0.9 < \Omega_c < 2.5$ where with increasing λ_C we go from an AFM to FM and back to AFM phase. This unusual behavior is understood as follows. As the impurity is moved away from the center of the QD the exchange matrix will have many nonzero off-diagonal terms that leads to a smaller FM-AFM critical transition magnetic field. Now let us turn our attention to the region $\lambda_C < 0.4$. For very small λ_C the electrons will repel each other only weakly and are therefore pulled towards the Mn-ion (the nonzero exchange matrix elements increase strongly) resulting in a very small FM-AFM magnetic field. For $\lambda_C \geq 0.4$, the electrons become more strongly correlated and the critical field stays about $\Delta\Omega_c \approx 0.02 \div 0.07$ from the result for $R_{Mn} = 0$. If one moves the Mn-ion further and further away from the center, the $\lambda_C \sim 0.4$ transition line moves to larger λ_C values. For

example, for $\lambda_C = 0.5$ and the Mn-ion located at $(0.5l_0, 0)$ the FM-AFM critical transition occurs at $\Omega_c = 0.08$, which is much smaller than 2.21 found for $R_{Mn} = (0.2l_0, 0)$.

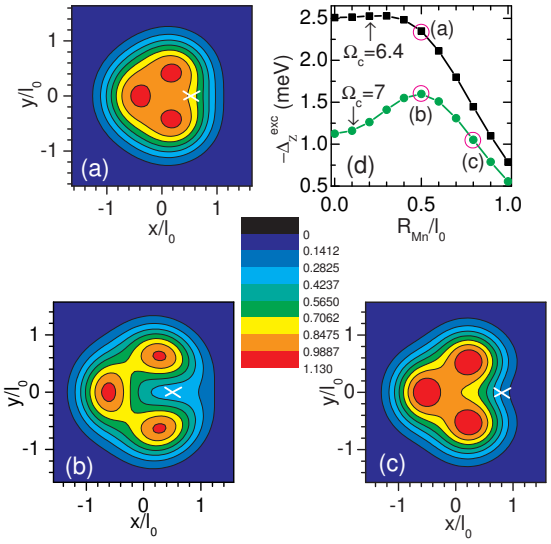

Figure 5.11: Radial density scaled by l_0^2 calculated for a three-electron QD with the Mn-ion (white cross) located at $(0.5l_0, 0)$ in (a), (b) and $(0.8l_0, 0)$ in (c) when $\lambda_C = 0.5$ in a magnetic field $\Omega_c = 6.4$ (see (a)) and $\Omega_c = 7$ (see (b) and (c)). (d) is the Mn-ion position dependence of $-\Delta_Z^{exc}$ with the magenta circles indicating the respective calculated positions of the Mn-ion in (a), (b), and (c). Red color region is for highest value of radial density.

The dependence of the FM-AFM transition of a three-electron QD system on the position of the magnetic ion is summarized in the phase diagram shown in Fig. 5.10 for two different magnetic fields $\Omega_c = 0.4, 1.9$. We can predict that with slightly larger (smaller) magnetic field the slope of the curve will be larger (smaller). From Fig. 5.9, we already learned that the FM-AFM transition magnetic field is largest for the ion in the center of the QD as is also seen in Fig. 5.10. The re-entrant behavior of the AFM phase as function of λ_C is found for small R_{Mn}/l_0 values, i.e. when the Mn-ion is not too far from the center of the QD, in case the magnetic field is not too small. The critical point $(R_{Mn}/l_0, \lambda_C)$=$(0.457, 0.656)$ for $\Omega_c = 1.9$ moves down (up) with increasing (decreasing) magnetic field.

5.2.4 Density and correlation

In high magnetic field, the Mn-ion tends to attract electrons because they are oppositely polarized. Because the exchange interaction is small as compared to the Coulomb interaction, the electrons and Mn-ion are arranged in such a way that the electrons repel each other and also try to be as close to the Mn-ion as possible. This picture holds above the FM-AFM critical magnetic field.

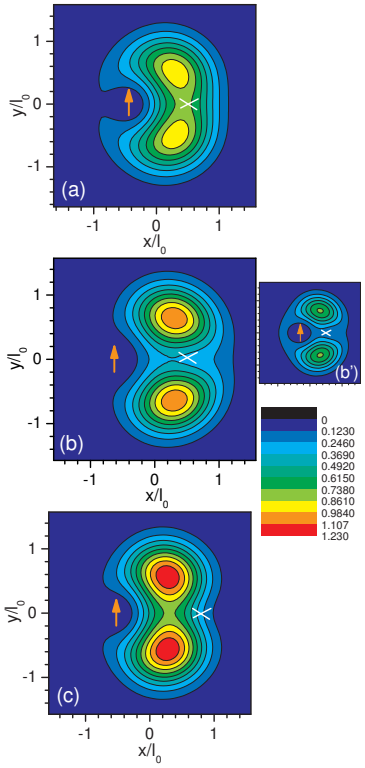

Figure 5.12: Spin up-up pair correlation functions scaled by l_0^4 calculated for the QD of Fig. 5.11 where one electron (orange arrow) is pinned at one of the three most-probable positions of the electrons as obtained in Fig. 5.11. It is at $(-0.44l_0, 0)$ in (a) for Fig. 5.11(a), $(-0.63l_0, 0)$ in (b) for Fig. 5.11(b), and $(-0.52l_0, 0)$ in (c) for Fig. 5.11(c), respectively. (b') The same correlation function for the case the position of the fixed electron is closer to the ion [at $(-0.3l_0, 0)$] as compared to (b). The position of the Mn-ion is indicated by the white cross.

To show this behavior explicitly, we studied the radial density and the

radial pair correlation functions. Their respective operators are defined as:

$$\rho(\overrightarrow{r}) = \sum_{i=1}^{N_e} \delta\left(\overrightarrow{r} - \overrightarrow{r_i}\right), \tag{5.2}$$

and

$$C_{\sigma\sigma'}(\overrightarrow{r}, \overrightarrow{r}') = \sum_{i\neq j}^{N_e} \delta_{\sigma\sigma_i}\delta\left(\overrightarrow{r} - \overrightarrow{r_i}\right)\delta_{\sigma'\sigma_j}\delta\left(\overrightarrow{r}' - \overrightarrow{r_j}\right). \tag{5.3}$$

We plot in Fig. 5.11 the radial density of a three electron QD that is polarized in high magnetic field for the case $\lambda_C = 0.5$ and the Mn-ion is located at two different positions for two magnetic fields. The electrons and the Mn-ion are AFM coupled. The strength of that coupling can be seen from Fig. 5.11(d) in which we plot the Mn-ion's position dependence of the exchange energy at two magnetic fields $\Omega_c = 6.4$, and 7. Those magnetic fields are typical in the sense that the exchange term is found to be very large ($\Omega_c = 6.4$) or the correlation between the electrons very high ($\Omega_c = 7$). Density plots are shown for R_{Mn} at $(0.5l_0, 0)$ and $(0.8l_0, 0)$. We observe three distinct peaks of maximum probability. They are found at: $(-0.44l_0, 0)$, $(0.22, 0.44)l_0$, and $(0.22, -0.44)l_0$ in Fig. 5.11(a); $(-0.63l_0, 0)$, $(0.26, 0.63)l_0$, and $(0.26, -0.63)l_0$ in Fig. 5.11(b); $(-0.52l_0, 0)$, $(0.26, 0.52)l_0$, and $(0.26, -0.52)l_0$ in Fig. 5.11(c). These figures show clearly the interplay effect where the three electrons on the one hand try to be close to the Mn-ion and on the other hand repel each other via the Coulomb potential energy. It results in the merging of the radial density such that the higher the exchange energy the larger the merging of the local maxima in the electron density and the smaller the correlations. Fig. 5.11(d) gives an idea about the variation of $-\Delta_Z^{exc}$ with the position of the Mn-ion and reaches a maximum at $(0.5l_0, 0)$ for $\Omega_c = 7$. In Fig. 5.11(c), the three electrons are less attracted to the Mn-ion via the AFM coupling as compared to that in Fig. 5.11(b). This is due to the fact that the $-\Delta_Z^{exc}$ for the case shown in Fig. 5.11(b) is larger than that in Fig. 5.11(c). The electrons are therefore found more correlated in the latter case presented by the extended red region in Fig. 5.11(c). Thereby, correlation between electrons in Fig. 5.11(c) is expected to be the highest and in Fig. 5.11(a) the smallest.

The position of the Mn-ion affects the ground-state property as is made clear in Fig. 5.12. We fix the spin state and the position of one electron (indicated by the orange arrow) and the position of the Mn-ion (the white cross). The magnetic field is such that $\Omega_c = 6.4$ in Fig. 5.12(a) and $\Omega_c = 7$ in the others. It also reflects the fact that the system in Fig. 5.11(a) exhibits

the smallest correlation as compared to the other two. This illustrates the point raised above about the density. At the magnetic field $\Omega_c = 7$, the electrons are strongly polarized resulting in the red regions of the up-up spin pair correlation function that tends to surround the Mn-ion. We see that the three electrons are most likely to localize around some specific positions defining a triangle with the three electrons at the three vertices, while they are attracted to the Mn-ion. When we locate one electron at a position closer to the Mn-ion, see Fig. 5.12(b'), the two peaks decrease in amplitude as compared to those in Fig. 5.12(b).

5.2.5 Addition energy

The addition energy (often called the chemical potential) is defined as the increase of the energy of the QD system when an electron is added: $\mu_{N_e} = E_{GS}(N_e) - E_{GS}(N_e - 1)$. This quantity can be measured experimentally and is plotted in Fig. 5.13 as function of the magnetic field.

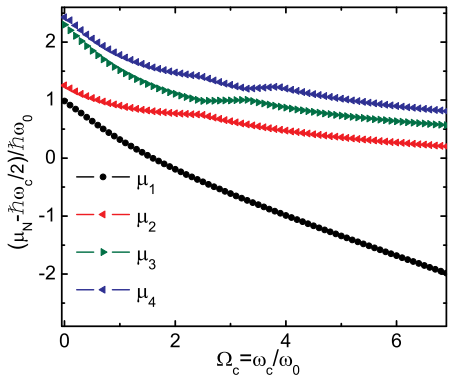

Figure 5.13: Addition energy for different number of electrons. The Mn-ion is located at $(0.41l_0, 0)$ and $\lambda_C = 0.2$.

There are several cusps appearing in the addition energy curves as a consequence of changes in the ground state. These changes are due to variations in the z-projection of the total spin of the electrons and/or the z-projection of the total angular momentum of the system when the magnetic field increases beyond some specific values. The presence of the Mn-ion leads to more cusps and the position of these cusps is also influenced by the number of electrons and the position of the Mn-ion. The cusps are from either of the two systems in the study. For instance, the green triangles in Fig. 5.13

are for $\mu_3 = E_{GS}(N_e = 3) - E_{GS}(N_e = 2)$ has two cusps at $\Omega_c = 2.6$ and $\Omega_c = 3.4$. The cusp at the point $\Omega_c = 2.6$ comes from the change in the configuration of the average of the total z-projection spin and the total z-projection of angular momentum (S_z, L_z) of the two-electrons in the QD from (0,0) to (1,1). While the other cusp $\Omega_c = 3.4$ comes from the change of the phase of the three-electron QD from $(0.5, 1)$ to $(1.5, 3)$. It is similar to the case for μ_4 (the blue left pointing triangles) where the cusp appears at $\Omega_c = 3.4$. At this point, we observed a change from configuration $(0, 2)$ to $(1, 3)$. The remaining one, $\Omega_c = 3.9$, is from the four-electron case when its configuration changes from $(1, 3)$ to $(2, 6)$.

5.2.6 Vortex structure: many-body correlations

Another way to obtain information on the correlations that are present in the many-particle wave function is to investigate the vortex structure. At a vortex the many-body wave function is zero and is characterized by a change of phase of 2π when we go around this point.

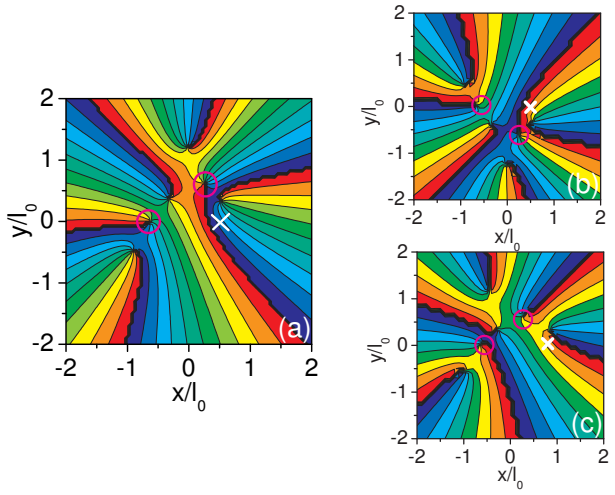

Figure 5.14: Contour plot for the phase of the reduced wave function of a three-electron QD in magnetic field $\Omega_c = 11$ with the Mn-ion (the white cross) located at $(0.5l_0, 0)$ in (a),(b) and at $(0.8l_0, 0)$ in (c) for $\lambda_C = 0.5$. Two fixed electrons (indicated by the two magenta circles) are located at the two peaks appearing in the radial density: $(-0.63l_0, 0)$ and $(0.26, 0.63)l_0$ in (a), (c); and $(-0.63l_0, 0)$ and $(0.26, -0.63)l_0$ in (b).

The zeros of the wave function are similar to flux quanta when e.g.

the wave function corresponds to the order parameter in a superconductor. The fixed electrons and the zero of the wave function follows closely the displaced electron and one may say that the electron plus its zero form a composite-fermion object. The composite-fermion [132, 153, 160, 161] (and references therein) is a collective quasi-particle that consists of one electron bound to an even number of vortices (flux quanta). The composite-fermion concept introduces a new type of quasi-particle that is used to understand the fractional quantum Hall effect in terms of the integer quantum Hall effect of these composite fermions.

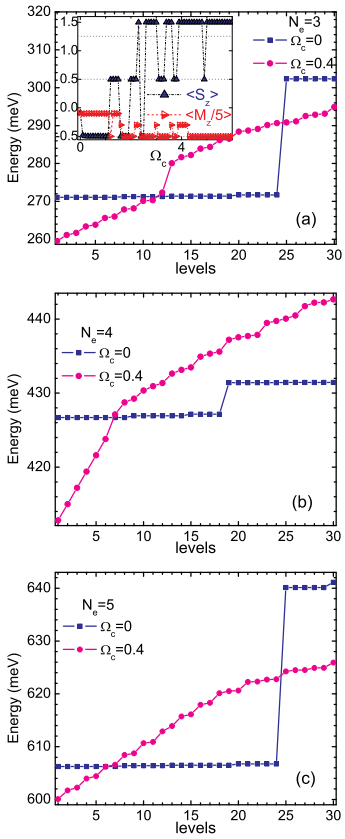

Figure 5.15: The energy spectrum of the first 30 levels of the three- (the top), four- (the middle), and five- (the bottom) electron QD with the Mn-ion located at $(0.5l_0, 0)$. The Coulomb strength is $\lambda_C = 0.5$ with magnetic fields $\Omega_c = 0.0$ (the blue squares) and $\Omega_c = 0.4$ (the magenta circles). The inset in the top figure shows the average of M_z (the dark-blue triangles) and S_z (the red triangles) as a function of Ω_c of the sixth energy level.

To obtain the zeros of the wave function of the system with N_e electrons, we fix N_e-1 electrons at some positions inside the QD and leave the remaining one free. The resulting reduced wave function gives the probability to find the remaining electrons at different positions in the QD and the zeros' of this function are those points where the phase of the wave function changes by 2π. As an example, we investigate the situation of a three-electron QD.

Figs. 5.14 shows the vortex pictures of a three-electron QD containing a Mn-ion located at positions (see the white cross) that are identical to its positions in Fig. 5.11(a). Two, among three, electrons are fixed at the respective peaks in the electron density. Red and black regions are referring to the highest (2π) and lowest phase 0, respectively. Those plots show that there are always two vortices near the pinned electrons' positions. For example, the number of vortices pinned to each electron in the case $N_e = 3$ at $\Omega_c = 11$ is 2 describing the system at filling factor $\nu = \frac{N_e(N_e-1)}{2<L_z>} \approx 1/3$. Notice also that one of the vortices appears to be pinned at a position very close to the Mn ion.

We realize that moving the Mn-ion to a different position changes the relative positions of the vortices that are pinned to the electrons with respect to one another, as shown in Figs. 5.14(a) and (c). As the electrons are AFM coupling to the Mn-ion this kind of movement consequently depends on the position of the Mn-ion.

In the case $\lambda_C = 0.5$, we found that the average of the maximum z-projection of the total angular momentum is $< L_z >= 9$ and the two vortices appear at the external field $\Omega_c = 3.0$. Apparently, the larger λ_C the smaller Ω_c for which the first two vortices appear at the pinned electrons.

5.3 Energy spectrum

In the presence of an external magnetic field, the many-fold degeneracy of the energy spectrum of the system is lifted. Fig. 5.15(a) illustrates that point for the case of three electrons. In the absence of the interaction between the electrons and the Mn-ion and in the absence of a magnetic field (blue squares), the energy spectrum is 7-fold degenerate for the first 7 lowest energy levels, the next level is then 5-fold degenerate, and the next 7-fold degenerate, and so on. The origin of this was explained in Ref. [82] and is due to the coupling of the electrons and the Mn-ion. When the magnetic field is different from zero, see red circles in Fig. 5.15, the degeneracy is lifted. In the inset of Fig. 5.15 we plot $< M_z >$ (the magenta triangles) and $< S_z >$ (the dark-blue ones) as a function of magnetic field for the sixth

level. The average of $< M_z >$ and $< S_z >$ change abruptly as compared to those found for the ground-state energy, e.g. see Fig. 5.2. M_z and $< S_z >$ of the sixth state jump between two different values, e.g. -1.5 and -2.5 for $< M_z >$ and 0.5 and 1.5 for $< S_z >$ as function of the field. This is a consequence of anti-crossings of energy levels as will be apparent later. The result for four- and five-electron QDs are also shown in Fig. 5.15. We see the degeneracy of 8, 6, 4, and 12 for the first 30 levels in the case $N_e = 4$ and of 7, 5, 7, 5, 5, and level 30 has the same degeneracy with the next energy level beyond the first 30 for the case $N_e = 5$ in $B = 0$ T.

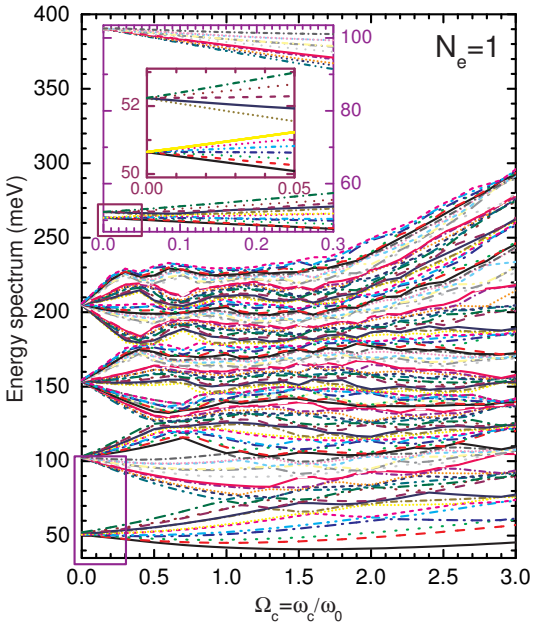

Figure 5.16: The magnetic field dependence of the energy spectrum (the first 120 levels are shown) of the one-electron QD with the Mn-ion located at $(0.5l_0, 0)$ and $\lambda_C = 0.5$ (the inset is a zoom of the first 24 levels at low magnetic fields and the inset in the inset shows the first 12 levels, it is a zoom of the rectangular region.

To have a clearer picture of the energy spectrum of the QD system we plot in Figs. 5.16, 5.17, and 5.18 the magnetic field dependence of the first 120 energy levels for $N_e = 1, 2, 3$, respectively. The spectra at small magnetic fields is enlarged (see insets) to see the Zeeman splitting and the nearly-linear behavior of the energy levels. Remember that this is due to

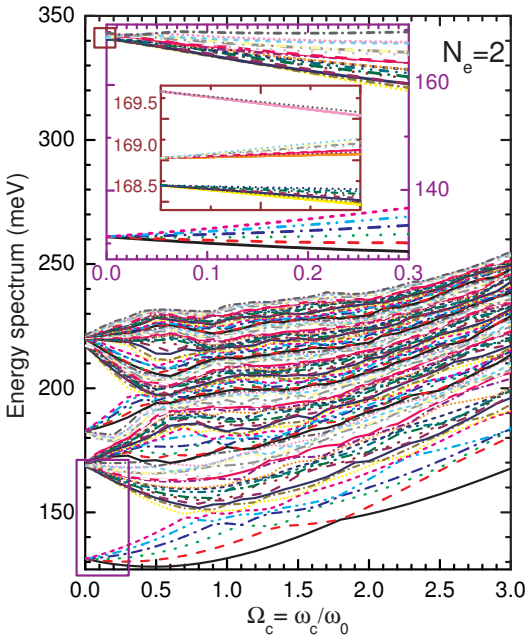

Figure 5.17: The same as Fig. 5.16 but now for the two-electron QD. The inset in the inset is a zoom of levels 7th to 24th for magnetic field close to zero.

the coupling of the electron spins with the Mn-ion spin. For $N_e = 1$ the first two levels for $B = 0$ are 7- and 5-fold degenerate (7-fold degenerate is due to the FM coupling of the s-shell electron spin 1/2 with the Mn-ion spin 5/2 and 5-fold degenerate of that electron now with spin $-1/2$ to the Mn-ion with spin 5/2), respectively. A closer inspection (see Fig. 5.16) tells us that these 12-levels are exchange split into two bundles of 7- and 5-levels (the inset in the inset in Fig. 5.16). Notice that there is a first large energy gap at very small fields between the first 12 levels and the next 24 ones as seen in Fig. 5.16 while that kind of gap appears between the first 6 and the next 36 for $N_e = 2$ (Fig. 5.17). For $N_e = 3$ (Fig. 5.18), this kind of gap appears after the first 24 energy levels. The origin is the coupling of the third electron, which can reside at either two states of the p-shell while the s-shell is already fully filled, with the magnetic ion with 6 z-components of the spin at very small fields, i.e. the intra-shell (p) exchange interaction. For $N_e = 2$ the electron ground state corresponds with a filled s-shell, i.e. $< S_z >= 0$, and therefor for $B = 0$ only a 6-fold degeneracy, as shown in Fig. 5.17, is found due to the z-component of the Mn-spin. The next level is 8-fold degenerate at $B = 0$ (8 come from the FM coupling of the

two-electron system with total spin 1 to the Mn-ion with spin 5/2) (see the inset in the inset in Fig. 5.17), etc.

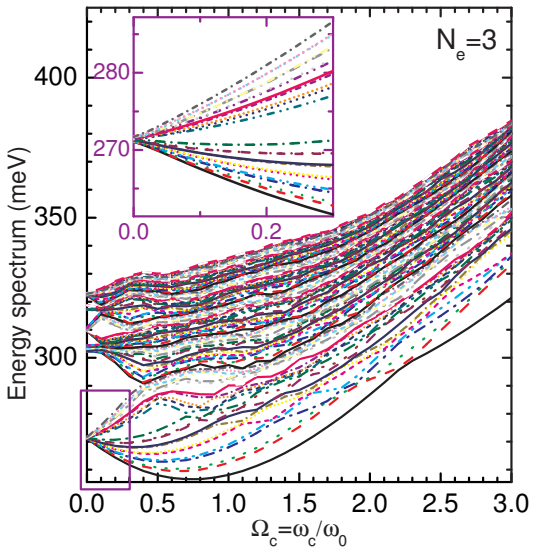

Figure 5.18: The same as Fig. 5.16 but now for the three-electron QD.

With increasing magnetic field, we see that for $N_e = 1$ there is periodically an opening of energy gaps in the spectrum. Similar energy gaps have been found earlier (as an example see e.g Ref. [108]) for a QD without a Mn-ion and are a consequence of the electron with two-fold spin degeneracy filling the equally-gaped-energy single-particle quantum states with different sets of the radial and angular quantum numbers. Notice that for $N_e = 2, 3$, these gaps have disappeared.

The spectra exhibit a lot of crossings and anti-crossings, the number of them has increased as compared to the QD case without a Mn-ion because of the Zeeman splitting of the Mn-spin. When the applied field increases the gaps in the spectrum of $N_e = 1$ are still open and appear more often than in the cases of $N_e = 2, 3$. Once again, we see a lot of cusps in the energy levels and that reminds us to abrupt changes in the configuration of the system with magnetic field as discussed before for the ground state.

5.4 Thermodynamic properties

5.4.1 Magnetization and susceptibility

We first calculate the magnetization and susceptibility of the system: $M = -\partial E_{GS}/\partial B$ and $\chi = \partial M/\partial B$ at zero temperature.

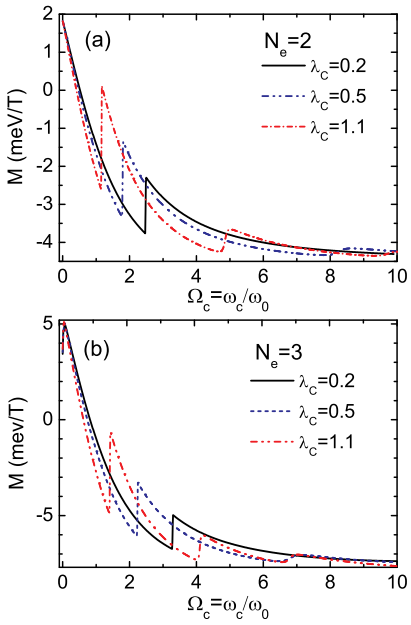

Figure 5.19: Magnetization of the ground state of the two- and three-electron QD with the magnetic ion located at $(0.5l_0, 0)$ for three values of the Coulomb strength $\lambda_C = 0.2$, 0.5, and 1.1.

The magnetization of a QD with the Mn-ion located at $(0.5l_0, 0)$ with $N_e = 2, 3$ electrons is plotted in Fig. 5.19. We see several jumps that are a consequence of changes in the ground state, e.g. changes in $< L_z >$ (see previous section). For example, the magnetization of the three-electron QD as plotted in Fig. 5.19(b) for the case $\lambda_C = 0.2$ and the Mn-ion at $(0.5l_0, 0)$ has a step at $\Omega_c = 3.3$. Consequently, the susceptibility also has a peak at $\Omega_c = 3.3$. The same thing happens at $\Omega_c = 1.4, 4.1$, and 6.8 for $\lambda_C = 1.1$ in the magnetization and the susceptibility.

For non-zero temperature, the temperature dependence of the magnetization and susceptibility is defined by: $M(T) = -\partial\langle E(T)\rangle/\partial B$, $\chi(T) =$

$\partial M(T)/\partial B$, respectively. The statistical average $< E(T) >$ is calculated as:

$$\langle E\left(\lambda_C, T, R_{Mn}\right)\rangle = \frac{\sum_{\alpha=1}^{N_\alpha} E_\alpha e^{-E_\alpha/k_B T}}{\sum_{\alpha=1}^{N_\alpha} e^{-E_\alpha/k_B T}}, \tag{5.4}$$

where the sum is over the energy levels as displayed in e.g. Fig. 5.15.

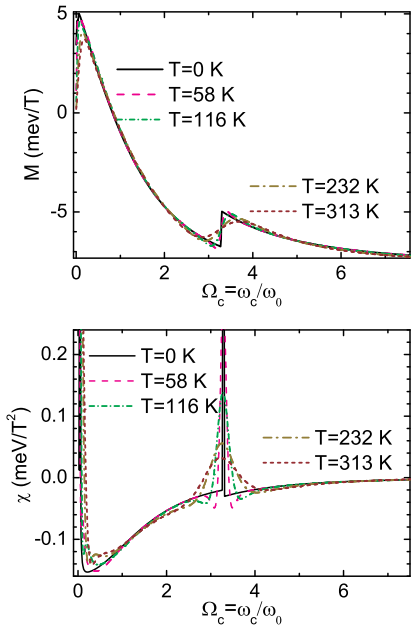

Figure 5.20: Temperature dependence of the magnetization and susceptibility for a three-electron QD with the Mn-ion located at $(0.5l_0, 0)$ and $\lambda_C = 0.2$.

These quantities are explored in Figs. 5.20 for $N_e = 3$ and a few different temperatures (including the zero temperature case). With increasing temperature the jumps become smoother. A very low magnetic field peak shows up because for $T \neq 0$ we have $M \approx 0$ at $\Omega_c = 0$.

5.4.2 Heat capacity

An important quantity that is related to the storage of energy is the heat capacity:

$$C_V\left(\lambda_C, T, R_{Mn}\right) = \frac{\partial\langle E\left(\lambda_C, T, R_{Mn}\right)\rangle}{\partial T} \tag{5.5}$$

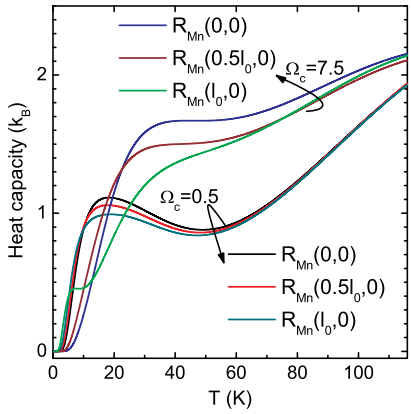

Figure 5.21: The heat capacity vs temperature of a three-electron QD with the Mn-ion located at three different positions for $\lambda_C = 1.0$ and $\Omega_c = 0.5$ (the three lower curves) and 7.5 (the three upper curves).

The heat capacity is investigated as a function of the Coulomb strength λ_C, temperature T, magnetic field, and the position of the Mn-ion R_{Mn}.

We plot in Fig. 5.21 the specific heat for two values of the magnetic field, i.e. $\Omega_c = 0.5$ and $\Omega_c = 7.5$, and three typical positions of the Mn-ion. For weak fields, the three electrons start to polarize and we see that the position of the main peak moves towards higher temperature as the Mn-ion is moved away but not too far from the center of the dot. For the high magnetic field case the three electrons are strongly polarized and we see a different behavior in the shift of the main peak. This results from the change of the statistical average of the energy levels at different fields.

Now we examine the behavior of the heat capacity at a specific temperature as function of magnetic field. Figs. 5.22 and 5.23 are the plots of the magnetic field dependence of the heat capacity of three (at two Coulomb interaction regimes) at some specific temperatures and two different $\lambda_C = 0.2, 0.5$. The peak at small magnetic fields broadens and moves to higher fields with increasing temperature. The heat capacity exhibits a number of peaks and a clear minimum around e.g. $\Omega_c = 3.4$ as shown in Figs. 5.22. Remember that this field corresponds to a cusp in the energy versus magnetic field behavior as discussed previously in the subsection 5.2.1. At very low temperatures, this cusp still affects the heat capacity through the sharpness of the minimum as shown in the figure and this gradually becomes small at high temperatures. In Fig. 5.23, we see a very interesting behavior of the heat capacity at $\Omega_c \approx 2.3$: the single peak becomes a double

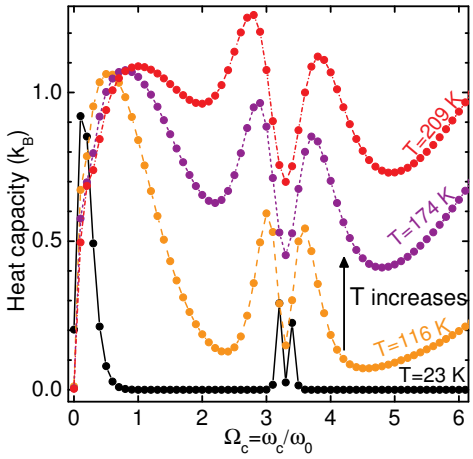

Figure 5.22: The heat capacity vs magnetic field of a three-electron QD with the Mn-ion located at $(0.41l_0, 0)$, $\lambda_C = 0.2$, at several temperatures: 23, 116, 174 and 209 K.

peak as temperature increases from $T = 5.8$ to $T = 11.6K$. This is due to the cusps now occurring around this field in the low-energy levels of the spectrum of the three-electron QD system as observed in Fig. 5.18. Besides, the structure of the heat capacity is more complex (more peaks) with increasing λ_C. This is made clear if one looks back to the previous discussion related to Figs. 5.1 and 5.2(a).

Temperature affects the heat capacity of the system in the sense that it increases the peak values and separates them in magnetic field.

The Coulomb interaction strength changes the structure of the magnetic field dependence of the heat capacity and is illusive through Figs. 5.22 and 5.23. The peak of the heat capacity for the case with smaller Coulomb interaction strength appears at higher magnetic field as compared to the case with larger one.

5.5 Conclusion

Due to the presence of the Mn-ion (and e-e interaction), electrons in the ground state do not always completely polarize in the presence of an external magnetic field. The configurations are mixed consisting of electrons having spins up and down. But for very large magnetic field, the Mn-ion tends

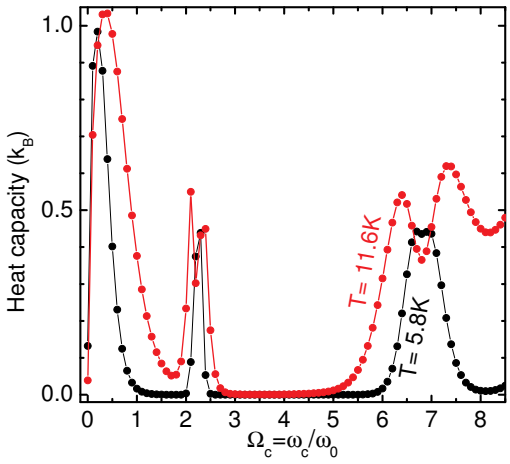

Figure 5.23: The heat capacity vs magnetic field of a three-electron QD with the Mn-ion located at $(0.5l_0, 0)$, $\lambda_C = 0.5$, and the temperatures are $5.8K$ and $11.6K$.

to pull the electrons closer to the ion forming a ring-like electron density profile. These are the consequences of the interplay of several effects such as the Zeeman effect (on the electrons' and the Mn-ion's spins), the Coulomb repulsion, the spin exchange interaction, etc. This competition results in a crossover from FM to AFM coupling between the electrons and the Mn-ion at some specific magnetic field. Interestingly, this effect is observed to appear at higher magnetic field when we move the Mn-ion further from the origin of the QD. A re-entrant behavior of the FM-AFM transition is found as function of the Coulomb interaction strength λ_C when the Mn-ion is moved out (but not too far) from the center of the QD.

The energy levels exhibit cusps as function of the magnetic field which correspond to changes of the configuration of the system as expressed by the values of $(< S_z >, < L_z >)$. These cusps move to lower magnetic field with increasing λ_C. The number of cusps increases with increasing number of electrons. These cusps show up in the addition energy.

The transformation of the electron system to those of composite fermions is studied. In high magnetic fields, the electrons attach an even number of quantized vortices which we made clear by examining the many-body ground-state wave function in the presence of a Mn-ion. Unlike the case without a Mn-ion where all the vortices are tightly bound to the electrons, when we fix the electrons at different positions the system of vortices stays

pinned to the electrons and moves with the electrons but the relative positions of the vortices are modified.

The contribution of the local Zeeman splitting energy to the total energy of the system in large external fields is very small as compared to the contributions from the other parts. However, a slight movement of the position of the Mn-ion inside the QD affects the result, slightly.

With increasing applied magnetic field, each time the system jumps to a different ($< L_z >, < S_z >$) configuration leads to the appearance of a peak in the thermodynamic quantities as e.g. the susceptibility and the heat capacity. In the presence of the Mn-ion, the structure of peaks in the heat capacity changes with the position of the Mn-ion. As temperature increases, these peaks split into two peaks and become smoother.

6

FIR absorption energy spectrum of few-electron quantum dots doped with a single magnetic impurity

Intraband cyclotron resonance (CR) transitions of a few-electron quantum dot containing a single magnetic ion is investigated for different Coulomb interaction strengths and different positions of the magnetic ion. In contrast to the usual parabolic quantum dots where CR is independent of the number of electrons, we found here that due to the presence of the magnetic ion Kohn's theorem no longer holds and CR is different for systems with different number of electrons and different effective electron-electron Coulomb interaction strength. Many-body effects result in shifts in the transition energies and change the number of CR lines. The position of the magnetic ion inside the quantum dot affects the structure of the CR spectrum by changing the position and the number of crossings and anti-crossings in the transition energies and oscillator strengths.

6.1 Introduction.

Cyclotron resonance (CR) has been an important experimental technique to investigate the properties of electrons (and holes). The advantage is that CR transitions involve only one type of carriers (electrons or holes) facilitating the interpretation of the results. CR is also often used to obtain information on the effective mass of the carriers.

CR has been studied in bulk semiconductors [177] and later on also in

The results presented in this chapter were published as:

- N. T. T. Nguyen and F. M. Peeters, Phys. Rev. B **78**, 245311 (2008).
- N. T. T. Nguyen and F. M. Peeters, Phys. Rev. B **80**, 115335 (2009).

semiconductor QDs [178, 179, 180, 181] where it was shown that in parabolic confined QDs Kohn's theorem still holds and thus the CR-transitions are independent of the number of electrons. The latter is no longer true if the confinement potential is non-parabolic [180] or when the carriers obey a non-parabolic energy spectrum.

Very recently [89], the intra-band optical properties of a 3D single-electron CdTe/ZnTe QD containing one or two Mn impurities confined by a potential that is parabolic in the xy-plane and has the quantum-well confinement along the z-axis was investigated. New absorption lines (mixing with the lines to higher excited levels for quantum-well system - as for example see Ref. [180] for studies of CR in quantum well system without a Mn-ion) were predicted as well as crossings and anti-crossings of allowed CR transitions as function of an external magnetic field.

In this chapter, we calculate the single-particle states of a quasi-2D parabolic QD in the presence of a single Mn-ion and an external perpendicular magnetic field. We investigate the allowed CR transitions and their corresponding oscillator strength (OS). We have in mind experimental realized systems [i.e. Cd(Mn)Te] where the lateral size is much larger than the height of the QD and consequently the system behaves like a quasi-2D QD. As in Ref. [89] we find new resonant transitions due to the electron-Mn spin-spin exchange interaction but we also investigate these transitions as function of the position of the Mn-ion in the QD. We find crossing and anti-crossing features that depend on the position of the Mn-ion in the QD and on the strength of the confinement potential. We will focus on the allowed transitions and concentrate on the new CR lines that become possible due to the presence of the Mn-ion. Due to the presence of the Mn-ion the electron spin will not always be parallel to the external magnetic field. It will together with the Mn-ion define two kinds of relative orientation of their spins called ferromagnetic (FM) and antiferromagnetic (AFM). The FM-AFM transition can be influenced by changing the exchange interaction parameters which we will realize by moving the Mn-ion to different positions. We show that this can change the position and the number of crossing and anti-crossing points and consequently influence the CR lines. We find that the CR transitions now contain information not only on the electron state but also on the magnetic-ion-electron interaction and the magnetic state of the Mn-ion.

Magnetic-optical properties of nonmagnetic few-electron QDs were investigated in e.g. Refs. [177, 178, 180, 181, 182, 183]. It was found theoretically [177, 181] and experimentally [178] that the optical cyclotron resonance energies in the case of quadratic confining potentials are independent of the

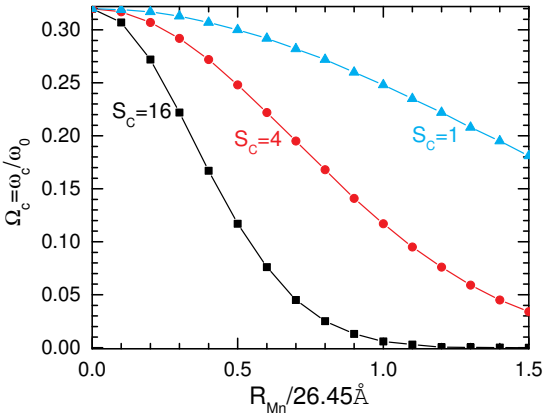

Figure 6.1: Phase diagram $\Omega_C - R_{Mn}$ plotted for three different S_C. The region below (above) the line corresponds each time to the ferromagnetic (antiferromagnetic) phase, respectively.

number of electrons. In other words, the electron-electron (e-e) interaction does not result in any observable changes in the far-infrared (FIR) spectrum for different N_e-electron systems. This theorem is no longer valid in the presence of impurities as found experimentally [185] and theoretically [178, 179].

A 2D few-particle circular parabolic QD was considered as a model system to study e.g. the pair Coulomb interaction effect [149, 184]. Here we will use this model to examine the effect of the e-e interaction on the intraband absorption spectrum of a two-electron QD containing a single Mn-ion. Detailed studies of the FIR spectra in the case without a Mn-ion were done for QD molecules [183] containing few electrons in which the e-e interaction leads to small shifts in the peak position of the CR spectrum.

6.2 FIR of a single-electron quantum dot

6.2.1 Energy spectrum

We introduce a dimensionless parameter $S_C = (a_B^*/l_0)^2$ called the confinement strength (square comes from the fact that $\omega_0 \sim 1/l_0^2$). In a many-electron system $S_C = 1/\lambda_C^2$ with $\lambda_C = l_0/a_B^*$ the Coulomb interaction strength [83].

The presence of the Mn-ion leads to different arrangements of the spins

of the electron and the Mn-ion depending on the strength of the magnetic field. This is due to the interplay between on the one hand the contributions of the Zeeman energies of the electron and the Mn-ion and on the other hand the exchange interaction, both depend on the magnetic field. Two different arrangements of the spins of the electron and the Mn-ion are possible: ferromagnetic and antiferromagnetic. The ferromagnetic arrangement is found for very small magnetic field when the exchange energy dominates over the Zeeman energy terms. In the reverse case the AFM arrangement of electron and Mn-ion spins is found. As illustrated in Fig. 6.1, the ferromagnetic - antiferromagnetic (FM-AFM) phase transition line depends also on the position of the Mn-ion. Note that in nonzero magnetic field, the Mn-ion is always antiparallel to the magnetic field due to the positive value of its g-factor.

When the Mn-ion is located at the center of the dot the FM-AFM transition occurs at the same magnetic field for any value of the confinement strength S_C as is made clear in Fig. 6.1. The e-Mn exchange energy is maximal for a Mn-ion situated in the center of the QD. Note that in one-electron system, the electron density is maximum at the center of the dot and the electron is found in the s-shell where the J_c matrix element is also found to be maximum at the center of the dot. Moving the Mn-ion out of the center of the QD will decrease this e-Mn exchange interaction. The electron probability at the Mn-ion is now a strong function of S_C. With decreasing e-Mn exchange energy (i.e. by moving the Mn-ion out the center of the QD or increasing the confinement) a smaller external magnetic field is needed to induce the FM-AFM transition, as can be seen from Fig. 6.1.

In the presence of the exchange energy the ground state (GS) consists of contributions from different configurations of (s_z, M_z). The electron is still found in the s-shell even at very high magnetic field. Unlike the system without a Mn-ion where the spin of the electron always orients parallel to the magnetic field, the system containing a Mn-ion has a wave function containing contributions from states where the electron is antiparallel to the magnetic field. This leads to an attraction to the Mn-ion and reduces the total energy.

When a Mn-ion is placed inside the QD the energy spectrum is modified to the one given in Fig. 6.2 which shows the results in the case the Mn-ion is situated at the center [Fig. 6.2(a)] and at $(0.5l_0, 0)$ [Fig. 6.2(b)] inside the QD. Note that now each $B = 0$ energy level is split into many different levels having different Zeeman splitting. There are also many more crossings and anti-crossings and periodic opening of energy gaps in the spectra. The position and the number of energy gaps, and consequently the crossing and

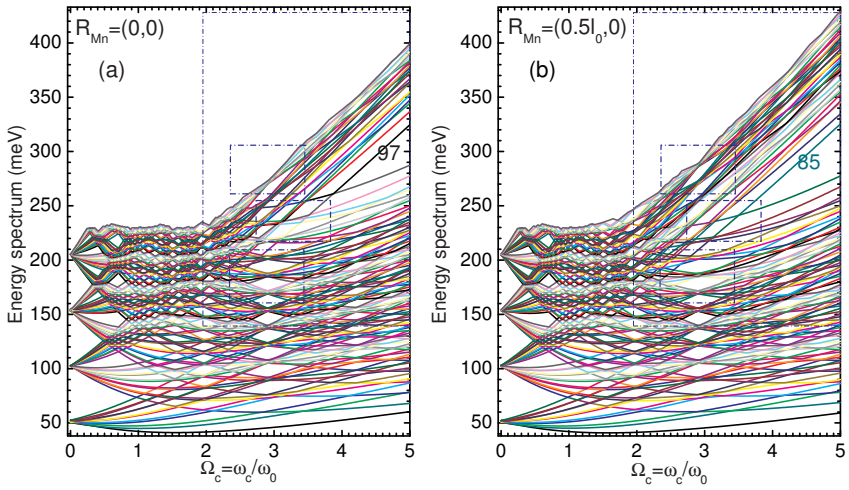

Figure 6.2: First 120 levels of the energy spectrum of a single-electron QD with the magnetic ion located at the center (a) and at $(0.5l_0, 0)$ (b) of the QD for confinement strength $S_C = 4$. The colors that match the corresponding energy levels are kept the same in the two plots. The blue dash-dotted boxes highlight the regions where both figures exhibit the largest difference.

anti-crossing points, depend on the position of the Mn-ion as can be seen in Fig. 6.2 in particular the regions inside the blue boxes. We explicitly refer to energy levels 85 [Fig. 6.2(a)] and 97 [Fig. 6.2(b)] to highlight the differences in the energy spectrum. When changing the position of the Mn-ion we find that some of the crossing points turn into anti-crossing points and at some of the anti-crossings the size of the energy gap increases. That will be shown and discussed in the following section.

The $B = 0$ ground state and the first excited level is split into, respectively, 7 and 5 levels because it is composed of $s_z = \pm 1/2$ and $M_z = \pm 5/2, \pm 3/2, \pm 1/2$ spin states. The next $B = 0$ level is the p-electron state and because the electron orbital momentum is 1 this level splits into 24 levels. Note that for small magnetic fields, the states whose wave function have the $(0, 1)$ or the $(0, -1)$ FD states as their largest contribution stay lower in energy as compared to e.g. the states whose wave function have $(0, 2)$ or $(1, 0)$ etc as the largest contribution. However, as the magnetic field increases, there are changes in relative position of the energy levels, i.e. whose wave function has $(0, -1)$ as the largest contribution will now be higher in energy than e.g. the state which has $(0, 2)$ as the major contributing FD

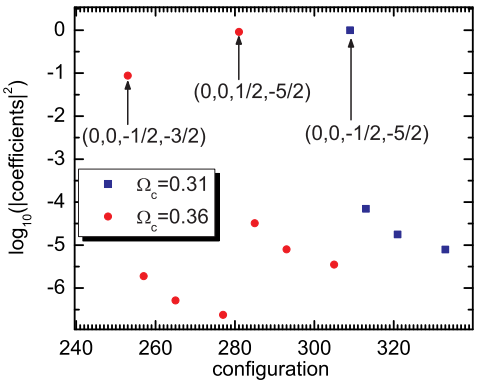

Figure 6.3: Contributions to the GS wave function from the different FD states (x-axis) in case of the QD of Fig. 6.2(a) for two different magnetic fields: $\Omega_c = 0.31$ (FM) and $\Omega_c = 0.36$ (AFM).

state.

The presence of the Mn-ion leads to a mixing of the FD orbitals for the different eigenstates in contrast to the QD without a Mn-ion where those FD orbitals are the eigenstates of the dot. We show in Fig. 6.3 the contribution of the different FD states to the wave function of the GS for two different values of the magnetic field: $\Omega_c = 0.31, 0.36$. N_c configurations that were defined in Sec. II are the x-axis. The configurations that contribute more than 1% are indicated by four quantum numbers (n, l, s_z, M_z). At $\Omega_c = 0.31$ where the system is in the FM phase, the GS wave function has the FD state (0,0,-1/2,-5/2) as the largest contribution while at AFM magnetic field $\Omega_c = 0.36$ the two states $(0, 0, -1/2, -3/2)$ and $(0, 0, 1/2, -5/2)$ give the dominant contribution.

6.2.2 Cyclotron transitions and oscillator strength

In a CR experiment, an electron in quantum state $i = (n, l)$ with energy E_i is excited to a higher energy state E_j $[j = (n', l')]$ with transition amplitude A_{ij}, the associated oscillator strength (OS) for circular polarized light is [180]:

$$f_{ij} = \frac{2\Delta E_{ij}}{\hbar\omega_H} \cdot \frac{|A_{ij}|^2}{l_H^2}, \tag{6.1}$$

where

$$A_{ij} = < \Psi_i(\overrightarrow{x^*}, \overrightarrow{M})|re^{\pm i\theta}|\Psi_j(\overrightarrow{x^*}, \overrightarrow{M}) > . \tag{6.2}$$

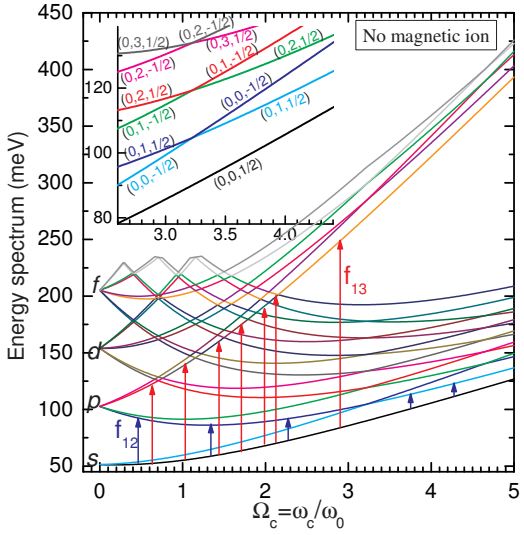

Figure 6.4: First 20 levels (up to the f-shell) of the energy spectrum of a one-electron QD without a Mn-ion. The inset is a magnification of the region $2.6 < \Omega_c < 4.4$ that clarifies the CR-transitions of the electron from the GS $(0, 0, 1/2)$ to either of $(0, 1, 1/2)$ and $(0, -1, 1/2)$ with OS f_{12} (blue) and f_{13} (red), respectively. The energy levels are indicated by their quantum numbers (n, l, s_z). The allowed transitions are indicated by the blue and red arrow.

The $\pm$ sign refers to right and left circular polarized light. $\Delta E_{ij} = E_j - E_i$ is the transition energy. It is clear that the state of the Mn-ion is not altered during such a transition. The electron transition fulfills the selection rules: $\Delta l = l' - l = \pm 1$; $\Delta s_z = 0$; and $\Delta M_z = 0$.

A general form for the wave function of state i is:

$$\Psi_i(\overrightarrow{x^*}, \overrightarrow{M}) = \sum_{\alpha}^{N_c} C_\alpha \Psi_{i\alpha}(\overrightarrow{x^*}, \overrightarrow{M}), \tag{6.3}$$

where $\Psi_{i\alpha}(\overrightarrow{x^*}, \overrightarrow{M})$ is the single-electron FD solution in the presence of the Mn-ion defined via Eq. (3.9). Now we calculate A_{ij} by integrating Eq. (6.2) over $\overrightarrow{r}$. The final expression for A_{ij} can be written as:

$$A_{ij} = \sum_{\alpha}^{N_c} \sum_{\beta}^{N_c} C_\alpha^* C_\beta \delta_{s_{z\alpha} s_{z\beta}} \delta_{M_{z\alpha} M_{z\beta}} A_{ij}^{\alpha\beta}, \tag{6.4}$$

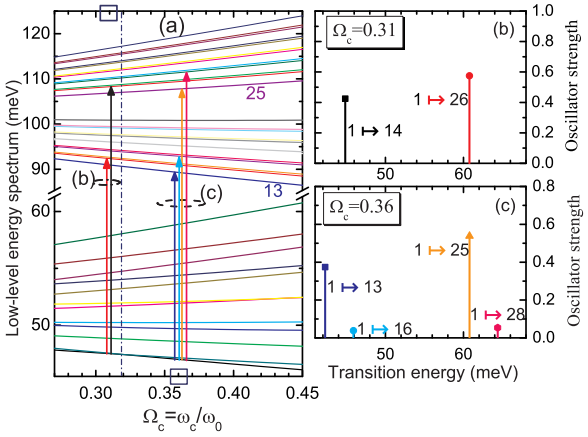

Figure 6.5: (a) Low energy spectrum where some of the allowed transitions are indicated by arrows around the magnetic fields $\Omega_c = 0.31$ and 0.36. The corresponding OS of these transitions are shown in (b) and (c). The Mn-ion is located at the center of the dot and $S_C = 4$. The blue dash-dotted line at $\Omega_c = 0.32$ indicates the FM-AFM transition.

where

$$A_{ij}^{\alpha\beta} = \delta_{n_\beta,n_\alpha}\delta_{l_\beta,l_\alpha\pm1} l_H \sqrt{n_\alpha + |l_\alpha| + 1} - \delta_{n_\beta,n_\alpha+1}\delta_{l_\beta,l_\alpha\pm1}(1-\delta_{l_\alpha,0}) l_H \sqrt{n_\alpha + 1} \tag{6.5}$$

is the transition amplitude element identical to Eq. (18) of Ref. [180]. The transition amplitude (6.4) is a sum over all possible transition amplitudes of the respective single states α and β.

To simplify the subsequent discussion we show in Fig. 6.4 first the results for the case when no Mn-ion is present. The selection rule allowed transitions (i.e. $\Delta n = 0$, $\Delta l = \pm 1$) are indicated by the vertical arrows which are transitions from the GS $(0,0)$ to the p-shell $(0,1)$ (p^+) and $(0,-1)$ (p^-) with the respective OS f_{12} (blue) and f_{13} (red). As we can see from this figure, with increasing the magnetic field, the states with positive l have lower transition energy as compared to the negative l. This is illustrated by the blue and red arrows in Fig. 6.4. From this figure, for the magnetic field range $\Omega_c < 3.22$, f_{12} corresponds to the transition of the electron from the GS to the third state (level $1 \rightarrow 3$) while the other transition f_{13} corresponds to the transition of the electron from the GS level to the fifth, and then seventh, and then ninth, and then eleventh, and then thirteenth level. Note that in the limit of $\Omega_c \rightarrow \infty$, $f_{12} \rightarrow 0$.

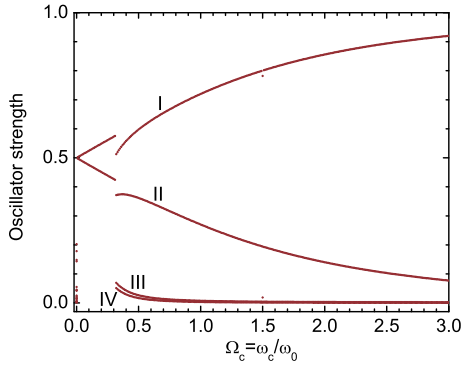

Figure 6.6: OS of the allowed electron transitions at various magnetic fields of the same magnetic QD as plotted in Fig. 6.5. I, II, III, and IV indicate the four branches of the OS curve as $\Omega_c \geq 0.32$.

In the presence of the Mn-ion, due to the ferromagnetic (at very small magnetic field) and antiferromagnetic (at larger magnetic field) coupling of the electron with the Mn-ion, the energy spectrum splits into many energy levels (see Fig. 6.2) and no simple selection rules hold. The CR spectrum now consists of many more peaks.

We first discuss in detail the electron transition for the case the Mn-ion is located at the center of the QD [$R_{Mn} = (0, 0)$] for magnetic fields $\Omega_c = 0.31$ (ferromagnetic phase) and $\Omega_c = 0.36$ (antiferromagnetic phase - as can be seen from Fig. 6.1). We found two allowed transitions as seen in Fig. 6.5 for $\Omega_c = 0.31$ with their respective resonant frequencies. Remember that at this magnetic field (within the region $\Omega_c < 0.32$), the system is in the ferromagnetic phase where the electron and the Mn-ion are both anti-parallel to the magnetic field. The transitions from the GS (level number 1) where the electron is mostly in the s orbital, to the state whose wave function has the orbital $(0, 1)$ as the largest FD contribution corresponding to the black line; and to the state whose wave function has the orbital $(0, -1)$ as the largest contribution corresponding to the red line, respectively. The resonances are found for transitions to the fourteenth and the twenty-sixth level. The corresponding result for the antiferromagnetic phase are shown in Fig. 6.5(c) for $\Omega_c = 0.36$. Notice that now we have four possible transitions with OS larger than 1% instead of two in previous case. This is in agreement with the effect found in Ref. [89] These four transitions correspond to the excitations of the electron from the GS to the energy levels: thirteenth (blue square), sixteenth (cyan rhombus), twenty-fifth (orange triangle) and twenty-eighth (pink circle). The first two: blue square and cyan rhombus belong to the

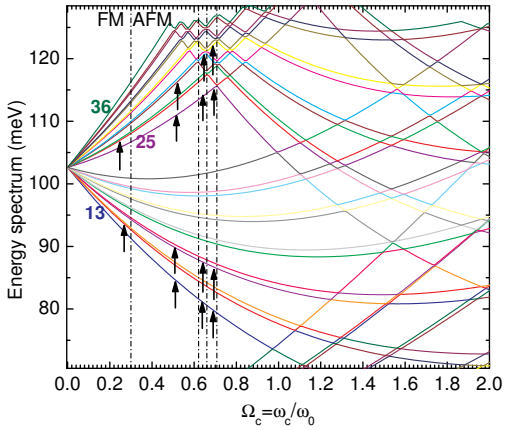

Figure 6.7: Low-level energy spectrum of the same QD as in Fig. 6.5 is plotted from the thirteenth to thirty-sixth levels to indicate the final states of the electron transition. The black arrows indicate the specific energy levels as the final state of the transition. The final states shift following the arrows as the magnetic field increases. The numbers: 13, 25, and 36 are the levels' numbers of the edge of subparts of the spectrum.

transition of the electron from the s GS to the p^+ state (with positive angular momentum); while the other two belong to the other transition of the electron to the p^- state (with negative angular momentum). The origin of this difference as compared to the case for $\Omega_c = 0.31$ can also be explained by looking at the GS wave function contributions of the FD states as shown in Fig. 6.3.

From Fig. 6.6 we find that the main transitions come from transitions to the two p-orbitals. The OS exhibits a discontinuity at $\Omega_c = 0.32$ where the FM-AFM transition takes place. The wave function of the GS changes from favoring the configurations with electron spin down to the configurations with electron spin up as can be seen from Fig. 6.3. As the magnetic field increases from $\Omega_c = 0.31$ where the system is in the FM phase to $\Omega_c = 0.36$ where the system is in the AFM phase, the largest FD contribution to the GS wave function goes from $(n, l, s_z, M_z) = (0, 0, -1/2, -5/2)$ to $(0, 0, -1/2, -3/2)$ and $(0, 0, 1/2, -5/2)$. Consequently, the final state of the electron transition shifts. We will clarify this point in Fig. 6.7 by using the black arrows to direct the attention of the reader to the final states for the transitions of the electron. For example, for $\Omega_c < 0.32$, the nonzero resonances are the lines from the GS to the fourteenth and the twenty-sixth

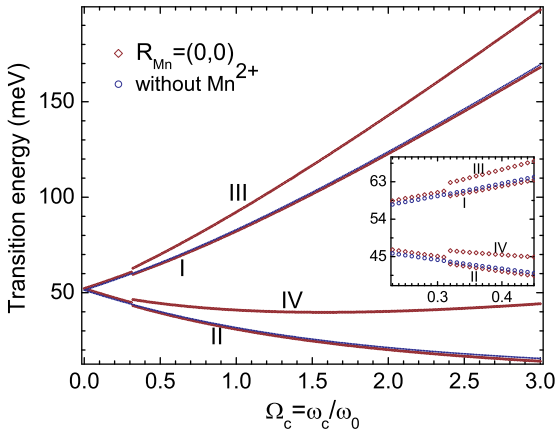

Figure 6.8: Transition energy for the same QD as plotted in Fig. 6.6 with four branches I, II, III, and IV corresponding to the four branches in the OS curve. Blue curves are the transition energy in the absence of a Mn-ion. The inset is a magnification around the FM-AFM transition magnetic field.

levels.

When the system transits to the AFM phase, the number of resonance lines increases from two to four. In the region $0.32 \leq \Omega_c < 0.62$, the transitions are to the thirteenth and sixteenth level; the twenty-fifth and twenty-eighth; and the main contributions are the lines to the thirteenth and the twenty-fifth, etc. This is explained as follows. For the FM magnetic field range $\Omega_c < 0.32$, the electron and the Mn-ion both are antiparallel to the magnetic field and $s_z + M_z = -3$ with the configuration of $(n = 0, l = 0, s_z = -1/2, M_z = -5/2)$ having the probability almost unity. This is due to the fact that the commutator of the z-component of the total spin commutes with the Hamiltonian, $[s_z + M_z, H] = 0$. Beyond this magnetic field region, $\Omega_c \geq 0.32$, the electron and the Mn-ion are antiparallel and since the Zeeman (spin) part of the Mn-ion is always larger than the electron's and the exchange energy becomes the smallest one among these three competing energies there are two configurations $(0, 0, 1/2, -5/2)$ and $(0, 0, -1/2, -3/2)$ with $s_z + M_z = -2$ of the GS wave function as the main contributions. It is obvious that the exchange energy now has the largest contribution coming from the second term [corresponding to configuration $(0, 0, 1/2, -5/2)$] and the second largest from the last term [corresponding to configuration $(0, 0, -1/2, -3/2)$] in the last sum in Eq. (3.6). As the system

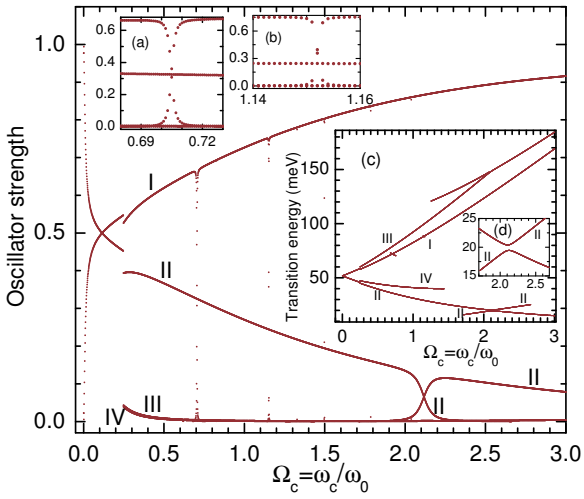

Figure 6.9: OS with two magnifications around $\Omega_c = 0.71$ (a) and $\Omega_c = 1.15$ (b) and transition energy (c) with a magnification around $\Omega_c = 2.12$ (d) for the same QD as plotted in Fig. 6.6 but the Mn-ion located at $(0.5l_0, 0)$. I, II, III, and IV indicate the four branches when $\Omega_c \geq 0.25$ in the OS and the corresponding transition energies.

is in the AFM, the final states of the major parts in the OS that are the branches I and II in Fig. 6.6 and the corresponding transition energies in Fig. 6.8 have wave functions that are the FD states $(0, -1, 1/2, -5/2)$ and $(0, 1, 1/2, -5/2)$, respectively, as the major contributions. The other two transitions (III and IV) come from the spin-spin exchange interactions corresponding to the final states that have wave functions containing FD states, respectively, $(0, -1, -1/2, -3/2)$ and $(0, 1, -1/2, -3/2)$ as their major contributions. In general, the largest one among all the small contributions can reach to about $5 \div 10\%$ of the total OS. With increasing magnetic field, these smaller contributions to the OS decrease to zero.

The OS for the case when the Mn-ion is located at the center of the dot samples the central region of the QD. In this situation the Mn-ion does not interact with the p-orbitals. The four branches in the OS (Fig. 6.6) and transition energy (Fig. 6.8) in the AFM phase are smooth with respect to magnetic field. Moving the Mn-ion to other positions away from the center of the dot gives rise to the interactions of the Mn-ion with the p-orbitals and this is expected to change the OS by the changes in the two main branches (I and II in Figs. 6.6 and 6.8). The influence of the position of

the Mn-ion on the CR-transitions is shown in Fig. 6.9 for the case when the Mn-ion is located e.g. at $(0.5l_0, 0)$. First of all, notice a discontinuity of the OS at $\Omega_c = 0.25$ which corresponds to the FM-AFM transition. Second, we find an unusual behavior at $\Omega_c = 2.12$ where the lower curve exhibits a crossing. Which is a consequence of the existence of an energy gap between the fourth and the fifth levels at $\Omega_c = 2.12$ as is clearly shown in Fig. 6.10(b) for the case the Mn-ion is located at $(0.5l_0, 0)$. These fourth

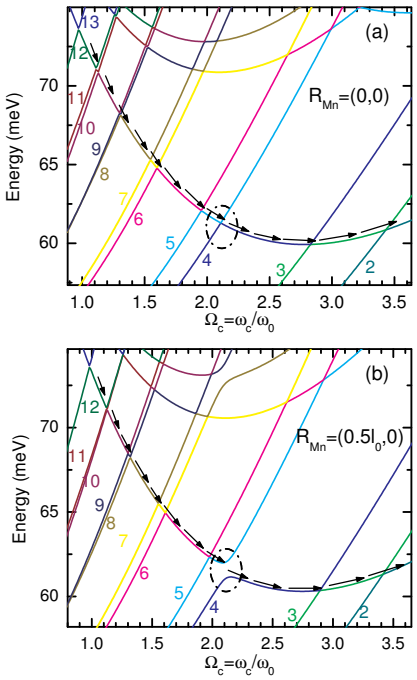

Figure 6.10: Magnification of the low-level spectrum of Fig. 6.2 for the cases the Mn-ion is located at the center and at $(0.5l_0, 0)$ in the QD. The black arrows indicate how the final state moves with magnetic field for the lowest energy CR transition.

and fifth levels have the FD states (0,1,1/2,-5/2) and (0,0,-1/2,-3/2) as their major contributions. When the Mn-ion is located at $(0.5l_0, 0)$ the exchange matrix elements between the p orbitals are nonzero which leads to the anti-crossing. This is the reason that the corresponding transition energy [see Figs. 6.9(c), (d)] exhibits an anti-crossing behavior at $\Omega_c = 2.12$. The energy gap is closed for the case the Mn-ion is located at the center of the QD [see Fig. 6.10(a)]. This similar behavior takes place at other magnetic fields

such as: $\Omega_c = 0.71$ [see Fig. 6.9(a)] and $\Omega_c = 1.15$ [see Fig. 6.9(b)] for the other kind of electron transitions: the transition to the final state with negative azimuthal quantum number. This is due to the fact that around the above magnetic fields there exist two final states contributing to the electron transition with their wave functions composed of the two major FD states $(0, -1, 1/2, -5/2)$ and $(0, 0, 1/2, -5/2)$. This results in a smaller region of the magnetic field as compared to the previous case around $\Omega_c = 2.12$.

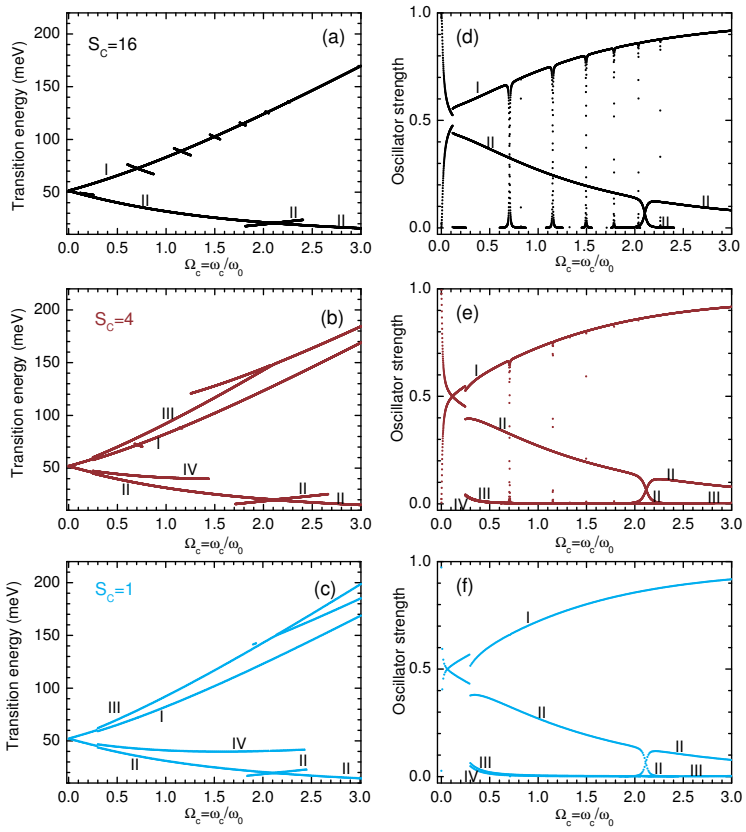

Figure 6.11: Transition energy [(a), (b), and (c)] and OS [(d), (e), and (f)] for the QD with the Mn-ion located at $(0.5l_0, 0)$ and for three different values of S_C. I, II, III, and IV indicate the four [two in (a)] main branches when the system is in the AFM phase. The transition energy is scaled by the ratio of S_C to $S_C = 4$.

Next we discuss the S_C-dependence of the electron transition first for the case that the Mn-ion is located at the center of the QD. We consider

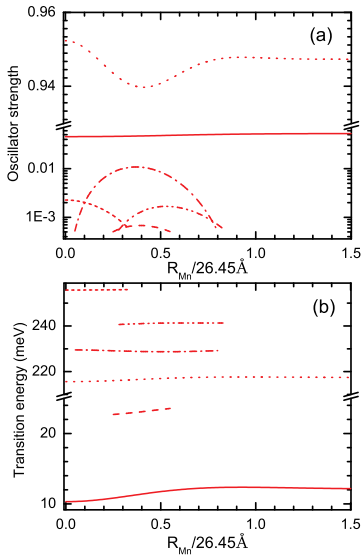

Figure 6.12: (a) The logarithm of the OS and (b) the transition energy vs. the position of the Mn-ion at magnetic field $\Omega_c = 4$ for $S_C = 4$. Solid and dotted lines are, respectively, the contributions from the second and the ninety-seventh level as the main contributions to the electron transitions to the two p orbitals.

two different values of S_C i.e. $S_C = 4$ and $S_C = 1$.

The OS curve does not change with changing the S_C while the transition energy is proportional to S_C. This scaling is no longer exact if one displaces the Mn-ion away from the center of the QD, i.e. for $R_{Mn} = (13.2\mathring{A}, 0) = (0.5l_0, 0)$, as can be seen from Fig. 6.11. The transition energies for three different $S_C = 16$, 4, and 1 that are all scaled to the case of $S_C = 4$ now exhibit different behaviors as seen in Figs. 6.11(a), (b), and (c). First, the FM-AFM transition that leads to a discontinuity is found at different magnetic fields, i.e. $\Omega_c = 0.12$, 0.25, and 0.3 for $S_C = 16$, 4, and 1, respectively. Besides, the anti-crossing point at $\Omega_c = 2.12$ as seen already from Fig. 6.9 is different for different S_C. It is now at 2.1, 2.12, and 2.11 for $S_C = 16, 4$, and 1, respectively. The OS also exhibits different features at the above magnetic fields as can be seen from Figs. 6.11(d), (e), and (f). As the electron is strongly confined, i.e. the case of $S_C = 16$, the wave function becomes strongly localized and because the Mn-ion is now located at $(0.5l_0, 0)$, that is far enough from the center of the dot, the exchange interactions between the p-electron and the Mn-ion reduce. Consequently, the effect of the e-

Mn-ion interaction on the CR-lines results in several anti-crossings in the transition energy (crossings in the OS) as can be seen from Figs. 6.11(a) and 6.11(d). The branches I and II in all six figures from Fig. 6.11(a) to Fig. 6.11(f) refer to the transitions of the electron from the GS to the final states which have the FD states $(0,-1,1/2,-5/2)$ and $(0,1,1/2,-5/2)$ as the major contributions, respectively.

We now explore the Mn-ion position dependence of the OS within a large range of R_{Mn}. We realize that at high magnetic field, the single-energy states "convert" to the Landau levels with the Landau indices $N_L = n + \frac{|l|-l+1}{2}$. We focus now on the high magnetic field transitions for different positions of the Mn-ion and different confinement strengths. As an example see Fig. 6.12, where at high magnetic field, e.g. $\Omega_c = 4$, the electron transitions are mainly between the GS to the second (solid) and the ninety-seventh (dotted) level, the upper part (dotted) of the OS curve oscillates and exhibits a maximum in case the Mn-ion is at the center of the dot. In the latter case we have the largest contribution of the exchange energy to the total energy as compared to the other positions. Note also that if one keeps increasing the magnetic field, the small-contribution branches (dashed, dash-dotted, dash-dot-dotted, and short-dashed corresponding to the 5^{th}, 98^{th}, 101^{st}, and 105^{th} level, respectively) in the OS curve, which are generally only about $2-5\%$ of their dominant branches (solid and dotted), become smaller. In the extremely high magnetic field limit, the first electron transition, namely to the energy level with the FD state $(0,1)$ dominant, becomes zero making the transition to the level with the FD state $(0,-1)$ dominant, increases to unity. Therefore, the small-contribution branches in the OS curve plotted in Fig. 6.12(a) can be neglected in experimental measurements.

6.3 Many-body effect in the FIR absorption spectrum

6.3.1 Cyclotron resonance

One way to see that the e-e interaction will affect the CR spectrum is by writing e.g. the two-electron Hamiltonian in terms of center-of-mass ($\overrightarrow{R_c} = \frac{\overrightarrow{r_1}+\overrightarrow{r_2}}{2}$, $\overrightarrow{P} = \overrightarrow{p_1} + \overrightarrow{p_2}$) and relative ($\overrightarrow{r} = \overrightarrow{r_1} - \overrightarrow{r_2}$, $\overrightarrow{p} = \overrightarrow{p_1} - \overrightarrow{p_2}$) coordinates:

$$H = H_{R_c} + H_r + H_{sM} + H_Z \tag{6.6}$$

where

$$H_{R_c} = \frac{1}{2M^*}(\overrightarrow{P} + Q\overrightarrow{A_c})^2 + \frac{1}{2}M^*\omega_0^2 R_c^2, \tag{6.7a}$$

$$H_r = \frac{1}{2M^*}(\overrightarrow{p} + \frac{1}{2}Q\overrightarrow{A_r})^2 + \frac{1}{2}M^*\omega_0^2(r/2)^2 + \frac{Q^2}{4\pi\epsilon_0\epsilon r}, \tag{6.7b}$$

and

$$H_{sM} = J_c\overrightarrow{M}\cdot[\overrightarrow{s_1}\,\delta(\overrightarrow{R_c} + \frac{\overrightarrow{r}}{2} - \overrightarrow{R}) + \overrightarrow{s_2}\,\delta(\overrightarrow{R_c} - \frac{\overrightarrow{r}}{2} - \overrightarrow{R})] \tag{6.7c}$$

are, respectively, the center-of-mass, the relative, and the electron spin Mn-ion spin Hamiltonian. H_Z is the total Zeeman spin energy. $M^* = 2m^*$ and $Q = 2e$ are, respectively, the total mass and total charge of the electrons. ω_0 is the confining frequency, $\overrightarrow{A_c} = \frac{1}{2}(\overrightarrow{B}\times\overrightarrow{R_c})$ and $\overrightarrow{A_r} = \frac{1}{2}(\overrightarrow{B}\times\overrightarrow{r})$ are the center-of-mass and relative magnetic vector potential, respectively. In a CR experiment the long-wavelength radiation interacts only with the center of mass through $e\overrightarrow{E}\cdot\overrightarrow{R_c}$ where $\overrightarrow{E}$ is the electric field of the FIR. Notice that due to the interaction of the electron spin with the Mn-ion spin $\overrightarrow{M}$ the center of mass is coupled with the relative coordinates which contain information on the e-e interaction.

The OS of the electron transitions (from GS i to excited state j) are calculated for N_e electrons using the transition amplitude:

$$A_{ij} = \sum_{p=1}^{N_e} < \Psi_i(\overrightarrow{r_1},...,\overrightarrow{r}_{N_e})|r_p e^{\pm i\theta_p}|\Psi_j(\overrightarrow{r_1},...,\overrightarrow{r}_{N_e}) > \tag{6.8}$$

with its corresponding transition energy $E_{ij} = E_j - E_i$. $\Psi_{i(j)}$ is the many-body wave function defined in Eq. (3.8) or (3.10) in chapter 3.

All allowed transitions with oscillator strength exceeding 1% are retained. Notice that due to spin exchange of the different types of particles, different types of transitions where the $z-$projection of the total spin of electrons and the spin of Mn-ion balance each other become possible leading to several cyclotron resonance peaks in the absorption spectrum.

The single-electron energy diagram in case without a Mn-ion is depicted in Fig. 6.13 as function of the applied magnetic field. We indicated the allowed transitions by dash-dotted arrows for the case of two magnetic field values. We add the electron Zeeman term to the theoretical FD levels to distinguish the $\pm 1/2$ spin states. Without the Mn-ion, the absorption spectra are independent of N_e for parabolic confinement due to Kohn's theorem [177, 181].

We introduce right- and left- (circular-) polarized eigenmodes σ^- and σ^+ of the single-electron transitions, which, respectively, refer to right and left circular light. σ^- and σ^+ connect to the FD (initial and final) states with

positive ($\Delta l = 1$) and negative ($\Delta l = -1$) difference of azimuthal quantum number, respectively. It is possible that σ^- (σ^+) has different frequencies (absorption energy branches), say $\sigma^-_{\alpha_1}(\sigma^+_{\alpha_1}), \sigma^-_{\alpha_2}(\sigma^+_{\alpha_2}), ...$, corresponding to the transition of different electrons. For simplicity in notation, we drop the subscripts $\alpha_1, \alpha_2, ...$ and classify all the right- (left-) polarized eigenmodes in the σ^- (σ^+) group. Configuration information will be included to clarify

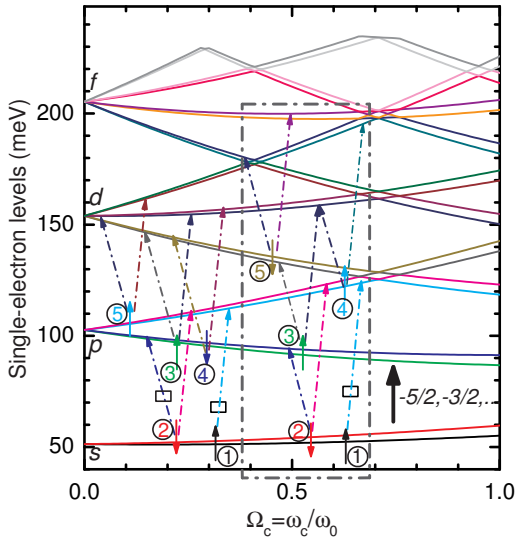

Figure 6.13: Single-particle energy levels (w/o Mn-ion) and allowed electron transitions for two magnetic fields (separated by dash-dotted rectangle box) for $N_e = 1 \div 5$ electrons referred by numbers 1 to 5. The transitions are indicated by dash-dotted arrows colored respectively by the color of the energy level as final state. Big black arrow stands for Mn-ion with six possible M_z. Transitions with small enclosed rectangles are forbidden in case N_e increases (up to 5) due to Pauli exclusion principle.

different electron transitions. A mode that is a combination of different right- (left-) polarized eigenmodes is also right- (left-) polarized.

In our calculation of the absorption spectrum, we use a Lorentzian broadening

$$\sigma_i(E) = \sum_j \frac{\Gamma_{ij}}{\pi} \cdot \frac{f_{ij}}{(E - E_{ij})^2 + \Gamma_{ij}^2} \tag{6.9}$$

where i and j refer to the initial and final states, respectively. In the following results we concentrate on the transitions where the initial state is the

GS and we will identify $\sigma_1(E)$ by $\sigma(E)$. Γ_{ij} is the broadening parameter that is taken to be $10 \div 100$ μeV.

6.3.2 Two-electron quantum dot

We first calculate the OS for the case without and with the presence of the Mn-ion taking into account all allowed transitions of the two electrons. The system with the Mn-ion located at the center of the dot has the energy spectrum as shown in Fig. 6.14 when the effective Coulomb interaction strength is $\lambda_C = 0.5$. Many crossings and anti-crossings are found in the spectrum that were not present in the case without a Mn-ion. The anti-crossings,

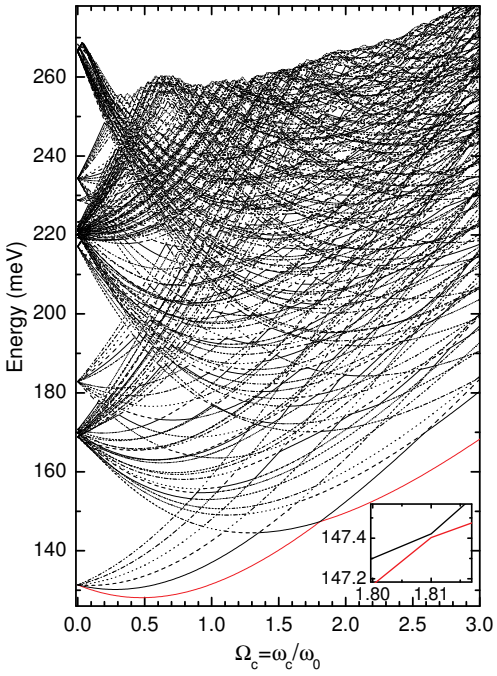

Figure 6.14: First 200 energy levels of the spectrum of a two-electron magnetic QD with the Mn-ion located at the center of the QD for $\lambda_C = 0.5$. The inset is the anti-crossing point of the first two energy levels at $\Omega_c = 1.81$.

which are a consequence of intermixing of higher quantum states due to the presence of the Mn-ion, lead to energy gaps between the levels, and result in unusual behaviors in the cyclotron resonance spectrum.

For $N_e = 2$, the pure FM phase, where the two electrons have spins parallel to the spin of the Mn-ion, does not exist. This is opposite to the

case for $N_e = 1$ which is a consequence of the closed s orbital for $N_e = 2$. This results in zero diagonal elements for the e-Mn exchange matrix. The neighboring off-diagonal elements that describe the spin exchange of the electrons with the Mn-ion of the configurations with different S_z and M_z but satisfying $S_z + M_z$ =const., which are in general very small, now turn to be the main contributions to the exchange interaction energy. Therefore, a *weakened* "FM" state is still found with a total spin slightly larger than zero. The magnitude of these off-diagonal contributions is small and depends on the position of the magnetic ion. Moving the Mn-ion to other positions inside

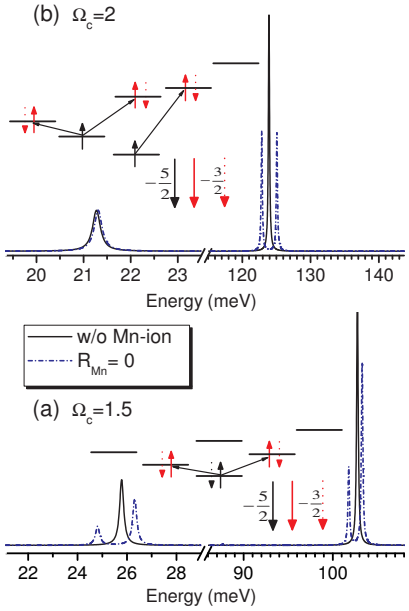

Figure 6.15: $\sigma(E)$ vs. energy for two different magnetic fields where the system is in the (a) FM and in the (b) AFM state for a two-electron QD with (blue dash-dotted curve) and without (black solid curve) the presence of a Mn-ion for $\lambda_C = 0.5$. The Mn-ion is positioned in the center of the QD. Two schematic plots in (a) and (b) describe the corresponding transitions in which black is for GS and red for excited state; solid is for main contribution and dotted for minor contribution to the total OS.

the QD when the system is still in the "FM" phase can affect the structure of the energy spectrum of the system. With increasing the magnetic field, the system will transit to a phase where the two electrons will have spin-up and are antiferromagnetically attracted to the Mn-ion. This phase is called antiferromagnetic (AFM). The FM-AFM transition can be seen from the

inset of Fig. 6.14 through the anti-crossing between the GS and the second level at $\Omega_c = 1.81$. The Mn-ion is always "frozen" with spin projection $-5/2$ in case of nonzero magnetic field.

Figs. 6.15(a) and 6.15(b) are the magneto-optical absorption spectrum $\sigma(E)$ for two values of the magnetic field $\Omega_c = 1.5$ (FM) and $\Omega_c = 2$ (AFM), respectively, for the system in case without (black solid) and with (blue dash-dot) the presence of the Mn-ion (at the center of the dot). Two schematic diagrams describe possible electron transitions with OS exceeding 0.1% of the total OS taking place within the s, p, and d shells. When the system is in the FM phase, the main transitions are such that the final state has the quantum numbers $(n_r, L_z, S_z, M_z) = (0, 1, 0, -5/2)$ (the second peak) or $(0, -1, 0, -5/2)$ (the fourth peak) as the major configuration and $(0, 1, -1, -3/2)$ (the first peak) or $(0, -1, -1, -3/2)$ (the third peak) as the minor configuration, respectively. We recall [85] that the number of CR lines in the case of a single electron QD doped with a Mn-ion when the system is in the FM state is two and the electron (spin down)-Mn-ion (spin down) interaction affects the CR spectrum in this state through shifting the cyclotron energy and/or the presence of crossings. The spin exchange interaction becomes stronger when the system is in the AFM state (electron and Mn-ion spin antiparallel) resulting in the presence of more CR lines. However, the major CR lines in this case are two. Let us go back to the current system when it is in the AFM state where we find three major CR lines as can be seen in Fig. 6.15(b). The first peak is due to an electron transition from the p^+ $[(n_r, l) = (0, 1)]$ orbital to the d^+ (0,2) orbital corresponding to the resonance from the GS with major configuration $(0, 1, 1, -5/2)$ to the final state with major configuration $(0, 2, 1, -5/2)$. For the other two pronounced peaks, the one that appears at the smaller transition energy is for the s-electron transition to the p^- $(0, -1)$ and its OS is slightly larger than the other peak that stands for the electron transition from the p^+ (0,1) orbital to the d^0 $(1, 0)$ orbital. Their final states have as dominant configurations $(0, 0, 1, -5/2)$ and $(1, 0, 1, -5/2)$, respectively. The CR transitions that become allowed due to spin exchange have a much smaller OS than the major transitions and can be neglected. For the case without a Mn-ion, the system transits from the state $(n_r, L_z, S_z) = (0, 0, 0)$ to the state $(0, 1, 1)$. Note that if one keeps increasing the magnetic field, the electrons will occupy higher quantum states resulting in the GS wave function having quantum numbers e.g. $(0, 3, 1)$ or $(1, 1, 1)$, and so on. Consequently, the number of possible CR lines increases.

Here, we will discuss in more detail the transitions resulting from the $(0, 1, 1)$ GS. Note that only two of the three allowed CR lines are observ-

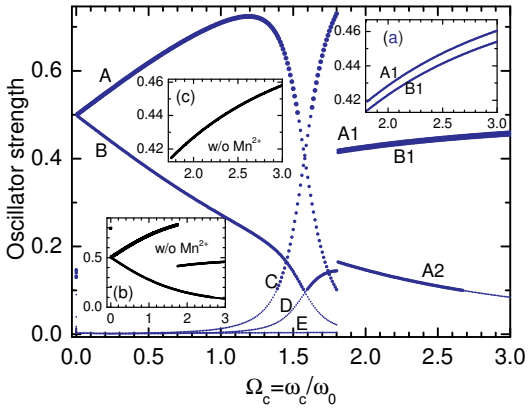

Figure 6.16: OS of a two-electron QD with the Mn-ion located at the center of the QD, (a) magnification of the region of $1.8 \leq \Omega_c \leq 3$ where the system transits to the AFM phase. (b) the OS of the same QD without a Mn-ion and (c) the magnification of the same region as in (a) but for the same situation as in (b). The thickness of the curve is proportional to the value of the OS. A, B, C, D, E labels the 5 branches when the system is in the FM and A1, A2, and B1 labels the branches when the system is in the AFM phase.

able, namely, the p^+-electron to the d^+ [the first solid peak in Fig. 6.15(b)] and the s-electron and the p^+-electron to, respectively, the p^- and the d^0 orbital that have the same OS and transition energy [the second solid peak in Fig. 6.15(b)]. These two coinciding CR lines split in the presence of the Mn-ion as can be seen by the dash-dotted curve where the system is in the AFM state. We note that for $\Omega_c = 2$ [Fig. 6.15(b)] the first peak corresponding to the transition of the p^+-electron to the d^+ orbital has almost the same transition energy in case without and with the Mn-ion. This is due to the zero exchange interaction energy between the s and the p orbitals when the Mn-ion is located at the center of the dot. The energy difference between these two peaks and the number of spin-exchange CR lines will increase as one moves the Mn-ion away from the center of the QD. We will come back to this point in a later discussion.

The OS and absorption energy spectrum of the above case over a wide range of magnetic field are found in Fig. 6.16 and Fig. 6.17, respectively. For the case without a Mn-ion, these quantities are, respectively, reviewed in the insets (b) and (c) of Fig. 6.16 and in the inset (b) of Fig. 6.17. Fig. 6.17(b)

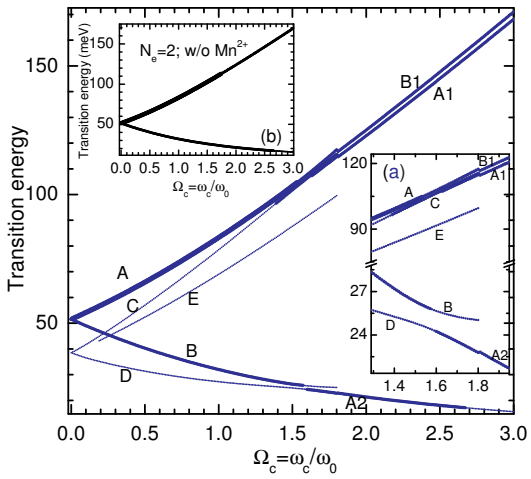

Figure 6.17: Transition energy corresponding to the OS of Fig. 6.16 and for the case without a Mn-ion [inset (b)]. (a) Magnification of the transition energy of the main plot for the magnetic field region $1.3 \leq \Omega_c \leq 2.0$. The thickness of the curve is proportional to the respective OS value and the labels corresponding to the transition energy branches of the respective OS ones plotted in Fig. 6.16.

is identical to the case of one-electron QD due to the N_e-independence of the absorption spectrum for parabolic confinement without a Mn-ion. The thickness of the transition absorption energy curves plotted in Fig. 6.17 is proportional to the OS whose values are plotted in Fig. 6.16. As we can see from these two plots, the CR transitions for the case when the Mn-ion is present is very different from the case without a Mn-ion. For the magnetic field region where the system is in the FM phase $\Omega_c \leq 1.81$, the differences are significant which can be seen from the presence of the two crossings in the OS in Fig. 6.16 that correspond to the two anti-crossings in the transition energy in Fig. 6.17. At the FM-AFM transition point, there are discontinuities. For the AFM region, the difference is in the separation of the two lines that was not present in the case without a Mn-ion as shown, respectively, in Figs. 6.16(a), 6.17(a) and Figs. 6.16(b), 6.17(b). Note that the discontinuity in the OS of Fig. 6.16(b) is due to the fact that the CR spectrum transits from two to three lines, where the last two CR lines have the same transition energy (they are the transitions $s \rightarrow p^-$ and $p^+ \rightarrow d^0$). If these OS are added, there would be no discontinuity in Fig. 6.16(b). Let

us first discuss the branches of the OS for the region $\Omega_c < 1.4$ (before the first crossing) - which we name region I. In this region, the system is in the FM phase. The two electrons mostly stay in the s-shell with antiparallel spins. The transitions are from the GS to the two p orbitals with high OS . The latter are the two higher branches in the OS curve plotted in Fig. 6.16. The final states, which now mix with several quantum states, include, respectively, $(0, -1, 0, -5/2)$ (higher) or $(0, 1, 0, -5/2)$ as their main contribution. We see also two lower branches; that are the curves corresponding to the electron transitions from the GS to the two p orbitals but with different spin states. The final states are now such that the electron that is excited to a higher state will flip its spin which is compensated by a change of the Mn-ion spin.

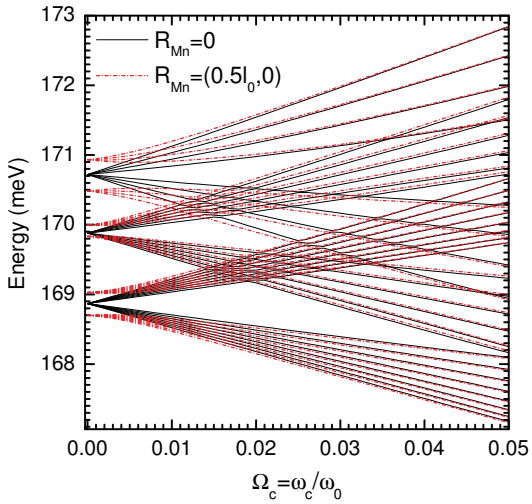

Figure 6.18: 36 energy levels (from level 7 to level 42 that are grouped into 8-8-6-6-4-4 lines) of a two-electron QD with the Mn-ion located at the center or at $(0.5l_0, 0)$ of the QD for $\lambda_C = 0.5$.

We found that the final states corresponding to these CR lines have, respectively, the quantum numbers $(0, -1, -1, -3/2)$ (higher) and $(0, 1, -1, -3/2)$ as their major contribution. This is understood via the e-Mn-ion spin-spin exchange interaction. These two curves have a smaller OS than the above two due to the small contribution of the configuration $(0, 0, -1, -3/2)$ in the GS while the major one is $(0, 0, 0, -5/2)$.

Now we will discuss the results for the higher magnetic field region. At the first crossing, $\Omega_c = 1.45$, we observe the exchange between two branches

as seen in Fig. 6.16. The higher branch of the two lower branches is higher in energy than the lower branch of the two higher branches in region I of the OS plot. This is the case up to the next two crossings at $\Omega_c = 1.58$. The region $1.45 \leq \Omega_c \leq 1.58$ is named region II. Within this magnetic field region, the final state which has the configuration $(0, -1, -1, -3/2)$ as its major contribution to the OS becomes larger in OS as compared to the state which has the configuration $(0, 1, 0, -5/2)$. At $\Omega_c = 1.58$ we find two crossings with an exchange of OS. This is a consequence of the fact that the energy spectrum exhibits crossings (and anti-crossings) of energy levels. Next we consider the AFM phase, $\Omega_c \geq 1.81$, and focus on the two higher branches that stay very close to each other. Remember that for the case without a Mn-ion, these branches are degenerate [as can be seen from Fig. 6.16(c) and Fig. 6.17(b)]. In the presence of the Mn-ion, this degeneracy is lifted and and their OS differ about 1% of the total OS and their energy differs by $3 - 4$ meV or about 6.8% of the confinement energy $\hbar\omega_0$. They correspond to transitions of the spin-up electron from the s-shell to the p^- orbital (lower branch) and of the spin-up electron from the p^+ orbital to the d^0 orbital as discussed before in Fig. 6.15, respectively. For these transitions, the Mn-ion spin with $M_z = -5/2$ is unaltered. The other lower branch corresponds to the transition of the p^+-electron to the d^+ orbital. The anti-crossings in the transition energy are illustrated in Fig. 6.17(a) which magnifies the region $1.3 \leq \Omega_c \leq 2.0$.

Mn-ion position dependence of the intra-band excitation spectrum

Moving the Mn-ion to another location inside the QD affects the energy spectrum as shown in Fig. 6.18 where we focus on the small magnetic field region. The black solid lines and the red dashed lines are the 36 energy levels starting from level 7 for the cases that the Mn-ion is located at the center and at $(0.5l_0, 0)$, respectively. We first notice that the $B = 0$ GS energy in both cases has the same degeneracy (i.e. 6). For the higher energy levels different degeneracies are found for $R_{Mn} = 0$ we have $16 - 12 - 8$ while for the other case we have $8 - 8 - 6 - 6 - 4 - 4$ fold degeneracy. When applying a magnetic field, these degeneracies are further lifted due to the Zeeman effect. We note that e.g. for the two eightfold-degenerate levels [in the case that the Mn-ion is located at $(0.5l_0, 0)$-the red dash-dotted curves] or the two 16-fold-degenerate-levels (in the case that the Mn-ion is located at the center of the dot-the black solid curves), as the magnetic field increases, the lower energy level corresponds to states with positive total azimuthal quantum number, in this case +1 - one electron in the s-shell and the other

in the p^+ orbital and the higher energy level has negative total azimuthal quantum number -1 - one electron in the s-shell and the other in the p^- orbital, etc. The degeneracy of the higher energy levels for $B = 0$, i.e. 8, 6, or 4, etc, comes from the ferromagnetic (e.g. $\overrightarrow{M} + \overrightarrow{S} = \overrightarrow{7/2}$ for the case of eightfold degeneracy) or antiferromagnetic (e.g. $\overrightarrow{M} + \overrightarrow{S} = \overrightarrow{5/2}$ for the case of sixfold degeneracy) coupling of the two electrons with the Mn-ion. Note that all the 36 energy levels in Fig. 6.18 refer to the s and p orbitals. At higher magnetic fields, the energy spectrum exhibits further differences when R_{Mn} is varied in e.g. the number and the positions of the crossings and anti-crossings, the energy gaps of the anti-crossings, etc.

As we discussed above, the system that consists of two electrons and a single Mn-ion does not exhibit a very clear FM phase since the state where the two electrons stay in the s-shell with antiparallel spins minimizes the GS. The energy gained by the direct antiferromagnetic coupling of the Mn-ion to the spin-up electron is balanced by the ferromagnetic exchange with the other spin-down electron. This holds as long as the two electrons occupy the s orbital. Therefore, the FM-AFM transition magnetic field is almost not changed when we vary the position of the Mn-ion. For example, the FM-AFM takes place at $\Omega_c = 1.81$ for the cases that the Mn-ion is located at the center and at $(0.5l_0, 0)$ and at $\Omega_c = 1.79$ for the case the Mn-ion is located at $(l_0, 0)$. To see the Mn-ion position dependence on the CR-spectrum, we will focus on the high magnetic field region where the system is in the AFM phase with both electrons having spin up and one of them accommodating a higher orbital e.g. the p^+ orbital. The allowed electron transitions now are the three lines that start from the GS to the p^- (for the s-electron) and to the d^+ and d^0 orbitals (for the p-electron). Note that for the case that the Mn-ion is located at the center of the dot, the exchange interactions between the s and p orbitals are zero while these terms increase as the Mn-ion is moved away from the center e.g. to $(0.5l_0, 0)$ or $(l_0, 0)$. Consequently, the behavior of the OS changes. The first transition that corresponds to the transition of the p^+-electron to the d^+ orbital is shifted. The other two transitions that stay very close in energy and correspond to the other transitions of the s-electron and the p^+-electron to the p^- and d^0 orbitals [the solid lines at the right hand side in the diagram in Fig. 6.15(b)], respectively, are most separated for the case the Mn-ion is located at the center of the QD. The reason is that for $R_{Mn} = 0$, only the exchange interactions between the s and the d^0 orbitals are nonzero (and equal) within the involved shells s, p, and d. This means that the final state with the configuration of the s-electron and the d^0-electron as their main contribution to the wave function is more

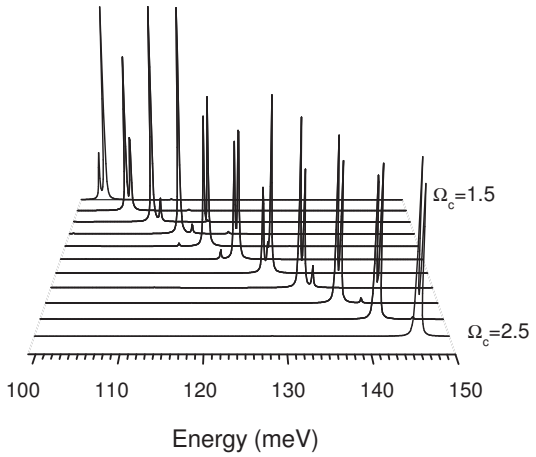

Figure 6.19: Magneto-optical absorption spectrum focused on the two higher transitions for the same QD as plotted in Fig. 6.17 for the case the Mn-ion is located at $(0.5l_0, 0)$. The magnetic field range is (1.5,2.5) with steps of 0.1.

enhanced in energy. This difference leads to a larger separation between the two CR lines for $R_{Mn} = 0$. Qualitatively, this separation is about $3 - 4$ meV for $R_{Mn} = 0$ and $0.9 - 1$ meV for $R_{Mn} = 0.5l_0$, 0.5 meV for $R_{Mn} = l_0$ and almost zero for $R_{Mn} = 2l_0$. In the last case the problem converts to the problem without a Mn-ion. The two transitions merge to a single one as seen before [black curve in Fig. 6.15(b)].

We complete this subsection by investigating the absorption spectrum of the system for $R_{Mn} = 0.5l_0$ in a range of magnetic field $\Omega_c = (1.5, 2.5)$ that includes the FM-AFM transition (see Fig. 6.19). We focus our discussions on the two transitions discussed in the previous paragraph that correspond to the right hand side CR lines in Fig. 6.15(b). As the system transits to the AFM phase, the "correlations" between the s and p, s and d, p and d, etc, become nonzero for almost all values of the coupling strength. Consequently, the final states of the two transitions gain energy from the exchange interaction part. Their difference reduces leading to the fact that these two peaks stay closer in energy as compared to the case that the Mn-ion is located at the center of the dot. However, the stronger peak (at smaller transition energy) which corresponds to the transition of the s-electron when the system is in the AFM phase can become more pronounced or smaller than the other transition as illustrated in Fig. 6.19. As the system transits to the AFM phase ($\Omega_c \geq 1.9$), we see that within the magnetic field range

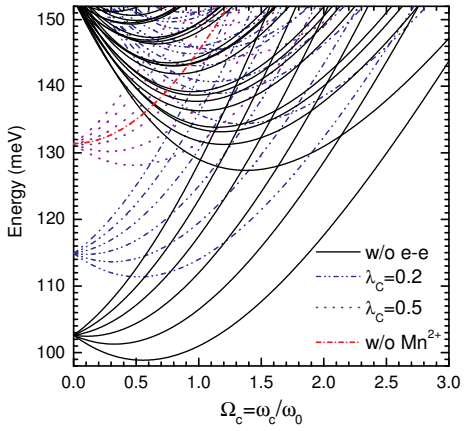

Figure 6.20: Energy spectrum plotted for the first 24 levels for several different Coulomb interaction strengths: without e-e interaction, $\lambda_C = 0.2$, 0.5. Red dash-dotted curve is the energy of the same QD ($\lambda_C = 0.5$) without a Mn-ion for reference. The energy spectrum for the case $\lambda_C = 0.2$ is scaled to the case of $\lambda_C = 0.5$.

$\Omega_c = 1.9 \div 2.1$ the peak that corresponds to the transition of the p^+ electron to the d^0 orbital is higher (having a larger OS) as compared to the other peak that corresponds to the transition of the s-electron to the p^- orbital. Within the magnetic field where $\Omega_c = 2.2 \div 2.3$ the OS of the two peaks exchange. This exchange happens again at $\Omega_c = 2.4$ and we obtain the last exchange in this figure for $\Omega_c = 2.5$. Each time that there is an OS exchange between these two peaks there is a crossing in the OS (and an anti-crossing) in the transition energy. When the Mn^{2+} is displaced to $(0.5l_0, 0)$, the difference in the OS value between these two peaks is now larger, but the difference in energy is smaller. Note that also smaller peaks appear next to the main ones. The small peak for $\Omega_c = 1.5$ is a transition from the GS with dominant configuration $(0, 0, 0, -5/2)$ which has $(0, 0, -1, -3/2)$ as a minor contribution, to the state with the configuration $(0, -1, -1, -3/2)$ as its main contribution to the wave function. For $\Omega_c = 1.9$ the small peak is due to the transition to the state with the configuration $(0, -1, -1, -3/2)$ as its main contribution.

Electron-electron interaction effect

Here we investigate how the strength of the e-e interaction influences the CR absorption spectrum. Its influence on the first 24 energy levels is plotted in Fig. 6.20 in case without e-e interaction (solid black curves) and two

different λ_C [0.2 (blue dash-dot-dotted curves) and 0.5 (violet dash curves)]. Crossings and anti-crossings of these energy levels occur at different magnetic fields (the smaller λ_C the larger the crossing field Ω_c).

Lets turn to the transition energy and for reference purposes we turn off the Coulomb interaction strength (see Fig. 6.21). Without the Coulomb interaction, the FM-AFM transition takes place at a larger magnetic field $\Omega_c = 3.44$ as compared to $\Omega_c = 1.81$ for the case with e-e interaction (see Fig. 6.17 and Ref. [85]). There are generally six CR lines (as com-

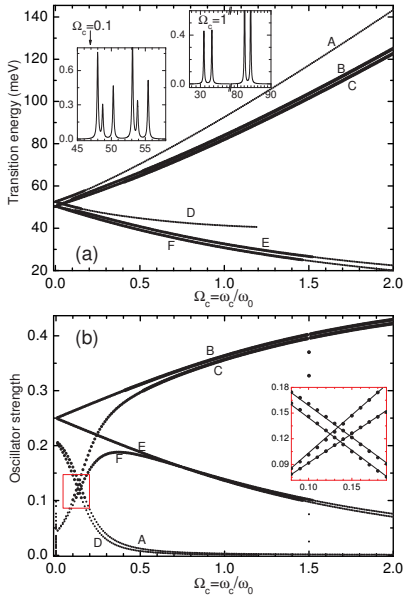

Figure 6.21: Transition energy (a) and OS (b) of a two-electron QD without e-e interaction for the case the Mn-ion is at the center of the dot. The thickness of the curve is proportional to the OS value (up to $\Omega_c = 2$, there is still no FM-AFM transition happening). The two insets in (a) are the $\sigma(E)$ plotted for two magnetic fields: $\Omega_c = 0.1$ and 1. A, B, C, D, E, and F label the six branches of the transition energy in (a) and the respective OS branches in (b). The inset in (b) is a magnification of the red rectangle where we use four lines to connect the data points of the four corresponding CR lines.

pared to four for the case with e-e interaction) with OS exceeding 0.1% of the total OS [Fig. 6.21(b)]. The main difference is that the dominant CR lines [conventional transitions e.g. from the GS with the quantum state $(0, 0, 0, -5/2)$ as the main configuration to the final state with the quantum

state $(0, \pm 1, 0, -5/2)$] do not have a much larger OS than the secondary transitions - the transitions appearing as a consequence of the e-Mn-ion exchange interactions, as can be seen from Figs. 6.16 and 6.21(b) ($\leq 15\%$ of the total OS). These six lines correspond to transitions of the electrons from the GS containing the major quantum state (n_r, L_z, S_z, M_z), to the six final states that contain their dominant contributions to the wave functions as combinations of the following four quantum states: $(n_r, L_z + 1, S_z, M_z)$, $(n_r, L_z + 1, S_z - 1, M_z + 1)$, $(n_r, L_z - 1, S_z, M_z + 1)$, and $(n_r, L_z - 1, S_z - 1, M_z + 1)$. Depending on the value of the applied magnetic field, the relative contributions of these states to the wave function will change leading to crossings as seen at $\Omega_c = 0.13$, 0.14 in the inset of Fig. 6.21(b).

If we increase the magnetic field further the CR spectrum collapses into four CR lines. The lines that are the results of the exchange e-Mn-ion interaction (C and F) become close in energy to the "conventional" lines (B and E). This behavior is not seen in case of interacting electrons. The reason

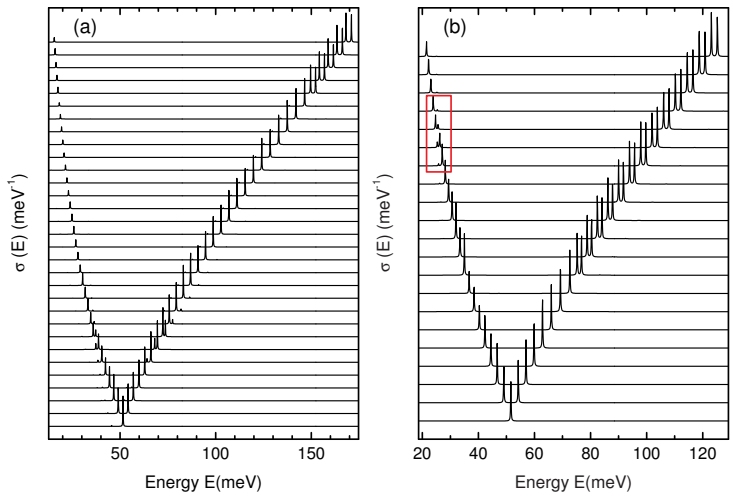

Figure 6.22: Magneto-optical absorption spectrum scaled to the case of $\lambda_C = 0.5$ obtained for the case the Mn-ion is located at the center of the QD for $\lambda_C = 0.2$ (a) and $\lambda_C = 2$ (b). Results are shown in the magnetic field range $(0, 3)$ (a) and $(0, 2)$ (b) with steps of 0.1.

is that when the Coulomb interaction is turned on, see Fig. 6.17, the e-Mn spin-spin interaction is weakened by the Coulomb repulsion. Note that the two additional peaks in the CR spectrum are a consequence of the breaking of the selection rule by the e-Mn exchange interaction.

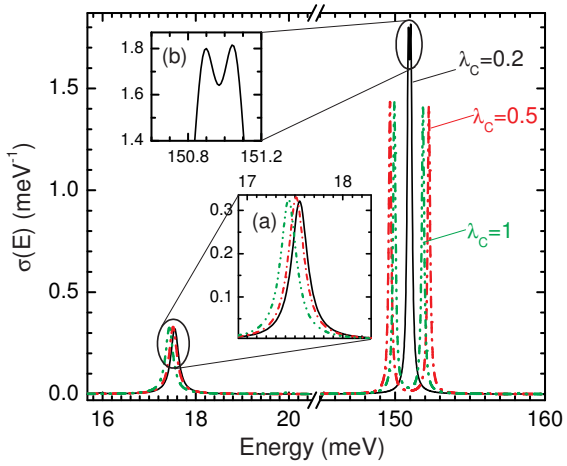

Figure 6.23: Magneto-optical absorption spectrum scaled to the case of $\lambda_C = 0.5$ obtained for the case the Mn-ion is located at $(0.5l_0, 0)$ for three different $\lambda_C = 0.2$, 0.5, and 1 and magnetic field $\Omega_c = 2.6$. (a) magnification of the first major peak. We focused on the three main transitions in each case with inset (b) the magnification to see the two upper peaks for the case of $\lambda_C = 0.2$.

When comparing the low magnetic field behavior (see Figs. 6.16 and 6.17) of the CR spectrum we note a very different behavior when we turn off the e-e interaction (see Fig. 6.21).

To understand this different behavior we plot in Fig. 6.22(a) the magneto-optical absorption spectrum for the system with a Mn-ion located at the center of the dot and $\lambda_C = 0.2$ for the magnetic field range $0 < \Omega_c < 3$. As compared to the system studied in Figs. 6.16 and 6.17 with $\lambda_C = 0.5$: first, the AFM phase takes place at a larger magnetic field ($\Omega_c = 2.53$ as compared to 1.81), second, the low OS branches survive up to higher fields. The FM-AFM transition occurs at $\Omega_c = 1.24$ and 0.96, for $\lambda_C = 1$ and 1.5, respectively. As λ_C increases, e.g. from $\lambda_C = 0.2$ [see Fig. 6.22(a)] to $\lambda_C = 2$ [see Fig. 6.22(b)], the low OS branches that appear due to the spin exchange of the electrons and the Mn-ion contribute less to the total OS. In Fig. 6.22(a), the contribution of the exchange terms to the total OS stays appreciable within the magnetic field range $(0, 1.7)$ (FM). The low OS branches appear on both "sides" of the transitions of the s-electrons: to the p^+ (left - lower transition energy) and to the p^- (right - higher transition energy) orbitals [see the lower peaks of Fig. 6.22(a)], meaning that the final

states with the configurations having $(0, 0, S_z + M_z = -5/2)$ as the main contribution have nonzero OS. While these low OS branches appear only on the "side" of the p^+-electron resonating to the d^+ orbital within the magnetic field region (1.4,1.7) (AFM), see the red rectangle in Fig. 6.22(b). It means that only the final state with the main quantum configuration as $(0, 2, 0, -3/2)$ has a nonzero contribution (as a minor) to the OS, while there is no gain from the exchange interactions during the transitions of the p^+-electron and the s-electron to the d^0 and p^- orbitals, respectively. However, in any case, the exchange interactions always separate these two transitions in energy (about 6.8% of $\hbar\omega_0$ for $R_{Mn} = 0$), as can be observed in Figs. 6.22(a) and 6.22(b), for magnetic field $\Omega_c \geq 2.53$ and $\Omega_c \geq 0.79$ for $\lambda_C = 0.2$ and 2, respectively.

Last, we study the combined effects of the position of the Mn-ion and the Coulomb interaction strength on the CR absorption spectrum. Due to the exchange interactions between all included quantum orbitals, the transitions of the s-electron to the p^- orbital and of the p^+-electron to the d^0 orbital have different energies depending on λ_C as can be seen in Fig. 6.23. We plot $\sigma(E)$ as a function of energy for three different λ_C (=0.2, 0.5 , and 1) at $\Omega_c = 2.6$ (AFM phase) with the Mn-ion located at $(0.5l_0, 0) = (13.2\mathring{A}, 0)$. For the smallest considered λ_C (i.e. 0.2) the two electrons are more strongly confined and the location of the Mn-ion in this case is almost out of the effective region of the electrons. Consequently, the separation between the two transitions of the electrons in two different orbitals becomes very small as can be seen from the black solid curve in Fig. 6.23 and its inset. The first transition, the transition of the p^+-electron to the d^+ orbital, slightly changes as λ_C changes as shown in Fig. 6.23(a).

6.3.3 Three-electron quantum dot

Given that the position of the Mn-ion affects the electron-Mn-ion ferromagnetic-anti-ferromagnetic (FM-AFM) transition [83, 84], the CR spectrum of a three-electron QD for two typically different Mn-ion positions $R_{Mn} = 0$ and $R_{Mn} = 0.5l_0$ exhibits significant differences particularly in the presences of low-OS transitions as a consequence of the spin exchanges (see Figs. 6.24 and 6.25). The spin exchanges for the latter case ($R_{Mn} = 0.5l_0$) are larger than that for the first case due to the absence of coupling between the s orbital with the p and d (as the lower states) orbitals when the Mn-ion is located at the center of the dot. For the FM phase we have the spin state $S_z = -1/2$ in the latter case which compares to 1/2 in the first case. As a consequence, its GS has only the quantum state $(n, L_z, S_z, M_z) = (0, 1, -1/2, -5/2)$ as

its main contribution while this are the quantum states $(0, 1, 1/2, -5/2)$ and $(0, 1, -1/2, -3/2)$ for the first case. Therefore, the number of allowed electron transitions from the GS for the first case when the system is in the FM phase (six) is larger than the latter case (three or five) as can be seen from Figs. 6.24 and 6.25. The contribution $(0, 1, -1/2, -3/2)$, which becomes

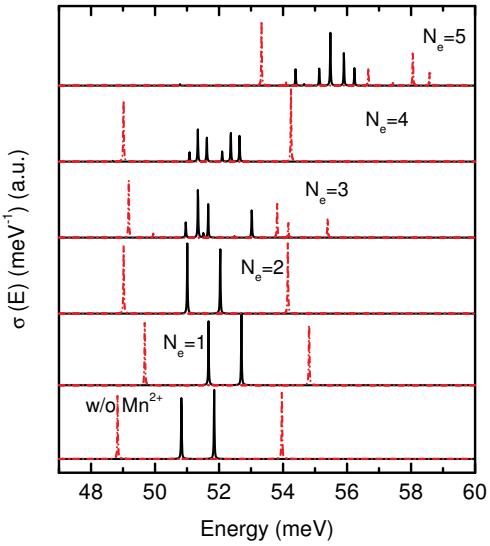

Figure 6.24: Magneto-optical absorption energy of a many-electron ($N_e = 1 \div 5$) QD for $\Omega_c = 0.02$ (solid black curves) and 0.1 (dash-dotted red curves) in case the Mn-ion is located at the center of the dot for $\lambda_C = 0.5$. The absorption energy for the case without a Mn-ion is plotted for reference.

dominant in the excited-state wave function, is ascribed to the presence of the double right-polarized modes (of the spin-down s-electron and spin-up $p^+_{(n_r,l)=(0,1)}$−electron) as the first (sorted ascending in energy) two large-OS peaks and double left-polarized modes (the other two large-OS peaks) for $\Omega_c = \omega_c/\omega_0 = 0.02$ (≈ 0.15T), and triple left-polarized modes for $\Omega_c = 0.1$ (see Fig. 6.24). The very-low-OS (4% of the total OS) black solid peak is the left-polarized mode combining the σ^+(s) of the spin-down s-electron and the p^+-electron where the configuration $(0, 1, -1/2, -3/2)$ strongly dominates the final state.

Increasing the field to $\Omega_c = 0.1$ results in a change of the absorption spectrum as shown by the dash-dotted red curves in Fig. 6.24 where there is only one right-polarized mode (the largest-OS peak). The triple left-polarized modes are the CR-lines that combine the σ^+(s) of, respectively, the two

s-electron transitions, and the spin-down $s-$electron and the p^+-electron transitions (double). In fact, the FM-AFM transition for $R_{Mn} = 0$ and $R_{Mn} = 0.5l_0$ occurs at, respectively, $\Omega_c = 2.3$ and 0.04 (see Ref. [83]). It means that one can observe the FM-AFM transition in the CR energy for the latter case in Fig. 6.25 as an increase in the number of CR peaks (from three to four). It is worth noting that with the presence of the Mn-ion it now

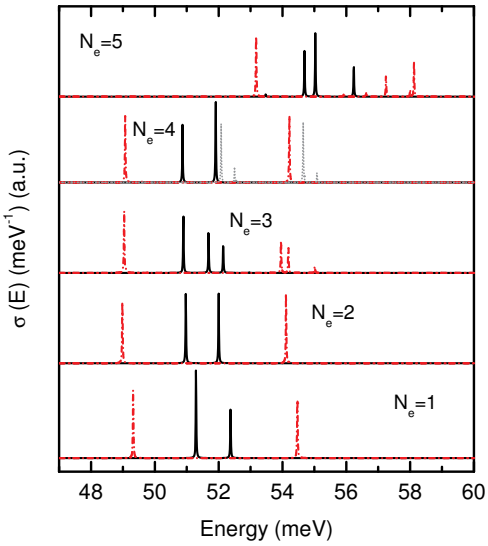

Figure 6.25: The same as Fig. 6.24 but for the case the Mn-ion position is moved to $(0.5l_0, 0)$. For $N_e = 4$ we added also the data for $\Omega_c = 0.05$ by the grey dotted curve.

becomes possible to observe transitions of different electrons *i.e.* different σ^+ and σ^- (*e.g.* for $\Omega_c = 0.1$) and the separation in energy will be much more pronounced for the highly polarized case. For $R_{Mn} = 0.5l_0$ in the FM phase, the three peaks are the absorption energies from the right-polarized mode and the double left-polarized modes.

The number of CR peaks increases when the system transits to the AFM phase as can be seen from Figs. 6.24, 6.25, and 6.26. In the high-field region where only the spin exchange interactions are active without changing M_z or S_z, the number of major CR peaks is four (Fig. 6.26), as compared to three for $N_e = 2$, that refer to the two modes (σ^- - *second-largest-OS peak* and σ^+ - *largest-OS peak*) of the most-outer electron and the other two (σ^+) for the s-electron (the third-largest-OS peak) and the p-electron. Using the quantum-state wave function formalism, the GS which has $(n, L_z, S_z, M_z) =$

$(0, 3, 3/2, -5/2)$ as its largest contribution will have four major electron transitions to $(0, 3, 1/2, -5/2)$ (σ^-), $(1, 1, 1/2, -5/2)$ (σ^+), $(1, 0, 1/2, -5/2)$ (σ^+), and $(0, -1, 1/2, -5/2)$ (σ^+). Note also that in the very-high-field limit, there is an influence of the exchange interaction on the CR spectrum as seen in the separated peaks which merge in the absence of the Mn-ion.

The polarized light couples only with the center-of-mass motion of the electrons. The above phenomenon where the different electron transitions of the three-electron QD are found to be different is a result of the coupling of the electron relative motions with their center-of-mass motion through the electron-Mn-ion spin exchange interaction term. These spin exchange

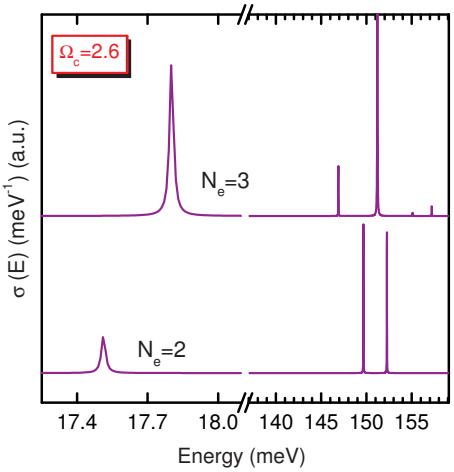

Figure 6.26: Magneto-optical absorption energy of a many-electron ($N_e = 2$ and 3) QD at high magnetic field $\Omega_c = 2.6$ (≈ 19.5T) in case the Mn-ion is located at the center of the dot for $\lambda_C = 0.5$.

elements depend on the quantum orbitals that the electrons occupy and on the position of the Mn-ion inside the dot. This leads to a coupling that is different for different electrons. In addition, the e-e interaction now turns out to be important in characterizing the absorption spectrum because its form depends on the electron relative coordinate ($\propto 1/|\overrightarrow{r_{ij}}|$). As proven for a two-electron QD [86], the Coulomb repulsion "weakens" the spin exchange interaction and reduces substantially the exchange energy contribution to the FIR spectroscopy as compared to that in case of the noninteracting QD system. For $2 < N_e < 6$ electrons, the GS of the FM phase partially fills the p-orbitals that have a maximum exchange energy for a position different from the center of the dot - the case for the s-orbital ($N_e \leq 2$ electrons).

The λ_C dependence of the IR spectroscopy results in changes as shown in Fig. 6.27 for $\Omega_c = 0.1$. The smaller λ_C the stronger the influence of the exchange energy on the electron transitions which results in almost equal large-OS peaks for the extreme case without e-e interaction. The smallest-OS peak discussed above for $\lambda_C = 0.5$ becomes more pronounced for smaller λ_C. The influence of the Coulomb interaction on the IR spectroscopy will be further examined for $N_e = 4$ and 5 electrons.

6.3.4 Four-electron quantum dot

Next, we will discuss in more detail the low-magnetic-field, say within the FM-state region, behavior of the four-electron QD system. Note that the FM-AFM transition magnetic field was found at $\Omega_c = 3.87$ and 2.5 for $R_{Mn} = 0$ and $R_{Mn} = 0.5l_0$, respectively. These transition magnetic fields are considered moderate as compared to the critical field at which the system becomes fully polarized. In the low-magnetic-field region, the CR peaks give us information on the spin exchange and are found as combinations of σ^+(s) or σ^-(s) of different electrons. These peaks only become more characteristic, *i.e.* each of which corresponds to a different transition referred to a different electron orbital, with increasing field (as seen in the cases for $N_e < 4$). For $R_{Mn} = 0.5l_0$, the system (in the FM phase) exhibits states $S_z = -1$ ($\Omega_c < 0.04$), $S_z = 1$ ($0.04 \leq \Omega_c < 0.1$), and 0 for the remaining FM region ($0.1 \leq \Omega_c < 2.5$). The intermediate states are $S_z = 1$ ($\Omega_c < 0.1$) and 0 ($0.1 \leq \Omega_c < 3.87$) for $R_{Mn} = 0$. Respectively, the number of CR peaks changes as shown in Figs. 6.24 and 6.25. This first intermediate FM state ($S_z = 1$) in case $R_{Mn} = 0$ exhibits six major transitions (three right- and left-polarized combined modes) where the larger the CR-peaks the more dominant the contribution of the final-state configurations appropriate to the GS wave function consisting of $(0, 0, 1, -5/2)$ (strongly dominant) and $(0, 0, 0, -3/2)$ (slightly larger than 0). These transitions can be schematically described in the example inside the black dash-dotted rectangle in Fig. 6.13. The remaining intermediate state (for $\Omega_c = 0.1$) has two large peaks that are the right- and left-polarized combined modes. Differences occur due to the position of the Mn-ion as illustrated in Fig. 6.25. The first intermediate FM state ($S_z = -1$) exhibits two major transitions (for $\Omega_c = 0.02$) while the second intermediate FM state ($S_z = 1$) exhibits four major transitions (for $\Omega_c = 0.05$). Differences induced by the Mn-ion position are found similar as in the $N_e = 3$ case. The number of non-zero exchange elements increases reducing the energy difference in the resonant absorption energy. Consequently, for $\Omega_c = 0.02$, only single right- and single left-polarized

modes are recognizable as shown in Fig. 6.25. For $\Omega_c = 0.05$, we have a very interesting situation. The system has both the properties of the previous case $R_{Mn} = 0$ because of the same $S_z = 1$ and the strong effective electron-Mn-ion interaction because of $R_{Mn} = 0.5l_0$. The GS mixes several quantum states of $M_z = -1/2, -3/2$, and $-5/2$ ($S_z + M_z = -3/2$). The number of major CR-lines increases (four) as shown by the dotted grey curve in Fig. 6.25 with two right- and two left-polarized combined modes.

We note that for an even number of electrons ($N_e = 2, 4, ...$) the FM phase generally is not as pronounced as that for the case of an odd number of electrons ($N_e = 1, 3, 5, ...$) and this fact leads to the appearance of only two major peaks (Figs. 6.24 and 6.25) for $\Omega_c \geq 0.1$. Apparently, Fermi-Dirac statistics plays an essential role because the filling effect, as seen clearly in case $N_e = 4$ for the intermediate states $S_z = \pm 1$ and 0, influences directly the spin exchange interaction. To witness a stronger influence of the electron-Mn-ion interactions on the IR absorption spectrum for $\Omega_c \geq 0.1$, we refer to the AFM phase.

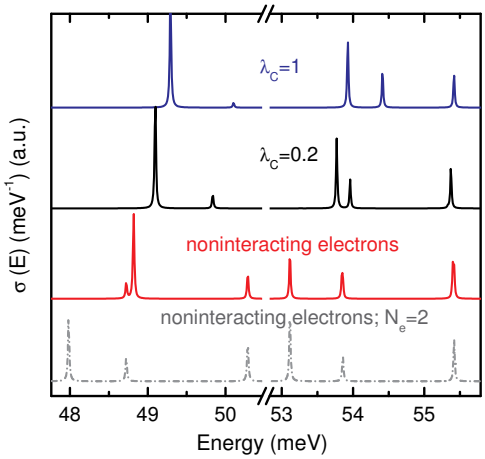

Figure 6.27: Coulomb interaction strength dependence of the magneto-optical absorption energy of a three-electron QD for $\Omega_c = 0.1$ in case the Mn-ion is located at the center of the dot. The absorption energy for the same QD in case without e-e interaction for $N_e = 2$ electrons (bottom) is plotted for reference.

6.3.5 Five-electron quantum dot

The IR absorption energies for $N_e = 5$ show a difference for $R_{Mn} = 0$ and $R_{Mn} = 0.5l_0$ when the system is in the FM phase. This is similar to the

case $N_e = 3$ (see Refs. [77, 83]) where the system for small field ($\Omega_c = 0.02$) for $R_{Mn} = 0$ ($S_z = 1/2$) reveals more peaks than for $R_{Mn} = 0.5l_0$ ($S_z = -1/2$) because of the spin-spin interaction. However, different from the case $N_e = 3$ due to p-p (orbital) e-e interaction effect, the absorption energies for $N_e = 5$ are considerably different for example for $\Omega_c = 0.02$. A left-polarized mode can be at a smaller energy as compared to a right-polarized mode. This is illustrated in Fig. 6.24 where the left-polarized combined modes of the spin-down s-, spin-up p^+-, and spin-up p^--electron and of the two spin-up p-electrons are, respectively, the first and the fourth peak (sorted in energy). The remaining peaks are, respectively sorted in energy, the right-polarized CR-lines of the three p-electrons and the left-polarized CR-line of the spin-down s- and spin-up p^+-electron. Idem remark holds for $R_{Mn} = 0.5l_0$ (Fig. 6.25) where the two largest-OS peaks are the left-polarized absorption energies. At a larger field ($\Omega_c = 0.1$), there is only one right-polarized CR-line (the lowest-energy one). Three remaining large-OS peaks are the left-polarized modes combining the σ^+(s) of, respectively, the spin-down s- and spin-up p^--electron, the two p^+- and p^--electron, and the two s- and spin-up p^+-electron(s). Besides the major CR-peaks discussed above we note the existence of the very-low-OS peaks ($\approx 2 \div 5\%$ of the total OS) in all three cases of N_e that are evidence of the influence of the electron-Mn-ion interactions when the small component to the GS becomes the dominant one in the excited states.

6.4 Conclusion

6.4.1 Concluding remarks for single-electron quantum dot

We studied the CR transition properties of a Mn^{2+}-doped QD containing a single electron confined by a parabolic potential in the presence of magnetic field. The transition energies and the OS were obtained for different positions of the Mn-ion with different confinement strengths.

As compared to the usual QD (see e.g. Ref. [180]) without a Mn-ion, new transition frequencies are found to be allowed. These new transitions are due to the presence of the spin exchange interaction of the electron with the Mn-ion which mixes the FD orbitals. Furthermore, the energy spectrum exhibits many anti-crossings of energy levels that are not present in the usual single-electron parabolic QD system.

At small magnetic fields the electron spin and the Mn-ion spin are parallel which is similar to a FM state. With increasing magnetic field a transition takes place where the electron spin becomes parallel to the magnetic field

direction leading to an AFM state. This FM-AFM transition exhibits clear signatures in the CR absorption spectrum: 1) the CR transition energies are discontinuous, 2) the OS of the allowed transitions are discontinuous, and 3) the number of allowed transitions, i.e. the number of peaks in the CR absorption spectrum, is different in the FM and in the AFM states. The magnetic field value at which the FM-AFM transition occurs depends on the position of the Mn-ion and on the confinement strength S_C which also influences the CR absorption spectrum. Besides, the anti-crossings in the energy spectrum, which are due to the spin-spin exchange interactions, result in anti-crossings in the transition energies and at the same time crossings in the OS. This is due to the fact that around these anti-crossings (in the energy spectrum), there are competitions between two energy levels as the major contribution to the electron transition. Both of these energy levels contribute about $40:60\%$ or $50:50\%$ to the transition e.g. from the GS to the p state with positive or negative azimuthal quantum number. The number and the positions of these anti-crossings (crossings) change with changing the Mn-ion position and S_C.

At high magnetic field where the energy levels "convert" to Landau levels, we obtained the magnetic-ion-position dependence of the CR-lines for different confinement strengths and investigated it for increasing confinement strength. The electron transition to higher energy levels exhibits an oscillatory behavior as function of the position of the Mn-ion. However, there is one particular Mn-ion position, i.e. the center of the QD, where the OS is independent of S_C.

6.4.2 Concluding remarks for many-electron quantum dot

We find that the electron transition energy in parabolic QD with a single Mn-ion depends on the strength of the e-e interaction λ_C and the number of electrons in the QD. The e-e interaction shifts and splits the two main branches (the upper-energy ones) of the absorption spectrum at the FM-AFM transition magnetic field. λ_C changes the position of the low-OS branches significantly and different branches are found.

In a many-electron QD without a Mn-ion the CR spectrum consists of two peaks due to Kohn's theorem. The reason for the breakdown of Kohn's theorem is the presence of the Mn-ion, which leads to spin exchange interaction with the electrons of the QD. Moving this Mn-ion to different positions in the QD corresponds to changing the magnitude of the exchange interactions and leads to changes in the absorption energy spectrum.

For $\mathrm{N}_e = 2$, in the FM region, the spin-spin e-Mn-ion interactions share

their contributions to the total OS with the two "direct" transitions of the two s-electrons in which the total S_z is conserved. In the AFM region, this leads to discontinuities in the OS and the respective transition energy and separate the two transitions of the s- and the p^+-electrons in energy. These two transitions address, respectively, the p^- and d^0 orbitals. At the FM-AFM transition magnetic field, we observed that the OS exhibits a discontinuity for all the CR peaks. When the system is in the FM phase, the transition energy exhibits only minor differences as compared to the case without a Mn-ion. When the system is in the AFM phase, however, there are major differences in the absorption energy spectrum. The separation of the two upper peaks in the CR spectrum depends on the effective e-e interaction strength and the position of the Mn-ion. The heights of these two upper peaks change with changing position of the Mn-ion and their relative heights exchange OS at each anti-crossing in the transition energy. The electrons spin-spin exchange with the Mn-ion and the strength of it depends on the position of the Mn-ion. Therefore, changing the Coulomb interaction strength λ_C will affect the absorption energy spectrum by e.g. separating or merging the two above electron transitions. When the Mn-ion is moved away from the center of the dot, the exchange interactions become nonzero resulting in additional CR peaks. The number of these branches reduces as λ_C increases. When the e-e interaction is turned off, we found that the transitions that become allowed due to the spin exchanges increase in OS.

E-e interaction in a few-electron QD doped with a single Mn-ion considerably affects the system IR absorption spectrum by changing the number and strength of electron transitions. The reason is that the center-of-mass motion now couples differently with the relative motions and also with the Mn-ion coordinate in the electron-Mn-ion spin exchange expression. Because the relative motions contain information about the e-e interactions. This fact leads to the existence of various IR absorption spectra for different number of electrons in which many transitions of different electrons have different energy. In the high-magnetic-field limit (strongly polarized electron system) different (lowest-Landau-level) electrons have separate transition energies and each time the number of electrons increases by one the number of major CR peaks increases by one *e.g.* from three (for $N_e = 2$) to four (for $N_e = 3$). Combined (right- or left-polarized) electron CR-lines reduce their contributions to zero. Only CR-lines that correspond to essential right- or left-polarized modes, *i.e.* each of which refers to a specific transition energy with a unique final state, are possible.

7

Few-electron quantum dots doped with two Mn^{2+} impurities

The magnetic properties of many-electron ($N_e = 1, 2, 3, 4$) CdTe QDs doped with two magnetic Mn-ions are studied in the presence of a magnetic field. We find that the short-range anti-ferromagnetic coupling between the Mn-ions compete with the contact spin exchange interaction between the electrons and the Mn-ions resulting in different magnetic phases that depend on the relative positions of the Mn-ions. In the presence of an external magnetic field, we obtain intermediate Mn-spin states which manifest themselves as steps in the magnetization and cusps in the (addition) energy curves. Different orientations of the spins of the electrons and the magnetic Mn-ions induce local anti-ferromagnetic-ferromagnetic and ferromagnetic-anti-ferromagnetic transitions. We present phase-diagrams of the different magnetic states of the Mn-ion sub-system for different N_e and arbitrary positions of the Mn-ions. We specify spin-glass-like state regions which are characterized by "frustration" of the spin-spin exchange interactions. Symmetric and asymmetric Mn-ion positions in the QD are examined and its influence on the magnetic polaron state, radial electron density, and electron spin-pair correlations are investigated.

7.1 Introduction

Diluted magnetic ion doping of CdTe/ZnTe semiconductor QDs has been recently realized experimentally. QDs containing a single, two, three,... Mn-ions could be realized [47, 48] and the interaction between the localized magnetic moment and the electron (hole) in a single dot was investigated through local probe photoluminescence. Scientists have gained a lot

Based on the manuscript:

- N. T. T. Nguyen and F. M. Peeters (submitted to Phys. Rev. B).

of experience in controlling the spin properties of single-manganese-doped solid-state systems (in particular in the II-VI semiconductors) [28, 34, 35, 44, 54, 87, 88, 89, 90, 93, 94, 95, 96].

In a diluted magnetic semiconductor (DMS) [10, 186] structure as for example a II(Mn)VI self-assembled QD, there exists a stable ferromagnetic ordering called magnetic polaron. A magnetic polaron is a combo of a single electron (hole) and a collection of ferromagnetically ordered Mn-ions [24, 55]. This state is a result of the electron-Mn-ion (e-Mn-ion) interaction which can be tuned by e.g. the gate voltage. Information can be stored in the magnetic moments of the Mn-ions based on such tunable magnetic states. Future interest is focused on the control of the hybrid states of a few spin objects which may be relevant for quantum computing.

The properties of few electrons interacting with few Mn-ions [24, 28, 54, 55, 87, 88, 89, 90, 93, 94, 95, 96] have been theoretically explored for a few specific quantum systems especially for self-assembled QDs. This system exhibits many prominent spin-related physics e.g. RKKY interaction in competition with screening of the electrons, magnetic polaron [24, 55], magnetic states, e-Mn-interaction induced exciton lines, etc. Cd(Mn)Se QDs which contain several manganese dopants have been prepared [44]. When injecting charged particles into these DMS QDs, a long life-time of excitons was measured which was a result of the exchange e-Mn interaction. They also observed photo-induced magnetization even up to room temperature. Cd(Mn)Te QDs, which have a negative product of the Landé g-factors of the host electrons and the Mn-ions are expected to exhibit interesting spin-related physics. It motivated us to present a numerical "exact" study beyond the single Mn^{2+} dopant quantum dot system. The breaking-symmetry spin-spin exchange interactions between the electrons and the Mn-ions are strongly affected by the presence of an external field and is modified when the position of the Mn-ions in the CdTe semiconductor QD is varied. The microscopic many-particle states of the above system are studied in the present work.

Previous studies of Cd(Mn)Te QDs containing a few Mn-ions include ferromagnetism in hard-wall-cubic noninteracting-electron structure [54], electronic properties of quasi-two-dimensional (2D) few-electron system at zero field [28], intra-band absorption spectrum for single-electron three-dimensional system [89], and magnetism [96] in low-density Mn-ion system using the local spin density approximation (LSDA). Magnetism of different II-VI materials e.g. Cd(Mn)Se (positive product of the g-factors of the host electrons and the Mn-ions) crystals were theoretically examined in e.g. Ref. [95]. Using exact diagonalization the author [95] found interesting magnetic

anisotropy, which is known as one of the important physical characteristics of a memory element.

Here, we study a 2D Cd(Mn)Te few-electron parabolic QD using the ED approach. In the presence of a magnetic field this becomes more involved due to the opposite g-factor signs, i.e. $g_e \cdot g_{Mn} < 0$. We investigate different local/system magnetic phases formed with respect to the spin orientation of the particles in strong/weak exchange interaction extremes. The obtained magnetic polaron states which are governed by the dominant e-Mn spin exchange are discussed in detail with respect to changes in the Mn-Mn interaction strength, the number of electrons, and the magnitude of external magnetic field. Spin arrangements in the high magnetic field limit provides an effective "tool" to evaluate the e-e correlations in the presence of the two Mn-ions.

7.2 Hamiltonian

The Hamiltonian of N_e-electron QD in the presence of several (N_{Mn}) Mn-ions (we consider $\mathrm{N}_{Mn} = 2$ with coordinates $\overrightarrow{R_1}$ and $\overrightarrow{R_2}$) - whose spin-spin couple interaction with each other is expressed as

$$H_{Mn}^{exc} = J_{12}^{Mn}(|\overrightarrow{R_1} - \overrightarrow{R_2}|)\overrightarrow{M_1} \cdot \overrightarrow{M_2} \tag{7.1}$$

- in second quantization form reads:

$$\begin{aligned}\hat{H} =& \sum_{i,\sigma} E_{i,\sigma} c_{i,\sigma}^{+} c_{i,\sigma} + \frac{1}{2} \sum_{ijkl\sigma\sigma'} \langle i,j|V_0|k,l\rangle c_{i,\sigma}^{+} c_{j,\sigma'}^{+} c_{k,\sigma'} c_{l,\sigma} \\ &+ \frac{1}{2}\hbar\omega_c[g_e m^* S_z + g_{Mn} m^* (M_{1z} + M_{2z})] \\ &- \sum_{k=1}^{N_{Mn}=2} \sum_{ij} \frac{1}{2} J_{ij}\left(\overrightarrow{R}\right)[\left(c_{i,\uparrow}^{+} c_{j,\uparrow} - c_{i,\downarrow}^{+} c_{j,\downarrow}\right) M_{kz} \\ &+ c_{i,\uparrow}^{+} c_{j,\downarrow} M_k^{-} + c_{i,\downarrow}^{+} c_{j,\uparrow} M_k^{+}] \\ &+ J_{12}^{Mn}(|\overrightarrow{R_1} - \overrightarrow{R_2}|)[\frac{1}{2}(M_1^{+} M_2^{-} + M_1^{-} M_2^{+}) + M_{1z} M_{2z}].\end{aligned} \tag{7.2}$$

The third term takes into account both Zeeman energies of, respectively, the electrons and the Mn-ions with the Landé g-factor g_e and g_{Mn}, respectively. Notation i in the first sum labels the single-particle Fock-Darwin (FD) states $\varphi_{i=\{nl\}}\left(\overrightarrow{r}\right) = \frac{1}{l_H}\sqrt{\frac{n!}{\pi(n+|l|)!}}\left(\frac{r}{l_H}\right)^{|l|} e^{-il\theta} e^{-\frac{r^2}{2l_H^2}} L_n^{|l|}\left(\frac{r^2}{l_H^2}\right)$ with cor-

responding on-site energy: $E_{i,\sigma} = \hbar\omega_H(2n + |l| + 1) - \hbar\omega_c l/2$. The hybrid frequency $\omega_H = \sqrt{\omega_0^2 + \omega_c^2/4}$, where $\omega_c = eB/m_e^*$ is the cyclotron frequency, defines a new length scale $l_H = \sqrt{\hbar/m_e^*\omega_H}$. The dimensionless parameter $\Omega_c = \omega_c/\omega_0$ is introduced for convenience. The zero-range e-Mn-ion spin-spin exchange interaction (strength $J_c = 1.5 \times 10^3 meV\mathring{A}^2$ for CdTe) is expressed by $J_{ij}(\overrightarrow{R}) = J_c\varphi_i^*(\overrightarrow{R})\varphi_j(\overrightarrow{R})$, the product of single-electron FD wave functions i and j at the position of the Mn-ion. The two-Mn-ions interact with each other through the anti-ferromagnetic spin exchange interaction, that is governed by the interaction strength J_{12}^{Mn} that exponentially decreases with the separation $R_{12} = |\overrightarrow{R_1} - \overrightarrow{R_2}|$ between the two Mn-ions. The form of the radial dependence of the Mn-ion interaction is $J_{12}^{Mn}(\overrightarrow{R_1}, \overrightarrow{R_2}) = J_{12}^0 \exp\{-\lambda(|\overrightarrow{R}_{12}|/a_0 - 1)\}$ with $J_0^{12} = 0.5$ meV and $\lambda = 5.1$, was chosen according to experiment work [186] where the two ions are assumed to interact most strongly when they are nearest neighbors in the Mn-lattice with lattice spacing $a_0 = 5.4\mathring{A}$. The next-nearest-neighbor interaction between the Mn-ions is five times less and could be negligible. The remaining parameters are taken the same as the ones applied for a CdTe based QD system used throughout the previous chapters.

For numerical implementations, it is worth to note that adding another Mn-ion increases the size of the Hilbert space that becomes now six times larger. Configuration state wave function Ψ_k in Eq. (3.8) is changed to

$$\Psi_k = \frac{1}{\sqrt{N_e!}} \begin{vmatrix} \psi_{\alpha_{1k}}(\overrightarrow{x_1^*}) & \psi_{\alpha_{1k}}(\overrightarrow{x_2^*}) & ... & \psi_{\alpha_{1k}}(\overrightarrow{x}^*_{N_e}) \\ \psi_{\alpha_{2k}}(\overrightarrow{x_1^*}) & \psi_{\alpha_{2k}}(\overrightarrow{x_2^*}) & ... & \psi_{\alpha_{2k}}(\overrightarrow{x}^*_{N_e}) \\ ... & & & \\ \psi_{\alpha_{N_e k}}(\overrightarrow{x_1^*}) & \psi_{\alpha_{N_e k}}(\overrightarrow{x_2^*}) & ... & \psi_{\alpha_{N_e k}}(\overrightarrow{x}^*_{N_e}) \end{vmatrix} \times \chi_{\sigma_{M_{1z}k}}(\overrightarrow{M_1}) \cdot \chi_{\sigma_{M_{2z}k}}(\overrightarrow{M_2}). \quad (7.3)$$

Effort in numeral implementations therefore will be added as compared to the work throughout chapters 4, 5, and 6.

In our numerical work we constrained the distance between the Mn-ions to be: $R_{12} \geq a_0$. The e-Mn spin exchange interaction $J_{ij}(\overrightarrow{R}) \propto \varphi_i^*(\overrightarrow{R})\varphi_j(\overrightarrow{R})$, however, depends not only on the individual Mn-ion position but also on the single-particle quantum states of the electrons that was studied in detail in e.g. Refs. [77, 82, 83]. At a nonzero magnetic field, due to the magnetic squeezing effect (e.g. on the wave function), the e-Mn interaction is strongly affected while the Mn-Mn exchange interaction $J_{12}^{Mn}(|\overrightarrow{R_1} - \overrightarrow{R_2}|)$ is independent on the magnetic field.

Following the previous studies [85], we define the ferromagnetic (FM)

and antiferromagnetic (AFM) phases in accordance with the spin states of the two subsystems (of the electrons and the Mn-ions) with respect to each other. Due to the fact that at high magnetic fields each couple of electron and Mn-ion has anti-parallel spins, this can be considered as an AFM phase. In the small magnetic field range, e.g. in particular the $N_e = 1$ case the FM phase is found mostly. The Mn-ions in their subsystem also exhibit two local

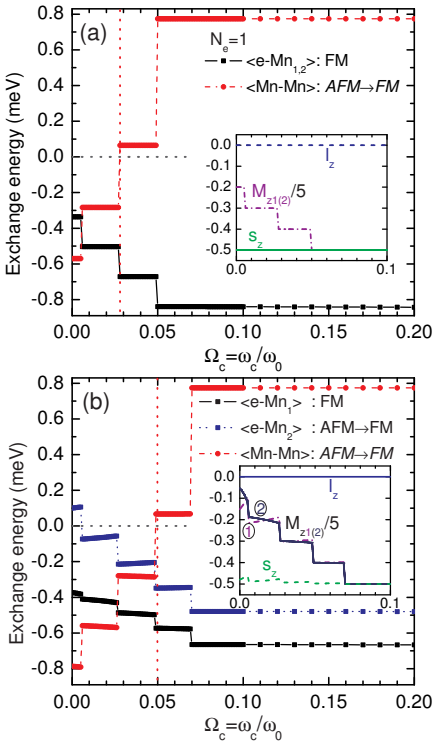

Figure 7.1: Spin exchange energies of the e-Mn [black curve with squares in (a), black and blue curves with squares in (b)] and the Mn-Mn interactions (red curve with circles) of one-electron QD for two different individual positions of the Mn-ions $[(\pm 0.13 l_0, 0)]$ (a) and $[(0.5 l_0, 0), (0.76 l_0, 0)]$ (b) with the same distance $R_{12} = 0.26 l_0$. The respective average properties including $(l_z, s_z, M_{1z}, M_{2z})$ of the single electron are shown in the two insets.

phases (*AFM* and *FM*) in accordance with their relative spin orientations, and from now on we will distinguish the FM and AFM phases of the overall system with that of the two phases of the subsystem by referring the latter phases as the local ones and we write them in *italic*.

With the presence of the second Mn-ion, which can be positioned at different positions (symmetric or asymmetric with respect to the center of the dot and at different relative distance), we obtain different spin arrangements of the two subsystems, and the study of the interactions of particles can become rather complex.

7.3 Single-electron quantum dot

In the above mentioned experiment [48], the authors started their measurements by inserting an electron and hole in the magnetic QD. The previous studies [28, 48, 82, 83] showed that at zero magnetic field, the Mn-ion ferromagnetically couples to the electrons. Its strength depends on the position of the Mn-ion, the number of electrons, and the Coulomb interaction strength. First we discuss the single-electron QD doped with a single Mn-ion and found that this ferromagnetic coupling holds only within a limited range of magnetic field. The electron can have two values of the z-component of its spin $s_z = \mp 0.5$, corresponding to the FM and AFM phases, as compared to the electron of the same system without a Mn-ion which has only $s_z = +0.5$ when $B \neq 0$. Now we introduce a second Mn-ion. We find that the Mn-ion is less sensitive to the presence of the external magnetic field as previously was found with one Mn-ion: with a slightly larger than zero magnetic field the Mn-ion spin instantly turns antiparallel to the direction of the magnetic field, with a minimum value $M_z = -5/2$ (see Ref. [83]). Here, the phase with the Mn-ion(s) spin $-5/2$ occurs after the presence of the intermediate phases where M_z of the Mn-ions can be $-1/2$, $-3/2$ ($> -5/2$) (see Fig. 7.1 and following discussion).

7.3.1 Local magnetic phases and addition phase-diagram in the FM phase of the system

We first consider the case of $R_{12} = 0.26 l_0$ where symmetric $\overrightarrow{R_1}, \overrightarrow{R_2} = (\pm 0.13 l_0, 0)$ and asymmetric $\overrightarrow{R_1}, \overrightarrow{R_2} = (0.5 l_0, 0), (0.76 l_0, 0)$ positions of the Mn-ions are examined in Fig. 7.1 for small B-field. Three energies are considered here: the spin-spin exchange of the electron with the Mn-ion - the fifth term - and of the Mn-ions with each other - the last term in Hamiltonian (7.2). At this separation, the Mn-Mn exchange interaction is AFM at $B = 0$ (Fig. 7.2) with its strength about 0.6 meV. Remember that in this case the Mn-Mn exchange energy dominates the e-Mn-ion energy. This M_z-intermediate region is $\Omega_c \leq 0.03$ for the case the Mn-ions are symmet-

rically located $[(\pm 0.13 l_0, 0)]$ [Fig. 7.1(a)] and $\Omega_c \leq 0.05$ for the other case $[(0.5 l_0, 0), (0.76 l_0, 0)]$ [Fig. 7.1(b)]. In Fig. 7.1, we also plot the exchange

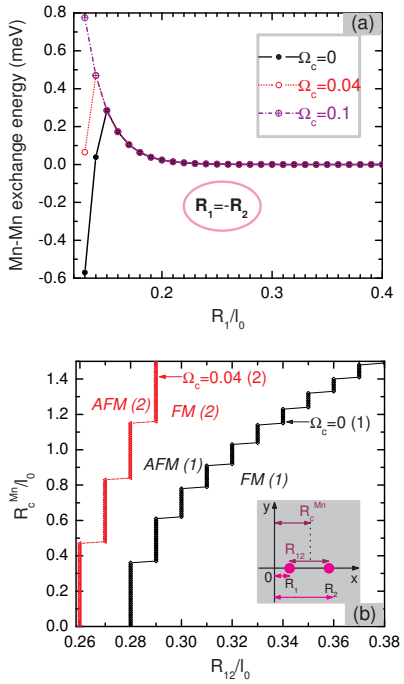

Figure 7.2: (a) Exchange energy of the Mn-Mn spin interaction for symmetric positions (b) Phase-diagram of the Mn-ion subsystem as a function of the center-of-mass and the radial coordinates of the two Mn impurities for $\Omega_c = 0$ and 0.04 indicated by (1) and (2), respectively. The region above each curve is the *AFM* and below the *FM* phase. The inset shows a schematic plot of the positions of the Mn-ions defining the Mn-ion relative (R_{12}) and center-of-mass (R_c^{Mn}) coordinates.

energies (of the e-Mn and the Mn-Mn spin interactions) as a function of magnetic field and find that the behavior of these properties (the spin exchange of the electron with the Mn-ions and between the Mn-ions) are different. The steps found in the exchange energies are identical to the steps found in the $< M_z >$ in the insets of Fig. 7.1 which are evidence that the system transits through the Mn-ion intermediate spin states. For the first case where the ions are symmetrically located, the electron couples equally ferromagnetically with the pair of Mn-ions. This is illustrated by the black curve with squares in Fig. 7.1(a). Within the plotted magnetic field range,

the electron and the Mn-ions clearly stay in the *FM* phase and the electron has spin $s_z = -0.5$. However, the Mn-Mn interaction (red curve with dots) exhibits two "local" phases (*AFM* and *FM*) of the Mn-subsystem with a crossover point around $\Omega_c = 0.03$. Maintaining the distance between the ions but changing the individual positions shifts the crossover point of the Mn-subsystem to a larger magnetic field $\Omega_c = 0.05$ [see Fig. 7.1(b)] and breaks the equality of the two Mn-contributions. These now separate into two different curves (the black full and blue dashed curves with square symbols) in which we focus our attention on the zero-field behavior of the three quantities. The spin-spin exchange interaction of the electron with Mn_1, $\overrightarrow{R_1}$, starts from the FM phase and stays in that phase while the spin exchange with the second Mn-ion, $\overrightarrow{R_2}$, starts at the AFM (at $B = 0$) and goes to the FM phase. The direct exchange interaction between the two magnetic impurities is now also different from the earlier one where the two Mn-ions are positioned symmetric around the center of the QD.

We note that the position $(0.76l_0, 0)$ by no means decides either FM or AFM coupling of the Mn-ions with the electron for $B = 0$. In other words, if these two Mn-ions are positioned symmetrically at $[(\pm 0.76l_0, 0)]$ or at another position that is not far from the center of the QD, the electron will ferromagnetically couple with both Mn-ions (see the phase-diagram Fig. 1 in Ref. [85]). The key is that the system becomes asymmetric when the Mn-ions are positioned asymmetrically inside the QD. Note that the two Mn-ions anti-ferromagnetically couple with each other hence they will couple with the electron with a definite spin state in two different manners as they do in the asymmetric case and the whole system stays without frustration, unlike the case when the two Mn-ions are symmetrically located. The symmetry of the Mn-ion positions results in equal e-Mn couplings while the Mn-ions are *AFM* coupled leading to frustration, which is similar to a spin-glass-like state in diluted magnetic semiconductors [10] and therefore we call it a *frustrated* state. In summary, the frustrated state occurs when e-Mn-ion interaction is in the pronounced FM phase and the Mn-ions stay in their local *AFM* state which occurs when R_{12} is small.

We illustrate the above frustrated behavior using the wave function in case $\overrightarrow{R}_{1,2} = (\pm 0.13l_0, 0)$ for zero magnetic field. Unlike the single-electron single-doped problem where the ground-state energy can have configurations with two different electron spin states ($s_z = \pm 1/2$), the electron spin in the double-doped system is always polarized with $s_z = -1/2$. Therefore, the commutation relation $[\widehat{H}, \widehat{s_z} + \widehat{M_{1z}} + \widehat{M_{2z}}] = 0$ with an unchanged s_z leads to the main spin exchange interaction between the Mn-ions. The $B = 0$

wave function can be approximated by: $\Psi \approx a(\Phi_1 - \Phi_4) - b(\Phi_2 - \Phi_3)$ where Φ_i is a configuration state function described by a set of quantum numbers $(n_r, l, s_z, \mathbf{M}_{1z}, \mathbf{M}_{2z})$. Φ_1, Φ_2, Φ_3, and Φ_4, respectively, have the following sets of quantum numbers $(n_r, l, s_z, \mathbf{M}_{1z}, \mathbf{M}_{2z}) = (0, 0, -1/2, \mathbf{1/2}, \mathbf{\text{-}5/2})$, $(0, 0, -1/2, \mathbf{\text{-}1/2}, \mathbf{\text{-}3/2})$, $(0, 0, -1/2, \mathbf{\text{-}3/2}, \mathbf{\text{-}1/2})$, and $(0, 0, -1/2, \mathbf{\text{-}5/2}, \mathbf{1/2})$ where energy minimization leads to the coefficients $a \approx 0.423$ and $b \approx 0.560$. The FD that gives the main contribution is the one with quantum numbers $(n_r, l) = (0, 0)$. The above expression explains the FM (between the electron and the Mn-ions) and the local *AFM* (between the Mn-ions) phase in the system. The e-Mn FM coupling is understood by the dominant direct exchange (without spin flip) of the electron and Mn-ion spins. Both Mn-ions have the same $< M_z >$ (in this case -1) but are anti-ferromagnetically coupled with each other. The reason is that the direct exchange of Mn-spins, that is the first component in the sum in the last line of Eq. (7.2), in this case is $< \Psi|M_{1z}M_{2z}|\Psi > \approx a^2\{< \Phi_1|M_{1z}M_{2z}|\Phi_1 > + < \Phi_4|M_{1z}M_{2z}|\Phi_4 > \} + b^2\{< \Phi_2|M_{1z}M_{2z}|\Phi_2 > + < \Phi_3|M_{1z}M_{2z}|\Phi_3 >\} = 2(-5/4a^2 + 3/4b^2)$, which is slightly larger than zero due to the fact that $a^2 \lesssim b^2$. Instead, the exchange terms [including spin flip - the two left terms in the last line of Eq. (7.2)], in this case $\sum_{|i-j|=1}(-ab) < \Phi_i|M_1^+M_2^- + h.c.|\Phi_j >$ in which each $< \Phi_i|M_1^+M_2^- + h.c.|\Phi_j >$ is positive, they are additive and negative. This leads to the existence of the *AFM* state for the Mn-ion subsystem.

By slightly increasing R_{12} to $0.3l_0$ while the Mn-ions are still symmetrically located we obtain the Mn-ion *FM* phase for $B = 0$. The symmetric wave function yields: $\Psi = -(a_1\Phi_1 + a_2\Phi_2)$ ($a_1 \approx 0.48$, $a_2 \approx 0.88$) with Φ_1 and Φ_2, respectively, the quantum state configuration $(n_r, l, s_z, M_{1z}, M_{2z}) = (0, 0, 1/2, 5/2, 5/2)$ and $(0, 0, -1/2, -5/2, -5/2)$, where $\sqrt{< M_{1z}M_{2z} >} = 5/2$.

Therefore, there exists another type of local $AFM - FM$ transition with respect to the Mn-ion separation $\overrightarrow{R}_{12}$ and center-of-mass $[\overrightarrow{R}_c^{Mn} = (\overrightarrow{R_1} + \overrightarrow{R_2})/2]$ besides the one discussed before. The latter transition is found when the magnetic field is sufficiently small because when increasing the field, the subsystem will start with the *FM* state. The frustrated state is then no longer found.

All of the above physics are mainly obtained when the subsystem overcomes the $AFM - FM$ transition while the whole system is still in the FM phase (e-Mn(s) couplings).

Note that the Mn-Mn spin exchange interaction is short ranged, say $R_{12} < 0.4l_0$, as seen in Fig. 7.2(a). For example, for $N_e = 1$ in case the Mn-ions are symmetrically located at $(\pm 0.13l_0, 0)$ this local transition is found

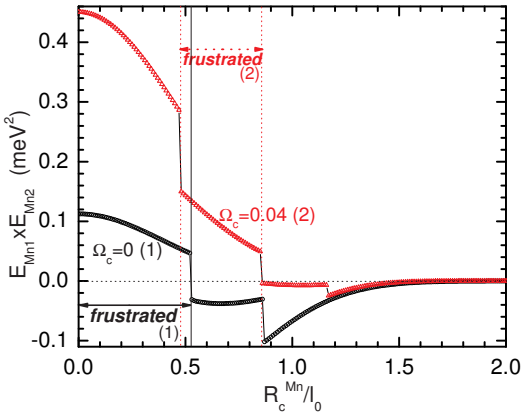

Figure 7.3: Product of the two electron-Mn-ion exchange energies as a function of the Mn-ion center-of-mass (with relative separation $R_{12} = 0.26l_0$). (1) and (2) differentiate $\Omega_c = 0$ and 0.04, respectively.

at $\Omega_c = 0.03$ [full red curve with circles in Fig. 7.1(a)] as compared to the FM-AFM transition which occurs for magnetic field $\Omega_c = 0.73$. We found that the corresponding values for $N_e = 2$ are 0.09 and 1.89, respectively and for $N_e = 3$ are 0.09 and 2.3, respectively, etc. Keeping this separation between the Mn-ions unchanged but displacing the individual Mn-ions will change the above values of the local and system magnetic transition fields slightly.

We summarize the behavior of the local magnetic phases with respect to the center-of-mass and the separation of the Mn-ions in Fig. 7.2(b) for two typical magnetic fields. Here, up to $\Omega_c = 0.1$ the Mn-ion subsystem is in the *FM* state which remains with changing magnetic field or/and the Mn-ion individual positions. Steps in the local phase-diagram are obtained each time M_z of the Mn-ions transit to a different intermediate Mn-spin state and $J_{12}^{Mn}(|\overrightarrow{R_1} - \overrightarrow{R_2}|)$ changes. In combination with the behavior of the e-Mn couplings in Fig. 7.3, regions appear where the system is frustrated. Such frustrated regions are the regions where two conditions are fulfilled: 1) local Mn-ion subsystem is in the *AFM* state, and 2) the product of the two e-Mn energies positive. As an example see Fig. 7.3, the frustrated region for $R_{12} = 0.26l_0$ is found for $R_c^{Mn} \leq 0.52l_0$ when $\Omega_c = 0$ and $0.48 \leq R_c^{Mn} \leq 0.85l_0$ for $\Omega_c = 0.04$.

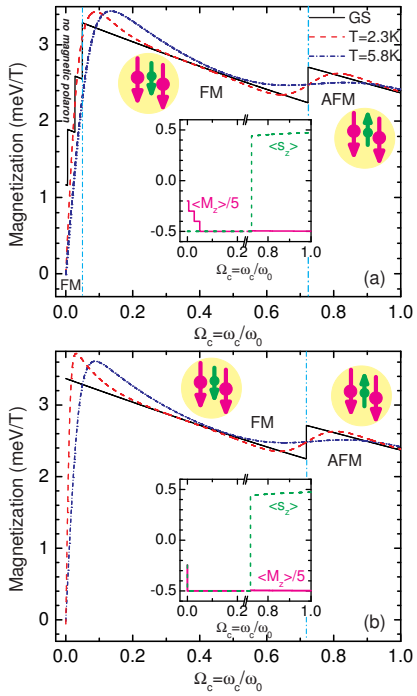

Figure 7.4: Magnetization of one-electron QD doped with two Mn-ions that are located at (a) $(\pm 0.13 l_0, 0)$ - the positions as plotted in Fig. 7.1(a) and at (b) $(\pm 0.15 l_0, 0)$ for two different temperatures. The insets are the average value of s_z and M_z. FM and AFM indicate the ferromagnetic and anti-ferromagnetic phases of the system. Big (small) arrows in each yellow circle refer to the Mn-ions (electron) in the magnetic polaron state.

7.3.2 Magnetic-polaron mechanism and the AFM phase of the system

Because the electron in our model can have two possible spin states there exist two possible magnetic polaron states: ferromagnetic polaron (electron and the Mn-ions ferromagnetically coupled) and anti-ferromagnetic polaron (electron anti-ferromagnetically couples with each Mn-ion). Conditions for the Mn-ions to be *FM* were discussed before: either the ions are largely separated or/and the magnetic field is sufficiently large i.e. $\geq$ the *AFM − FM transition* field. By further increasing the field under the latter condition the whole system will transit to the AFM phase. If both conditions are simultaneously fulfilled a magnetic polaron state is obtained at zero field and

the crossover of the two (ferromagnetic and anti-ferromagnetic) magnetic polaron states occurs at the FM-AFM transition field. As an example, for $\overrightarrow{R}_{1,2} = (\pm 0.15 l_0, 0)$ this critical (identical) field is found at $\Omega_c = 0.72$.

In this chapter, we demonstrate that the magnetization ($< M >_{B=0} = -\partial < E_{GS} > /\partial B$), which is studied in Fig. 7.4 for two typical symmetric cases of the Mn-ion positions as a function of magnetic field, can be used to examine the e-Mn-ion spin exchange interaction. For small R_{12} i.e. the Mn-Mn interaction is sufficiently strong, the magnetization exhibits a large variation as R_{12} slightly increases. The magnetic field dependence of the magnetic polaron states (yellow circles containing electron and two Mn-ions) is observed in different manners for the two cases. The steps which

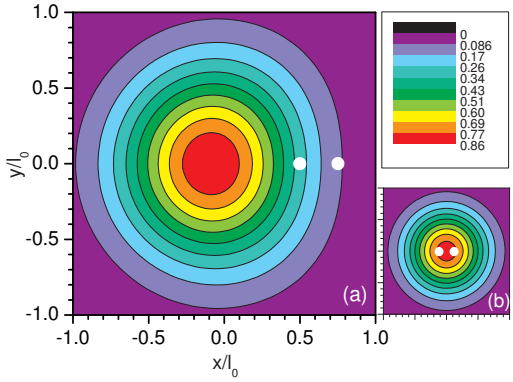

Figure 7.5: Radial density scaled to l_0^2 of one-electron QD with the two Mn-ions (white dots) located at (a) $(0.5 l_0, 0)$ and $(0.76 l_0, 0)$, and at (b) $(\pm 0.13 l_0, 0)$ at $\Omega_c = 5$. Radial density in (a) and (b) are plotted for the same range.

appear each time the spins of either the electron or the Mn-ions transit to a smaller/larger intermediate state have the same nature as the steps discussed above in Fig. 7.1 and change with changing R_{12}. The thermodynamic magnetization $< M(T) >= -\partial < E(T) > /\partial B$ for several different temperatures intersects at the FM-AFM transition. This offers a tool to study the magnetic properties at the transition field.

As the system transits to the AFM phase in which the electrons anti-ferromagnetically couple with the Mn-ions (the Mn-ions ferromagnetically couple with each other), see Fig. 7.5, the magnetic polaron is always formed. The electron density distribution in the magnetic polaron is shown in Fig. 7.5. The electron radial density is not much affected by the presence of the two

Mn-ions as compared to the case with a single or without a Mn-ion. The reason is that the electron is mostly found at the s-FD-level (with the center of the dot as the largest density point). However, the Mn-ions break the circular symmetry as illustrated in Fig. 7.5(a). The electron density near the presence of the Mn-ions [around the two points $(0.5l_0, 0)$ and $(0.76l_0, 0)$] seems to be pushed towards the center of the dot even though the electron is attracted to the Mn-ion. This is due to the repulsion between the Mn-ions which couple FM with each other.

7.4 FM and AFM phases for N_e=3

7.4.1 Reentrance of the frustrated state in a three-electron system

The existence of intermediate M_z values (such as $M_{1(2)z} = -1/2, -3/2$) which is due to the presence of the second Mn-ion does not depend on the individual position of each Mn-ion provided that their separation is small, i.e. $R_{12} < 0.4l_0$ and that the spin Mn-Mn exchange interaction is strong. This effect can still be observed for the case of many electrons in small magnetic fields.

However, we found that for the two-Mn-ion system, odd and even number of electrons behave differently. The reason is that the z-projection of the total spin of the electrons is zero for e.g. $N_e = 2$ and nonzero for e.g. $N_e = 3, 5$. In addition, for odd number of electrons that half fills either the two p-orbitals in case of $N_e = 3, 5$ while the s- or either p-shell are the fully filled states, interacts weakly with the Mn-ions [in this case $\overrightarrow{R}_{1,2} = (\pm 0.13l_0, 0)$]. The Mn-Mn interaction dominates and becomes the only appreciable spin-exchange contribution. This leads to an interesting phenomenon for the ground state in which the total $S_z \approx 1/2$ (not $-1/2$ as for the case of $N_e = 1$) and all the states that have either the two electron configurations $(n_r, L_z, S_z) = (0, \pm 1, 1/2)$ and $M_{1z} = -M_{2z}$ share the same contribution. Explicitly, the wave function is expressed as: $\Psi \approx -c\{[\psi_1 + \psi_2 + \psi_5 + \psi_6 + \psi_9 + \psi_{10}] - [\psi_3 + \psi_4 + \psi_7 + \psi_8 + \psi_{11} + \psi_{12}]\}$ where all of the twelve state configuration functions $\{\psi_i; i = 1, 3, 5, 7, ...\}$ have the same electron configuration of $(n_r, L_z, S_z) = (0, 1, 1/2)$ and the others with even i have $(0, -1, 1/2)$. The Mn-spin parts of the configuration i are as mentioned above $M^i_{1z} = -M^i_{2z}$ and $M^{1,2}_{1z} = 5/2$, $M^{3,4}_{1z} = 3/2$, ..., $M^{11,12}_{1z} = -5/2$. The state with $S_z = -1/2$ does not exist as GS, in contrast to the case when there is only a single Mn-ion [85]. Instead, we found $S_z = 1/2$.

The reason for the above difference for $N_e = 1$ and $N_e = 3$ relates to the positions of the Mn-ions and consequently to the e-Mn exchange strength that is proportional to the overlap of the electron configuration state functions ψ_i and ψ_j in the product $\psi_i^*(\overrightarrow{R}_{Mn})\psi_j(\overrightarrow{R}_{Mn})$ evaluated at the position of one Mn-ion. Practically, when the Mn-ions are located at

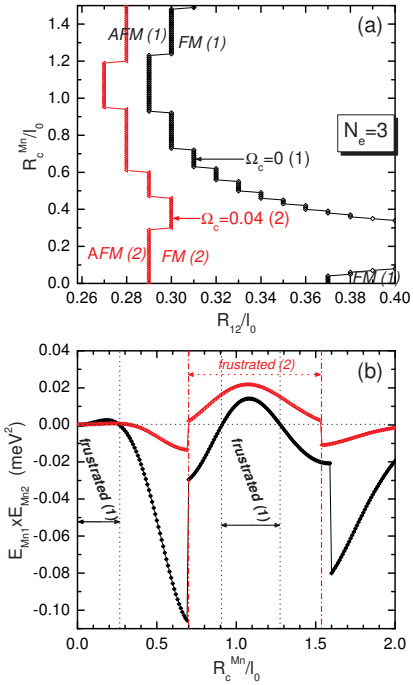

Figure 7.6: (a) Phase-diagram of the local magnetic orders of the Mn-ion subsystem in a three-electron QD for two magnetic fields $\Omega_c = 0, 0.04$ indicated by (1) and (2), respectively. (b) Product of the two e-Mn-ion energies as a function of the Mn-ion center-of-mass for the above two fields in (a) for the case $R_{12} = 0.26l_0$.

$(\pm 0.13l_0, 0)$, the diagonal element of the e-Mn interaction Hamiltonian for $N_e = 1$ is the s-FD and for $N_e = 3$ the p-FD state. For the Mn-ion positions very close to the center of the dot the s-FD state element is much larger than the p elements. The e-Mn coupling in both cases are found ferromagnetic even though the magnitude of the coupling in the case $N_e = 3$ is almost zero but still negative.

Frustration appears again for $N_e = 3$. Filling effect makes the $N_e = 1$- and $N_e = 3$-electron QDs behave differently and affects the e-Mn-ion interac-

tion. Apparently, the frustration effect appears more complex as compared to the case of a single electron as can be summarized in Fig. 7.6 where we examine the magnetic order of the Mn-ion-subsystem in a three-electron QD for two typical fields $\Omega_c = 0$ and 0.04. A reentrance of the local magnetic-state is found [see Fig. 7.6(a)]: $FM - AFM - FM$ as a function of R_c while keeping the "composed" Mn-ions at a constant R_{12} e.g. $0.38l_0$. This is due to the shell-filling effect in the three-electron problem [83]. Qualitatively, for $\Omega_c \geq 0.1$ and similar to the case $N_e = 1$, the Mn-ion subsystem is always found in the FM phase. The steps in the local phase-diagram for N_e=3 have the same nature as the steps obtained in the local phase-diagram for N_e=1. Frustrated regions are found in the two regions $0 < R_c < 0.27l_0$ and $0.91l_0 < R_c < 1.28l_0$ that are "sandwiched" between the normal (negative product of the two e-Mn-ion energies) magnetic state regions. The reentrant frustrated region is more pronounced and coincides with the maximum behavior of the e-Mn interactions for $N_e = 3$ [around $(l_0, 0)$ for B=0]. Increasing the field to $\Omega_c = 0.04$ (red line with triangles in Fig. 7.6) the subsystem is still found in the AFM state and the frustrated region is mainly found within $0.7l_0 \leq R_c \leq 1.53l_0$. Note that as the Mn-ions are located far away from the center of the dot, the problem converts to the situation without a Mn-ion and this results in a zero product $E_{e-Mn_1} \mathrm{x} E_{e-Mn_2}$. As before, in the presence of a magnetic field, the frustration will be eased with the occurrence of the local AFM-FM transition of the Mn-ion subsystem. Besides, when the two Mn-ions, in case of $N_e = 3$, are moved further away from the center of the dot, states with total $S_z \approx 1/2$ are found.

For $\Omega_c \in (0, 0.1)$, before the state with fully polarized Mn-ions, we observed the intermediate spin states. For $N_e = 1$, the electron state has spin $s_z = -1/2$ where the coupling between the electron and the Mn-ions are FM for $\Omega_c \leq 0.73$ (Fig. 7.4). For $N_e = 3$, this range is shortened to $\Omega_c \lesssim 0.1$. We note that the intermediate state co-exists with the local AFM state of the Mn-ion subsystem. For illustrative purpose, we plot in Fig. 7.7 the exchange energy of the two types of spin couplings e-Mn and Mn-Mn for the case $R_{12} = 0.26l_0$. The local AFM-FM transition of the Mn-ion subsystem is found at $\Omega_c = 0.09$ for the cases $\overrightarrow{R_1} = (-0.13l_0, 0)$, $\overrightarrow{R_1} = (0.5l_0, 0)$, and at $\Omega_c = 0.07$ for the case $\overrightarrow{R_1} = (l_0, 0)$. The FM-AFM transition magnetic field is: $\Omega_c = 2.3$, 2.28, and 0.22, respectively. In this figure, we observe three different behaviors both in the local AFM-FM and the system FM-AFM transitions. For the case with symmetric coupling between the Mn-ions (red squares) these two transitions in Fig. 7.7(b) appear at $\Omega_c = 0.09$ and 2.3, respectively. M_{1z} in this case [red triangles in Fig. 7.7(c)] visits several in-

termediate M_z states before the subsystem transits to the stable local *FM* state at $\Omega_c = 0.09$. At the same time the e-Mn and the Mn-Mn exchange

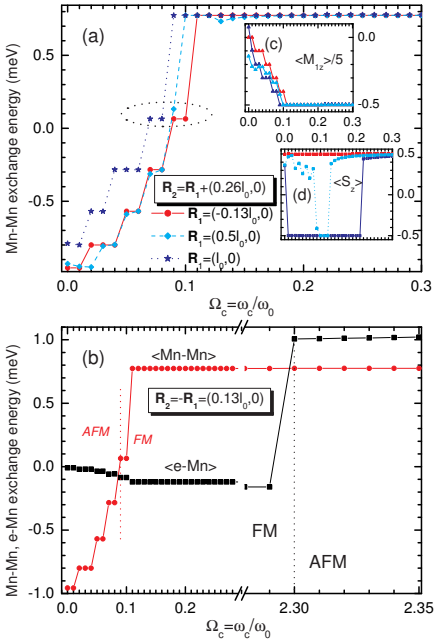

Figure 7.7: (a) Local *AFM-FM* and (b) system FM-AFM of a three-electron QD with strongly coupled Mn-Mn ($R_{12} = 0.26l_0$) that are located at different individual positions (a). Insets (c) and (d) are the M_{1z} and S_z for (a). Dotted ellipse in (a) highlights the local *AFM-FM* transition. Red and black vertical dotted lines in (b) indicate, respectively, the local *AFM-FM* and the system FM-AFM for the case of symmetric coupling [red curve with circles in (a)].

energy [Fig. 7.7(b)] go through several corresponding steps with one negative e-Mn interaction and the other positive. Their signs correspond to the system e-Mn FM and the local Mn-Mn *AFM* couplings. When the two Mn-ions transit to the local *FM* state, the e-Mn energy stays negative until the whole system transits to the AFM phase at $\Omega_c = 2.3$. The magnetic field transition for $N_e = 1$ occurs when $\Omega_c = 0.73$. In this case is $s_z = 0.5$ as the magnetic field is slightly larger than zero and s_z stays unchanged through the system FM-AFM transition. When the first Mn-ion is located at $\overrightarrow{R_1} = (l_0, 0)$ i.e. the position when the diagonal element J_p (p shell) is maximal at $B = 0$, S_z equals -0.5 in the FM state and when the system

transits to the AFM state at $\Omega_c = 0.22$ it increases to 0.5 [see Fig. 7.7(a)]. The system FM-AFM occurs at a rather large magnetic field of $\Omega_c = 2.28$.

7.4.2 Weak Mn-Mn coupling

Neither the intermediate Mn-spin states nor frustration is found in case of a slightly larger R_{12}. For example, if the two Mn-ions are symmetrically located at $(\pm 0.2l_0, 0)$ (thus $R_{12} = 0.4l_0$) [see Fig. 7.6(a)] it corresponds to an almost-zero Mn-Mn exchange interaction. The spin states of the Mn-ions become again very sensitive to the presence of the magnetic field. Plus, for the cases of $N_e = 1, 3$ the total S_z is negative $(-1/2)$ as the system is in the FM state and positive (1/2 or 3/2) as the system transits to the AFM state. The Mn-ion spins turn to be $-5/2$ in a slightly larger than zero magnetic field. These properties are found similar to the single-doped-Mn-ion case. Only the system FM-AFM transition occurs at a larger value. As the Mn-Mn interaction becomes weakly interacting, the frustration that appears as a consequence of the strong competition between the e-Mn interactions and the Mn-Mn interaction no longer exists.

7.4.3 Large magnetic fields and anti-ferromagnetic phase

For large magnetic field, complexity reduces in large magnetic fields as compared to the small magnetic field case due to the strong spin polarization of both Mn-ions and the electrons. The electrons in high magnetic field have spin up while the Mn-ions have spins down with respect to the direction of the magnetic field. We recall that the subsystem of two Mn-ions transits to the *FM* phase, where these two Mn-ions have their spins parallel, at a magnetic field smaller than the overall FM-AFM transition magnetic field. This happens only when the two Mn-ions are located very close to each other, i.e. when the exchange interaction between them is appreciable. The system with these Mn-ions located far away from each other, as referred to the case of weak coupling above, has only one type of transition. The two subsystems at high magnetic fields have pronounced sub-phases with the same spin orientation for the same type of particles and the overall system forms the AFM phase as a result of the e-Mn coupling. The problem in case of larger magnetic field now becomes interesting as we can see from the spin correlations between the electrons that on the one hand repel each other and on the other hand are attracted to the Mn-ions. The whole system becomes strongly polarized. In the next paragraph, this property will be examined in more detail. It is worth noting that due to the above effect the frustration

effect is no longer found at high fields.

For $N_e > 1$, the radial electron density distribution becomes more complex due to the repulsion between the electrons which increases when they tend to move towards the Mn-ion spins which couple FM (i.e. repulsive). Studies of the geometrical arrangement of electrons have been probed by

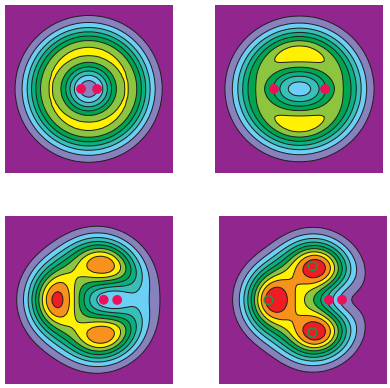

Figure 7.8: Radial electron density of three-electron QD scaled to l_0^2 with the value range (0,1.07) corresponding to a color range from violet to red in a square box where both coordinates span the region $(-1.5l_0, 1.5l_0)$ for various positions of the Mn-ion pair (magenta dots) and $\Omega_c = 6.7$. The top row, from left to right, corresponds to the symmetric cases $[\overrightarrow{R_1}, \overrightarrow{R_2}] = [(\pm 0.13l_0)]$ and $[(\pm 0.5l_0)]$, respectively. The bottom row, from left to right, corresponds to the asymmetric cases $[\overrightarrow{R_1}, \overrightarrow{R_2}] = [(0.3l_0, 0), (0.56l_0, 0)]$ and $[(0.5l_0, 0), (0.76l_0, 0)]$ (green circles are the maximal density positions in case of a single Mn-ion [85] located at $(0.5l_0, 0)$ for reference), respectively.

optical means in an experiment on an array of a large number of identical four-electron GaAs/AlGaAs QDs [187] through the examination of the roto-vibrational modes of the electron molecular states in an applied magnetic field. In this experiment, a Ti:sapphire continuous-single-mode laser was used with a back-scattering geometry where the QD array created a inelastic scattering light. The obtained excitation spectrum in the charge/spin channel gives information of the electron configuration of the system. In our system, it is clear that the position of the Mn-ion will influence the molecular state of the electrons.

For $N_e = 3$, we show the radial electron density in Fig. 7.8 with symmetric $[(\pm 0.13l_0, 0)$ and $(\pm 0.5l_0, 0)$ - top row] and asymmetric $[(0.3l_0, 0)$, $(0.56l_0, 0)$ and $(0.5l_0, 0)$, $(0.76l_0, 0)$ - bottom row] positions of the Mn-ions.

The latter cases with asymmetric positions of the Mn-ions exhibit a much stronger correlated electron state as compared to the symmetric case. Since the electrons repel each other the whole system forms a polarized arrangement. The stronger the attraction between the electrons and the Mn-ions, the less the polarization. This is illustrated in the two latter cases where in the last case with $(0.5l_0, 0)$, $(0.76l_0, 0)$ the Mn-ions are further from the high electron density region, the electrons become more polarized and their maximal density positions are the vertices of a triangle. This case exhibits the highest electron density peaks as compared to the others plotted in Fig. 7.8.

Note that under the same conditions as above but without impurities, these three electrons are found in the maximum density droplet (MDD) state where the radial electron density exhibits a single peak at the center of the dot. The physics discussed in the presence of the Mn-ions (Fig. 7.8)

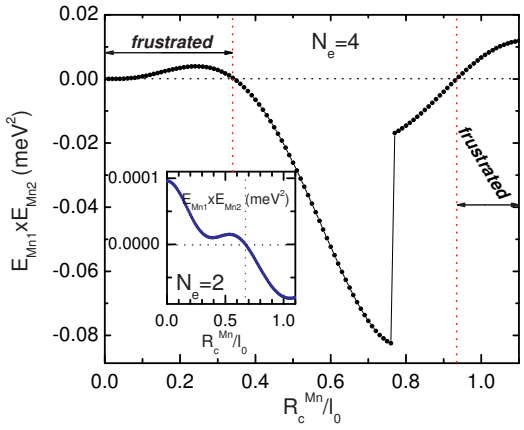

Figure 7.9: Product of the two e-Mn interaction energies as a function of the Mn-ion center-of-mass in case $\Omega_c = 0$ for $R_{12} = 0.26l_0$ and for $N_e = 2$ (inset) and 4.

is similar to the anisotropic effect induced by noncircular (e.g. triangular [188], elliptic [189]) confinement, i.e. it leads to the MDD decay: the center becomes a zero-density point.

7.5 Spin arrangements in two- and four-electron quantum dots

We discuss here results of a two- and four-electron QD in the strong Mn-Mn coupling limit. For $N_e = 2$, the two electrons are found mainly in the s

shell, the state has nonzero diagonal e-Mn exchange element, however, their total spin $S_z \approx 0$ leads to an almost-zero spin exchange e-Mn energies. The

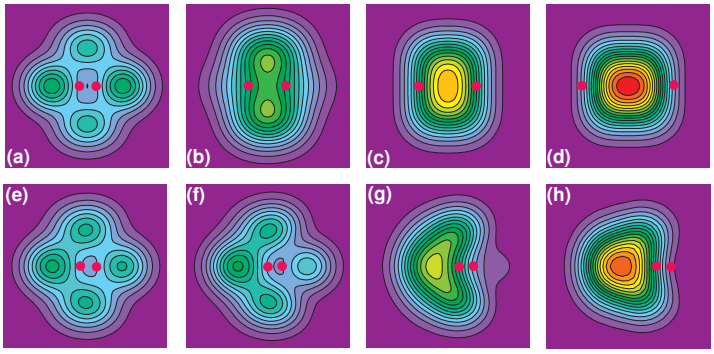

Figure 7.10: Radial electron density of two-electron QD scaled to l_0^2 with the value range (0,1.035) corresponding to a color range from violet to red in a square box where both coordinates are in the range $(-1.4l_0, 1.4l_0)$ for various positions of the Mn-ion pair (magenta dots) for $\Omega_c = 7$. The top row, from left to right, corresponds to the symmetric cases $[\overrightarrow{R_1}, \overrightarrow{R_2}] = [(\pm 0.13l_0)]$ - (a), $[(\pm 0.3l_0)]$ - (b), $[(\pm 0.5l_0)]$ - (c), and $[(\pm l_0, 0)]$ - (d), respectively. The bottom row, from left to right, corresponds to the asymmetric cases of $[R_1, R_2] = [(-0.1l_0, 0), (0.2l_0, 0)]$ - (e), $[(0, 0), (0.26l_0, 0)]$ - (f), $[(0.2l_0, 0), (0.46l_0, 0)]$ - (g), and $[(0.5l_0, 0), (0.76l_0, 0)]$ - (h), respectively.

frustration effect hence is negligible (see the inset of Fig. 7.9). The system of $N_e = 4$ is, similar to the case $N_e = 3$ and different from the system with a single Mn-ion, an a clear FM phase with total spin of the triple state $S_z = 1$ is found. For a single Mn-ion system, S_z could be ± 0.5. This makes the FM phase for $N_e = 4$ more pronounced as compared to $N_e = 2$. Intermediate states (of $M_{1,2z}$) also exist. The frustration/normal states generally have a similar structure but with smaller magnitude as compared to the case $N_e = 3$ discussed above (see Fig. 7.9). In the high magnetic field region when the whole system is polarized, spin correlations increase. Due to the existence of repulsive/attractive spin interactions, we expect to observe four maximum peaks, corresponding to the highest spin-up probabilities for the electrons.

The overall symmetry breaking as previously observed for $N_e = 1, 3$ is balanced only in case the two Mn-ions are symmetrically located as shown in Fig. 7.5(b). However, such a balance in the effective e-Mn strength can

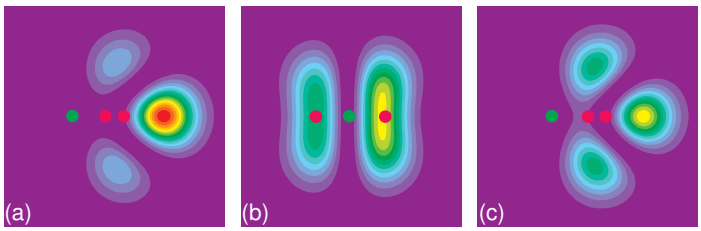

Figure 7.11: Spin-up-up pair correlation scaled to l_0^4 with the value range $(0, 0.392)$ corresponding to the color range from violet to red in a square box where both coordinates are in the range $(-1.4l_0, 1.4l_0)$ of the two electrons plotted for, from left to right, respectively, (a), (c), and (f) of Fig. 7.10 where one electron (green dot) is fixed at the position at which the probability for finding the electrons is maximum.

also be found when N_e is even. We plot in Fig. 7.10 the radial density for a two-electron QD for different positions of the Mn-ions where the maximum radial density is found in Fig. 7.10(d). For the first case where the Mn-ions are symmetrically located at $(\pm 0.13l_0, 0)$, no high electron density is found at the center of the dot because at high magnetic field the system that stays in the AFM phase transits to a state with larger quantum numbers $(n_r, L_z, S_z) = (0, 3, 1)$ where the electrons are found in the p^+ $[(n_r, l) = (0, 1)]$ and d^+ $(0, 2)$ orbitals.

Asymmetry of the positions of the Mn-ion pair breaks the symmetry of the electron radial density of the system as shown in the bottom row of Fig. 7.10. The competition between the Coulomb repulsion, Zeeman energies, and spin exchanges leads to such geometrical arrangements with a few separate density peaks.

To see the correlation between these two electrons and also to demonstrate the exchange interaction between the electrons and the Mn-ions, we study the e-e spin correlation:

$$\widehat{P}_{\sigma\sigma'}(\overrightarrow{r}, \overrightarrow{r}') = \sum_{\sigma_i,\sigma_j,i,j} \delta(\overrightarrow{r} - \overrightarrow{r_i})\delta(\overrightarrow{r}' - \overrightarrow{r_j})\delta_{\sigma\sigma_i}\delta_{\sigma'\sigma_j}. \tag{7.4}$$

The electrons are attracted to the Mn-ions, which are strongly *FM* coupled with each other, due to the AFM coupling in a highly polarized system (i.e. at larger magnetic field). We plot in Fig. 7.11 the spin-spin correlation between the electrons for the case $N_e = 2$ with the corresponding radial

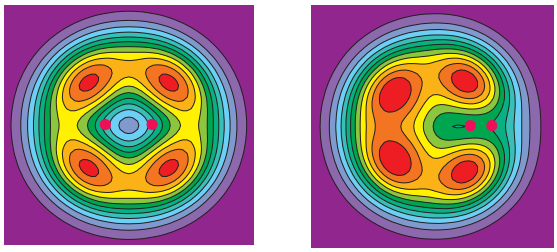

Figure 7.12: Radial electron density of four-electron QD scaled to l_0^2 with the value range (0,1.08) corresponding to a color range from violet to red in a square box where both coordinates are in the range $(1.5l_0, 1.5l_0)$ for, from left to right, respectively, symmetric $(\pm 0.3l_0, 0)$ and asymmetric $(0.3l_0, 0), (0.56l_0, 0)$ positions of the Mn-ion pair (magenta dots) for $\Omega_c = 6.7$.

densities in Figs. 7.10(a), (c), and (f). The fixed electron is positioned at the high electron density positions. Respectively, this position is chosen at $(-0.63l_0, 0)$, $(-0.05l_0, 0)$, and $(-0.54l_0, 0)$. In all three cases, the high probability for finding spin-up electrons is found at the region close to the Mn-ions.

Electron radial density for a four-electron QD is shown in Fig. 7.12 for a fixed Mn-ion separation $R_{12} = 0.26l_0$ for symmetric $(\pm 0.13l_0, 0)$ [Fig. 7.12(a)] and asymmetric $(0.5l_0, 0), (0.76l_0, 0)$ [Fig. 7.12(b)] location. In both cases, the maximal radial density of the four electrons form four peaks that mainly stay rigid from each other however are slightly pulled towards the Mn-ion positions. The former case has four peaks located at the corners of a square that is the GS configuration as a result of the symmetric positions of the Mn-ions. By displacing the two Mn-ions to asymmetric positions, as in the latter case, a deformed square structure is obtained as a result of the dominance of the e-e repulsion over the e-Mn attraction. For the latter case, the electrons are arranged in a molecular configuration (for comparison with the case without Mn-ions, see Refs. [152, 153, 154, 187]) with AFM coupling with the Mn-ions.

It is worth to note that the relative position of the Mn-ions with respect to the electrons in the case of parabolic confinement can be tuned experimentally by applying an in-plane uniform electric field $\overrightarrow{E}$, i.e. the minimum of the confinement potential is moved to $\langle \overrightarrow{r} \rangle = \frac{e\overrightarrow{E}}{m_e^* \omega_0^2}$.

7.6 Addition energy

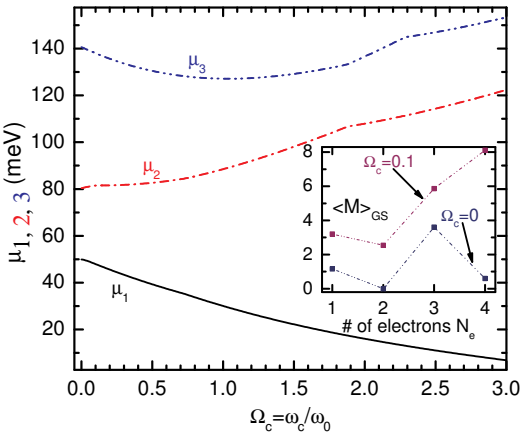

Figure 7.13: Addition energy as a function of magnetic field for Mn-ion symmetric positions $\overrightarrow{R}_{1,2} = (\pm 0.13 l_0, 0)$. Inset is the GS magnetization $< M >_{GS}$ for $N_e = 1 \div 4$ at two different fields $\Omega_c = 0$ and 0.1.

The number of confined electrons in the self-assembled system can be controlled by the gate voltage. The addition energy is defined as:

$$\mu_{N_e} = E_{GS}(N_e) - E_{GS}(N_e - 1). \tag{7.5}$$

We examine this quantity as a function of the magnetic field for fixed $\overrightarrow{R}_{1,2} = \pm(0.13 l_0, 0)$ (Fig. 7.13) and of Mn-ion center-of-mass radial coordinate for a fixed field e.g. $B = 0$ (Fig. 7.14). The cusps in the magnetic-field dependence of the addition energy (Fig. 7.13), are a consequence of the transition of the electrons higher angular momentum states and/or when the entire system transits to the AFM phase. The Mn-ion position dependence (Fig. 7.14) exhibits more cusps and these cusps exist along with the frustration effects seen in Figs. 7.3, 7.6(b), and 7.9. Note that the cusps in Fig. 7.14 are found when the whole system is in the FM phase. These cusps occur at the same Mn-positions when $N_e = 1$ and 2, and for $N_e = 3$ and 4 and are related to filling effects where the one- and two-electron QD has a GS wave function consisting of the major s-FD level and the three- and four-electron QD the p-FD levels. Thereby, the cusp found at $\Omega_c = 0.77$ in μ_4 will also occur in the μ_5 curve.

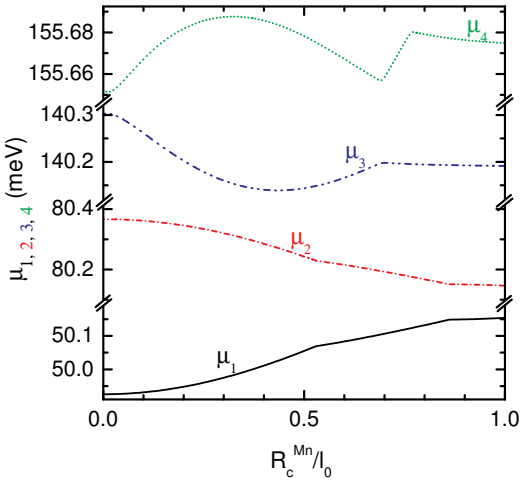

Figure 7.14: Addition energy as a function of the Mn-ion center-of-mass radius in case $R_{12} = 0.26l_0$ for $B = 0$.

7.7 Conclusion

Adding one more Mn-ion to a few-electron QD doped with a single Mn-ion is more than adding/subtracting an amount of spin-related energy. We investigated several quantum mechanical spin properties of a many-body QD system in the presence of two Mn impurities such as: ground state energy, magnetic phases, magnetic-phase transitions, electron densities, and e-e correlations.

We find that these Mn-ions can be in the AFM or FM state depending on their separation and depends strongly on the magnetic field strength. A local phase-diagram was obtained for $N_e = 1, 3$ which exhibits a series of steps corresponding to transitions of the intermediate Mn-ion spin states or/and change of order of the Mn-ion interaction (by engineering the Mn-ion distance). Each intermediate Mn-ion spin state is seen as a step in the magnetic field dependence of the magnetization. Particularly, in the small magnetic field limit the interplay of the (AFM) Mn-Mn spin exchange with the (FM) e-Mn-ion spin-spin exchange results in a spin-glass-like order called "frustrated". The larger the N_e the more complex the structure. Spin properties in this state differ from the case with a single-doped QD with the presence of the intermediate Mn-ion spin states that could be examined again as cusps in the (electron) addition energy behavior.

For the single-electron system when these two Mn-ions are in the FM ordering we obtain either a FM or a stable AFM polaron state where the crossover is found at the FM-AFM transition of the system. Plus, the magnetic polaron is found stable and during its existence the Mn-ion spin states are unchanged, i.e. there is no step observed in e.g. the magnetization. Increasing the field, first leads to a magnetic-state transition in the Mn-ion subsystem from *AFM* to *FM*. At the local transition point, the spin of the Mn-ions decreases to their minimum value $-5/2$. Keeping increasing the field, the system transits to the AFM phase where the electrons become more polarized and their AFM couplings with the Mn-ions also increase. One no longer observes such phenomenon as "frustration". If the Mn-Mn interaction is decreased (e.g. by increasing R_{12}) the system behaves just slightly differently from the case with a single dopant. Many quantities such as spin-exchange energies are enhanced by a factor of two. The intermediate states no longer occur and the whole system exhibits only one system FM-AFM transition.

In the highly polarized situation, we found that the density is the one of strongly correlated electrons in attractive AFM spin exchange with the Mn-ions. The highest density peaks are arranged in a polygon e.g. triangle for $N_e = 3$ and rectangular for $N_e = 4$. This physics is found similar to the molecule states formed due to an anisotropic confining potential i.e. the breakdown of the MDD state. We find that symmetry breaking due to the existence of asymmetric magnetic orderings can be balanced in case the Mn-ions are symmetrically located or N_e is even. These theoretical results can be useful for future measurements of e.g. the roto-vibrational modes of the electron molecular arrangements which now can be varied by displacing the magnetic impurities to different positions inside the QD or by moving the electrons with respect to the fixed Mn-ions as can be realized by an in-plane electric field.

8

Summary and future prospects

The last chapter of my thesis is devoted to summarize all the results I have achieved on parabolic magnetic QDs containing few electrons and few magnetic ion spins in the presence of a perpendicular magnetic field. Next, I propose several potential directions for future work.

8.1 Summary of the thesis

The spin-spin exchange interaction of the electrons with the Mn-ions and of the Mn-ions with each other in a QD lead to the appearance of much interesting physics. Using the CI method and the ED technique I studied the electronic and magnetic properties of QDs with few electrons confined by a parabolic potential doped with up to two magnetic impurities Mn^{2+} subjected to a perpendicular magnetic field. Such systems can be considered as model systems to examine magnetism on a micro-scale and to investigate the competition of different types of interactions e.g. electron-electron correlation, electron-Mn-ion exchange interaction, and Mn-Mn spin exchange. My thesis presents a thorough look into their interplay with one another under different circumstances of e.g. magnetic field, confinement strength, Mn-ion position, etc which lead to the occurrence of a variety of spin-related phenomena as summarized hereafter.

For numerical purposes we investigated strongly-correlated few-electron CdTe based QDs with one or two magnetic-ions. Such systems have raised much interest recently [47, 48, 62]. Experimentally, the magnetic moment of the localized Mn-ion can be probed using optical means where the exchange interaction of the electron (hole) with the localized Mn-ion results in a series of pronounced multi-peaks in PL-spectroscopy. For $B = 0$, the number of the peaks is 6 corresponding to FM coupling of the Mn-ion with the electron and the hole. The structure of these peaks change quantitatively and qualitatively by changing magnetic field. Also, the excited states in the

above system were examined [48, 75].

These important phenomena make this type of dots interesting for information readout devices where the Mn-ion spin states can be used to store information.

Chapters 4 and 5 of the thesis contributes to an understanding of the different quantum phenomena as a consequence of the spin exchange interaction between the electrons and a single Mn-ion with and without a magnetic field. The number of electrons N_e can be tuned by the gate voltage which holds great promise to control the spin states of the Mn-ions. I pointed out that the presence of the Mn-ion alters the shell-filling of the electrons due to the exchange energy $-\Delta_Z$ which strongly depends on N_e (and the Coulomb interaction strength λ_C), Mn-ion position $\overrightarrow{R}_{Mn}$, and the magnetic field $\overrightarrow{B}$. Positioning the Mn-ion at different locations results in a different exchange interaction (J) which represents the interaction between different single-particle quantum states; changing the number of electrons results in different occupation possibilities with important quantum many-body effects; and increasing the field affects the interplay between the different spin-related terms. For B=0, we found an FM coupling in the GS between the electrons and the Mn-ion whose maximal strength samples, respectively, the region around the center of the dot for the case of a single electron, and around $(l_0, 0)$ for the cases $N_e = 3, 4, 5$ electrons, etc. This peak can be predicted approximately by collecting information from: 1) Hund's rule for the occupation of the different electron states, and 2) the exchange matrix elements of the most outer orbitals these N_e electrons fill up. The cases $N_e = 2$ and 6 electrons exhibit an almost zero FM coupling ($-\Delta_Z \lesssim 0$) due to, respectively, the closed s- and p-shells. The FM coupling results in a degenerate GS energy. For the excited states, we obtained different degeneracies which are a consequence of either the FM or AFM coupling between the electrons and the Mn-ion.

These degeneracies are lifted for $B \neq 0$. Electrons in the GS do not always completely polarize. Energy levels consist of configurations which mix different spin states of the electrons and the Mn-ion. But for very large magnetic field, the Mn-ion tends to pull the electrons closer together forming a ring-like electron density profile. These are the consequences of the interplay of several effects such as the Zeeman effect (on the electrons' and the Mn-ion's spins), the Coulomb repulsion, the spin exchange interaction, etc. This competition results in a crossover from the FM to the AFM state. A re-entrant behavior of the FM-AFM transition is found as a function of the Coulomb interaction strength when the Mn-ion is moved out (but not

too far) from the center of the QD.

Collective excitations by FIR light are examined by calculating the magneto-optical spectrum of the few-electron dots with a single Mn-ion which was presented in chapter 6. As compared to QDs without Mn-ions, new allowed transition frequencies are found to be allowed. These new transitions are a consequence of the spin exchange interaction of the electron with the Mn ion which mixes the FD orbitals. Furthermore, the energy spectrum exhibits many anti-crossings of energy levels that are not present in the usual single-electron parabolic QD system. The anti-crossings, which are a consequence of the intermixing of higher quantum states due to the presence of the Mn-ion, lead to energy gaps between the levels, and result in unusual behaviors in the CR spectrum. The number and the positions of these anti-crossings (and crossings) change with changing the Mn-ion position and confinement strength S_C.

Many-body effects are found to be influenced by the strength of the e-e interaction which weakens the effective e-Mn-ion coupling and considerably affects the system IR absorption spectrum by changing the number and strength of the electron transitions. The reason is that the center-of-mass motion now couples with the relative motions and also with the Mn-ion coordinate through the electron-Mn-ion spin exchange expression. The relative motions contain information about the e-e interaction. This fact leads to different IR absorption spectra for different number of electrons in which many transitions of different electrons have different energy. In the high-magnetic-field limit (strongly polarized electron system) different (lowest-Landau-level) electrons have separate transition energies and each time the number of electrons increases by one the number of major CR peaks increases by one e.g. from three (for $\mathrm{N}_e = 2$) to four (for $\mathrm{N}_e = 3$). Combined (right- or left-polarized) electron CR-lines reduce their contributions to zero. Only CR-lines that correspond to essential right- (σ^-) or left- (σ^+) polarized modes, i.e. each of which refers to a specific transition energy with a unique final state, are possible.

Finally, the direct spin exchange between the Mn-ions is studied in chapter 7. The ultimate system of single-electron QD with two Mn-ions forms a robust [ferro(anti-ferro)] magnetic polaron state which is governed by their separation, magnetic field, and the number of electrons.

A local phase-diagram is obtained for $\mathrm{N}_e = 1, 3$ with the presence of a series of steps corresponding to the transitions of the intermediate Mn-ion spin states or/and change of order of the Mn-ion interaction (by engineering the Mn-ion distance). Each intermediate Mn-ion spin state is identical to a step found in the magnetic field dependence of the magnetization. Particu-

larly, in the small magnetic field limit the interplay of the (AFM) Mn-Mn spin exchange with the (FM) e-Mn-ion spin-spin exchange results in a spin-glass-like order called "frustrated". Keeping increasing the field, the system transits to the AFM phase where the electrons become more polarized and their AFM couplings with the Mn-ions also increases. One no longer observes "frustration" in this limit.

If the Mn-Mn interaction is decreased (e.g. by increasing $\overrightarrow{R}_{12}$) the system behaves just slightly differently from the case with a single dopant. Many quantities such as spin-exchange energies are enhanced by a factor of two. Intermediate states no longer become the GS and the whole system exhibits only one system FM-AFM transition. In the highly polarized situation, we calculated the radial density of the strongly correlated electron system with the attractive AFM spin exchange with the Mn-ions. The highest density peaks are arranged in a polygon e.g. triangle for $N_e = 3$ and rectangular for $N_e = 4$. This physics is similar to the molecule states formed in an anisotropic confining potential of a QD in the absence of magnetic impurities, i.e. we see the breakdown of the MDD state. I find that symmetry breaking due to the existence of asymmetric magnetic orderings can be balanced in case the Mn-ions are symmetrically located or when N_e is even. These theoretical results can be useful for future measurements of e.g. roto-vibrational modes of the electron molecular arrangements which now can be tuned by displacing the magnetic impurities to different positions inside the QD.

8.2 Future prospects

Using an electric field makes it possible to manipulate the Mn-ion spins. It is worth to note that the relative position of Mn-ions with respect to the electrons in the case of parabolic confinement can be tuned experimentally by applying an in-plane uniform electric field $\overrightarrow{E}$, i.e. the zero-point is moved to $\langle\overrightarrow{r}\rangle=\frac{e\overrightarrow{E}}{m_e^*\omega_0^2}$. Therefore, such few-electron dots with few impurities in an applied electric field are of interest to investigate the anisotropy of the exchange energy. In case the dot contains holes, the electric field provides a tool to examine the Stark shift under the influence of the $e(h)$-Mn and Mn-Mn exchange interactions.

For single-Mn-doped CdTe dots [47], the number of holes can be controlled over an external bias voltage V_g on an Al-Schottky gate [48] with the back-contact of the CdTe/ZnTe heterostructure. This leads to the physics of charged exciton including e.g. neutral X (the case studied in

Refs. [47, 60, 75]), bi-exciton X^2, positively and negative charged, respectively, X^+ and X^- [48]. The PL-emission of such charged QD can be tuned optically and can then be compared with the PL-lines of nonmagnetic dots. Around the resonant exciton energy $E_{ex} = 2.147$, 2.092, 2.09, and 2.088 eV, respectively, for X, X^+, X^-, and X^2, multi-peak lines were observed for the QD doped with a single Mn-ion. Such QDs are important for future research to establish deeper insights in quantum many-body effects and magnetism. The Hamiltonian describing such systems reads:

$$\hat{H} = \hat{H}_e + \hat{H}_h + \hat{V}_{e-h} + \hat{H}_{e-Mn} + \hat{H}_{h-Mn} \tag{8.1}$$

where

$$\hat{H}_e = \sum_{i=1}^{N_e} \left[\frac{\left(-i\hbar\overrightarrow{\nabla}_i^e + e\overrightarrow{A_i}(\overrightarrow{r}_i^e)\right)^2}{2m_e^*} + V_c^e\left(\overrightarrow{r}_i^e\right) \right] + \frac{1}{2}\hbar\omega_{c,e}m^{*e}g_eS_z^e + \frac{1}{2}\sum_{i\neq j}^{N_e} V\left(\overrightarrow{r}_i^e - \overrightarrow{r}_j^e\right), \tag{8.2}$$

$$\hat{H}_h = \sum_{i=1}^{N_h} \left[\frac{\left(i\hbar\overrightarrow{\nabla}_i^h + e\overrightarrow{A_i}(\overrightarrow{r}_i^h)\right)^2}{2m_h^*} + V_c^h\left(\overrightarrow{r}_i^h\right) \right] + \frac{1}{2}\hbar\omega_{c,h}m^{*h}g_hS_z^h + \frac{1}{2}\sum_{i\neq j}^{N_h} V\left(\overrightarrow{r}_i^h - \overrightarrow{r}_j^h\right), \tag{8.3}$$

$$\hat{H}_{e-Mn} = \frac{1}{2}\hbar\omega_{c,e}m^{*e}g_{Mn}^eM_z - J_c^e\sum_{i=1}^{N_e}\overrightarrow{M}.\overrightarrow{s}_i^e\delta\left(\overrightarrow{r}_i^e - \overrightarrow{R}_{Mn}\right), \tag{8.4}$$

$$\hat{H}_{h-Mn} = \frac{1}{2}\hbar\omega_{c,h}m^{*h}g_{Mn}^hM_z + J_c^h\sum_{i=1}^{N_h}\overrightarrow{M}.\overrightarrow{s}_i^h\delta\left(\overrightarrow{r}_i^h - \overrightarrow{R}_{Mn}\right), \tag{8.5}$$

and V_{e-h} is the $e-h$ self-confining potential.

The main challenge with Mn-doped III-V DMS QDs is that the Mn-ion is not isoelectronic, i.e. it results in a strongly-bound acceptor state.

Consequently, the orbital motion of carriers can be strongly perturbed due to the presence of the Mn-ion. Since the recent first investigation (2007) of single-Mn-doped InAs QDs [21] via optical means, the investigation of their magnetic were limited [21, 72] to the first excited state of the single exciton. This work is expected to be relevant for the investigation of e.g. the individual interactions in III-V QD doped with a single Mn^{2+} where the Mn-acceptor is strongly bound to the dot hole(s). FIR spectroscopy, collective excitation properties, or anisotropy energy has not been investigated yet for this system.

Coupled magnetic QDs are another promising system with novel physics. The model of two single-electron dots coupling with each other through tunneling and doped with a single Mn-ion (for the case of nonmagnetic dots see e.g. Ref. [190]) is expected to exhibit fundamental new physical properties because the single-electron coupled-dots are similar to a H_2-molecule. Now a single Mn-dopant is introduced to the coupled system which can visit both dots by an applied electric field $\overrightarrow{E}$ perpendicular to the interface. The magnetic properties of such a system are expected to be altered by the presence of the Mn-spin.

9 Samenvatting

Het laatste hoofdstuk van mijn proefschrift is gewijd aan een samenvatting van mijn resultaten over parabolische magnetische kwantumstippen met enkele elektronen en magnetische ionenspins in de aanwezigheid van een loodrecht magnetisch veld.

De spin-spin uitwisselingsinteractie van de elektronen met de Mn-ionen en van Mn-ionen onderling in een kwantumstip levert veel interessante fysica. Met behulp van de configuratie-interactie-methode en de exacte-diagonalization-techniek bestudeerde ik de elektronische en magnetische eigenschappen van elektronen met weinig kwantumstippen (KSn) begrensd door een parabolisch potentiaal gedopeerd met maximaal twee magnetische Mn^{2+} onzuiverheden onderworpen aan een loodrecht magnetisch veld. Dergelijke systemen kunnen beschouwd worden als modelsysteem om magnetisme op een micro-schaal en de competitie tussen de verschillende soorten interacties te onderzoeken. Zoals bijvoorbeeld de elektron-elektron correlatie, de elektron-Mn-ionen-uitwisselingsinteractie, en de Mn-Mn spin uitwisseling. In mijn proefschrift presenteer ik een grondige blik in hun onderlinge interactie tijdens verschillende omstandigheden van bijv. het magnetisch veld, de opsluitingssterkte, de positie van het Mn-ion, etc. die leiden tot het optreden van een groot aantal spin-gerelateerde verschijnselen, die hieronder worden samengevat.

Voor numerieke doeleinden onderzochten we sterk gecorreleerde-elektron, weinig electron CdTe gebaseerde KSn met een of twee magnetische-ionen. Dergelijk systemen staan recentelijk in de belangstelling [47, 48, 62]. Het magnetisch moment van het gelokaliseerde Mn-ion kan experimenteel bestudeerd worden met behulp van optische technieken waar de uitwisselingsinteractie van het elektron (het gat) met de gelokaliseerde Mn-ionen resulteert in een reeks van uitgesproken pieken in de multi-PL-spectroscopie. Voor $B = 0$, is het aantal van de pieken 6 overeenkomstig de ferromagnetische (FM)-koppeling van het Mn-ion met het elektron en het gat. De struc-

tuur van deze pieken veranderen kwantitatief en kwalitatief door het magnetisch veld te veranderen. Ook de aangeslagen toestanden in het hierboven beschreven systeem werden onderzocht [48, 75].

Deze belangrijke verschijnselen maken van dit soort stipjes interessantesystemen voor informatie-uitleesdoeleinden waar de Mn spin-ion-toestanden kunnen gebruikt worden voor het opslaan van informatie.

Hoofdstukken 4 en 5 van het proefschrift dragen bij tot het inzicht van de verschillende kwantumverschijnselen als gevolg van de spin-uitwisselingsinteractie tussen de elektronen en een Mn-ion met of zonder een magnetisch veld. Het aantal N_e-elektronen kan afgestemd worden door de gatspanning te veranderen, wat interessant is voor een elektrische controle van de spintoestanden van de Mn-ionen. Ik wijs erop dat de aanwezigheid van het Mn-ion de schil-vulling van de elektronen wijzigt als gevolg van de energie uitwisseling $-\Delta_Z$ die sterk afhankelijk is van N_e (en de Coulomb interactiesterkte λ_C), de Mn-ion positie van $\overrightarrow{R}_{Mn}$, en het magnetisch veld $\overrightarrow{B}$. Positionering van het Mn-ion op verschillende locaties resulteert in verschillende uitwisselingsinteracties (J), die de interactie tussen de verschillende enkel kwantum-deeltjes-toestanden voorstellen. Verandering van het aantal elektronen resulteert in verschillende bezettingsmogelijkheden van de toestanden en vertegenwoordigt het kwantum veel-deeltjes effect. Het verhogen van het veld beïnvloedt de wisselwerking tussen de verschillende spin-gerelateerde termen. Voor $B = 0$, verkreeg ik een FM-koppeling in het grondtoestand (GS) tussen de elektronen en het Mn-ion die maximal is voor respectievelijk de streek rond het midden van de stip voor het geval van een enkel elektron en rand $(l_0, 0)$ voor de gevallen N_e=3, 4, 5 elektronen, enz. Deze piek kan ruwweg voorspeld worden door rekening te houden met: 1) Hund's regel van de bezetting van de N_e elektronen en 2) de uitwisselingsmatrix componenten van de buitenste orbitalen die deze Ne elektronen vullen. De gevallen N_e=2 en 6 elektronen vertonen een bijna nul FM-koppeling ($-\Delta_Z \lesssim 0$) ten gevolge van, respectievelijk, de gesloten s- en p-schillen. De FM-koppeling resulteert in een ontaarde GS energie. Voor de aangeslagen toestanden, verkregen we verschillende ontaardingen als gevolg van hetzij de FM, hetzij de antiferromagnetische (AFM)-koppeling tussen de elektronen en het Mn-ion.

Deze ontaardingen worden opgeheven voor $B \neq 0$. Elektronen in de GS zijn niet volledig gepolariseerd. Energieniveaus bestaan uit lineaire combinaties van configuraties van verschillende spintoestanden van de elektronen en het Mn-ion. Maar voor een zeer groot magnetisch veld, brengt het Mn-ion de elektronen dichter bij elkaar dat aanleiding geeft tot de vorming van een ring-achtig elektronendichtheidsprofiel. Dit als een de gevolg van het samen-

spel van verschillende effecten, zoals het Zeeman-effect (op de elektronen en de Mn-ion spins), de Coulomb afstoting, de spin-uitwisselingsinteractie, etc. Deze competitie resulteert in een overgang van de FM naar de AFM toestand. Een nieuw "re-entrant" gedrag van de FM-AFM-overgang werd gevonden als functie van de Coulomb interactiekracht wanneer het Mn-ion wordt verplaatst (maar niet te ver) uit het centrum van de KS.

Collectieve excitaties door FIR licht zijn onderzocht in hoofdstuk 6 door het berekenen van het magneto-optische spectrum van KSn die enkele elektronen bevatten en één enkel Mn-ion. In vergelijking met KSn zonder Mn-ionen, blijken nieuwe overgangsfrequenties toegestaan. Deze nieuwe overgangen zijn een gevolg van de spinuitwisselingsinteractie van het elektron met het Mn-ion, dat aanleiding geeft tot een menging van de Fock-Darwin orbitalen. Bovendien vertoont het energiespectrum vele anti-kruisingen van de energie-niveaus die niet aanwezig zijn op het gebruikelijke enkelvoudige elektron parabolisch KS-systeem. De anti-kruisingen, een gevolg van de vermenging van hogere kwantumtoestanden als gevolg van de aanwezigheid van het Mn-ion, leiden tot een kloof tussen de energieniveaus, en resulteren in een ongewoon gedrag in het cylotron-resonantie (CR)-spectrum. Het aantal en de posities van deze anti-kruisingen (en kruisingen) veranderen met een veranderende Mn ion-positie en de opsluitingssterkte S_C.

Veel-deeltjes-effecten blijken beïnvloed door de sterkte van de e-e-interactie die de effectieve e-Mn-ion koppeling verzwakken en beïnvloeden aanzienlijk het IR-absorptiespectrum door het veranderen van het aantal en de sterkte van de toegestane elektron-overgangen. De reden hiervoor is dat het massa-centrum zich koppelt met de relatieve bewegingen en met het Mn-ion via de uitdrukking van de elektron-ion-Mn-spinuitwisseling. De relatieve bewegingen bevatten informatie over de e-e-interactie. Dit feit leidt tot verschillende IR-absorptie waneer het aantal elektronen wordt gewijsigd. In de limiet van een hoog-magnetisch veld (sterk gepolariseerde elektronen systeem) hebben verschillende (laagste-Landau-niveau) elektronen aparte overgangsenergieën en telkens als het aantal elektronen toeneemt, verhoogt het aantal pieken in het CR spectrum met één bv. van drie (voor N_e=2) tot vier (voor N_e=3). Gecombineerde (rechts-of links-gepolariseerd) elektron CR-lijnen verkleinen hun bijdragen tot nul. Alleen de CR-lijnen die overeenkomen met rechts-(σ^-) of links-(σ^+) gepolariseerde modes, d.w.z. waarvan elk naar een specifieke transitie-energie met een unieke eindtoestand verwijst, zijn mogelijk.

Ten slotte, wordt de directe spinuitwisseling tussen de Mn-ionen bestudeerd in hoofdstuk 7. We beschouwden een systeem bestaande uit enkele elektronen in een KS met twee Mn-ionen. Een robuust [ferro (anti-ferro)]

magnetisch polaron toestand werd gevonden die beinvloed wordt door de afstandtussen de Mn-ionen, het magnetisch veld, en het aantal elektronen.

Een volledige lokale fase-diagram werd verkregen voor N_e= 1, 3 met de aanwezigheid van een reeks stappen die overeenkomen met de overgangen van Mn tussentijdse-ion spintoestanden en/of verandering van volgorde van de Mn-ion interactie (door "engineering" van de Mn-ion afstand). Elke intermediaire Mn-ion spintoestand geeft aanleiding tot een stap in de magnetische veld afhankelijkheid van de magnetisatie. Met name in de limiet van een klein magnetische veld resulteert het samenspel van de (AFM) Mn-Mn spin-uitwisseling met de (FM) e-Mn-ion spin-spin-uitwisseling in een spinglas-achtige orde die "gefrustreerd" genoemd wordt. Met toenemend veld gaat het systeem over naar de AFM-fase waar de elektronen steeds meer gepolariseerd geraken en hun AFM-koppelingen met de Mn-ionen toeneemt. Men observeert geen "frustratie" meer in deze limiet.

Als de Mn-Mn interactie wordt verkleint (bijvoorbeeld door een toename van $\overrightarrow{R}_{12}$), gedraagt het systeem zich net iets anders dan in het geval met één enkel Mn-ion. Veel grootheden zoals de spin-uitwisselingsinteractie energie neemt toe met een factor twee. De tussenfasen doen zich niet langer voor en het hele systeem vertoont slechts één systeem FM-AFM overgang. In de sterk gepolariseerde situatie, krijgen we een radiale dichtheid van een sterk gecorreleerd elektronen-systeem binnen de aantrekkende AFM spin-uitwisseling met de Mn-ionen. De elektronen dichtheid vertoont pieken die gerangschikt in een veelhoek bv. een driehoek voor N_e=3 en een rechthoek voor N_e=4. Deze fysica is vergelijkbaar met de molecuultoestanden die men bekomt door een anisotrope in perkingspotentiaal voor de KS te beschouwen in de afwezigheid van magnetische onzuiverheden (dat wil zeggen het resulteert in de verdwijning van de MDD toestand). Ik vond dat symmetriebreking te wijten aan kan de asymmetrische magnetische ordeningen in evenwicht gebracht kunnen worden in geval de Mn-ionen symmetrisch gelokaliseerd zijn, of wanneer N_e even is. Dit theoretisch resultaat kan nuttig zijn voor toekomstige metingen van bijvoorbeeld roto-vibrationele toestanden van de elektron moleculaire ordeningen die nu gemanipuleerd kunnen worden door het verplaatsen van de magnetische onzuiverheden naar verschillende posities binnen de KS.

Bibliography

[1] T. Dietl, D. D. Awschalom, M. Kaminska, H. Ohno, *Spintronics, Volume 82 (Semiconductors and Semimetals)*, Ed. by E. R. Weber (Academic Press, USA, 2008).

[2] S. A. Wolf, D. D. Awschalom, R. A. Buhrman, J. M. Daughton, S. von Molnár, M. L. Roukes, A. Y. Chtchelkanova, and D. M. Treger, *Spintronics: A Spin-Based Electronics Vision for the Future*, Science **294**, 1488 (2001).

[3] *Nanomagnetism and Spintronics*, Ed. by T. Shinjo (Elsevier, Amsterdam, 2009).

[4] H. Ohno, *Semiconductor Spintronics and Quantum Computation*, edited by D. D. Awschalom, N. Samarth, and D. Loss (Springer, Berlin, 2002).

[5] R. C. Myers, M. H. Mikkelsen, J.-M. Tang, A. C. Gossard, M. E. Flatté, and D. D. Awschalom, *Zero-field optical manipulation of magnetic ions in semiconductors*, Nature Materials **7**, 203 (2008).

[6] S. Mack, R. C. Myers, J. T. Heron, A. C. Gossard, and D. D. Awschalom, *Stoichiometric growth of high Curie temperature heavily alloyed GaMnAs*, Appl. Phys. Lett. **92**, 192502 (2008).

[7] G. Binasch, P. Grünberg, F. Saurenbach, W. Zinn, *Enhanced magnetoresistance in layered magnetic structures with antiferromagnetic interlayer exchange*, Phys. Rev. B **39**, 4828 (1989).

[8] M. N. Baibich, J.M. Broto, A. Fert, F. Nguyen Van Dau, F. Petroff, P. Eitenne, G. Creuzet, A. Friederich, and J. Chazelas, *Giant Magnetoresistance of (001)Fe/(001)Cr Magnetic Superlattices*, Phys. Rev. Lett. **61**, 2472 (1988).

[9] R. T. Delves, *HgTe-MnTe alloys-II. Electrical properties*, J. Phys. Chem. Solids **24**, 885 (1963).

[10] J. K. Furdyna, *Diluted magnetic semiconductors*, J. Appl. Phys. **65**, 29 (1988).

[11] H. Ohno, *Making Nonmagnetic Semiconductors Ferromagnetic*, Science **281**, 951 (1998).

[12] T. Dietl, *Handbook of Semiconductors* volume 3B, Ed. by S. Maha jan (North Holland, Amsterdam, 1994).

[13] T. Jungwirth, J. Sinova, J. Mašek, J. Kučera, A. H. McDonald, *Theory of ferromagnetic (III,Mn)V semiconductors*, Rev. Mod. Phys. **78**, 809 (2006).

[14] M. A. Nielsen and I. Chuang, *Quantum computation and quantum information* (Cambridge University Press, Cambridge, England, 2000).

[15] I. Zutic, J. Fabian, and S. Das Sarma, *Spintronics: Fundamentals and applications*, Rev. Mod. Phys. **76**, 323 (2004).

[16] K. Olejnik, M. H. Owen, V. Novk, J. Maek, A. C. Irvine, J. Wunderlich, and T. Jungwirth, *Enhanced annealing, high Curie temperature, and low-voltage gating in (Ga,Mn)As: A surface oxide control study*, Phys. Rev. B **78**, 054403 (2008).

[17] H. Munekata, H. Ohno, S. von Molnar, Armin Segmüller, L. L. Chang, and L. Esaki, *Diluted magnetic III-V semiconductors*, Phys. Rev. Lett. **63**, 1849 (1989).

[18] H. Drexler, D. Leonard, W. Hansen, J. P. Kotthaus, and P. M. Petroff, *Spectroscopy of Quantum Levels in Charge-Tunable InGaAs Quantum Dots*, Phys. Rev. Lett. **73**, 2252 (1994).

[19] T. Dietl, P. Peyla, W. Grieshaber, and Y. Merle d'Aubigné, *Dynamics of Spin Organization in Diluted Magnetic Semiconductors*, Phys. Rev. Lett. **74**, 474 (1995).

[20] T. Jungwirth, K. Y. Wang, J. Mašek, K. W. Edmonds, Jrgen König, Jairo Sinova, M. Polini, N. A. Goncharuk, A. H. MacDonald, M. Sawicki, A. W. Rushforth, R. P. Campion, L. X. Zhao, C. T. Foxon, and B. L. Gallagher, *Prospects for high temperature ferromagnetism in (Ga,Mn)As semiconductors*, Phys. Rev. B **72**, 165204 (2005).

[21] A. Kudelski, A. Lemaître, A. Miard, P. Voisin, T. C. M. Graham, R. J. Warburton, and O. Krebs, *Optically Probing the Fine Structure of a Single Mn Atom in an InAs Quantum Dot*, Phys. Rev. Lett. **99**, 247209 (2007).

[22] A. M. Yakunin, A. Yu. Silov, P. M. Koenraad, J. H.Wolter, W. Van Roy, J. De Boeck, J.-M. Tang, and M. E. Flatté, *Spatial Structure*

of an Individual Mn Acceptor in GaAs, Phys. Rev. Lett., **92**, 216806 (2004).

[23] A. M. Yakunin, A. Yu. Silov, P. M. Koenraad, J.-M. Tang, M. E. Flatté, W. Van Roy, J. De Boeck, and J. H. Wolter, *Spatial Structure of Mn-Mn Acceptor Pairs in GaAs*, Phys. Rev. Lett., **95**, 256402 (2005).

[24] A. Kaminski and S. Das Sarma, *Polaron Percolation in Diluted Magnetic Semiconductors*, Phys. Rev. Lett. **88**, 247202 (2002).

[25] A. C. Durst, R. N. Batt, and P. A. Wolff, *Bound magnetic polaron interactions in insulating doped diluted magnetic semiconductors*, Phys. Rev. B. **65**, 235205 (2002).

[26] P. M. Krstajić and F. M. Peeters, *Double-exchange mechanisms for Mn-doped III-V ferromagnetic semiconductors*, Phys. Rev. B **70**, 195215 (2004).

[27] B. L. Sheu, R. C. Myers, J.-M. Tang, N. Samarth, D. D. Awschalom, P. Schiffer, and M. E. Flatté, *Onset of Ferromagnetism in Low-Doped* $Ga_{1-x}Mn_xAs$, Phys. Rev. Lett. **99**, 227205 (2007).

[28] F. Qu and P. Hawrylak, *Theory of Electron Mediated Mn-Mn Interactions in Quantum Dots*, Phys. Rev. Lett. **96**, 157201 (2006).

[29] H. Ohno, A. Shen, F. Matsukura, A. Oiwa, A. Endo, S. Katsumoto, and Y. Iye, *(Ga,Mn)As: A new diluted magnetic semiconductor based on GaAs*, Appl. Phys. Lett. **69**, 363 (1996).

[30] Ohno, H., Munekata, H., Penny, T., von Molnar, S., and Chang, L. L., *Magnetotransport properties of p-type (In,Mn)As diluted magnetic III-V semiconductors*, Phys. Rev. Lett. **68**, 2664 (1992).

[31] K. C. Ku, S. J. Potashnik, R. F. Wang, M. J. Seong, E. Johnston-Halperin, R. C. Meyers, S. H. Chun, A. Mascarenhas, A. C. Gossard, D. D. Awschalom, P. Schiffer, and N. Samarth, *Highly enhanced Curie temperatures in low temperature annealed (Ga,Mn)As epilayers*, cond-mat/0210426 (2002).

[32] T. Jungwirth, Jürgen König, Jairo Sinova, J. Kučera, and A. H. MacDonald, *Curie temperature trends in (III,Mn)V ferromagnetic semiconductors*, Phys. Rev. B. **66**, 012402 (2002).

[33] *Diluted Magnetic Semiconductors*, edited by M. Jain (World Scientific, Singapore, 1991).

[34] K. Chang, J. B. Xia, and F. M. Peeters, *Longitudinal spin transport in diluted magnetic semiconductor superlattices: the effect of the giant Zeeman splitting*, Phys. Rev. B **65**, 155211 (2002).

[35] K. Chang, J. B. Xia, and F. M. Peeters, *Magnetic field tuning of the effective g factor in a diluted magnetic semiconductor quantum dots*, Appl. Phys. Lett. **82**, 2661 (2003).

[36] N. Shibata, A. Ohki, and A. Katsui, *Iodine-doped low-resistivity n-type ZnSe films grown by MOVPE*, J. Cryst. Growth **93**, 703 (1988).

[37] T. Gurung, S. Mackowski, G. Karczewski, H. E. Jackson, and Leigh M. Smith, *Ultralong spin memory of optically excited single magnetic quantum dots*, Appl. Phys. Lett. **93**, 153114 (2008).

[38] Y. R. Lee and A. K. Ramdas, *A piezomodulation study of the absorption edge and Mn^{++} internal transition in $Cd_{1-x}Mn_xTe$, a prototype of diluted magnetic semiconductors*, Solid State Commun. (51), 861 (1984).

[39] S. Mackowski, T. Gurung, T. A. Nguyen, H. E. Jackson, and L. M. Smith, G. Karczewski and J. Kossut, *Optically-induced magnetization of CdMnTe self-assembled quantum dots*, Appl. Phys. Lett. **84**, 3337 (2004).

[40] S. Mackowski, T. Gurung, H.E. Jackson, L.M. Smith, G. Karczewski, J. Kossut, *Exciton-controlled magnetization in single magnetic quantum dots*, Appl. Phys. Lett. **87** 072502 (2005).

[41] H. Boukari, P. Kossacki, M. Bertolini, D. Ferrand, J. Cibert, S. Tatarenko, A. Wasiela, J. A. Gaj, and T. Dietl, *Light and Electric Field Control of Ferromagnetism in Magnetic Quantum Structures*, Phys. Rev. Lett. **88**, 207204 (2002).

[42] D. Ferrand, J. Cibert, A. Wasiela, C. Bourgognon, S. Tatarenko, and G. Fishman, T. Andrearczyk, J. Jaroszyński, S. Kolesńik, and T. Dietl, Phys. Rev. B **63**, 085201 (2001).

[43] B. E. Larson, K. C. Hass, H. Ehrenreich, and A. E. Carlsson, *Theory of exchange interactions and chemical trends in diluted magnetic semiconductors*, Phys. Rev. B **37**, 4137 (1988).

[44] R. Beaulac, P. I. Archer, X. Liu, S. Lee, G. M. Salley, M. Dobrowolska, J. K. Furdyna, and D. R. Gamelin, *Spin-Polarizable Excitonic Luminescence in Colloidal Mn^{2+}-Doped CdSe Quantum Dots*, Nano Lett. **8**, 1197 (2008).

[45] R. Beaulac, L. Schneider, P. I. Archer, G. Bacher, and D. R. Gamelin, *Light-Induced Spontaneous Magnetization in Doped Colloidal Quantum Dots*, Science **325**, 973 (2009).

[46] A. Haury, A. Wasiela, A. Arnoult, J. Cibert, S. Tatarenko, T. Dietl, and Y. Merle d'Aubigné, *Observation of a Ferromagnetic Transition Induced by Two-Dimensional Hole Gas in Modulation-Doped CdMnTe Quantum Wells*, Phys. Rev. Lett. **79**, 511 (1997).

[47] L. Besombes, Y. Léger, L. Maingault, D. Ferrand, H. Mariette, and J. Cibert, *Probing the Spin State of a Single Magnetic Ion in an Individual Quantum Dot*, Phys. Rev. Lett. **93**, 207403 (2004).

[48] Y. Léger, L. Besombes, J. Fernández-Rossier, L. Maingault, and H. Mariette, *Electrical Control of a Single Mn Atom in a Quantum Dot*, Phys. Rev. Lett. **97**, 107401 (2006).

[49] L. Besombes, Y. Léger, L. Maingault, D. Ferrand, J. Cibert, and H. Mariette, *Optical probing of the spin state of a single magnetic ion in an individual quantum dot*, Phys. Stat. Sol. (b) **242**, 1237 (2005).

[50] J. Fernández-Rossier and Ramón Aguado, *Single-Electron Transport in Electrically Tunable Nanomagnets*, Phys. Rev. Lett. **98**, 106805 (2007).

[51] J. Seufert, G. Bacher, M. Scheibner, A. Forchel, S. Lee, M. Dobrowolska, and J. K. Furdyna, *Dynamical Spin Response in Semimagnetic Quantum Dots*, Phys. Rev Lett **88**, 027402 (2002).

[52] D. Loss and D. P. DiVincenzo, *Quantum computation with quantum dots*, Phys. Rev. A **57**, 120 (1998).

[53] G. Burkard, D. Loss, and D. P. DiVincenzo, *Coupled quantum dots as quantum gates*, Phys. Rev. B **59**, 2070 (1999).

[54] J. Fernández-Rossier and L. Brey, *Ferromagnetism Mediated by Few Electrons in a Semimagnetic Quantum Dot*, Phys. Rev. Lett. **93**, 117201 (2004).

[55] A. O. Govorov, *Voltage-tunable ferromagnetism in semimagnetic quantum dots with few particles: Magnetic polarons and electrical capacitance*, Phys. Rev. B **72**, 075359 (2005).

[56] A. K. Bhattacharjee and C. Benoit à la Guillaume, *Exciton magnetic polaron in semimagnetic semiconductor nanocrystals*, Phys. Rev. B **55**, 10613 (1997).

[57] W. Zhang, T. Dong, and A. O. Govorov, *Electronic states in a magnetic quantum-dot molecule: Instabilities and spontaneous symmetry breaking*, Phys. Rev. B **76**, 075319 (2007).

[58] T. Dietl, A. Haury and Y. Merle d'Aubigné, *Free carrier-induced ferromagnetism in structures of diluted magnetic semiconductors*, Phys. Rev. B **55**, R3347 (1997).

[59] T. Baron, S. Tatarenko, K. Saminadayar, N. Magnea, and J. Fontenille, *Plasma nitrogen doping of ZnTe, $Cd_{1-x}Zn_xTe$, and CdTe by molecular beam epitaxy*, Appl. Phys. Lett. **65**, 1284 (1994).

[60] L. Besombes, Y. Leger, L. Maingault, D. ferrand. and H. Mariette, *Carrier-induced spin splitting of an individual magnetic atom embedded in a quantum dot*, Phys. Rev. B **71**, 161307(R) (2005).

[61] Y. Léger, L. Besombes, L. Maingault, D. Ferrand, and H. Mariette, *Geometrical Effects on the Optical Properties of Quantum Dots Doped with a Single Magnetic Atom*, Phys. Rev. Lett. **95**, 047403 (2005).

[62] C. Le Gall, L. Besombes, H. Boukari, R. Kolodka, J. Cibert, and H. Mariette, Phys. Rev. Lett. **102**, 127402 (2009).

[63] C. L. Cao, L. Besombes, and J. Fernndez-Rossier, *Modelling optical spin pumping of a single Mn atom in a CdTe quantum dot*, Journal of Physics Conference Series **210**, 012046 (2010).

[64] A. O. Govorov and A. V. Kalameitsev, *Optical properties of a semiconductor quantum dot with a single magnetic impurity: photoinduced spin orientation*, Phys. Rev. B **71**, 035338 (2005).

[65] L. Maingault, L. Besombes, Y. Léger, C. Bougerol, and H. Mariette,*Inserting one single Mn ion into a quantum dot*, Appl. Phys. Lett. **89**, 193109 (2006).

[66] L. Marsal, L. Besombes, F. Tinjod, K. Kheng, A. Wasiela, B. Gilles, J. L. Rouviè re, and H. Mariette, *Zero-dimensional excitons in CdTe/ZnTe nanostructures*, J. Appl. Phys. **91**, 4936 (2002).

[67] T. A. Nguyen, S. Mackowski, T. B. Hoang, H. E. Jackson, L. M. Smith, G. Karczewski, *Resonant photoluminescence imaging and the origin of excited states in self-assembled quantum dots*, Phys. Rev. B **76**, 245320 (2007).

[68] F. Tinjod, B. Gilles, S. Moehl, K. Kheng, and H. Mariette, *II-VI quantum dot formation induced by surface energy change of a strained layer*, Appl. Phys. Lett. **82**, 4340 (2003).

[69] W. Grieshaber, A. Haury, J. Cibert, Y. Merle d'Aubigné, A. Wasiela, and J. A. Gaj, *Magneto-optic study of the interface in semimagnetic semiconductor heterostructures: Intrinsic effect and interface profile in CdTe-$Cd_{1-x}Mn_xTe$*, Phys. Rev. B **53**, 4891 (1996).

[70] C. Aku-Leh, F. Perez, B. Jusserand, D. Richards, W. Pacuski, P. Kossacki, M. Menant, and G. Karczewski, *Measuring the spin polarization and Zeeman energy of a spin-polarized electron gas: Comparison between Raman scattering and photoluminescence*, Phys. Rev. B **76**, 155416 (2007).

[71] C. Le Gall, R. S. Kolodka, C. Cao, H. Boukari, H. Mariette, J. Fernández-Rossier, and L. Besombes, *Optical initialization, readout and dynamics of a Mn spin in a quantum dot*, arXiv:1003.0370v1 (2010).

[72] J. van Bree, P. M. Koenraad, and J. Fernández-Rossier, *Single-exciton spectroscopy of single Mn doped InAs quantum dots*, Phys. Rev. B **78**, 165414 (2008).

[73] M. Goryca, D. Ferrand, P. Kossacki, M. Nawrocki,1 W. Pacuski, W. Maslana, J. A. Gaj, S. Tatarenko, J. Cibert, T. Wojtowicz, and G. Karczewski, Phys. Rev. Lett. **102**, 046408 (2009).

[74] B. Patton, W. Langbein, U. Woggon, L. Maingault, and H. Mariette, *Time- and spectrally-resolved four-wave mixing in single CdTe/ZnTe quantum dots*, Phys. Rev. B **73**, 235354 (2006).

[75] M. M. Glazov, E. L. Ivchenko, L. Besombes, Y. Léger, L. Maingault, and H. Mariette, *Fine structure of exciton excited levels in a quantum dot with a magnetic ion*, Phys. Rev. B **75**, 205313 (2007).

[76] S. J. Cheng, *Magnetic response of magnetic ion-doped nanocrystals: Effects of single Mn^{2+} impurity*, Phys. Rev. B **72**, 235332 (2005).

[77] F. Qu and P. Hawrylak, *Magnetic Exchange Interactions in Quantum Dots Containing Electrons and Magnetic Ions*, Phys. Rev. Lett. **95**, 217206 (2005).

[78] J. Fernández-Rossier, R. Aguado, *Mn-doped II-VI quantum dots : artificial molecular magnets*, Phys. Status Solidi C **3**, 3734 (2006).

[79] J. Fernández-Rossier, *Single-exciton spectroscopy of semimagnetic quantum dots*, Phys. Rev. B **73** 045301 (2006).

[80] F. Qu and P. Vasilopoulos, *Influence of exchange interaction on spin-dependent transport through a single quantum dot doped with a magnetic ion*, Phys. Rev. B **74**, 245308 (2006).

[81] F. Qu and P. Vasilopoulos, *Spin transport across a quantum dot doped with a magnetic ion*, Appl. Phys. Lett. **89**, 122512 (2006).

[82] N. T. T. Nguyen and F. M. Peeters, *Correlated many-electron states in a quantum dot containing a single magnetic impurity*, Phys. Rev. B **76**, 045315 (2007).

[83] N. T. T. Nguyen and F. M. Peeters, *Magnetic field dependence of the many-electron states in a magnetic quantum dot: The ferromagnetic-antiferromagnetic transition*, Phys. Rev. B **78**, 045321 (2008).

[84] N. T. T. Nguyen and F. M. Peeters, *Ferromagnetic-antiferromagnetic transition in a magnetic quantum dot containing few electrons*, Physicalia Magazine **30**, 169 (2008).

[85] N. T. T. Nguyen and F. M. Peeters, *Cyclotron resonance of a magnetic quantum dot*, Phys. Rev. B **78**, 245311 (2008).

[86] N. T. T. Nguyen and F. M. Peeters, *Many-body effects in the cyclotron resonance of a magnetic dot*, Phys. Rev. B **80**, 115335 (2009).

[87] S. J. Cheng, *Theory of magnetism in diluted magnetic semiconductor nanocrystals*, Phys. Rev. B **77**, 115310 (2008).

[88] P. Wojnar, J. Suffczyński, K. Kowalik, A. Golnik, G. Karczewski, and J. Kossut, *Microluminescence from $Cd_{1-x}Mn_xTe$ magnetic quantum dots containing only a few Mn ions*, Phys. Rev. B **75**, 155301 (2007).

[89] I. Savić and N. Vukmirović, *Intraband magneto-optical properties of magnetic quantum dots*, Phys. Rev. B **76**, 245307 (2007).

[90] R. M. Albofath, P. Hawrylak, and I. Zutić, *Tailoring Magnetism in Quantum Dots*, Phys. Rev. Lett. **98**, 207203 (2007).

[91] R. M. Albofath, P. Hawrylak, and I. Zutić, *Electronic states of magnetic quantum dots*, New J. Phys. **9**, 353 (2007).

[92] R. M. Abolfath, A. G. Petukhov, and I. Zutić, *Piezomagnetic Quantum Dots*, Phys. Rev. Lett. **101**, (2008).

[93] S. J. Cheng and P. Hawrylak, *Controlling magnetism of semi-magnetic quantum dots with odd-even exciton numbers* , EPL **81**, 37005 (2008).

[94] A. O. Govorov, *Optical and electronic properties of quantum dots with magnetic impurities*, C. R. Phys. **9**, 857 (2008).

[95] S. J. Cheng, *Magnetic anisotropy in symmetric magnetic colloidal quantum dots doped with few Mn^{2+} impurities*, Phys. Rev. B **79**, 245301 (2009).

[96] R. M. Albofath, *Para-ortho transition of artificial H2 molecule in lateral quantum dots doped with magnetic impurities*, Phys. Rev. B **80**, 165332 (2009).

[97] A. O. Govorov, *Optical probing of the spin state of a single magnetic impurity in a self-assembled quantum dot*, Phys. Rev. B **70**, 035321 (2004).

[98] N. T. T. Nguyen and F. M. Peeters (unpublished).

[99] L. Besombes, Y. Léger, J. Bernos, H. Boukari, H. Mariette, J. Fernández-Rossier, R. Aguado, *Optical probing of spin fluctuations of a single paramagnetic Mn atom in a semiconductor quantum dot*, Phys. Rev. B **78**, 125324 (2008).

[100] L. Jacak, P. Hawrylak, and A. Wójs, *Quantum dots*, (Springer-Verlag, Berlin, 1998).

[101] T. Chakraborty, *Quantum Dots: A Survey of the Properties of Artificial Atoms*, (Elsevier Science, Amsterdam, 1999).

[102] M. A. Reed, *Spatial quantization in GaAs-AlGaAs multiple quantum dots*, J. Vacuum Sci. Technol. B **4**, 358 (1986).

[103] M. A. Kastner, *Artificial atoms*, Physics Today, **46**, 24 (1993).

[104] A. C. Ashoori, *Electrons in artificial atoms*, Nature **379**, 413 (1996).

[105] *Quantum dots: Research, Technology and applications*, edited by R. W. Knoss (Nova Science, New York, 2009).

[106] S. M. Reimann, M. Manninen, *Electronic structure of quantum dots*, Rev. Mod. Phys. **74**, 1283 (2002).

[107] R. Hanson, L. P. Kouwenhoven, J. R. Petta, S. Tarucha, and L. M. K. Vandersypen, *Spins in few-electron quantum dots*, Rev. Mod. Phys. **79**, 1217 (2007).

[108] S. Tarucha, D. G. Austing, T. Honda, R. J. van der Hage and L. P. Kouwenhoven, *Shell Filling and Spin Effects in a Few Electron Quantum Dot*, Phys. Rev. Lett., **77**, 3613 (1996).

[109] L. P. Kouwenhoven, D G Austing, and S Tarucha, *Few-electron quantum dots*, Rep. Prog. Phys. **64**, 701 (2001).

[110] L. P. Kouwenhoven, T. H. Oosterkamp, M. W. Danoesastro, M. Eto, D. G. Austing, T. Honda, and S.Tarucha, *Excitation Spectra of Circular, Few-Electron Quantum Dots*, Science **278**, 1788 (1997).

[111] T. H. Oosterkamp, *Artificial atoms and molecules: on many body effects and coherence in semiconductor quantum dots*, PhD thesis, Delft University of Technology (1999).

[112] P. L. McEuen, E. B. Foxman, U. Meirav, M. A. Kastner, Y. Meir, N. S. Wingreen, and S. J. Wind , *Transport spectroscopy of a Coulomb island in the quantum Hall regime*, Phys. Rev. Lett. **66**, 1926 (1991).

[113] *Self-Assembled Quantum Dots*, Lecture Notes in Nanoscale Science and Technology, edited by Z. M. Wang (Springer-Verlag, Berlin, 2008).

[114] P. M. Petroff and S. P. Denbaars, *MBE and MOCVD growth and properties of self-assembling quantum dot arrays in III-V semiconductor structures*, Superlattices and Microstructures **15**, 15 (1994).

[115] D. Bimberg, M. Grundmann, and N. N. Ledentsov, *Quantum Dot Heterostructures*, (John Wiley and Sons Ltd., 1999).

[116] V. M. Ustinov, N. A. Maleev, A. E. Zhukov, A. R. Kovsh, A. Yu. Egorov, A. V. Lunev, B. V. Volovik, I. L. Krestnikov, Yu. G. Musikhin, N. A. Bert, P. S. Kopíev, Zh. I. Alferov, N. N. Ledentsov, and D. Bimberg, *InAs/InGaAs quantum dot structures on GaAs substrates emitting at 1.3 μm*, Appl. Phys. Lett. **74**, 2815 (1999).

[117] D. J. Eaglesham and M. Cerullo, *Dislocation-free Stranski-Krastanov growth of Ge on Si (100)*, Phys. Rev. Lett. **64**, 1943 (1990).

[118] D. Leonard, K. Pond, and P. M. Petroff, *Critical layer thickness for self-assembled InAs islands on GaAs*, Phys. Rev. B **50**, 11687 (1994).

[119] R. J. Warburton, *Self-assembled semiconductor quantum dots*, Contemporary Physics **43**, 351 (2002).

[120] R. J. Warburton, C. S. Dürr, K. Karrai, J. P. Kotthaus, G. Medeiros-Ribeiro, and P. M. Petroff, *Charged Excitons in Self-Assembled Semiconductor Quantum Dots*, Phys. Rev. Lett. **79**, 5282 (1997).

[121] V. Kloper, R. Osovsky, J. Kolny-Olesiak, A. Sashchiuk, and E. Lifshitz, *The Growth of Colloidal Cadmium Telluride Nanocrystal Quantum Dots in the Presence of Cd^0 Nanoparticles*, J. Phys. Chem. C **111**, 10336 (2007).

[122] Y. Kobayashi, L. Pan, and N. Tamai, *Effects of Size and Capping Reagents on Biexciton Auger Recombination Dynamics of CdTe Quantum Dots*, J. Phys. Chem. C 113, 11783 (2009).

[123] T. H. Oosterkamp, J. W. Janssen, L. P. Kouwenhoven, D. G. Austing, T. Honda, and S. Tarucha, *Maximum-Density Droplet and Charge Redistributions in Quantum Dots at High Magnetic Fields*, Phys. Rev. Lett. **82**, 2931 (1999).

[124] W. Izumida, O. Sakai, S. Tarucha, *Tunneling through a Quantum Dot in Local Spin Singlet-Triplet Crossover Region with Kondo Effect*, Phys. Rev. Lett. **87**, 216803 (2001).

[125] G. W. Bryant, *Electronic structure of ultrasmall quantum-well boxes*, Phys. Rev. Lett. **59**, 1140 (1987).

[126] N. F. Johnson and M. C. Payne, *Exactly solvable model of interacting particles in a quantum dot*, Phys. Rev. Lett. **67**, 1157 (1991).

[127] D. Pfannkuche, R. R. Gerhardts, P. A. Maksym, and V. Gudmundsson, *Theory of quantum dot helium*, Physica B **189**, 6 (1993).

[128] Y. Alhassid, *The statistical theory of quantum dots*, Rev. Mod. Phys. **72**, 895 (2000).

[129] E. Wigner, *On the Interaction of Electrons in Metals*, Phys. Rev. **46**, 1002 (1934).

[130] X. Hu and S. Das Sarma, *Hilbert-space structure of a solid-state quantum computer: Two-electron states of a double-quantum-dot artificial molecule*, Phys. Rev. A **61**, 062301 (2000).

[131] B. Szafran, J. Adamowski, and S. Bednarek, *Few-electron systems in quantum cylinders*, Phys. Rev. B **61**, 1971 (2000).

[132] H. Saarikoski, A. Harju, M. J. Puska, and R. M. Nieminen, *Vortex Clusters in Quantum Dots*, Phys. Rev. Lett. **93**, 116802 (2004).

[133] B. Reusch, Wolfgang Husler, and Hermann Grabert, *Wigner molecules in quantum dots*, Phys. Rev. B **63**, 113313 (2001).

[134] C. Yannouleas and U. Landman, *Spontaneous Symmetry Breaking in Single and Molecular Quantum Dots*, Phys. Rev. Lett. **82**, 5325 (1999).

[135] C. C. J. Roothaan, *New Developments in Molecular Orbital Theory*, Rev. Mod. Phys. **23**, 69 (1951).

[136] C. C. J. Roothaan, *Self-Consistent Field Theory for Open Shells of Electronic Systems*, Rev. Mod. Phys. **32**, 179 (1960).

[137] M. Fujito, A. Natori, and H. Yasunaga, *Many-electron ground states in anisotropic parabolic quantum dots*, Phys. Rev. B **53**, 9952 (1996).

[138] K. Hirose, and N. S. Wingreen, *Spin-density-functional theory of circular and elliptical quantum dots*, Phys. Rev. B **59**, 4604 (1999).

[139] D. G. Austing, A. Sasaki, S. Tarucha, S. M. Reimann, M. Koskinen, and M. Manninen, *Ellipsoidal deformation of vertical quantum dots*, Phys. Rev. B **60** 11514 (1999).

[140] S. M. Reimann, M. Koskinen, M. Manninen, and B. R. Mottelson, *Quantum Dots in Magnetic Fields: Phase Diagram and Broken Symmetry at the Maximum-Density-Droplet Edge*, Phys. Rev. Lett. **83**, 3270 (1999).

[141] B. Partoens and F. M. Peeters, *Molecule-Type Phases and Hund's Rule in Vertically Coupled Quantum Dots*, Phys. Rev. Lett. **84**, 4433 (2000).

[142] B. Partoens, *Artificial Molecules: A theoretical study of electron correlations in two vertically coupled quantum dots*, PhD thesis, University of Antwerp (2000).

[143] L. F. Lemmens, F. Brosens, and J. T. Devreese, *Many-body diffusion and path integrals for identical particles*, Phys. Rev. E **53**, 4467 (1996).

[144] F. Brosens, J. T. Devreese, and L. F. Lemmens, *Thermodynamics of coupled identical oscillators within the path-integral formalism*, Phys. Rev. E **55**, 227 (1997).

[145] S. N. Klimin, V. M. Fomin, F. Brosens, and J. T. Devreese, *Ground state and optical conductivity of interacting polarons in a quantum dot*, Phys. Rev. B 69, 235324 (2004).

[146] F. Fock, *Bemerkung zur Quantelung des harmonischen Oszillators im Magnetfeld*, Z. Phys. **46**, 446 (1928).

[147] C. G. Darwin, *The Diamagnetism of the Free Electron*, Proc. Camb. Philos. Soc. **27**, 86 (1931).

[148] Gradshteyn, I. S. and Ryzhik, I. M., *Table of Integrals, Series, and Products*, edited by A. Jeffrey, fifth edition (Academic Press, 1994).

[149] P. A. Maksym and T. Chakraborty, *Quantum dots in a magnetic field: Role of electron-electron interactions*, Phys. Rev. Lett., **65**, 108 (1990).

[150] S. A. Mikhailov, *Quantum-dot lithium in the strong-interaction regime: Depolarization of electron spins by a magnetic field*, Phys. Rev. B **66**, 033307 (2002).

[151] S. A. Mikhailov, *Two ground-state modifications of quantum-dot beryllium*, Phys. Rev. B **66**, 153313 (2002).

[152] M. B. Tavernier, E. Anisimovas, F. M. Peeters, B. Szafran, J. Adamowski, and S. Bednarek, *Four-electron quantum dot in a magnetic field*, Phys. Rev. B **68**, 205305 (2003).

[153] M. B. Tavernier, E. Anisimovas, and F. M. Peeters, *Correlation between electrons and vortices in quantum dots*, Phys. Rev. B **70**, 155321 (2004).

[154] M. B. Tavernier, E. Anisimovas, and F. M. Peeters, *Ground state and vortex structure of the N=5 and N=6 electron quantum dot*, Phys. Rev. B **74**, 125305 (2006).

[155] G. J. Iafrate, K. Hess, J. B. Krieger, and M. Macucci, *Capacitive nature of atomic-sized structures*, Phys. Rev. B **52**, 10737 (1995).

[156] M. Macucci, Karl Hess, and G. J. Iafrate, *Numerical simulation of shell-filling effects in circular quantum dots*, Phys. Rev. B **55**, R4879 (1997).

[157] M. Manninen, S. Viefers, M. Koskinen, and S. M. Reimann, *Many-body spectrum and particle localization in quantum dots and finite rotating Bose condensates*, Phys. Rev. B **64**, 245322 (2001).

[158] P. A. Maksym, *Magic number ground states of quantum dots in a magnetic field*, Physica B **184**, 385 (1993).

[159] T. Seki, Y. Kuramoto, and T. Nishino, *Origin of Magic Angular Momentum in a Quantum Dot under Strong Magnetic Field*, Journal of Physical Society of Japan, **65**, 3945 (1996).

[160] J. K. Jain, *Composite-fermion approach for the fractional quantum Hall effect*, Phys. Rev. Lett. **63**, 199 (1989).

[161] J. K. Jain, *Theory of the fractional quantum Hall effect*, Phys. Rev. B **41**, 7653 (1990); see also *Erratum: Theory of the fractional quantum Hall effect: Incompressible quantum Hall states*, Phys. Rev. B **42**, 9193(E)(1990).

[162] S. Bednarek, B. Szafran, and J. Adamowski, *Many-electron artificial atoms*, Phys. Rev. B **59**, 13036 (1999).

[163] P. A. Maksym, *Eckardt frame theory of interacting electrons in quantum dots*, Phys. Rev. B **53** 10871 (1995).

[164] A. H. MacDonald, S.-R.Eric Yang, M.D. Johnson, *Quantum Dots in Strong Magnetic Fields: Stability Criteria for the Maximum Density Droplet*, Aust. J. Phys. 46, 345 (1993); or can be achieved at arXiv:cond-mat/9301019v1 (1993).

[165] B. Szafran, S. Bednarek, and J. Adamowski, *Magnetic-field-induced transformations of Wigner molecule symmetry in quantum dots*, Phys. Rev. B **67**, 045311 (2003).

[166] S. M. Reimann, M. Koskinen, and M. Manninen, *Formation of Wigner molecules in small quantum dots*, Phys. Rev. B **62**, 8108 (2000).

[167] C. de Chamon and X. G. Wen, *Sharp and smooth boundaries of quantum Hall liquids*, Phys. Rev. **49**, 8227 (1994).

[168] V. M. Bedanov and F. M. Peeters, *Ordering and phase transitions of charged particles in a classical finite two-dimensional system*, Phys. Rev. B **49**, 2667 (1994).

[169] N. F. Mott, *Metal-Insulator Transitions*, (Taylor and Francis, London, 1990).

[170] S. M. Girvin and T. Jach, *Interacting electrons in two-dimensional Landau levels: Results for small clusters*, Phys. Rev. B **28** 4506 (1983).

[171] E. V. Tsiper, *Analytic Coulomb matrix elements in the lowest Landau level in disk geometry*, J. Math. Phys. **43**, 1664 (2002).

[172] M. Stone, H. W. Wyld, and R. L. Schult, *Edge waves in the quantum Hall effect and quantum dots*, Phys. Rev. B **45**, 14156 (1992).

[173] E. Anisimovas and A. Matulis, *Energy spectra of few-electron quantum dots*, J. Phys.: Condens. Matter **10** 601 (1998).

[174] A. Weiße and H. Fehske, *Exact Diagonalization Techniques*, Lect. Notes, Phys. **739**, 529 (2008).

[175] LAPACK – Linear Algebra PACKage, www.netlib.org/lapack/

[176] ARPACK - Arnoldi Package, www.caam.rice.edu/software/ARPACK/

[177] W. Kohn, *Cyclotron Resonance and de Haas-van Alphen Oscillations of an Interacting Electron Gas*, Phys. Rev. **123**, 1242 (1961).

[178] Ch. Sikorski and U. Merkt, *Magneto-optics with few electrons in quantum dots on InSb* , Surf. Sci. **229**, 282 (1990).

[179] U. Merkt, *Cyclotron Resonance of Localized Electron Systems in the Magnetic Quantum Limit*, Phys. Rev. Lett. **76**, 1134 (1996).

[180] F. Geerinckx, F. M. Peeters, and J. T. Devreese, *Effect of the confining potential on the magneto-optical spectrum of a quantum dot*, J. Appl. Phys. **68**, 3435 (1990).

[181] F. M. Peeters, *Magneto-optics in parabolic quantum dots*, Phys. Rev. B **42**, 1486 (1990).

[182] J. M. Luttinger, *Quantum Theory of Cyclotron Resonance in Semiconductors: General Theory*, Phys. Rev. **102**, 1030 (1956).

[183] M. Helle, A. Harju, and R. M. Nieminen, *Far-infrared spectra of lateral quantum dot molecules* , New J. Phys. **8**, 27 (2006).

[184] A. Wojs and P. Hawrylak, *Charging and infrared spectroscopy of self-assembled quantum dots in a magnetic field*, Phys. Rev. B **53**, 10841 (1996).

[185] R. J. Nicholas, M. A. Hopkins, D. J. Barnes, M. A. Brummell, H. Sigg, D. Heitmann, K. Ensslin, J. J. Harris, C. T. Foxon, and G. Weimann, *Anomalies in the cyclotron resonance in high-mobility GaAs-Ga1-xAlxAs heterojunctions*, Phys. Rev. B **39**, 10955 (1989).

[186] Y. Shapira, Jr. and N. F. Olivera, *High-field magnetization steps and the nearest-neighbor exchange constant in* $Cd_{1-x}Mn_xS$, $Cd_{1-x}Mn_xTe$, *and* $Zn_{1-x}Mn_xSe$, Phys. Rev. B **35**, 6888 (1987).

[187] S. Kalliakos, M. Rontani, V. Pellegrini, C. P. García, A. Pinczuk, A., G. Goldoni, E. Molinari, L. N. Pfeiffer, and K. W. West, *Evidence of the molecular state of correlated electrons in a quantum dot*, Nature Phys. **4**, 467 (2008).

[188] T. Ezaki, N. Mori, and C. Hamaguchi, *Electronic structures in circular, elliptic, and triangular quantum dots*, Phys. Rev. B **56**, 6428 (1997).

[189] B. Szafran, F. M. Peeters, S. Bednarek, and J. Adamowski, *Anisotropic quantum dots: Correspondence between quantum and classical Wigner molecules, parity symmetry, and broken-symmetry states*, Phys. Rev. B **69**, 125344 (2004).

[190] B. Partoens, A. Matulis, and F. M. Peeters, *Two-electron artificial molecule*, Phys. Rev. B **59**, 1617 (1999).

Curriculum Vitae

Nga Thi Thuy Nguyen

University of Antwerp
Department of Physics
171 Groenenborgeraan
Antwerpen, B-2020 BE

GSM: (32) 494 717 382
Work: (32) 265 3659
Email: nga.nguyen@ua.ac.be

Citizenship: Vietnamese

Date of birth: June 5, 1980

Place of birth: Namdinh, Vietnam

Education:

- PhD in Physics, expected 2010
  Department of Physics, University of Antwerp.
- Diploma in Condensed Matter Physics, August 2004
  The Abdus Salam International Centre for Theoretical Physics, Trieste, Italy.
- Bachelor of Science, July 2002
  Hanoi University of Education, Honored program for the talented, Department of Physics, Hanoi, Vietnam.

Research Interests

- Quantum dots, Diluted Magnetic Semiconductors, Quantum computing.

Publications

- List of publications is attached at the end.

Teaching experience

- Tutorial: Mechanics, Statistical Mechanics, spring 2005,
  Hanoi University of Education.

Computer skills

- Operating systems: Window, Linux
- Office: Word, Excel, Powerpoint
- Programming languages: FORTRAN, C/C++
  Numerical method: Exact Diagonalization, (Quantum) Monte Carlo
- Package: ARPACK

Language proficiency

- Vietnamese (native), English (fluent)

Awards and Honors

- Referee for Physica E, J. Phys.: Conf. Ser.
- The 3th poster prize, Belgian Physical Society 2008 general meeting, Brussels, Belgium.

List of publications

- *Correlated many-electron states in a quantum dot containing a single magnetic impurity*
  Nga T. T. Nguyen and F. M. Peeters, Phys. Rev. B **76**, 045315 (2007).
  Also selected for the July 30, 2007 issue of Virtual Journal of Nanoscale Science & Technology

- *Magnetic field dependence of the many-electron states in a magnetic quantum dot: The ferromagnetic-antiferromagnetic transition*
  Nga T. T. Nguyen and F. M. Peeters, Phys. Rev. B **78**, 045321 (2008).
  Also selected for the July 15, 2008 issue of Virtual Journal of Nanoscale Science & Technology

- *Ferromagnetic-antiferromagnetic transition in a magnetic quantum dot containing few electrons*
  Nga T. T. Nguyen and F. M. Peeters, Physicalia Magazine **30**, 169 (2008).
  A special issue for the winners of the young and poster prize at the Belgian Physical Society 2008 general meeting

- *Cyclotron resonance of a magnetic quantum dot*
  Nga T. T. Nguyen and F. M. Peeters, Phys. Rev. B **78**, 245311 (2008).
  Also selected for the December 22, 2008 issue of Virtual Journal of Nanoscale Science & Technology

- *Many-body effect in the cyclotron resonance of a magnetic dot*
  Nga T. T. Nguyen and F. M. Peeters, Phys. Rev. B **80**, 115335 (2009).
  Also selected for the October 12, 2009 issue of Virtual Journal of Nanoscale Science & Technology

- *Influence of electron-electron interaction on the cyclotron resonance spectrum of magnetic quantum dots and breakdown of Kohn's theorem*
  Nga T. T. Nguyen and F. M. Peeters (submitted to Phys. Rev. B)

- *The breakdown of Kohn's theorem in few-electron parabolic quantum dots doped with a single magnetic impurity* Mn^{2+}
  Nga T. T. Nguyen and F. M. Peeters (accepted for publication in J. Phys.: Conf. Ser. in the proceedings of the Quantum dot 2010 conference, Nottingham, UK, 2010)

- *Phase-diagram for the magnetic states of the Mn-ion subsystem in a magnetic quantum dot*
  Nga T. T. Nguyen and F. M. Peeters (accepted for publication in J. Phys.: Conf. Ser. in the proceedings of the Quantum dot 2010 conference, Nottingham, UK, 2010)

- *Magnetic phases of a few-electron quantum dot doped with two Mn^{2+} in the presence of a magnetic field*
  Nga T. T. Nguyen and F. M. Peeters (submitted to Phys. Rev. B)